



Aus dem Institut für Rechtsmedizin der
Ludwig-Maximilians-Universität München
Vorstand: Prof. Dr. med. Matthias Graw

Insassenschutzauslegung mit Menschmodellen / Occupant Protection Design with FE Human Body Models

Dissertation
zum Erwerb des Doktorgrades der Humanbiologie
an der Medizinischen Fakultät der
Ludwig-Maximilians-Universität München

Vorgelegt von

Rommel David Segura Novoa
2018

München 2018

Mit Genehmigung der Medizinische Fakultät
der Ludwig-Maximilians-Universität München

Berichterstatter: Prof. Dr. med. Matthias Graw _____

Mitberichterstatter: Prof. Dr. med. Stefan Milz

Mitbetreuer: Prof. Dr. rer. biol. hum. Dipl.-Ing. Steffen Peldschus _____

Dekan: Prof. Dr. med. dent. Reinhard Hickel

Tag der Mündliche Prüfung: 20.12.2018



Promotionsbüro Medizinische
Fakultät



Eidesstattliche Versicherung

Segura Novoa, Rommel David

Name, Vorname

Ich erkläre hiermit an Eides statt,

dass ich die vorliegende Dissertation mit dem Titel

Insassenschutzauslegung mit Menschmodellen /
Occupant Protection Design with FE Human Body Models

selbständig verfasst, mich außer der angegebenen keiner weiteren Hilfsmittel bedient und
alle Erkenntnisse, die aus dem Schrifttum ganz oder annähernd übernommen sind, als
solche kenntlich gemacht und nach ihrer Herkunft unter Bezeichnung der Fundstelle
einzeln nachgewiesen h a b e .

Ich erkläre des Weiteren, dass die hier vorgelegte Dissertation nicht in gleicher oder in
ähnlicher Form bei einer anderen Stelle zur Erlangung eines akademischen Grades
eingereicht wurde.

Stuttgart, den 15.06.2018

Ort, Datum

Rommel David Segura Novoa

Doktorand

ACKNOWLEDGEMENTS

To my grandmother, Mercedes Novoa. To my parents Isabel Novoa and René Segura. To my sisters and brothers. To Johanna Müller ML. To Prof. Dr. med. Matthias Graw from the Institute of Legal Medicine of the LMU. To Prof. Dr. Steffen Peldschus from the Institute of Legal Medicine of the LMU and my tutor Franz Fürst from the AUDI AG for all the discussions and readiness to share their knowledge and experience with me. To Anja Wagner from the Institute of Legal Medicine of the LMU for the invaluable help on image processing and discussions on biomechanics. To Dr. Kai-Uwe Hess from the Department of Earth and Environmental Sciences of the LMU for the invaluable help performing the μ CT-Scans. To the complete team of the Institute of Legal Medicine for the technical and logistical support (Anja, Ketuo, Therese, Michael and you). To Adrian Langer for the support on specific simulation problems and accident reconstruction. Special thanks to Dr. Andre Eggers who opened me the door for the crash simulation field. To the team of the University of Virginia – Center of Injury Biomechanics for giving me the chance to work on real testing. To my friends in Colombia from the Highschool and University, to my friends in Germany and in the rest of the world. Thanks to the Life itself for allowing me jumping into this great adventure. Remember, la vida son dos días.

CONTENT

Acknowledgements	2
Content	3
Notation	6
Introduction	8
1 Background	10
1.1 The Abbreviate Injury Scale (AIS)	10
1.2 Thorax Anatomy Review	12
1.3 Epidemiological Review: Thoracic Injuries, Ageing and Sternal Fractures in Frontal Car Crashes	16
1.4 Crash Test	22
1.4.1 Background	22
1.4.2 Regulations and Consumer Tests	22
1.5 Dummies	24
1.5.1 Review on the H350 dummy	27
1.6 Human Body Models (HBMs)	30
2 Development of an Elderly HBM	35
2.1 Method	35
2.1.1 Method: Sternum and 3D μ CT Scans	36
2.1.2 Method: Ribs and Variable Cortical Thicknesses	40
2.1.3 Method: Costal Cartilage Calcification	42
2.1.4 Validation Method	44
2.2 Results	65
2.2.1 Results Sternum and 3D μ CT Scans	65

2.2.2	Results Ribs and Variable Cortical Thicknesses	67
2.2.3	Results Costal Cartilage Calcification.....	69
2.2.4	Validation Results	72
3	Development of Assessment Procedures	96
3.1	Introduction: Occupant Restraint Method	96
3.1.1	Principles, Functions and Components for Occupant Restraint.....	97
3.1.2	Design Method	103
3.1.3	Crash Severity Criteria and OLC	105
3.1.4	Thoracic Injury Criteria: Review and Summary	108
3.2	Method: Thoracic Injury Assessment Procedures for HBMs.....	117
3.2.1	Split of analysis: Rib fractures (AIS3+) and Sternal fractures (AIS2).....	117
3.2.2	Identification of injury mechanisms for ribs and sternum	118
3.2.3	Correlation of the injury mechanism with injury reference values with and without Age-dependency (Ribs).....	121
3.2.4	Energy Plots	126
3.2.5	Comparison to the H350	126
3.3	Results	127
3.3.1	Restraint System Variants for Simulations (as result of design guidelines)	127
3.3.2	Sternal Injury Mechanism and Injury Reference Value (IRV)	131
3.3.3	Report summary and Method Validation	136
4	Application and Results: Simulation Matrix and Real World Accident Reconstruction	140
4.1	Crash Case 1: Real-World Accident Reconstruction	140
4.1.1	Method and Simulations.....	141
4.1.2	Results Crash Case 1: Accident Reconstruction	147
4.2	Crash Cases 2 to 7	158
4.2.1	Method and Simulations.....	158
4.2.2	Results Crash Case 2	160
4.2.3	Results Crash Case 3	164
4.2.4	Results Crash Case 4	168
4.2.5	Results Crash Case 5	172
4.2.6	Results Crash Case 6	176
4.2.7	Results Crash Case 7	180
4.3	Summary of Results: All occupants, all crash cases	184
4.3.1	H350 Driver and Passenger.....	184

4.3.2	Thums-original Driver and Passenger.....	185
4.3.3	Thums-elderly Driver and Passenger	186
4.3.4	Correlations	187
5	Discussion	191
5.1	Relevance of sternal fractures.....	191
5.2	Development of an elderly model and validation.....	192
5.3	Development of Assessment Procedures.....	196
5.4	Results: Discussion on Simulation Matrix Outcome.....	198
6	Conclusions and Future Work.....	202
6.1	Relevance of sternal fractures.....	202
6.2	Development of an elderly model and validation.....	202
6.3	Development of Assessment Procedures.....	203
6.4	Results: Conclusions on Simulation Matrix Outcome	204
6.5	Future Work.....	205
7	Summary / Zusammenfassung	207
	References	211
	Index of Figures	218
	Index of Tables.....	224
A.	Appendix: Crash Tests	227
B.	Appendix: Dummies	232

NOTATION

<i>AB</i> : Airbag	<i>H3</i> : Hybrid III Dummy
<i>AB-VENT</i> : Airbag Ventile	<i>H305</i> : Hybrid III Dummy 5 th Percentile female
<i>ACEA</i> : European Automobile Manufacturer Association	<i>H350</i> : Hybrid III Dummy 50 th Percentile male
<i>AM</i> : American Male	<i>H395</i> : Hybrid III Dummy 95 th Percentile male
<i>AF</i> : American Female	<i>HIC</i> : Head Injury Criterion
<i>AIS</i> : Abbreviate Injury Scale	<i>HBM</i> : Human Body Model
<i>ANSA</i> : Automatic net generation for structural analysis (Software for Pre-processing)	<i>HUMOS</i> : Human Model for Safety
<i>AP</i> : Anterior-Posterior	<i>IARV</i> : Injury Assessment Reference Values
<i>APROSYS</i> : Integrated Project on Advanced Protection Systems	<i>IIHS</i> : Insurance Institute for Highway Safety USA
<i>ARL</i> : Alderson Research Lab	<i>IRC</i> : Injury risk curve
<i>ATD</i> : Anthropomorphic Test Device	<i>IRV</i> : Injury Risk Values
<i>Bast</i> : Bundesanstalt für Straßenwesen	<i>INRETS</i> : Institut National de Recherche sur les Transport et leur Sécurité
<i>Belt-TTF</i> : Seatbelt pretensioner time to fire	<i>ICS</i> : Intercostal Space
<i>BioRID</i> : Biofidelic Rear Impact Dummy	<i>ISOFIX</i> :
<i>C</i> : Central Chest Deflection	<i>JAMA</i> : Japan Automobile Manufacturers Association
<i>CAD</i> : Cadaver	<i>JARI</i> : Japan Automobile Research Institute
<i>CAE</i> : Computer-Aided Engineering	<i>LC</i> : Load Cell
<i>CEESAR</i> : Centre Europeen d'Etudes de Securite et d'analyse des Risques	<i>LLim</i> : Load Limiter
<i>CFR</i> : Code of Federal Regulation	<i>LL1</i> : Load Limiter Level 1
<i>CIREN</i> : Crash Injury Research Engineering Network	<i>LL</i> : Lower Left Chest Deflection
<i>CO2</i> : Carbon dioxide	<i>LR</i> : Lower Right Chest Deflection
<i>COVER</i> : Coordination of Vehicle and Road Safety Initiatives	<i>LS-Dyna</i> : Simulation Software by LSTC
<i>CRS</i> : Child Restraint System	<i>LSTC</i> : Livermore Software Technology Corporation
<i>CTI</i> : Combined Thoracic Index	<i>μCT</i> : Micro Computed Tomography
<i>σ</i> : Standard Deviation	<i>MXYZ</i> : Resultant bending moment
<i>COG</i> : Center of Gravity	<i>MDB</i> : Movable Deformable Barrier
<i>DOF</i> : Degrees of freedom	<i>NASS</i> : National Automotive Sampling System-Crashworthiness Data System
<i>ECE</i> : Economic Commission for Europe	<i>NCAP</i> : New Car Assessment Program
<i>FE</i> : Finite Elements	<i>NHTSA</i> : National Highway Traffic Safety Administration USA
<i>FEM</i> : Finite Element Method	<i>n</i> : Sample size
<i>FLEX PLI</i> : Flexible Pedestrian Leg Impactor	<i>Nij</i> : Normalized Neck Injury Criterion
<i>FMVSS</i> : Federal Motor Vehicle Safety Standards	<i>NFR</i> : Number of Fractured Ribs
<i>FTSS</i> : First Technology Safety Systems	<i>NFS</i> : No Further Specified
<i>GIDAS</i> : German In-Depth Accident Study	<i>O</i> : Oxygen
<i>GIE RE PR</i> : Renault and PSA in-depth accident database	<i>OLC</i> : Occupant Load Criterion
<i>GS1</i> : Gold Standard I	<i>ODB</i> : Offset deformable barrier
<i>GTR</i> : Global Technical Regulation	<i>P-chestAIS3+</i> : Probability of AIS3+ thoracic injury
	<i>PID</i> : Part ID

PHC: Possible Head Contact
PMHS: Post-Mortem Human Surrogates
PMTO: Post-Mortem Test Object
RS: Restraint System
SSF: Static Stability Factor
STL: Stereo Lithography
T1: 1st Thoracic Vertebra
T4: 4th Thoracic Vertebra
T12: 12th Thoracic Vertebra
TTF: Time to Fire
THOMO: Development of a finite element model of the human thorax and upper extremities project
THOR: Test Device for Occupant Restraint
THORAX: Thoracic Injury Assessment for Improved Vehicle Safety
Thums: Thums®
Thums®: Total Human Model for Safety Version 3
Thums-elderly: Thums® with age-dependent factors included

Thums-original: Thums® in VPS
TMC R&D Labs: Toyota Motor Corporation Research and Development Laboratories
TNO: Nederlandse Organisatie voor toegepast-natuurwetenschappelijk onderzoek
TTI: Thoracic Trauma Index
UL: Upper Left Chest Deflection
UR: Upper Right Chest Deflection
UN: United Nations
UMTRI: University of Michigan Transportation Research Institute
VC: Viscous Criterion
VF: Ventricular Fibrillation
VM: Von Mises
VPS: Virtual Performance Solution Crash Simulation Solver
VX: X-Velocity
VY: Y-Velocity
VZ: Z-Velocity
YO: Years old

INTRODUCTION

The second leading cause of occupant fatalities in traffic accident are thoracic injuries. Sternal fractures are the most typical moderate thoracic injury in frontal car crash in adult and elderly population [1]. Until now there is no clear understanding on sternal injury mechanisms and how to assess the risk of sternal fracture of the occupants in a frontal crash. The design and assessment of advanced restraint systems capable to avoid or minimize such injuries is currently based on the injury prediction of the Hybrid-III (H3) dummy, an anthropomorphic test device (ATD) for frontal crash. Although the prediction capabilities of the H3 have encouraged automakers worldwide to boost the performance of restraint system in high crash severities, implicit dummy-design limitations as extreme simplified ribcage morphology, low biofidelity in low rate loading and lack of age-dependent factors question its applicability for moderate-injury prediction in lower crash severities.

The hypothesis is whether moderate injuries as sternal fractures can be predicted based on the H3 dummy, or whether the assessment needs to be complemented with more accurate and biofidelic tools such as human body models (HBMs) for a variety of crash cases in simulation environment. The fact that a H3 hardware does not have a transducer to convert the metrics of the thoracic deformation into an engineering metric for sternal loading suggests a gap of information where the restraint system may be erroneously optimized in terms of minimization of sternal injury risk. In order to analyze this hypothesis three main dimensions were addressed:

- (i) Development of a novel elderly HBM denominated Thums-elderly (based on the Thums-original) as an attempt to address age-dependent factors and realistic geometrical properties of the cortical bone based on real μ CT data.
- (ii) Development of novel assessment methods and tools specific to HBMs for rib- and sternal injury risk.
- (ii) Comparison in driver and passenger positions of the dummy model and both HBMs (Thums-original and Thums-elderly) in terms of injury prediction in a wide range of crash severities including a real-world accident reconstruction. In addition, the influence of adaptive restraint system variants on the injury prediction of each model and loadcase was analyzed.

These three dimensions are approached starting on the chapter 1 with a general background and epidemiological review on thoracic and sternal injuries. It also includes an overview crash testing and dummy development history. The chapter 2 titled “Development of an Elderly HBM” presents the development steps of the Thums-elderly including data from μ CT scans performed on real elderly sterna. The validation process of the models was addressed in material-, component-, body region- and full-scale level serving also as benchmark cases for ageing effects on the mechanical response of the components and full-body. In addition, the H350 (H3 dummy, 50th percentile male) simulation response in one of the validation test was included for comparison purposes. The chapter 3 contains methods for crash severity classification, design guidelines for restraint system management as the description of the restraint variants applied for the simulation matrix in the chapter 4. Furthermore, new methods for specific HBM analysis are developed addressing in first line rib fracture- and sternum fracture risk. The identification of the related injury mechanisms and a proposal for method validation are presented. The chapter 4 presents a simulation matrix where the models and methods developed in the previous chapters are applied. One accident reconstruction and six field-relevant crash cases are included. The models (H350, Thums-original and Thums-elderly) in driver and passenger positions, were simulated under four restraint system variants each, for a total of 168 simulations (seven crash cases * two positions * three occupant models * four restraint variants). The results are summarized per case as AIS2 (as sternum fracture) and AIS3+ injury prediction outcome, including correlation plots. The chapter 5 addresses the discussion on the results of model development, assessment method validation and injury prediction comparison between the H350 and HBMs in the simulation matrix. Closing, the chapter 6 presents the conclusion and recommended next steps for future work. The summary, in English and German languages, is included in the 7th chapter.

1 BACKGROUND

This chapter starts with the injury classification method used in this study followed by a thorax anatomy review and a statistical survey on thoracic injuries in frontal crashes. The topics aging society and its relationship with sternal injuries are depicted in the sub-chapter 1.3. This topic is followed by an overview on crash testing and frontal crash test dummies. The chapter closes with an introduction on human body models (HBMs) and bone ageing.

1.1 The Abbreviate Injury Scale (AIS)

The AIS is a widely accepted code for medical assessment of injury in traffic accidents. Based initially on the work of John D. States [2], the AIS code is a detailed reference for single injury coding. Single injuries are classified based on “life-threatening” levels (also called “injury severity”) as follows

Life Threatening Level (Injury Severity)	AIS Code
Minor	X.1
Moderate	X.2
Serious	X.3
Severe	X.4
Critical	X.5
Untreatable	X.6
Not further specified	X.9

Table 1.1 Injury severities defined in the AIS code [3]

Where “X” is an anatomical-specific reference code.

The AIS Codes [3] define for the thorax region (skeletal) the following classification:

Injury Description (For thoracic skeletal injuries)			AIS Code	
Ribcage	NFS*		450299.1	
	contusion		450289.1	
	multiple rib fractures ³ NFS		450210.2	
	fracture(s) without flail*, any location unilateral or bilateral	NFS	450200.1	
		one rib	450201.1	
		two ribs	450202.2	
		>=3 ribs	450203.3	
	fractures with flail ²	NFS	450210.3	
		unilateral	NFS	450211.3
			3-5 ribs	450212.3
			>5 ribs	450213.4
		bilateral flail chest		450214.5
Sternum	NFS		450899.1	
	contusion		450802.1	
	fracture		450804.2	
Thoracic Wall	NFS		451099.1	
	avulsion of chest wall tissues including rib cage	NFS	451020.4	
		minor; <=15% of chest wall including rib cage		451021.4
		major; >15% of chest wall including rib cage		451022.5

Table 1.2 AIS Codes for thoracic skeletal injuries

*NFS: Not Further Specified

²Flail chest: Defined as three or more ribs fractured in more than one location and/or resulting in paradoxical chest movement.

³Costal cartilage fracture or tear is coded as a rib fracture

1.2 Thorax Anatomy Review

From the very basics, the thorax is defined as the body region between the neck and abdomen consisting of ribcage and soft tissue including skin, fat, muscles and internal organs. The ventral limit of the thorax is the diaphragm, separating the thoracic to abdominal components. The ribcage consist of a sternum and 24 ribs organized in 12 rib-rings attached posteriorly to the thoracic vertebrae (T1 to T12) at the costal facet joints [4]. Anteriorly, the 1st to the 7th ribs are attached to the costochondral junction. The costal cartilage is attached to the sternum at the chondrosternal junction. The 8th to 9th ribs are normally attached anteriorly to the costal cartilage tissue that attaches the seventh rib to the sternum while the 10th (in some cases), 11th and 12th are floating ribs with no anterior attachment points. See Fig. 1.1.

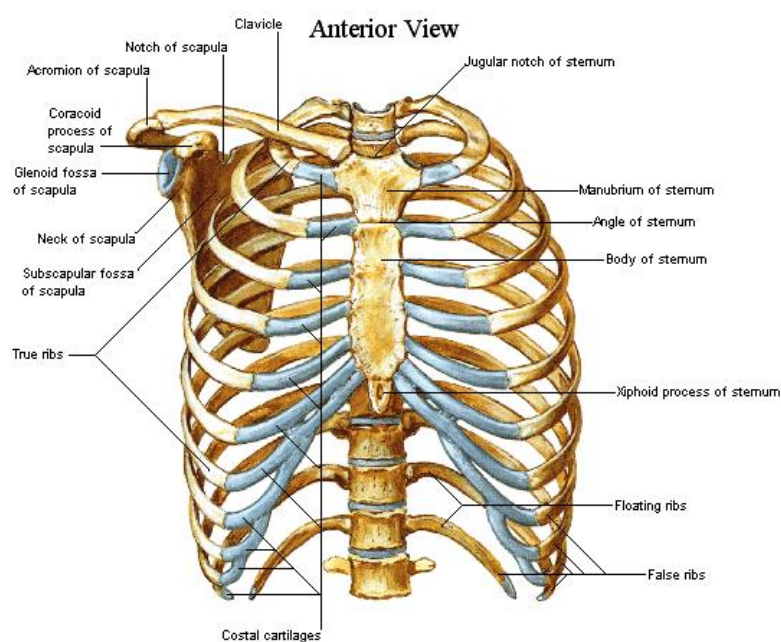


Fig. 1.1 Bony thorax

Sternum

The sternum [5] is a narrow and flat bone that belongs to the main structural components of rib cage and serves stabilizing the thoracic skeleton and also protects the thoracic internal organs including heart, aorta, vena cava and thymus gland among others. It is located along the chest anterior midline. The sternum includes insertion points of head-, arm- and neck-muscular systems. Anatomically the sternum is composed of three regions: (i) The manubrium, (ii) gladiolus (body of the sternum) and (iii) xiphoid process.

(i) The manubrium is the most superior region of the sternum, is connected via synovial joints (clavicular notches) with the clavicles forming the sternoclavicular joint. This point is the only skeletal attachment between the shoulder skeletal subsystem and the rib cage. Slight concave indentations on the lateral sides of the manubrium provide also the attachments points [5] for the costal cartilages of the first row of ribs. Inferiorly, the manubrium connects to the body of the sternum at the joint where transversally the costal cartilage of the second rib

meets both regions. This interface manubrium-sternum body is normally posteriorly bended, forming the so-called sternal angle. This point serves as an anatomical landmark. Regarding insertion points of the muscular system, the sternocleidomastoid, pectoralis major, sternohyoid, and sternothyroid muscles [6] are attached via tendons to the manubrium.

(ii) The gladiolus has a rectangular shape oriented sagittally. The 2nd through 10th ribs meet the sternal body laterally by the costal cartilages closing the skeletal ribcage ring.

The attachment points between the costal cartilage and the gladiolus are similar as in the manubrium. Concave indentations in the lateral sides of the body of the sternum provide kind of joint to prevent rib separation. Attachments of the muscular system includes the pectoralis major (function includes contribution to adduction and flexion of the humerus)

(iii) The xiphoid process is the smallest and most inferior region of the sternum. The xiphoid process goes through an ossification process throughout childhood and adulthood [5] until around age of 40 when the cartilage is completely replaced by bone. The xiphoid process includes attachment points for the tendons of the diaphragm, rectus abdominis, and transverse abdominis muscles [5].

Micro- and Macrostructure of Ribs and Sternum

The human ribs and sternum are “composite” [7] structures composed of an external and hard region called cortical bone and an inner and porous region called trabecular bone (or spongy bone). See Fig. 1.2.

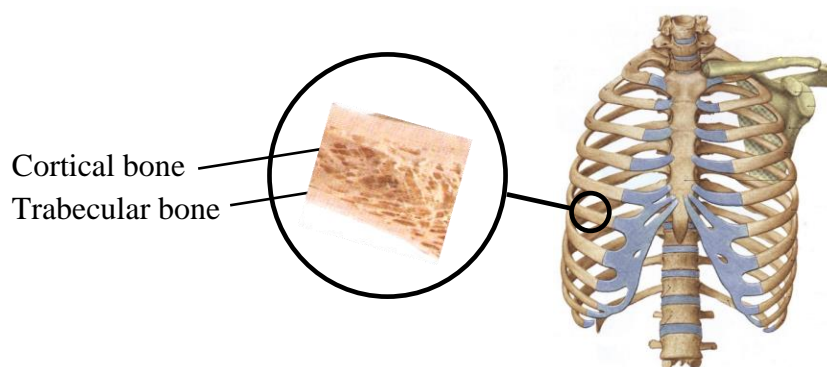


Fig. 1.2 Cortical and trabecular bone

The microstructure of both regions can be summarized as a hierarchical [7] structure starting with three amino acid chains that form collagen protein molecules (tropocollagen form). These molecules are the basic components of the mineralized collagen fibrils, which are known as the basic building unit of the bone. This collagen fibrils form fibril arrays that compose a single collagen fiber. This collagen fibers form different geometric patterns creating a lamellar structure on which the cellular components of the bone grow. See Figure below.

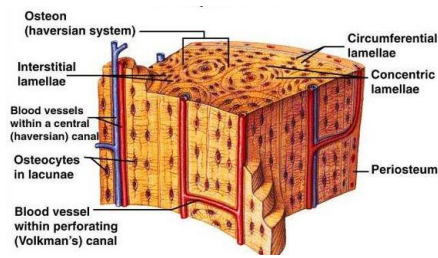


Fig. 1.3 Hierarchical structure of the bone

The boundary between these clusters of fibers are called lamellar interfaces. The different arrangement of these clusters and lamellar interfaces form the structure of a cortical or a trabecular bone.

The macrostructure of a trabecular bone is composed by these clusters of fiber about 100 micrometers thick and separated each other about 1mm. The macrostructure of the cortical bone is composed of osteocytes connected to each other with thin channels known as canaliculi. In the same hierarchical level are the osteons: cylindrical array of concentric lamellae that protect blood vessels and cells that dissolve old bone for the renewing tissue process.

Costal Cartilage

Anatomically, the costal cartilage is composed of irregular cylinder-type [8] structures of hyaline cartilage that connects the anterior end of the ribs 1st to 7th to the sternum and the ribs 8th -10th to each other and to the connecting cartilage of the 7th ribs. This array varies slightly in the population. As a connecting structure, the costal cartilage influences the coupling behavior of the anterior rib cage components and subsequently the force transference patterns. The force transfer patterns determine the stress and strain distribution on the material and governs the thorax effective stiffness influencing the thorax deformation patterns. The microstructure [9] of the cartilage consist of chondrocytes cells lying in groups in a homogeneous matrix form of the hyaline cartilage. When arranged in groups, the chondrocytes have commonly straight outlines being those a “tangential” contact with each other. The rounded shape contributes to a high elastic behavior in a macroscale level. The matrix consists of translucent protoplasm, interlacing filaments and minute granules. In a macrostructure level, the anatomical structure of the costal cartilage function as a composite structure in form of a cylinder, with a hyaline “core” surrounded by a thicker and fibrous structure called perichondrium. This core consists of a dense matrix of collagen fibers, produced by chondrocytes cells as explained in the last section.

Thoracic Organs

Briefly summarizing, the thoracic internal organs include the lungs, mediastinum, heart and great vessels as described in [10]. Both lungs are composed of two and three lobes respectively being the right lung slightly bigger than the left one. A serous membrane called visceral pleura covers the lungs with the physiological function of reducing the friction between lungs and chest wall. The parietal pleura covers the diaphragm and group the structures on the middle of the thorax [4]. The left and right lungs in the adult male weight around 450 g and 400 g respectively [11]. The physiological function of the lungs is the gas exchange between the blood and the atmosphere, replacing the carbon dioxide and by oxygen. Between lungs, sternum and thoracic spine the mediastinum is located. The mediastinum contains the great vessels, heart, thymus gland, esophagus, lower trachea, thoracic duct, lymph nodes and thoracic aspects of nerves as the vagus and phrenic. As mentioned, the heart is located in the mediastinum, is a hollow organ weighting around 300 g in the adult male and 250 g in the adult female. Structurally, the heart is divided in four chambers: Left and right atria, left and right ventricles. Its main function is pumping blood through the body receiving it first deoxygenated in the right atrium, coming from the superior and inferior venae cavae. The right ventricle pumps the blood though the four pulmonary veins hence the oxygenation process in the lungs starts. The oxygenated blood enters the left atrium to be later pumped though the body by the left ventricle.

1.3 Epidemiological Review: Thoracic Injuries, Ageing and Sternal Fractures in Frontal Car Crashes

Road Accidents

More than 34000 fatalities occurred in 2009 in the EU in traffic accidents [12]. Around 17000 were car occupants. A total of 1.5 million persons were injured. The related costs of these accidents for the society (including physical and psychological damage to the victims and their families) represent approximately 130 billion € [12]. Based on this societal burden, the European Commission proposed to continue with the target of halving the overall number of road deaths in the European Union by 2020 starting from 2010 [12].

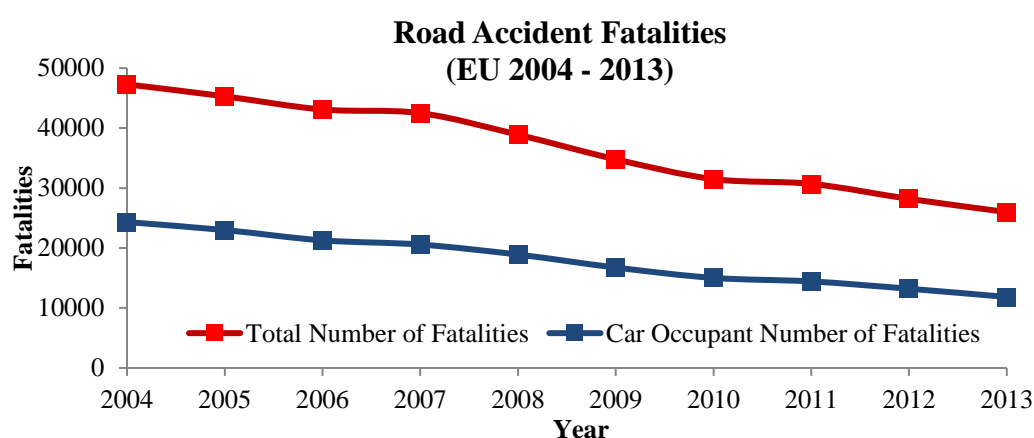


Fig. 1.4 Road Accident fatalities in Europe [13]

Thoracic Injuries and Frontal Crashes

Statistical analysis on road accidents often underlines the relevance of thoracic trauma in the field. Published data from the European project COVER (Coordination of Vehicle and Road Safety Initiatives) [14] showed the results of an accident databases survey conducted into the framework of the THORAX and THOMO projects [15]. Data from the CCIS (United Kingdom Cooperative Crash Injury Study), GIDAS (German In-Depth Accident Data Survey) and GIE RE PR (Renault and PSA in-depth accident database, France) was analyzed. The survey was constrained to (i) recent vehicle models (model year 2000 or newer, in order to ensure the inclusion of modern restraint systems), (ii) belted occupants, (iii) only frontal impacts. Injury outcome was analyzed. The results showed that the most frequent skeletal thoracic injuries are rib- and sternal fractures. The most frequent visceral thoracic injuries occurred were lung and heart injuries [16] (see Fig. 1.5). Other studies present similar findings: Nirula et al. [17] affirm that thoracic trauma is a major cause of mortality in vehicle crashes. Cuerden et al. [18] reported, based on previous researches, that 81% of drivers fatalities in frontal impact had a thoracic injury of at least AIS3 (serious injury, see subchapter 1.1); Mulligan, G.W.N. et al. [19] published a study on blunt chest trauma affirming that “thoracic trauma is a principle causative factor in 30% of traffic deaths”.

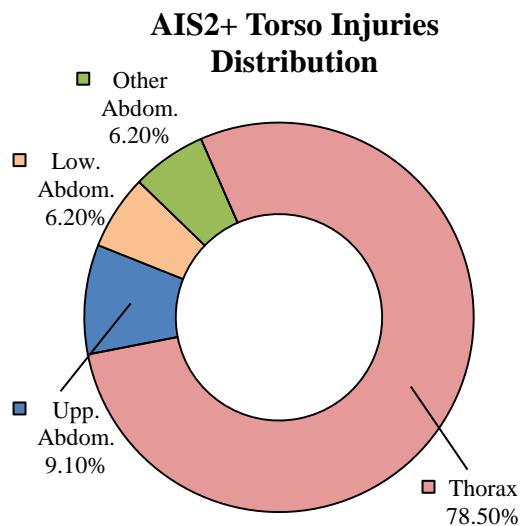


Fig. 1.5 Torso injuries overview form EU data. Taken from [16]

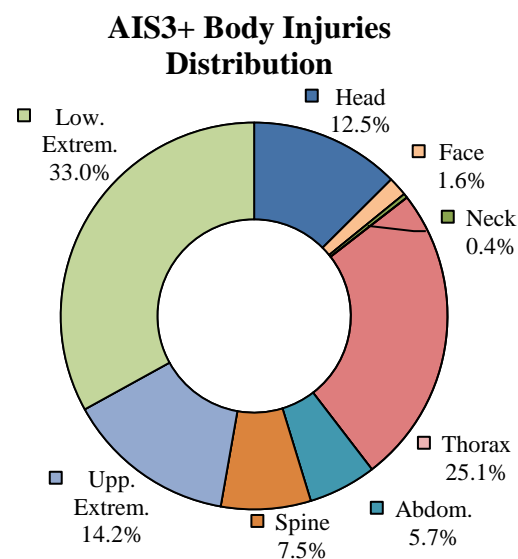


Fig. 1.6 AIS3+ Injuries distribution in frontal crashes. Subsample from the NASS-CDS. Taken from [1]

Other statistical surveys depicting the crash panorama in the US are briefly addressed here. Ridella et al. [1] analyzed a sample of $n = 18371$ from the NASS-CDS (National Automotive Sampling System-Crashworthiness Data System, US) classifying the data by crash mode. The frontal crash subsample showed that AIS3+ thoracic injuries are the second most common injuries on US roads, preceded only by lower extremities injuries (see Fig. 1.6). Frontal crashes, according to [20], represent 52% of crash modes on US roads in 2014.

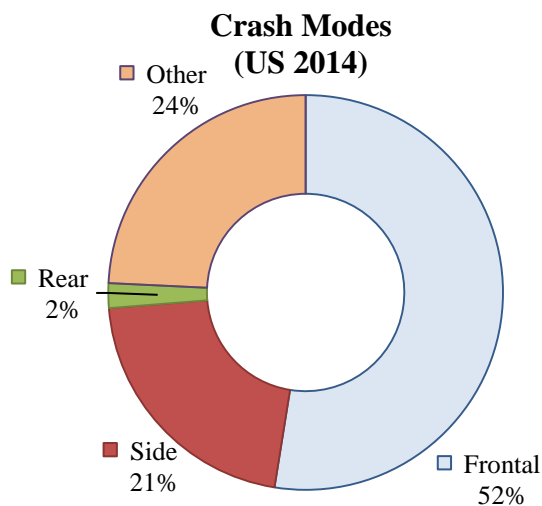


Fig. 1.7 Distribution of crash modes in the US according to [20]

Ageing and Sternal Fractures

Demographic changes generated by the ageing society phenomenon will include a pronounced increase in the percentage of elderly vehicle occupants in the coming years. Ageing trends have been quantified in several studies. For the US, and European population, a shift up to 25% by 2030 is expected [1] [21] [22]. See Fig. 1.8.

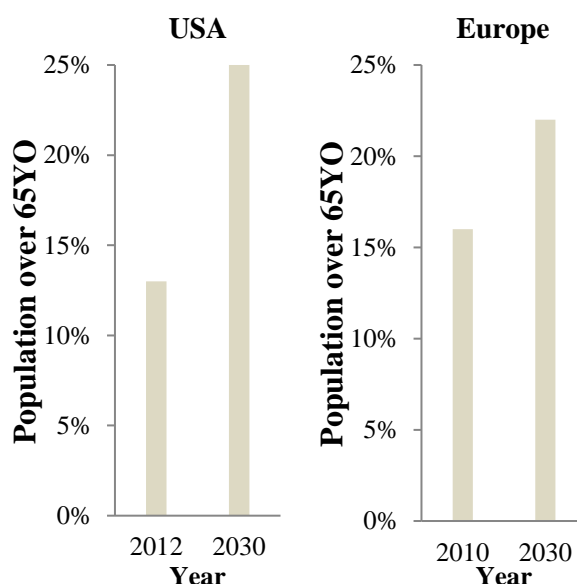


Fig. 1.8 Aging population projection for USA [1] and Europe [21]

The distribution of car occupant fatalities in 2013 [13] in EU (see Fig. 1.9) roads revealed already the elderly sample (>65 YO) as the second most vulnerable population. It is known that treatment cost and mortality are higher for older people than for younger people.

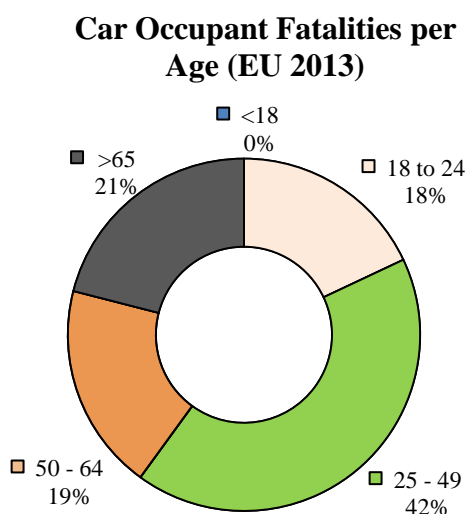
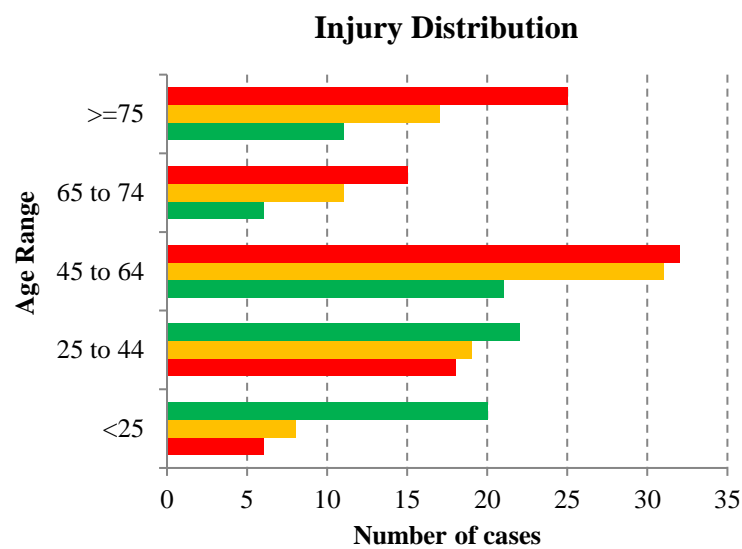


Fig. 1.9 Distribution of car occupant fatalities in the EU per age [13]

In the abovementioned study from Ridella et al. [1], a wider analysis was conducted on accident cases out of both NASS-CDS and the CIREN (Crash Injury Research Engineering Network) databases. Correlations between the occupant age and thoracic injury severity were

analyzed. The results showed that age correlates with an increased risk of AIS3+ injury in the thoracic region for all crash modes. The highest correlation was found for the thoracic region in frontal crashes. A total of 1289 cases of the CIREN sample proved that occupants older than 25 years (< 25YO) sustained greater proportions of head injuries and occupants older than 65 years (> 65YO) sustained higher number of thoracic injuries. By clustering the dataset by frontal crashes, the thoracic injuries type changed from soft tissue to bone fractures as age increased. The data was also clustered by age and frequency of thoracic injury. The most frequent moderate thoracic injury for a population older than 45 years (> 45YO) were sternal fractures. No data for single rib fractures were clustered. Rib fractures were the most common severe thoracic injury. A summary of the findings of Ridella et al. [1] is presented in the Fig. 1.10.



Injury	Color
Sternal fractures	Red
Unilateral or bilateral lung contusion with or without hemo-/ pneumothorax	Green
>3 rib fractures on one side and <=3 on the other with hemo-/ pneumothorax or >3 rib fractures on one side and <=3 on the other	Yellow

Fig. 1.10 Thoracic injuries clustered by age. Based on [1]

By analyzing moderate injuries distributions, sternal fractures appear to be also common when addressing again the database survey done in [16], a distribution of a subsample of thoracic injuries is depicted in the Fig. 1.5 and Fig. 1.11.

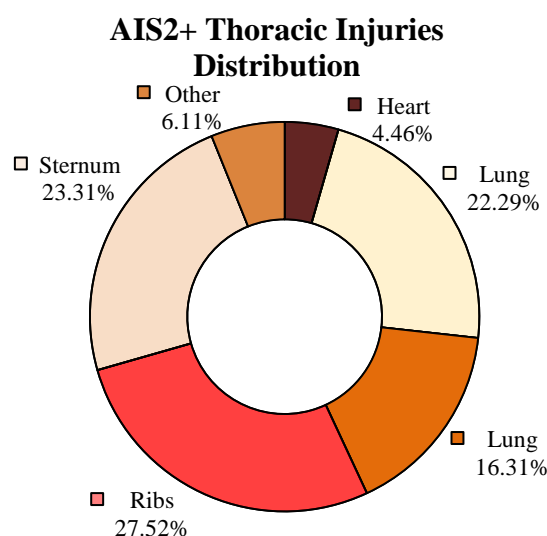


Fig. 1.11 Only thoracic injuries distribution. Adapted from [16]

Several studies address sternal injuries as typical outcome from anterior chest blunt trauma. Mentioned by [23], sternal fractures occur in five to eight percent of the population that sustained significant blunt chest trauma. Traffic accidents are the usual cause of sternal fracture [24]; the injury is estimated to occur in about 3% of car accidents [25]. As reported in the COVER-D5 Annex I [26], an analysis based on a subsample $n = 320$ from the CCIS [27] was run in the UK. In a comparative analysis on single injury pattern vs. combination of injuries it was found that the most common single injury in frontal crashes are sternal fractures, reaching 20% and 25% in males and females respectively. This suggest again that females are more likely to sustain this type of injuries than males. Another relevant epidemiological study on sternal fractures was presented by Brookes et al. [28] in 1993 (also referenced in [26]). The study presented a retrospective analysis of 6.5 years' data from the emergency department records of the Box Hill Hospital in Melbourne (Australia) with a $n = 272$. According to the results, sternal injuries were identified as a common pattern in traffic accidents and, supporting the findings in COVER, female patients older than 50 were reported as a special population in risk to sustain sternal fractures. In 1988 Breederveld et al. [29] run an study about insolated sternal injury cases in a dataset with $n = 71$ from the Academic Hospital Amsterdam. Records from 1975 to 1986 were analyzed. From the 71 cases 52 patients sustained sternal injuries without any other concomitant injury. Forty-two cases were the result of a traffic accident. Twenty-nine of them were belted. No patients with isolated sternal fracture died. The author suggested that the morbidity in cases with isolated sternal fractures is very low. Another study from Wedde et al. [30] run a retrospective review of a dataset $n = 72$ from patients with sternal fractures at the A and E (Accident and Emergency) department at Our's Lady, Navan, Country Meath (Ireland) with data from 1998 to 2003. Sixty-seven patients sustained sternal fractures from traffic accidents and 52 of them reported the use of seatbelt at the event. Sternal-related, or concomitant sternal injuries were also

review in [26]. A brief summary is presented here for reference: *Pain*. Normally sternal fractures are unlikely to generate further complications after the trauma [29] but are related to prolonged derivate chest pain in the patients [30]. *Ventricular fibrillation*. Analyzing derivate complications following sternal fractures, studies from Cooper et al. [31] with a $n = 38$ and Kroell et al. [32] with a $n = 23$ investigated a possible relationship between sternal fractures and ventricular fibrillation (VF) based on impactor test on porcine specimens sterna in prone position. It was found that the synchronization between impact time on the sternum and the T wave from the electrocardiogram would have generated a VF in four of seven specimens [31]. This could suggest a “vulnerable” period where VF is likely to occur under this impacting conditions. Nevertheless, this type of impact condition would be not relevant for modern restraint system loading, as mentioned in [26]. *Myocardial contusion*. Hamilton et al. [33] analyzed three traffic accident cases where the occupant were restrained with three-point belts and suffer sternal fractures. The derivate injuries of the sternal fractures were myocardial contusion (as analyzed by Hamilton) indicating that sternal injuries could be an indicator of possible cardiac trauma. *Poly Trauma*. In 1996 Jolly and Martinez [34] presented an analysis of the US NASS-CDS (National Accident Sampling System Crashworthiness Data System) from the year 1993 to 1994 with $n = 558516$. The authors affirmed that 50% to 60% of the cases with sternal fracture where associated with moderate and serious injuries. This suggested that sternal fractures are typically associated with severe mechanism of injury. In 2008 Knobloch [35] suggested that a severe sternal fracture could be an indicator of possible cardiac trauma, nevertheless, an analysis of the GIDAS database suggested that the rates of sternal fractures in traffic accidents reach just 0.64% (sample analyzed, $n = 42055$ only the rural area of Hannover, Germany). The sternal fracture associated concomitant injuries are headed by soft tissue bruises, spinal- and head injuries, multiple rib fractures and lung injuries. A recent review by Yeh et al. [36] on the US National Trauma Data Bank reported on a subsample of 23985 cases with patients that sustained closed sternal fractures. Cases coming from motor vehicle crashes were found to be the majority. Crash included several modes. The most common concomitant injuries were reported as lung injuries followed by vertebral spine injuries.

1.4 Crash Test

1.4.1 Background

The first references about motor vehicle accident goes back to the 19th century in the UK when a scientist died after being run over by a steam-powered automotive. With the increasing volume of vehicles on the road and the consequent changes in the society it was not a surprise when concerns about traffic safety, crashworthiness and crash safety features jumped into the public scenario. Gradually, carmakers started to include vehicle safety topics into the design process, aiming for safer cars.

The main development on this field started in the 30's with General Motors and the introduction of the first barrier crash test in a proving ground in Michigan (US). Structural analysis and in-crash behavior opened the way to crashworthiness analysis. In parallel, the Wayne State University (US) started research activities on vehicle safety in an attempt to understand the underlying principles of injury biomechanics of the human body in a crash. The lack of crash test dummies at that time (they were at the very beginning of their development) just allowed to test new developments with cadavers (with known ethical and moral discussions in the background), animal surrogates or with volunteers, of course with the “drawback” of a restriction of the testing conditions to a “non-injurious” range without considering the implicit uncertainties of repeatability, replicability and biofidelity. A short background of the dummy development will be addressed in the next sub-chapter.

Crash tests are per-definition destructive tests. They represent the keystone of the vehicle safety development of a new model. Crashworthiness analysis, crash-compatibility, occupant protection design, pedestrian safety, sensing systems development and crash-simulation are some of the fields involved into the outline of crash testing. Crash tests are performed during the design process aiming to accomplish legal requirements (regulations), reach high ratings in consumer test and, of course, to ensure safety levels that will minimize the risk of injuries and fatalities of the occupants or external road users involved in a road accident.

1.4.2 Regulations and Consumer Tests

Governments and independent institutions of the major automotive markets in the world have developed safety regulations and consumer tests that run in parallel. The structure and technical protocols for testing are in a constant process of re-evaluation and improvement, adapting themselves to the rapid changing technologies in the automotive business.

Among others, governmental institutions as the NHTSA (National Highway Transport Safety Standards Administration) in the US and the EC in Europe (from the old designation ECE: UN Economic Commission for Europe) have developed safety regulations, attempting to demand a minimum requirements of safety standards for on-road and new vehicles coming to the market. In the US, for example, these regulations are included in the Register 49 CFR (Code of Federal Regulation) part 571 as FMVSS (Federal Motor Vehicle Safety Standards). In Europe, similar regulations are defined as the UN RXX (old ECE RXX, e.g. UN R94

Offset Frontal Crash). A global harmonization is currently on progress, boosted principally by the efforts of mixed organizations (Government and Industry) as the UN/ECE/WG.29 (Working Group 29) on the development of GTRs (Global Technical Regulations). Despite the remarkable advances in harmonization, the low spread of test results to the public and the sluggish political decision-making process have generated that independent institutions, as the IIHS (Insurance Institute for Highway Safety, US) and worldwide NCAPs (New Car Assessment Programs), develop in parallel crash test procedures in an attempt to encourage car makers to exceed the minimum regulations requirements and spread the results to the public. These non-governmental efforts help consumers to have detailed and reliable information at disposal regarding the safety performance of the vehicles on the market.

Frontal Test

A summary of current (2015) frontal crash testing is shown in the table below. The data was classified by crash type and safety program (regulation or consumer test) in the US and Europe [37]. For a wider overview, including side crash tests will be found into the Appendix A.

Level	Test Type	Regulation	Consumer Test
Full Scale	Full Frontal	FMVSS 203	US NCAP 56km/h
		FMVSS 204	EURO NCAP 50km/h
		FMVSS 205	
		FMVSS 208	
		FMVSS 209	
		FMVSS 210	
		FMVSS 212	
		FMVSS 301	
		UN R12	
		UN R14	
		UN R16	
		UN R33	
		UN R94	
	Offset Frontal	FMVSS 208	IIHS 64 km/h (40% ODB)
	Small Overlap	UN R94	EURONCAP 64 km/h
		-	IIHS 64 km/h (25%)

Table 1.3 Current frontal crash testing programs

Detailed information for each test type will be found in [38], [39], [40], [20] and [41]. A complete overview of regulation and consumer test for side-, rear-, rollover-, pedestrian-configurations and child safety is presented into the Appendix: Crash Test. The following two test descriptions help to depicture the current status of frontal crash-testing into the EURONCAP (Taken mainly from the Euroncap website [41]).

Full Frontal Test

A car is driven at 50 km/h against a rigid barrier. The occupants are H305 (Small 5th percentile Hybrid-III dummy) seated on both front and rear positions. This crash was introduced to test the structural integrity of the occupant cell, helping to reduce lower leg and

head injuries generated by intrusion of the structure. Also introduced as a complement of the frontal offset test (see next item) in order to ensure a full restraint system performance: High energy dissipation with a heavier occupant (H350) but at the same time avoiding excessive deceleration peaks for the small occupant (H305).

Fig. 1.12 Full Euroncap frontal test

Frontal ODB (Offset Deformable Barrier)

Car driven at 64 km/h. Barrier: Offset deformable. The offset is 40% overlap. H350 dummies are seated in the front and child dummies (Q3 and Q1.5) in the rear positions. Introduced to represent a head-on collision between two cars driving in opposite directions with partial contact. The energy dissipation has to be managed with a smaller crumple-zone compared to the full frontal test. Steering wheel and pedals intrusion must be limited in order to minimize the risk of occupant injuries due to intrusions.

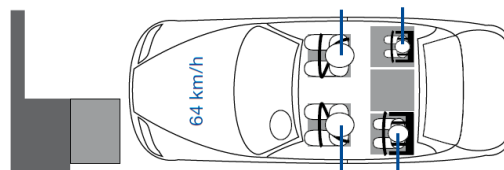


Fig. 1.13 Frontal Euroncap ODB (Offset Deformable Barrier)

Other NCAPs protocols slightly differ from the Euroncap test. Specific local-market-defined requirements and political decisions shape the protocols conditions. Detailed information about other NCAPs can be found in [42].

1.5 Dummies

As noted in the previous sub-chapter, in each crash-case an ATD (Anthropomorphic Test Device) -or Dummy- is used as sensing tool to evaluate the effectiveness of a restraint system or the energy dissipation capabilities of the front-end structure of a vehicle. Dummies have been developed for decades [43], the world's first crash-test dummy was developed in 1949 by Alderson Research Lab (ARL) [44] to assess ejection seats for the US Air force. This pioneer dummy was called "Sierra Sam". The Sierra Sam had the size of an adult male. Part of this initial research were shared with the automotive industry in the 50's, boosting the development of a vehicle-safety-dedicated dummies which have been continually improved and re-designed until our days attempting to reach higher biofidelity under impact conditions. This biofidelity level is defined as how "human-like" is the response of a dummy in a specific application (frontal crash, side crash etc.). The base line in a dummy built-up is to reproduce the same weight, size and proportions as the type of human they are made to simulate, e.g. the H350 (Hybrid III 50th Percentile) represents an American male with the size and weight of a

50th percentile subject. The morphological accuracy of the dummies influence directly its biofidelity level. With the development of more sophisticated electronics and materials, dummies were improved step by step to respond under impact much more like the human body. The right morphology is just the frame to build up a complex measuring device, dummies are instrumented with tri-axial accelerometers to trace the accelerations time histories of different part of the body (head, neck, chest, pelvis, femur and tibia). Bending moments, shearing forces and chest deflection (human thorax compression) are sensed using transducers in order to analyze loads on the human body in a crash situation. The definition of the biomechanical limits, and validation of the dummy's response is a complex process based on volunteer and cadaver test. This topic will be addressed in the next sub-chapter. Many types of dummies have been developed mostly dependent on the final application. In addition to the 50th percentile dummy, several frontal-crash dummies have been developed: An extra tall and heavy variant, the H395 (Hybrid-III 95th Percentile), the H305 (Hybrid-III 5th Percentile), child dummies representing children ten, six and three years old, baby dummies representing eighteen, twelve, nine and six months, and newborn babies. For other applications several types of dummies were developed: WS50 in side-, BioRID in the rear-crash, POLAR dummy for pedestrian test among others. The following two tables summarize the more relevant steps in the development of frontal crash test dummies the current dummies applied in crash testing sorted by application respectively.

Year	Designation	Developer	Comment
1946	ALDERSON	ARL (Alderson Research Laboratory) & Sierra Engineering	Mechanical surrogate of Para-gliders
1949	Sierra-SAM	Sierra Engineering	Dummy for the US-Air Force
1952	GARD	Grumman-Alderson	Research-Dummy
1954	FBP	ARL	Evolution of the GARD to be applied in both US-Air Force und Automotive industry
1956	ASP	ARL	Dummy for the APOLLO Space program
1962	VIP	ARL	Dummies in seated position for automotive applications in sizes 50 th , 5 th , and 95 th percentiles. Child dummy (3 und 6 Y.O.).
1963	Biofidelity test: Sierra-SAM vs. VIP	Holliman Air Force Base	Comparison test of SIERRA SAM- und ARL's VIP-Dummy to volunteer test. From this point the VIP proved to be more biofidelic than the Sierra-SAM.
1964-69	VIP 50 A and B Versions	ARL	Improved versions based on the VIP 50 th Percentile to test ejection seats for the US-Navy and the US-Air Force.
1950-70	ACTD	ARL & Sierra Engineering	Joint development of Crash-Test-Dummies for vehicle safety resulting in the ACTD based on GARD, VIP and SAM.
1971	Hybrid-I	ARL	Merge of the ARL- and SAM resulting in a hybrid dummy with the body of the ARL and head of the SAM.
1972	Hybrid-II	General Motors (GM)	Improvements of the Hybrid-I head, neck, shoulder, spine and knee.
1973	Part 572	NHTSA	Adoption of the Hybrid-II as standard test device for the FMVSS208 / Part 572.
1973	ATD 502	NHTSA / GM	Evolution of the Part 572 (or Hybrid-II). Improvements of the head, neck, articulations and ribs. The spine and knees were redesign. The posture were improved.

1976	Hybrid-III (H350)	NHTSA / GM	Evolution of the ATD 502: Redesign neck and thorax. More sensors implemented. Optional use to replace the Hybrid-II as standard for the FMVSS 208.
1988-89	Hybrid-III (H395 and H305)	HUMANETICS & SAE	Derivatives development of the Hybrid-III: 95 th Percentile (male) and the 5 th Percentile (female)
1985-95	TAD-50M	NHTSA / GESAC (General Engineering and Systems Analysis)	Predecessor of a new generation of frontal-crash dummies: The THOR.
1995	THOR-ALPHA	NHTSA / GESAC	New development for a more biofidelic frontal-crash dummy “THOR” (Test Device for Human Occupant Restraint). Planned to replace the current Hybrid-III in regulations and consumer test.
2005	THOR-NT	NHTSA	Improved version of the THOR-ALPHA after evaluation by JARI (Japan Automobile Research Institute) and JAMA (Japan Automobile Manufacturers Association). Anthropometry, biofidelity, durability and usability were improved for this release [44]
2000- 2009	THOR-FD	FID / APROSYS	Updated version of the THOR-NT carried out in the projects FID and APROSYS
2011	THOR-K (SAE)	NHTSA / SAE	Re-evaluated version of the THOR-NT by the THOR-TASK-FORCE (formed by SAE supported by NHTSA) and including recommendations based on the FID and Aprosys projects. This dummy includes an add-on modification kit that improves it's biofidelity.
2011	THOR-M (Metric)	NHTSA / HUMANETICS	Humanetics was contracted by the NHTSA to develop a metric version of the THOR-K called THOR-M (Metric)

Table 1.4 Highlight of frontal crash test dummies-development

		ECE-R94	ECE-R95	ECE-R44	EuroNCAP	FMVSS208	FMVSS214	FMVSS213	FMVSS202a	USNCAP	IIHS	Research
Frontal	H395											X
	H350	X			X	X			X	X	X	
	H305					X				X		
	H350+THOR LX Leg											X
	THOR50 – X*									X	X	X

Table 1.5 Current application fields for frontal crash test dummies. Partly taken from Safety Update 2012 proceedings. Child dummies not addressed here.

1.5.1 Review on the H350 dummy

In the next chapters a comparison between H350 and HBMs in terms of injury risk prediction will be carried out. A brief overview on relevant technical data related to the H350 is presented here.

Designation and use. The H350 was the next iteration after the H250's development. The H350 is a regulated ATD described in the US Code of Federal Regulations Title 49 (49CFR), Part 571E. The dummy is currently used in the FMVSS208, ECE-R94, NCAPs, IIHS test program and research among others. Detailed information can be found in [45]

Morphology. As mentioned the H350 represents the external morphology of a 50th percentile American Male. The main dimensions are summarized in the following table.

Reference	Dimensions [mm]
Total Sitting Height	884
Shoulder Pivot Height	513
H-Point Height	86
H-Point from Seat Back	1372
Shoulder Pivot from Backline	89
Thigh Clearance	147
Elbow to Wrist Pivot	297
Skull Cap to Backline	43
Shoulder to Elbow	338
Elbow Rest Height	201
Buttock to Knee	592
Popliteal Height	442
Knee Pivot to Floor	493
Buttock Popliteal Length.	465
Chest Depth	221
Foot Length	259
Foot Width	99
Shoulder Width	429
Hip Width at H-Point	363
Chest Circumference	986
Waist Circumference	851
Ref. Location for Chest Circumference	432
Ref. Location for Waist Circumference	227

Table 1.6 Taken External dimensions of the H350 dummy [46]

The H350 torso is composed of six pairs of ribs composed of steel layered by a polymer damping material. The ribs are screwed posteriorly to the so-called thoracic spine and anteriorly to the so-called sternum. A rotary potentiometer is attached to the spine and connected to the sternum via slider joint. The complete assembly is surrounded by a high density foam representing the outer torso soft tissues.

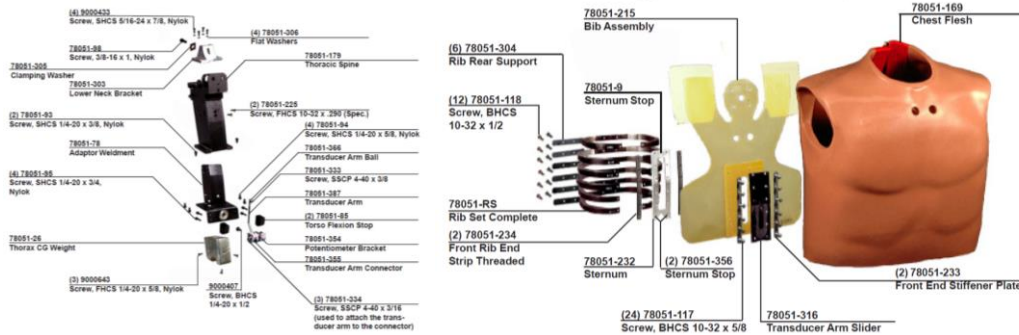


Fig. 1.14 Left: Spine and chest deflection transducer. Right: Torso assembly [46]

Instrumentation. The following table summarizes the full-package instrumentation of a H350 for the thoracic region. Note only three metrics can be extracted: Thoracic spine tri-axial accelerations and forces, bi-axial spine moments and chest deflection. A full instrumentation overview for all body regions will be found into [46].

Region	Description	Accelerometer			Loadcell			Transducer	
Thorax	Accelerometers in a triaxial array	AX	AY	AZ					
	Chest Displacement Transducer								DX
	Rib/Spine Load Cells				FX	FY	FZ	MY	
	Thoracic Spine Load Cell				FX	FY	FZ	MX	MY

Table 1.7 Overview of the H350 thorax instrumentation. Fully equipped.

Injury Assessment Reference Values (IARV) and Risk Curve for Chest Deflection. The IARVs represent the biomechanical limits where the risk of sustaining a specific injury is lower than 5 percent. The IARVs for the H350 do not represent the biomechanical limits of a human population [47]. Here the thoracic IARVs are presented. A full overview for all body regions is presented in Appendix: Dummies.

Region	Metric	Intercepts
Thorax	Peak sternal deflection with shoulder belt [mm]	50
	Peak sternal deflection w/out shoulder belt [mm]	47.7
	Peak deflection rate [m/s]	8.3
	Peak T4 Acceleration [G]	60

Table 1.8 Injury assessment reference values for the H350. Taken from [47]

Thoracic injury risk. In the US new car assessment program the H350 thoracic injury risk is currently calculated based on Laituri et al. [48] for an AIS3+ severity. Only the risk of rib fractures is addressed. For more information on the development process of this curve please refer to 3.1.4. Note that no transducer, metric or IARV is included specifically for sternal loading assessment.

$$P_{chest(AIS3+)} = \frac{1}{1 + e^{[(10.5456 - 1.568(Chest\ deflection))^{0.4612}]}}$$

Eq. 1.1

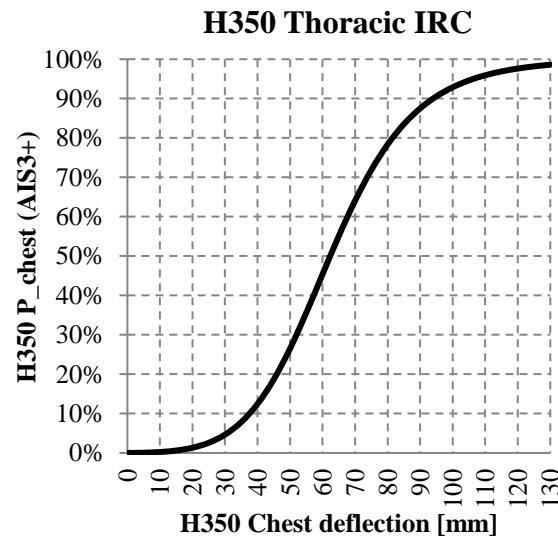


Fig. 1.15 Current H350 USNCAP thoracic injury risk curve [48]

1.6 Human Body Models (HBMs)

Crashworthiness and restraint system design have been boosted by virtual modeling in the last two decades. The application of dynamic systems, multi-body models and the extensive use of the finite element (FE) method are mainly motivated by the cost-benefit balance compared to real testing. Initially applied only on the concept phase of the development of a new vehicle model, digitalization is growing exponentially into the field. These virtual technologies opened the way to the development of dummy models and detailed human body models (HBMs). Recently, HBMs have been used intensively as an advanced assessment tool in automotive, aerospace, defense and production applications. The possibility to expand the classical dummy approach to a more realistic representation of the human body offers radical advantages for the assessment of safety systems.

Although automakers around the world gradually implement HBMs into the restraint system design, the Hybrid-III dummy (H3) continues as main assessment tool for frontal crash since the earliest 90s. Even though the prediction capabilities of the H3 have encouraged automakers to boost the performance of restraint system in high crash severities, implicit dummy-design limitations as extreme simplified morphology, low biofidelity in low rate loading and lack of age-dependent factors question its applicability for more for moderate-injury prediction analysis as sternal fracture risk. Summarizing, the H3's injury prediction presents four main drawbacks listed below contrasted to the HBMs potential:

H3 (5th, 50th or 95th %-ile)	HBMs
Fixed representation of a specific population: Biomechanical limits are scaled per body region to match a single subject-type	Capable to represent different populations, percentiles and genders. Subjected to geometrical and material modifications age-dependency can be addressed
Lack of a transducer to convert the metrics of the thoracic deformation into an engineering metric for sternal loading	Human-like thoracic morphology able to represent a more realistic response and injury mechanisms specific for sternal fractures
Fixed number of sensors for injury risk evaluation	Unlimited engineering metrics for injury risk evaluation
Low biofidelity level in low crash severities, frontal-crash dedicated	Biofidelity independent on crash severity or crash mode

Table 1.9 Comparison H350 vs. HBMs

A more detailed biomechanical analysis based on HBMs contributes to distinguish improvements of the restraint systems in situations where the dummy metrics are not capable. In a long term, HBMs will contribute to minimize risks of injury in any crash scenario as a supplementary tool.

Thums®

The Thums® v3 (Total HUMAN Model for Safety Version 3) is the baseline model utilized in this dissertation. The model was converted from LS-Dyna to VPS code by Dynamore [49]. The model was integrated into the crash simulation environment of Audi AG. The Toyota Motor Corporation (TMC) and Toyota Central R&D Labs developed the model in the late 90's. Originally just representing 50th percentile American male (AM) (178 cm height, 77 kg weight and about 40 years old), now a complete family with different sizes and genders have been developed [50]. This FE model is supposed to be used as a tool to simulate more realistically human body kinematics and injury response. The Thums is principally modelled by elastic-plastic materials (bony materials) and hyper-elastic materials representing soft tissues. The development of the model resulted in different versions with different capabilities for injury prediction under impact conditions. The version 3 is supposed to predict bony fractures and ligament rupture. The version 4 was further developed with the purpose of predicting internal organ injuries [51].

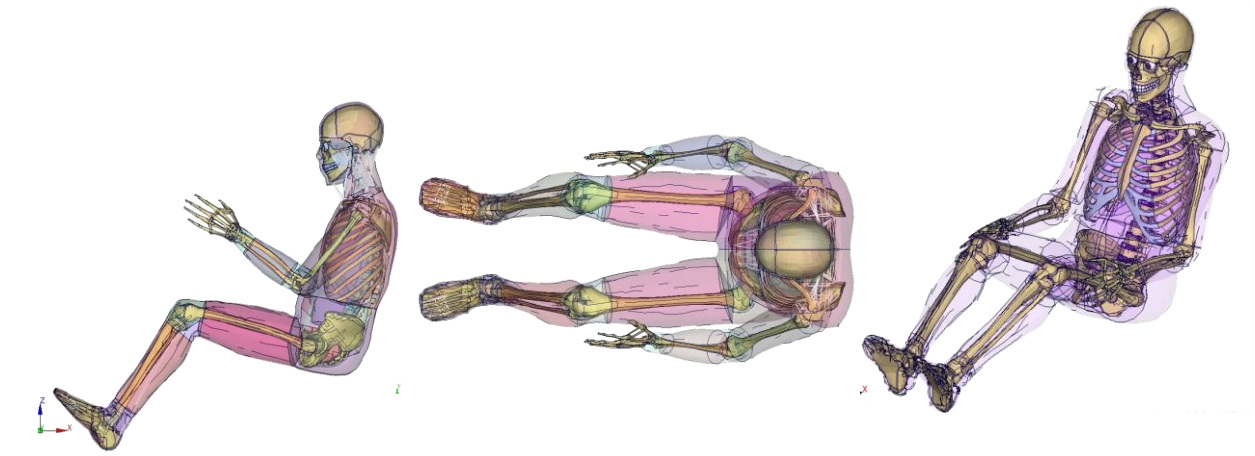


Fig. 1.16 Thums® v3 (Total Human Model for Safety). Some parts not displayed for visualization

The continuous improvement of the original Thums® resulted in three upgrades [50]:

Version	Year	Main development / Characteristics
v.1	2001	Major bones and ligaments develop, rough internal organs modeling.
v.2	2004	Development of facial bones for fracture prediction.
v.3*	2008	Detailed brain modeling, for brain injury prediction
v.4	2010	Detailed internal organs modeling, injury prediction capability
v.5	2015	Based on the version 3. Muscle activation for Pre-crash applications

Table 1.10 Thums® upgrades (*Baseline in this dissertation)

The next table summarizes the principal characteristics of the Thums version 3 model converted to VCP:

Item	#
Nodes	111600
Elements	113500
Part IDs	1170
Material IDs	260
Contact Definitions ¹	160
Rigid Bodies ²	30
Weight	77.3 Kg
BMI	24.3

Table 1.11 Thums® v3 in VPS. Model data with rounded numbers.

¹Referred to pair or set of Part IDs where the FE Solver defines a mathematical interaction to simulate a physical contact. See Table 1.11.

²Referred to a set or single Part IDs which the FE Solver simulate with a high elasticity modulus in order to simulate an ideal rigid behavior. See Table 1.11.

Focusing the description on the thoracic region, the rib bone model could be considered as a composite material made of two types of bone: Cortical and trabecular (or cancellous, see 1.2). The material characteristic of the cortical bone typifies high stress and lower strain under loading while trabecular bone exhibits relatively higher energy storage capacity. Cortical bone is modeled with fully integrated shell elements and spongy bones with solid elements. Internal thoracic organs are represented as a single continuum body modeled with solid elements.

A comparison between a human thorax and the FE counterpart as Thums® v3 is shown in the Fig. 1.17 and Table 1.12:

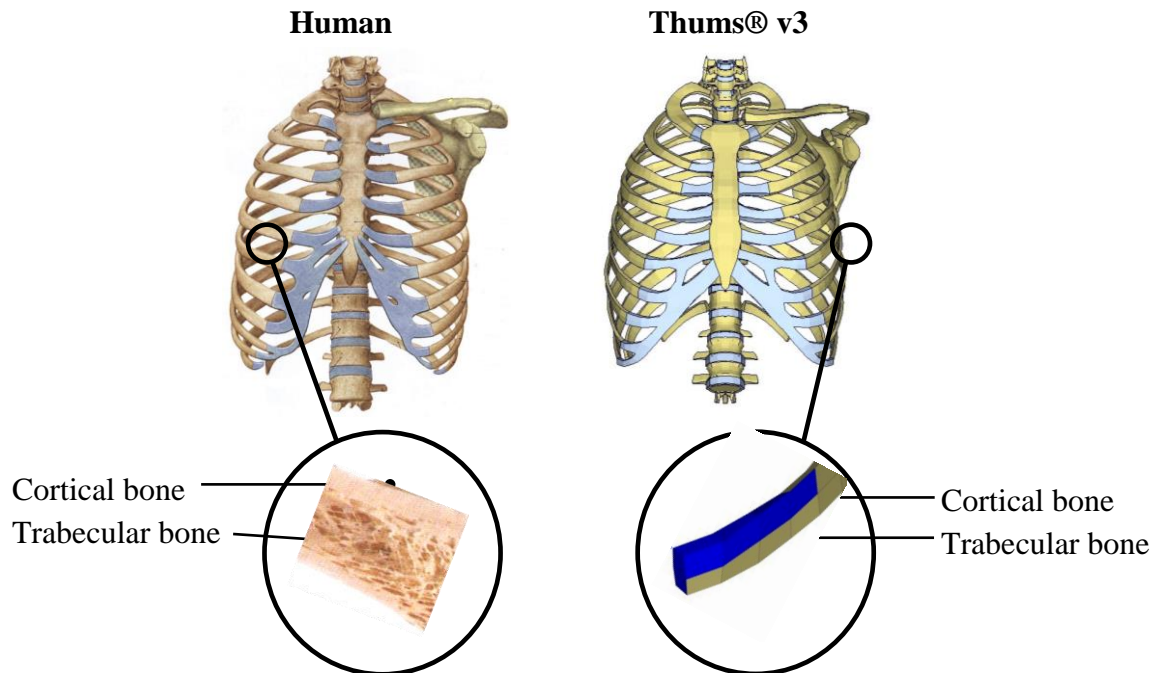


Fig. 1.17 Left: Human thorax structure [10]. Right: Thums thorax structure

	Component	Element Type	Young's Modulus [GPa]	Yield's Stress [GPa]	Failure Strain Definition [microstrain]
Ribs	cortical bone	Shell	13	0.0935	18000
	trabecular bone	Solid	0.01379	0.00045	100000
Sternum	cortical bone	Shell	11.5	0.123	(Failure w/out element elimination)
	trabecular bone	Shell	0.01379	0.00045	100000
Cartilage	Hyaline + Perichondrium	Solid	G = 0.0175 K = 0.082	0.00485	330000

Table 1.12 Bony Material descriptions of the Thums thorax components in VPS®

Bone Ageing: Sternum, Ribs and Costal Cartilage

The increase of the bony fracture risk due to aging can be defined as the consequence of bone mass loss process called osteoporosis and degradation of the bone quality. Experiments with human cortical bone in an age group of 34- to 99 YO (years old) show close to 40% decrease in micro-crack initiation resistance and a poor crack-growth resistance when correlated with aging [7].

Starting in a nanoscale level, several degradations in the collagen environment occur, with a special influence on the fibers cross-linking “density”. One order up, at the sub-micrometer scale, the mechanical properties of individual collagen fibrils deteriorate, and finally at scales between 1 and 100 micrometers, the bone structure changes due to a reduced density of osteons, which seems to be the principal factor on the bone fracture resistance.

As the age increases, the bone re-modeling process could be summarized as follows: The growing of the cements lines obstruct the tiny canals that connect interstitial bone cells producing an increase rate of cell death. Note that in the cement lines is where the micro-cracks normally forms and the increment of osteons density correlates with an increase of micro-crack density [7]. This fact correlates clearly with a severe decrease in fracture resistance. The fracture of trabecular bone with the age could be explained as a struts density and diameter decrease, especially among post-menopausal women. An osteoporotic process changes dramatically the spongy bone architecture. The change in bone quantity is until today the wider approach to explain the age related spongy bone, parallel to internal changes in the bone micro-structure with age which are also likely to affect the bone resistance to cracking in ways comparable to those in the cortical bone.

With this background, the micro-structure changes derive into punctual facts which are likely to be summarized as a cortical bone thickness reduction, lower density of trabecular bone, and among these factors, the geometrical changes of the component in a macro-scale level.

Sternal loading modeling

The relevance of sternum fractures in car crashes and its age dependency has been pointed out in 1.3. As explained in the problem formulation, despite advanced restraint systems and injury mitigation mechanisms, rib and sternal fractures still occur in vehicle crashes. For development of advanced restraint systems that maximize the occupant protection a more accurate geometrical description of the occupants and the ageing effects on specific body parts (e.g. sternum) are needed. The response of the bones under loading is strongly dependent on the cortical thickness, as mechanical response of a hollow beam depends on the wall thickness. Current HBMs define cortical thickness with a predetermined value for each bone whereas real cortical thickness is non-uniform along real bones. The sternum is not an exception.

2 DEVELOPMENT OF AN ELDERLY HBM

Following the outline on Human Body Models (HBMs) in the subchapter 1.6, this chapter presents the development process of a novel HBM denominated “Thums-elderly”. This process is described starting with methods for data acquisition, data transfer and validation, followed by results of each mentioned method. The validation method and results of both Thums® v3 and Thums-elderly are presented separately in the subchapters 2.1.4 and 2.2.4.

2.1 Method

This subchapter contains the development process of an “elderly” HBM, from now denominated “Thums-elderly”. The baseline is the original Thums® v3, from now denominated “Thums-original”. Modifications on the material properties and cortical thickness of ribs and sternum based on μ CT scans as the validation methods are presented in this subchapter. Validation methods on material-, component-, body region- and full-scale level are contained into the subchapter 2.1.4.

2.1.1 Method: Sternum and 3D μ CT Scans

The mechanical response of human bones is strongly dependent on its cortical thickness, as the mechanical response of a hollow beam depends on the wall thickness. Current HBMs define cortical thickness with a predetermined value for each bone whereas real cortical thickness is non-uniform along real bones. The sternum is not an exception. Following the background presented on 1.6 “*Sternal loading modeling*”, tridimensional micro computed tomography (3D μ CT) scans on sterna were performed in order to obtain the real cortical bone thickness distribution. This work was done in collaboration with the Mineralogy Research Department of the LMU [52]. The scan data was set to a modified HBM in an attempt to simulate a more realistic mechanical response by setting a human-like structure of the sternal cortical bone. A set of three male sterna were harvested from post mortem following the University of Munich (Institute of Legal Medicine) ethical approval. Extraction, handling and storage procedures were done at the institute in collaboration with medical staff. The extraction protocol specified the cuts at the sterno-costal junction for all attached ribs. Clavicles were removed in each case by cutting the synovial capsules. Soft tissues were removed but the sterna were not completely scraped. See Fig. 2.1.

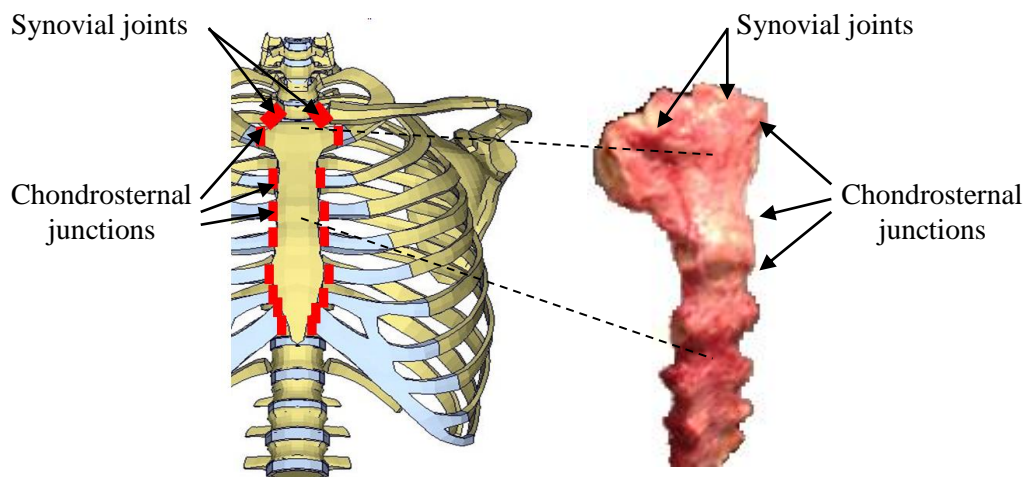


Fig. 2.1 Diagram for the sterna extraction protocol (red represents the cutting locations) and specimen

Subject's age, height and weight are summarized in the table below. Note that the CPR (Cardiopulmonary resuscitation) information was hence included due to hypothesis that fractures or micro-fractures could induce an error after processing the images where the cortical thickness estimation in the fractured region could be erroneous. Afterwards it was established that when averaging the cortical thickness in a wider area (e.g. 15 x 15 mm which represents the typical element size in a HBM sternum) this hypothesis becomes irrelevant.

Subject	Age[Years]	Height [cm]	Weight [kg]	CPR
CAD161	65	171 cm	95 kg	Not clear
CAD162	44	188 cm	82 kg	No
CAD163	72	170 cm	89 kg	Yes
Average	60.3	176.3	88.7	-

Table 2.1 Subjects details. All male

The sterna were frozen until the 3D μ CT scans were performed. Prior to the scans, the specimens were let to reach the room temperature (approx. 20°C). For the fixation with the machine chuck initially wood chopsticks were attached to the sterna and then those to the chuck jaws. Due to vibrations problems it was decided to cover the xiphoid process with a simple layer of paper and mount the sternum on the chuck by fixing the xiphoid directly with the chuck jaws as shown below.



Fig. 2.2 Left: GE phoenix 3D v/tome/x m. Center: Sternum mounted. Right: Voxel size.

The μ CT specification are summarized in the next table. A diagram of the machine parts and basic configuration are shown in addition in the next figure.

Machine	GE phoenix 3D v/tome/x m
X-ray type	Microfocus
Detector	GE DXR, 1000 x 1000 Pixels, Area 200 x 200 mm
Voltage / Amp.	80kV / 120 μ Amp.
Resolution	1390 μ m (0.139 mm)
Axial images generated	1000
Time elapsed per μCT	20 Min
Chuck / Manipulator Type	6-axis

Table 2.2 μ CT specifications



Fig. 2.3 Diagram of the μ CT Machine. Credits GE Measurement & Control, Volume Graphics [53]

In order to keep the 0.139 mm Voxel resolution and maximize the scanned volume in one run, a detector window of approx. 100 cm² was chosen. The scanned area is shown in dark in the Fig. 2.4. The Fig. 2.5 shows an example of the cross section of one specimen. In the Fig. 2.6 the cross section coordinates and a measuring point of local thickness is shown.



Fig. 2.4 Example of the scanned region on the detector

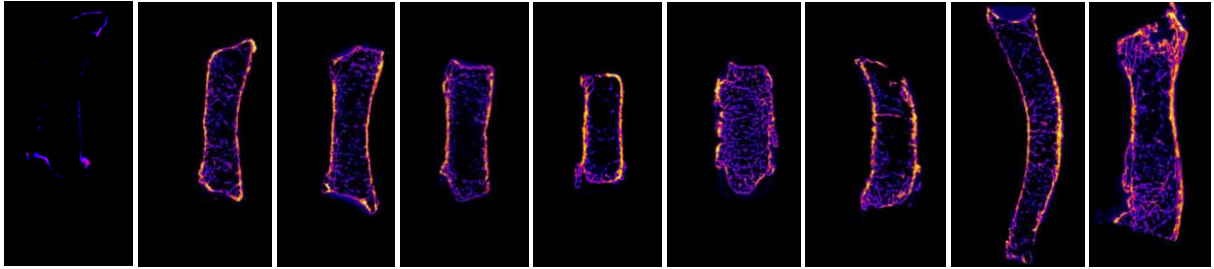


Fig. 2.5 CAD162, example of sternum cross sections ventral to coronal from the μ CT-Scan (left to right). Step approx. 1 cm

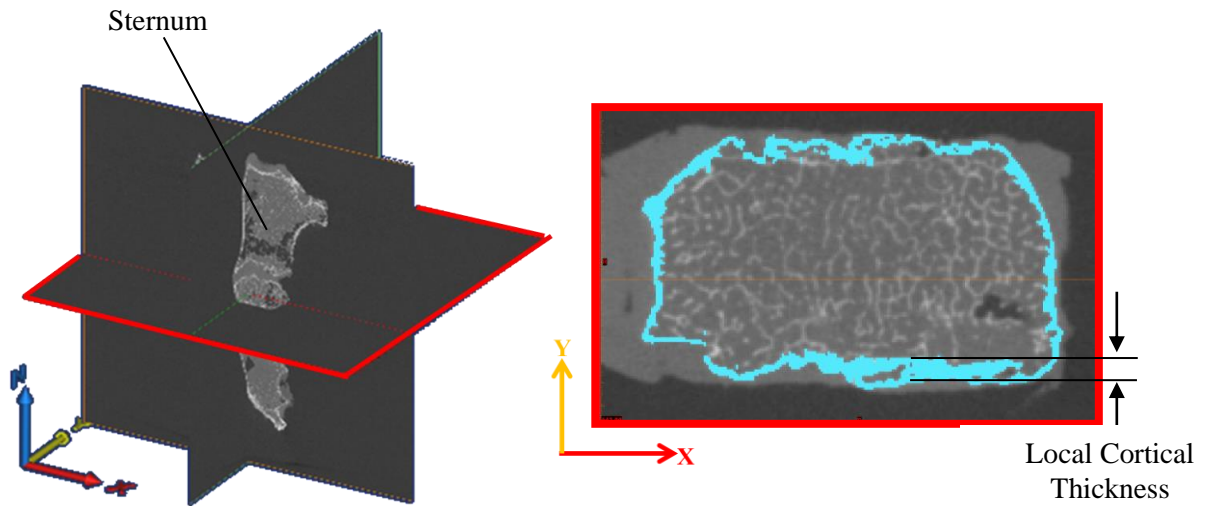


Fig. 2.6 Left: Diagram and coordinates of sternum μ CT Scan. Right: Cross section as an example of a local cortical thickness

Results of the μ CT Scans can be found in 2.2.1

2.1.2 Method: Ribs and Variable Cortical Thicknesses

As part of the development of an “elderly model” the subsequent step involved the modification of the cortical layer of the ribs since the original thickness for the shell elements (cortical) in the Thums model is a default value of 0.7 mm. The target was to represent the aging process based on a new cortical thickness distribution per rib. This new cortical thickness distribution was extrapolated from one real rib μ CT scan (7th rib, male, age at time of death 67) generated by Del Pozo et al. (bending test results in [54]). The modified ribs were then introduced into the Thums-original model, in order to generate a “Thums-elderly” where the cortical thickness of the ribs follow a realistic distribution obtained from one elderly subject. The process for the data implementation is described below. The base line is the Thums-original, the rib modeling characteristics are summarized in the Table 2.3.

Rib (Cortical layer)	Element Type	Integration Points	Cortical Thickness [mm]
3 rd to 10 th	Shell	5	0.7

Table 2.3 Rib modeling characteristics (cortical layer of the Thums-original)

Del Pozo et al. developed one STL (Stereo Lithography) model of a real 7th right rib which was generated from a μ CT scan (30 μ m of isometric resolution) [54]. The model was analyzed and post-processed internally by the Biomechanics Group of the Institute for Legal Medicine of the LMU. The data contained into the STL model includes the cortical thickness distribution of the rib. The age dependency is implicitly defined by the age of the subject (67 YO).

The data was analyzed in order to be transferred to the Thums-original thus generating a Thums-elderly version with realistic “elderly” rib cortical thickness distribution. The data was processed by clustering the cortical thickness distribution in four groups, representing the 25th, 50th, 75th and 100th percentiles of the cortical thickness distribution as presented in the following table.

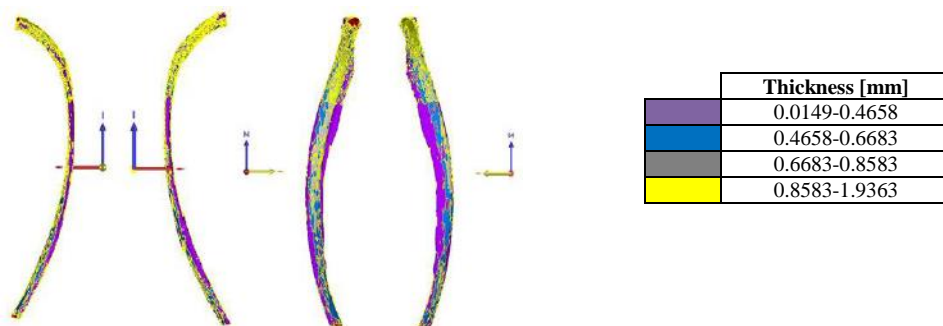


Fig. 2.7 Cortical thickness groups for the 7th rib generated by 3-Matic Software Package. Credits: Anja Wagner LMU

7th Rib (Right)		
Thickness Group	Thickness [mm]	Average [mm]
0-25%ile (purple)	0.0149-0.4658	0.4658
25-50%ile (Blue)	0.4658-0.6683	0.6683
50-75%ile (grey)	0.6683-0.8583	0.7634
75-100%ile (yellow)	0.8583-1.9363	1.3973

Table 2.4Cortical thickness groups for the 7th rib

The thickness-groups were manually transferred to the Thums-original's 7th rib. See results in 2.2.2. This approach was taken for the ribs 3rd to 10th assuming a similar distribution along each rib. Resultant values of cortical thickness per group and diagram with the thickness per group and rib level will be found also in 2.2.2.

2.1.3 Method: Costal Cartilage Calcification

Material modifications on specific costal cartilage regions were the chosen method for the representation of calcification as ageing process. These modifications are mainly based on the concepts presented by Forman et al. [8] as follows: The calcification process can be summarized as mineral calcium build up in soft tissues. The mechanical consequence of this process is an increased stiffness of the calcified component, and for instance, the cartilaginous tissue is not an exception. As a reference, the typical stiffness in tension of human costal cartilage is around 0.049 GPa (defined by the elastic modulus) [8] whereas after a calcification process this stiffness tends to increase up to levels comparable to the cortical bone of the ribs [55]. Note also, as explained in 1.2, that the cartilage is a “composite structure” of hyaline (inner core) cartilage and a fibrous layer (outer) called perichondrium. In a bigger context, recent studies (referred also by Forman in [8]) as Rejtarova et al. [56] and Bahrami et al. [57] correlate the calcification process with aging. Incidence and calcium deposition increases dramatically with increasing age [58]. Severe cartilage calcification can start already at the age of 60 [59]. Another relevant factor for the mechanical analysis is the location of the calcified regions since the calcification, citing Forman [8], “has the potential to affect the structural behavior of the costal cartilage ...”. The growing pattern of the calcified areas seems to correlate with the proximity to both “bone boundaries”: Sternum and rib. Lau et al. [55] presented in 2011 a study where 52 specimens (extracted costal cartilages) from 11 subjects underwent μ CT scans. Morphology, mineral density and volume fraction of costal cartilage were analyzed. The mineralized volume plots revealed a pattern where the calcification tends to start in the adjacent region of the costochondral joint.

The abovementioned facts can be summarized in:

- (i) Increase of stiffness due to cartilage calcification
- (ii) Age dependency of the calcification process
- (iii) Growing pattern of the calcification

Combining those, a test-bench model was generated in order simulate their influence on the mechanical behavior of the rib cage. Four models were prepared and tested in table-top belt loading as described by Kent et al. [60] (see Fig. 2.9). Each model represents a different costal calcification level. The calcified elements of the cartilage were represented by increasing their elastic modulus close to the bony range, according to (i). The growing pattern of the calcification start was assumed to start in the adjacent bony edges based on (iii). The material properties of the ribs were kept in order to isolate the influence of the calcification levels on the mechanical response of the rib cage.

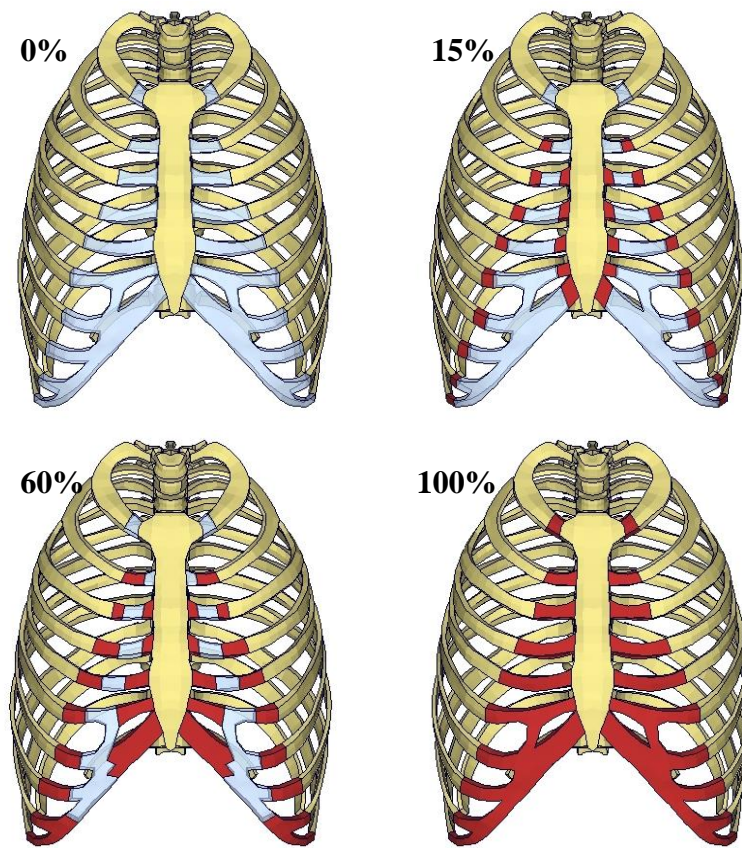


Fig. 2.8 Four calcification levels from left to right: 0%, 15%, 60% and 100% represented by the growing of the brown region

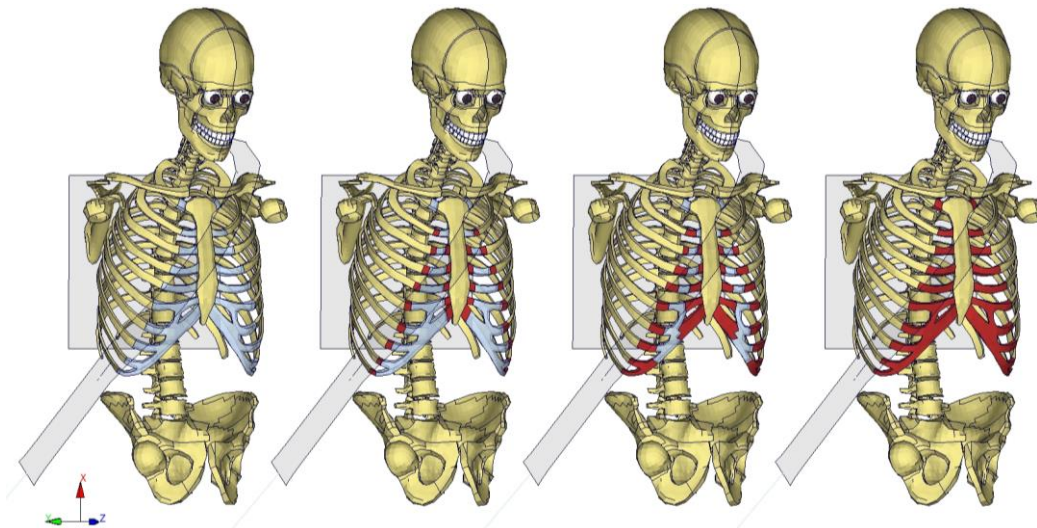


Fig. 2.9 Four calcification levels in Table-Top environment. Soft tissues blended.

Simulation results are presented in 2.2.3.

2.1.4 Validation Method

Accurate geometry, correct material properties and representative loading conditions constitute the basic framework for a HBM validation. This section shows a survey of representative experimental data organized in a multi-level validation method in material-, component-and body-region-level. New bio-corridors were created for sternum- and rib bending based on the available experiment data from the literature. Simulation results are shown in 2.2. The analysis includes: Rib cortical bone, sternum cortical bone, costal cartilage and, on a material level, internal organs (defined as a single viscoelastic super-organ). Finally, a validation protocol was created summarizing all levels. This section presents a selected set of relevant validation cases that best represents the real injury mechanisms of specific components of a driver in typical frontal crash conditions.

2.1.4.1 Material Level

Biological and specifically human body materials are typically anisotropic, non-linear, viscoelastic (including implicitly a strain-rate dependency) and show high variability of failure mechanisms and levels. This variability is mainly based on the differences in age, gender, ethnic group, geometrical differences and even daily life health factors as nutrition, sport activity level, injury records etc. From the perspective of a HBM validation using the FE method, the best-fitting constitutive model and a representative material characterization load case from the experimental data are fundamental as a biofidelity check. No specific failure was defined in this study. For the material level tensile and compression real test have been chosen and simulated.

2.1.4.1.1 Sternum and Rib Cortical Bone (Method)

No reference was found in the literature specifically for tensile test or dog bone test (see Fig. 2.10) with human sternal cortical bone. The material properties of the human cortical sternum are assumed to be similar to the cortical rib bone. Kemper et al. published a study in 2005 [61] where a sample of $n = 117$ coupons from human rib cortical bone were tested dynamically in tension. The testing rate was 0.5 strain/s generated in a high rate servo-hydraulic Material Testing System. The coupons were extracted and machined in “dog bone” shape (see Fig. 2.10). Anterior, lateral and posterior aspects of the ribs were used to extract the samples. Stress vs. Strain curves were generated. Six PMHSs were included in the study. See the table below for more information as presented in [61].

Subject	Gender	Age[Years]
6	M	18
2	M	45
5	F	46
4	F	61
1	F	64
3	M	67
$\bar{X} = 50$		

Table 2.5 PMHS details, sorted by age [61]

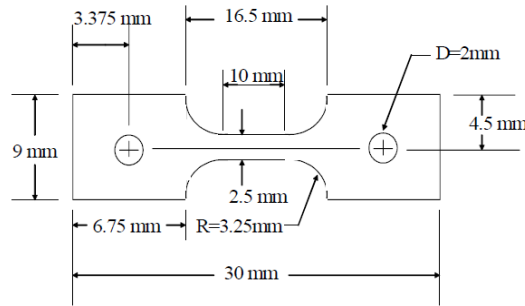
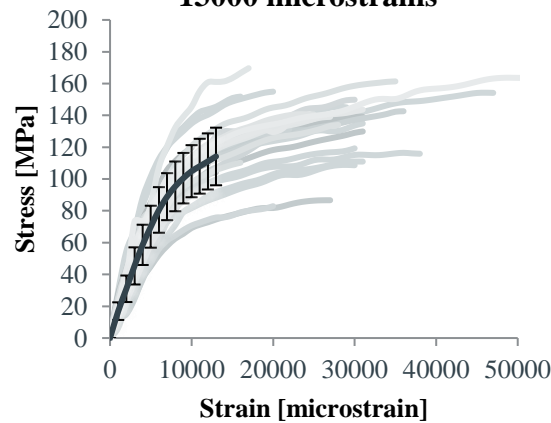


Fig. 2.10 From Kemper [61] experiments: Coupon test dimensions or “dog bone”

Kemper et al. reported no significant statistical significance regarding thoracic region, rib level and gender. By age, it was found a significance but, strongly dependent on the only “young” surrogate data. Therefore, all curves were taken into account for a response corridor. Anterior and lateral strain-stress curves were plotted. Data for average response and \pm one standard deviation (σ) was plotted until 13000 microstrain. Note that: (i) The data from the rib 7 anterior from the subject 4 and rib 7 lateral from the subject 1 were excluded due to the early failure. (ii) All the remaining data was plotted in the background as a reference for higher microstrain as 13000. However, no specific corridor can be generated due to the heterogeneity in the ultimate strains for all coupon test.

Anterior and Lateral Exp. Data and Corridor \pm Std. Dev. until 13000 microstrains

Fig. 2.11 From Kemper experiments [61]: Grey curves represent the experimental data. In black the average and $\pm\sigma$ until 13000 microstrain.

2.1.4.1.2 Cartilage (Method)

Yamada et al. [62] published in 1970 a summary of mechanical characterization test done on biological materials, including human and animal tissues. Apart from several experiments conducted by himself, Yamada reported summarized results of several studies mainly carried out in the University of Kyoto between 1940 and 1970. One of those is the battery of tensile test done by Ko and Takigawa in 1953 [63] where a large sample of human costal cartilage was tested in quasi-statically in tension. From twenty-eight PMHS straps of costal cartilage were harvested and prepared for the test. No detailed individual information of the PMHS is presented in the papers. The dimensions of the sample are described as 25 mm long, and 1 mm thick in [62] whereas in [63] they are described as 30 mm long straps. The width of the samples is not specifically described. It was assumed the width of the costal cartilage in situ. Ko and Kitagawa summarized the results in stress-strain curves for a age group of 20 to 29 YO, as presented in the Fig. 2.12.

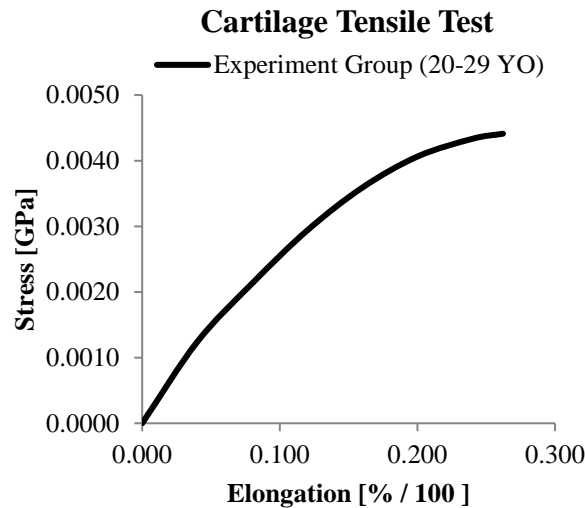


Fig. 2.12 Stress-Strain curve of human costal cartilage in tension as published by Yamada [62]

2.1.4.2 Component Level

Selected sternum-, ribs-, clavicle- and costal cartilage-bending tests taken from the literature are presented below. The modeling procedure used in VPS for each case is also explained. The results are presented in the section 2.2.4.2.

2.1.4.2.1 Sternum Bending Test(Method)

Anterior-posterior three-point bending test from experiments published by Kerrigan et al. [64] were taken as reference for sternum response in bending. A set of sterna $n = 9$ including 7 male and 2 female (age = 62.7 ± 10.9 years) were prepared following harvesting by potting of both ends and mounting on the posts as shown in the figure below (described in [64]). The reaction forces in the posts were recorded by 6-axis loadcells (LC1 and LC2). The bending was generated by a servo-hydraulic actuator in quasi-static (0.0002mm/ms) and dynamic (1117 mm/ms) rates.

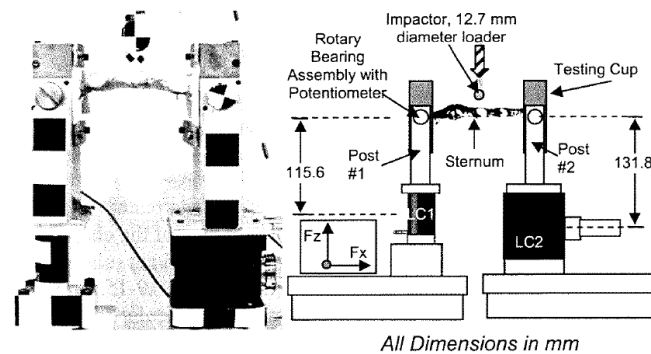


Fig. 2.13 Left: Test setup for sternum bending. Right: Test diagram taken from [64]

The reaction forces in LC1 and LC2 were translated to bending moments using an average bending arm = $70 \pm 4\text{mm}$ (distance from the average middle point of the sterna from the LCs).

Also, as described in [64], although the test were designed for the analysis of the sterna under bending, the nature of the setup generated significant forces in X direction (compression forces for the sterna) in at least the initial phase of the loading. These forces are the result of the bending of a convex-like structure in a 1-DOF (degree of freedom) setup, where just one rotation DOF was allowed by the system. See Fig. 2.14.

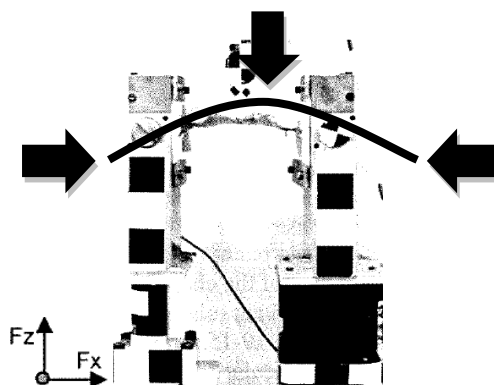


Fig. 2.14 Convexity of the sterna generate significant forces in X due to the fixation setup with pin-joints: Rotation [64]

Based on these remarks, the convexity of the sterna is the dominating factor in order to analyze the change of polarity (from compression to tension) of the loading mode. The x-reaction forces F_x (measured by the LC1 and LC2) would register this change of loading mode. Kerrigan mentioned several problems on the data recording at both loadcells [64] hence the corridors will be plotted here but not considered to be compared to the simulations. Following the method for the abovementioned bending corridor, the experimental data was considered just until 35 mm of displacement as show below.

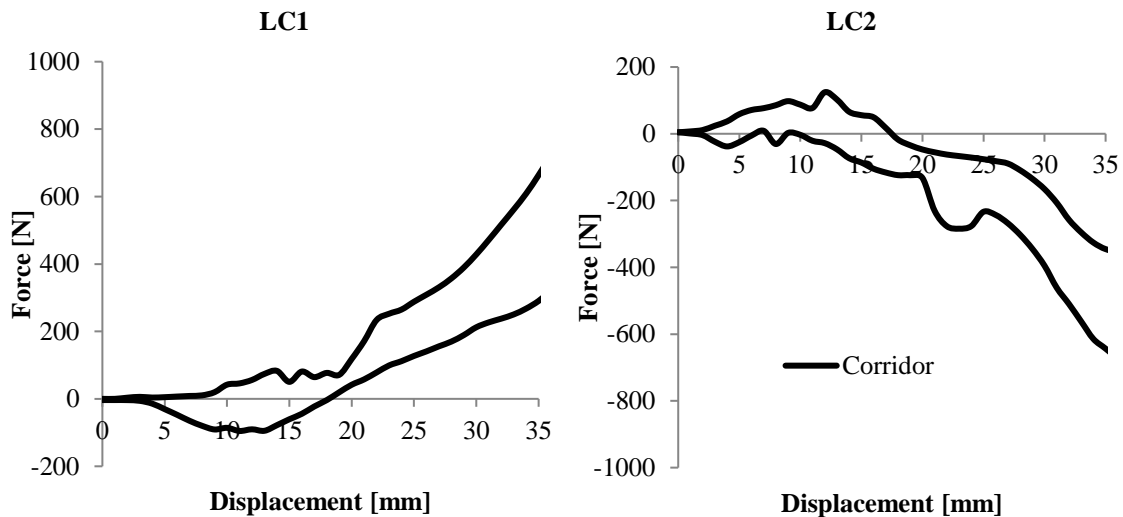


Fig. 2.15 Dynamic response corridor for sternum: Right: F_x on LC1. Left: F_x on LC2. Accuracy of experimental data under question.

For bending, a corridor based on Kerrigan's experiments were generated. The following facts were noted: (i) As mentioned by Kerrigan, the data from test 453 and 454 showed inaccuracies from 38.5 mm and 47.7 mm impactor displacement respectively. Kerrigan mentioned a hypothesis where the sterna convexity generated high F_x forces that would derive into vibrations in the posts (supports) and hence generated inaccuracies. Therefore, the response corridor excluded both time stories from 38 ms. (ii) The test 170 data ends at around 35 mm impactor displacement, therefore a corridor involving data of all nine test will be restricted to 35 mm in order to maximize the representativeness of the sample. (iii) The initial peak responses appear to be an inertial effect. Nevertheless, due to the observed heterogeneity of the response data, and the uncertainties associated to the stiffness of the 9 samples, it was decided to include these peaks until new test data that support this hypothesis is generated. (iv) Some of the curve responses are not clearly defined on the plots available in the commercial version of the Kerrigan's paper. In order to avoid a source-error by generating an average curve and standard deviations on not reliable data extraction, it was decided to take the upper and lower bounds of the test responses in order to generate the corridor. Hence, a response corridor for bending was generated. See plot below.

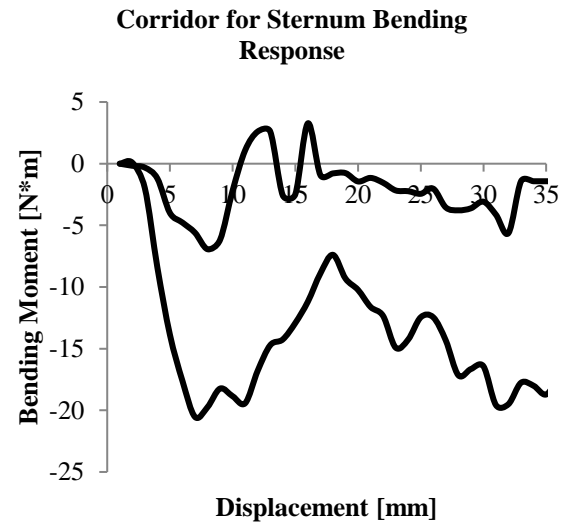


Fig. 2.16 Dynamic response corridor for sternum under bending loading [65]

Simulation method and results are shown in 2.2.4.2.1.

2.1.4.2.2 Rib Bending Test (Antero-Posterior) (Method)

The deformation pattern of a human rib cage in frontal crash suggests that the individual ribs are loaded in anterior-posterior (AP) direction and will intend to rotate around the costo-vertebral joint. This joint acts also as a boundary constraint that generates a state of bending. Charpail et al. [65] presented in 2005 a battery of AP loading experiments with ribs extracted from five PMHS rib cages. Summarized data of the sample is presented in the Table 2.6.

Gender	Age	Extracted Ribs
Female	58	4th to 9th
Male	65	4th to 9th
Female	66	4th to 9th
Male	67	4th to 9th
Male	70	4th to 9th
Mean	-	65

Table 2.6 Summary of the PMHSs as presented by Charpail et al. [65]

In the test setup both end of the ribs was potted. The posterior cup was set with all degrees of freedom constrained but the rotation in Z direction (111110) with a pin joint. The anterior end was mounted on a cap with a pin joint attached to a trolley. The resultant degrees of freedom of the trolley-cap are 011110 allowing the trolley sliding along X as the cap rotates around Z. The horizontal displacement was generated by the impact of a pendulum as shown in the diagram presented by Charpail. A honeycomb block was attached to the cap truck as an engage component that was set free when the desired constant velocity was reached (1.56 to 1.80 m/s). The reaction forces were measured on the posterior cap. The battery of 5th ribs were additionally instrumented with 6 strain gauges (3 on both external internal sides of the ribs).

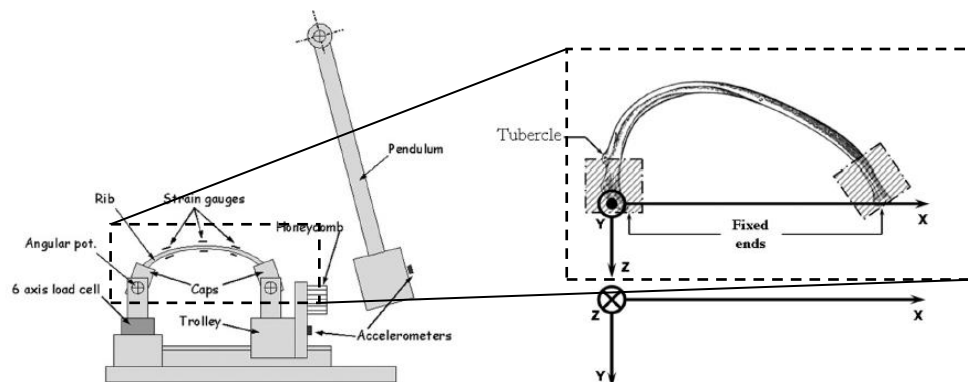


Fig. 2.17 Test setup diagram as presented by Charpail et al. [65]

The anterior cap mean displacement rates was 1.7274 m/s ($\sigma = \pm 0.1075$ m/s) representing a reasonable chest deflection rate in a frontal crash [60]. Charpail et al. characterized and summarized the experiment results by defining a linear stiffness “K [N/m]” in bending in a self-defined displacement range (probably where the load-displacement response was linear). In other words, the rate of loading change over the cap displacement. Based on the experiment data, the following K-, reaction force- and rupture energy-plots were built in order summarize the mean and $\pm\sigma$ values per rib level:

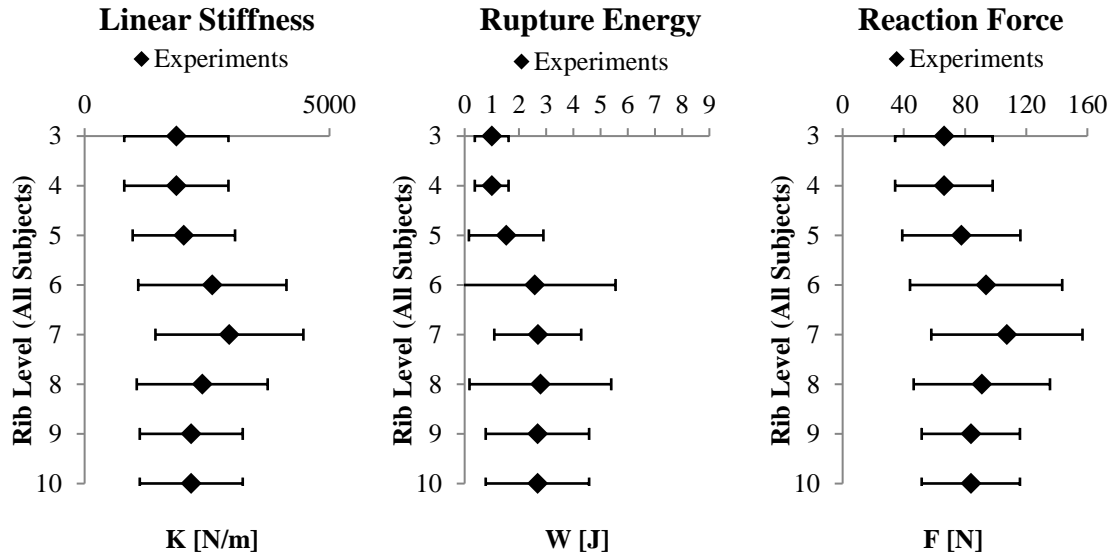


Fig. 2.18 K, rupture energy and reaction forces (mean and $\pm\sigma$ per rib level) from the experiments

For comparison purposes it was assumed a similar response for the third and tenth rib compared to the fourth and ninth ribs respectively. The test was simulated in VPS using isolated ribs extracted from the Thums for both original thickness distribution and an “elderly” thickness distribution (Thums-elderly ribs). Simulation results can be found in the sub-section 2.2.4.2.2.

2.1.4.2.3 Clavicle Bending Test (Method)

In a frontal crash, the occupant anterior shoulder region will be directly loaded by the seatbelt. The immediate underlying structure is the clavicle which supports the loading in a bending state by the clavicle-sternal and clavicle-scapular joints. The response of the clavicle is thus a relevant factor when analyzing the force transfer process to the sternum and ribs. During the Humos2 project, response corridors were developed for clavicle 3-point bending response [66]. A sample of clavicles $n=11$ from was tested under bending velocities of 4 m/s. A rigid impactor and supports imposing only a “vertical” constraint (001000) were used as shown in the figure below. The response force vs. time was taken as response reference for validation. The simulation results are presented in the 2.3.4.2.

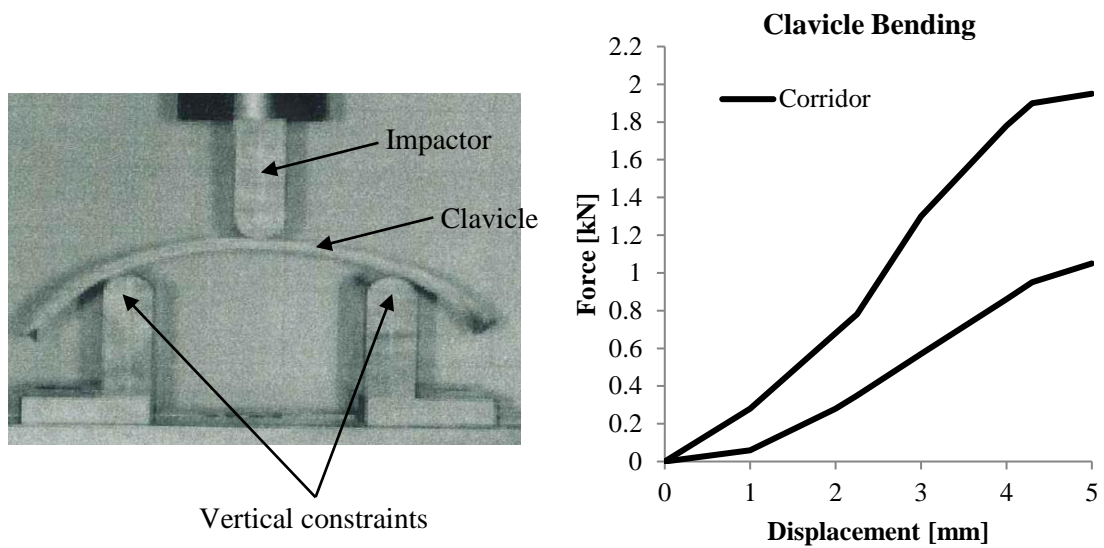


Fig. 2.19 Left: Clavicle three-point bending test from the HUMOS2 project. Right: Test corridor

2.1.4.2.4 Costal Cartilage (Method)

Forman et al [8] published in 2011 a study on dynamic characterization of costal cartilage under bending. In this study a set of five cartilage segments were harvested from five PMHS. Both ends were potted and prepared for an anterior-posterior (AP) loading test. The extracted sections included bilateral cartilages from the 4th chondrosternal joint. A testing machine generated controlled displacement to the chondrosternal end with a ramp function of 400 mm/s. The costochondral end remained fixed. Reaction forces were measured at the costochondral end. Detailed information on the test procedure can be found in [8].

	Gender	Age	Extracted Section
	M	47	4 th rib left
	M	49	4 th rib left
	M	53	4 th rib left
	M	54	4 th rib right
	F	57	4 th rib right
Mean	--	52 (± 5)	-

Table 2.7 Summary of PMHS data as presented by Forman et al. [8]

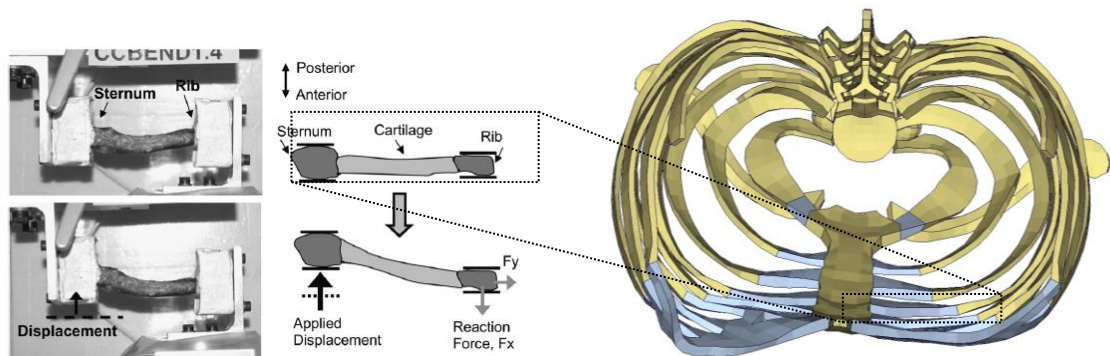


Fig. 2.20 Left: Costal cartilage specimens [8]. Right: Loading configuration

Note that those tests were performed without perichondrium which could account for approximately 50% of the stiffness response of the complete unit (hyaline core plus perichondrium). The costal cartilage is simulated in the Thums models as a single part representing both hyaline core and perichondrium, therefore response corridors generated on Forman's data were scaled.

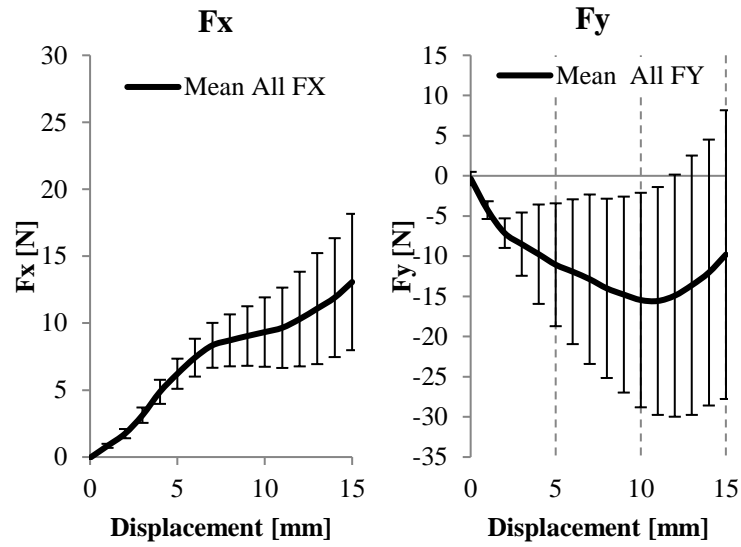


Fig. 2.21 Left: FX mean $\pm\sigma$. Right: FY mean $\pm\sigma$. Unscaled data.

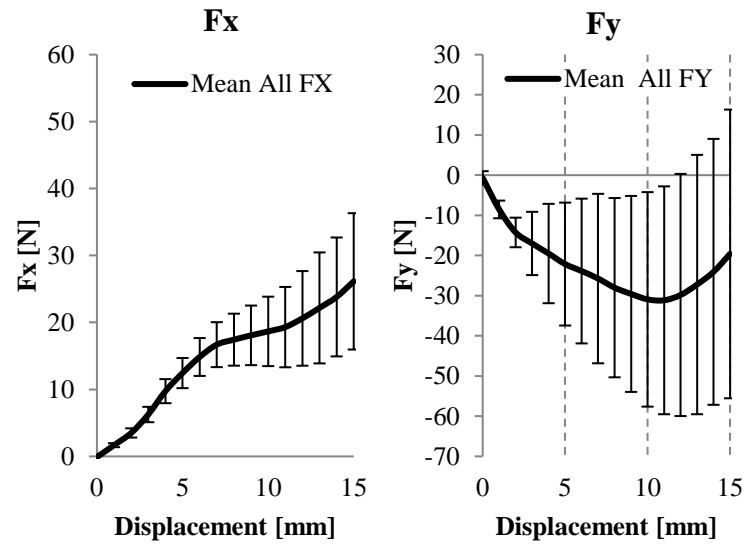


Fig. 2.22 Left: Fx mean $\pm\sigma$. Right: Fy mean $\pm\sigma$. Scaled data.

The tests were simulated in VPS using isolated sternum-cartilage-rib systems extracted from the Thums-original and Thums-elderly. Simulation results can be found in the sub-section 2.2.4.2.4.

2.1.4.2.5 Internal Organs (Method)

Individual material characterization data for thoracic internal organs can be found in [62], Shah [67] and Hayamizu et al. [68]. Nevertheless, in the Thums model version 3 those organs are modeled as a whole single-mesh where no individual organ geometry nor individual materials have been modeled. Therefore, a direct comparison of those tests vs. the response of the mentioned single-mesh make less sense than validating this single-mesh as a component, focusing the analysis on its influence on the overall chest response. Kent et al [69], published a study in 2005 where three PMHS underwent anterior thoracic loading test in an attempt to analyze the influence of the superficial tissue and internal organs on the stiffness response of the thorax. Specifically two subjects underwent a diagonal belt table-top test [60] in two conditions: (i) “Intact”, where the superficial tissue and internal organs were kept and , (ii) “eviscerated”, where the internal organs were removed. The results were summarized as linear stiffness response. The results shown scaled results to a 50th %-ile male chest depth (See Fig. 2.23). Simulation results are shown in 2.2.4.2.5.

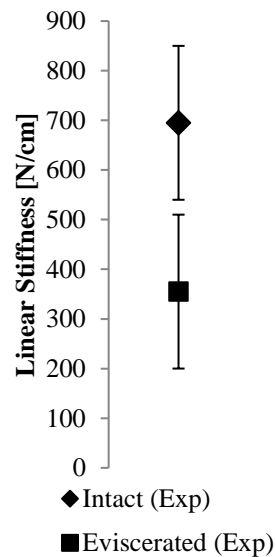


Fig. 2.23 Intact and eviscerated linear stiffness of the experimental data as presented by Kent et al. [69]

2.1.4.3 Body Region Level

The mechanical response of the thoracic region is the result of the interaction of its main components: Clavicle, ribs, sternum, cartilage and internal organs. Following the component test presented in 2.1.4.2, this sub-section addresses four validation cases representing realistic loading conditions of restraint systems and/or interaction with the vehicle interior. From their nature, the cases are grouped in non-impacting (as belt loading) and blunt loading (rigid impactor). Table-top test from Kent et al. [60] and blunt impact cases from Kroell et al. [70] [71] and Shaw et al. [72] are explained below.

2.1.4.3.1 Table-Top Test (Method)

In 2004 Kent et al. presented a study [60] underlining the advantages of non-impact loading tests in order to obtain a better understanding on PMHS thorax deflection under realistic loading rate conditions (restraint system-like) avoiding undesired inertial effects of blunt loading. The loading setup developed by Kent is based on an early configuration test designed by Cesari and Bouquet in 1990 [73]. The PMHS were supine positioned over a test plate which was fixed to an underlying structure. The subjects were belted using 5 mm wide belt-like straps components for the belt loading, and 203 mm wide straps for the distributed loading case. Note that no standard belts were utilized in these test but fiber-reinforced sail cloth [60]. The ends of both straps (in each case) were attached to a cable system connected mechanically to a hydraulic cylinder which, in turn, was attached to a high-speed Instron testing machine. The testing machine was needed to generate the belt-pulling at specific rates, so that the complete system generates controlled chest deflection rates of the PMHS. The testing rate represents an average chest deflection on belt restrained PMHS under frontal 48 km/h sled loading conditions as explained by Kent, for simplification purposes it can be roughly approximated to 1 m/s. Chest deflections on the mid-sternal are measured anteriorly via potentiometer. Anterior reaction forces were recorded using a load cell between the subject and the plate. The following diagrams illustrate the test setup:

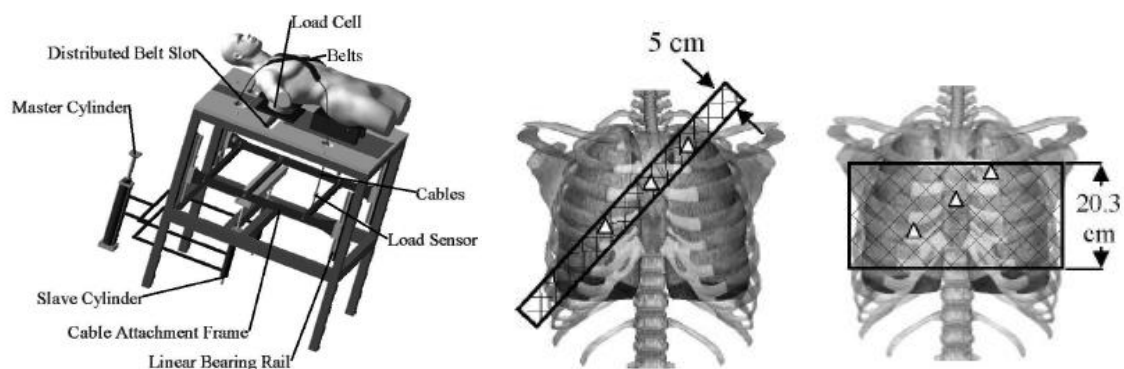


Fig. 2.24 Table-top test set up [60] for imposed chest deflection with diagonal belt (middle) and distributed load (right)

The engage areas of the single-belt and distributed load are approximately 250 cm² and 730 cm² respectively. The anterior reaction force was recorded.

Fifteen PMHS with an average age at time of death of 69.5 ± 10.5 years underwent the test. Linear stiffness corridors (reaction force vs. chest deflection) were developed by Kent. Accounting for the variability of the PMHS sample, the anterior reaction forces were scaled to a 45 YO 50th %-ile male. Effects of age involving changes of stiffness module on bone and soft tissues were addressed but found to be almost irrelevant for the resultant reaction force. Effects of size were mass-based scaled following the method of Eppinger et al [74]. Additionally, the recorded chest deflections were normalized to 230 mm chest depth as reference. Simulation results are presented in 2.2.4.3.1.

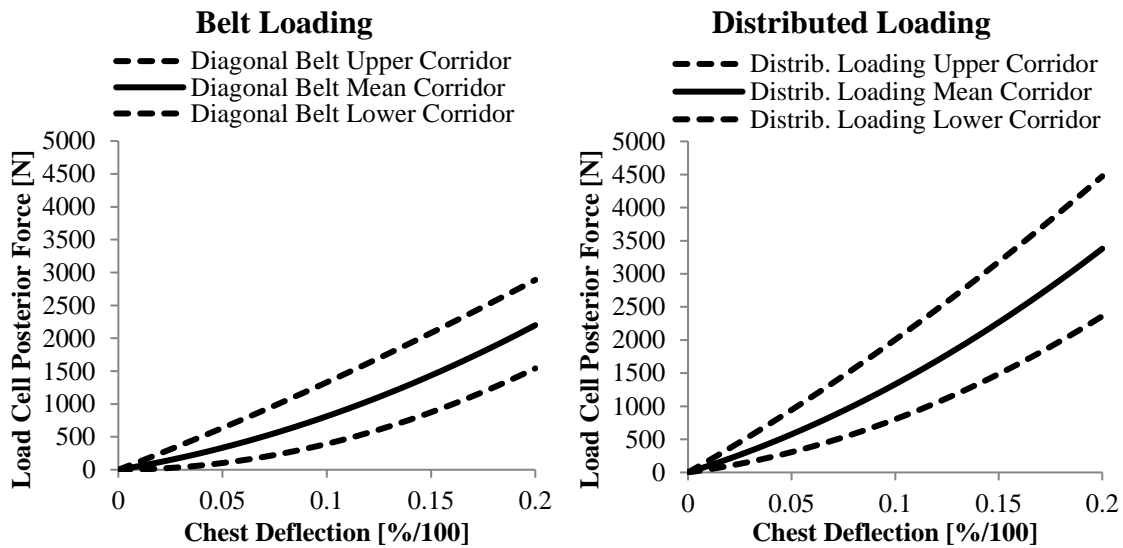


Fig. 2.25 Left: Corridor for posterior force scaled to 45 YO 50th %-ile male vs. chest deflection in belt loading [60].
Right: Distributed loading corridor

2.1.4.3.2 Frontal Hub Impact Test (Method)

The “Impact Tolerance and Response of the Human Thorax” parts I and II [75] [76] are the most widely cited test protocols for thoracic force-deformation response with PHMS. Although the experiments were originally designed to represent a direct impact of the chest with steering-wheel (as typical loading condition before the development and massive introduction of airbags), it was still considered in this study based on its reproducibility characteristics and large amount of published data. Fifteen and twenty-three tests were published in [70] and [71] respectively. The experiments consisted of anterior-posterior blunt impacts with a 152.4 mm diameter cylindrical wooden impactor of different masses, impact velocities and back restraint types. The PMHS were impacted in anterior-posterior direction, mid-sagittally at the fourth inter-costal space measured at the sternal height. For validation purposes a sub-sample of the data was clustered by 23.1 kg impactor, impact velocity between 6.66 and 7.2 m/s and no back-constraint. The following table summarizes the experimental data published in 1971 und 1974:

Published in	Total number of tests	Clustered data by:		PMHS average age of clustered data
		-Impactor mass =23kg	-Impact velocity = (6.66 to 7.2 m/s)	
		-No back restraint	-No out-putting factors	
1971	15 (10M / 5F)	7 (4M / 3F)		62.75
1974	23 (20M / 3F)	2 (2M)		62.5

Table 2.8 Summary of the Kroell's experimental data published in 1971 and 1974.

Data acquisition: Accelerometers on the impactor and vertebral column at the 4th intercostal space height were installed. Chest deflection was measured by “differential motion analysis” [76]. For technical details of the equipment refer to [70] and [71].

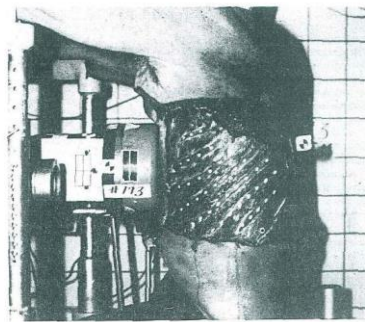


Fig. 2.26 Blunt impact configuration with PMHS [76]. Here the skin was removed for visualization purposes.

Based on these nine tests Lobdell and Kroell published in 1973 [77] linear stiffness response corridors for blunt impact at 6.9 ± 0.2 m/s. Note that the chest deflection is measured starting from the contact impactor-skin and hence, it includes the superficial soft tissue deformation for the chest deflection calculation. A second relevant point is that the response corridors based on PMHS test exclude, for obvious reasons, the mechanical effect of muscle activation and hence underestimates the overall stiffness response. The effect of muscle tensing of an occupant in a collision was estimated by Kroell et al. to be 667 N thus the corridors for the 6.9 m/s test were shifted according to this assumption. At the time of the test, no standard method was used to generate the upper and lower boundaries, as Neathery [78] mentioned, the response corridors were “eyeball averaged”. See the Kroell corridor in Fig. 2.27.

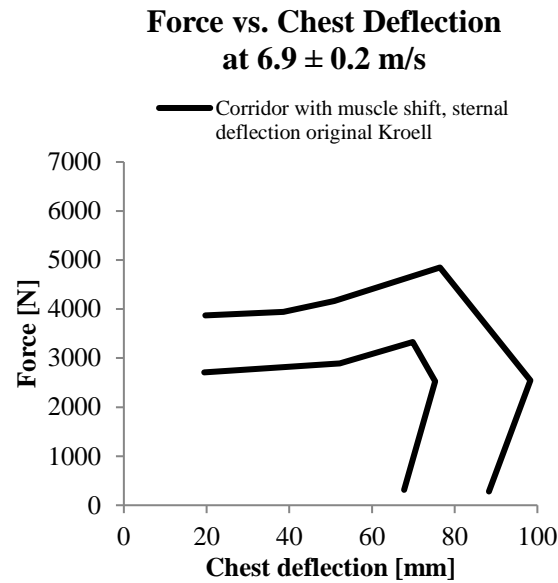


Fig. 2.27 Original corridor from Kroell with muscle tensing shift and chest deflection including superficial soft tissue

Neathery et al. published in 1974 [78] a dimensional analysis in order to generate scaled response corridors to account for the variance of characteristics between the subjects (age, chest depth and height) and testing variants (impactor mass, velocities, force response and chest deflection). The dataset for male response was also the Kroell's published series of experiments. With the dimensional analysis the sample was expanded including impactor masses from 19.3 to 23.6 kg and impact velocities ranged from 5.14 to 9.66 m/s. A total of 10 tests were taken for the corridor development.

Neathery's clustered data by:	
-Impactor mass = 19.3 to 23.6 kg	PMHS range of age of clustered data
-Impact velocity = 5.14 to 9.66 m/s	
-No back restraint	
-No out-putting factors	
Number of test = 10 M	19 to 83

Table 2.9 Data used by [78] for the scaled corridors

As defined by [77], the 667 N muscle tensing shift was also included. For the chest deflection measurement, a 12.7 mm shift was proposed to represent the sternal deflection (skeletal) instead of the total chest deflection including superficial soft tissue deformation. The corridors are shown in the Fig. 2.28.

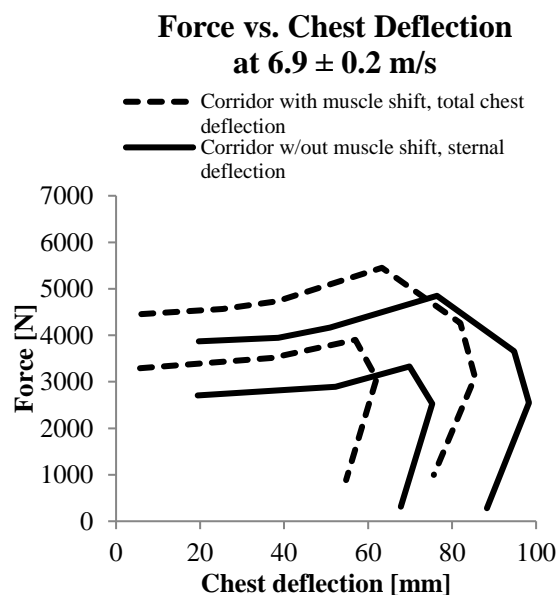


Fig. 2.28 Modified corridors from [78]. The dotted line corridor includes muscle tensing shift and represents total deflection

Recently, some other efforts to develop more statistically significant response corridors including expanded datasets and revised scaling and regression methods have been done in a framework by the CEESAR (Centree Europeen d'Etudes de Securite et d'analyse des Risques) and ACEA (European Automobile Manufacturer Association) for the ISO/TC22/SC22/WG5. The interim reports (not public available) presented by M. Lebarbé contained new corridors for hub impact tests at 4.3 m/s and 6.9 m/s. It is recommended to consider those after they undergo a peer-review process.

2.1.4.3.3 Lateral and Oblique Hub Impact Test (Method)

J. Shaw et al. [72] published in 2006 a study on lateral and oblique hub impact test on PMHS underlining the relevance of the characterization of the thoracic response in oblique direction due to the similarity of loading conditions to a side impact crash situation. As mentioned by J. Shaw, Eppinger [74] and Viano [79] conducted in the 80's separately series of PMHS tests including sled test, lateral hub impact test (Eppinger), lateral and oblique hub impact test (Viano) under different configurations and impact velocities. These two datasets compose the experimental data used for the ISO/TR9790 lateral impact biofidelity corridor, currently defined as the baseline for dummy biofidelity assessment in lateral impact.

The publication of J. Shaw et al. contains new biofidelity corridors for oblique impact and a revision of the ISO/TR9790 corridor based on fourteen test. Seven PMHS (average age 74) were prepared, positioned and instrumented for the impact test. Each one underwent a 2.3 m/s lateral and oblique hub impact test for a total of fourteen runs. The impactor characteristics are similar to those described for the frontal hub impact test consisting of a 23 kg aluminum impactor ram and a 152.4 mm diameter head. The PMHS were impacted in lateral-medial and oblique direction at the fourth inter-costal space (measured at the sternum height). The oblique direction was defined with an angle of 60 degrees from the sagittal to the frontal plane of the upright seated subjects as shown below [72]:



Fig. 2.29 PMHS positioned for lateral hub impact [72]

The subjects were instrumented with accelerometers screwed to the vertebrae. Chest bands were used to track the chest deflection contours at T4 and T8 levels.

Corridors

For lateral hub impact test the ISO/TR 9790 corridor defined in [80] for 4.3 m/s was taken. A -700 N shift was included also in order to represent the impact response without muscle tone effect as mentioned in [72]. The test data for lateral and oblique was normalized to a 50th %-ile AM using the impulse-momentum method described by [79]. A corridor for lateral hub impact at 2.3 m/s was scaled using the same method.

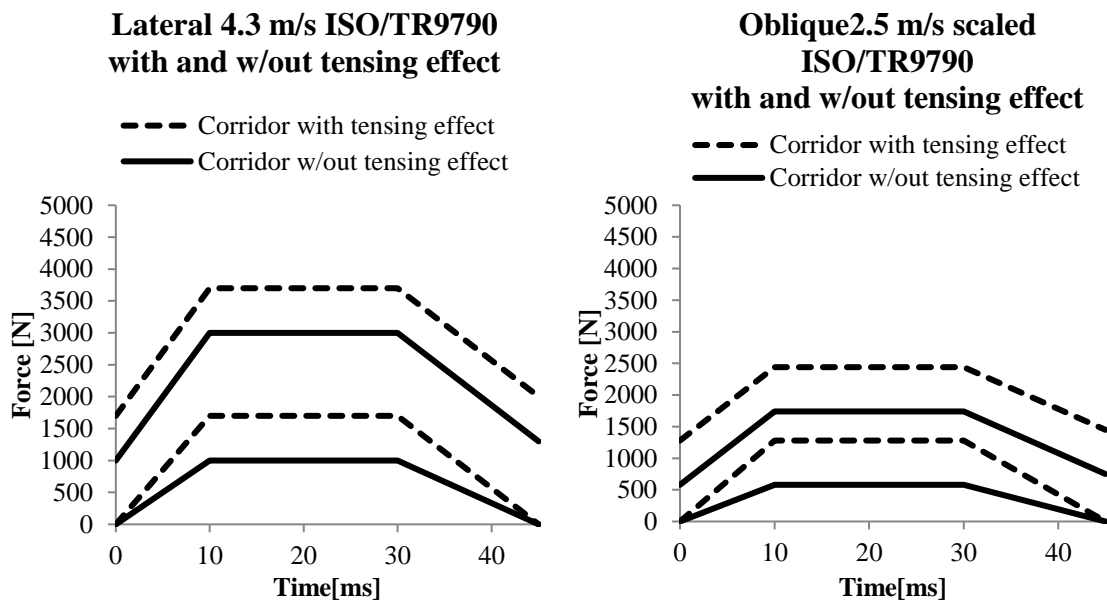


Fig. 2.30 Corridors for lateral and oblique hub impact response

2.1.4.4 Full-Scale Test (Sled Test / Gold Standard) (Method)

Shaw et al. [81] published in 2009 a study on frontal sled tests with PMHS for thoracic kinematic and deformation characterization under realistic automotive restraint loading. A sled buck and deceleration pulse often called “gold-standard-1” (GS1) were used. The GS1 was developed at the Center of Applied Biomechanics of the University of Virginia. The buck and deceleration pulse represents a frontal 40 km/h crash of a standard midsize US vehicle in terms of seating position and pulse severity. The GS1 configuration offers advantages in terms of replicability, simplicity and robustness compared to other test setups and hence was chosen in this study as full-body validation case. The buck consists principally of a rigid plate representing the seat, vertical welded beams to anchor the D-ring and supporting wires, a non-force limited 2 + 2 belt, knee bolster and footrest. No seat backrest is used, instead, wires attached to the vertical beams support the trunk and head to reach a natural passenger position. Standard belt webbing type was used for seatbelts. The following table shows the relevant characteristics of the GS1, a detailed description can be found in [81]:

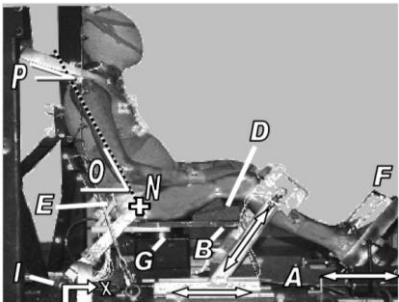
Gold Standard-I (GS1)	
Developed by	Shaw et al. [81]
Lateral view (Dimensions and details can be found in [81])	
Pulse	40 km/h (approx. 14 Gs)
Buck Configuration	Rigid seat
	No belt retractors
	No belt load limiters
	No airbag
Test subjects	Eight male PMHS close to a 50 th AM %-ile in passenger position. Average age 54
Runs	8
Rating	Dimensions and boundary conditions well described. PMHS close to the Thums anthropometry. Adequate for simulations.

Table 2.10 GS1 characteristics

The eight PMHS (Male, average age at time of death 54) underwent the instrumentation-, positioning-, test run and injury assessment (autopsy) process. Instrumentation mounts were screwed to the head, T1, T8, T12, L2, L4 vertebrae and pelvis. Seven additional mounts were

screwed to the anterior ribcage in five locations upper right, upper left, lower right, lower left and mid-sternal and both acromia for thirteen in total. Accelerometers (not in all locations) and spherical reflective markers attached to the mounts served for the kinematic data collection. Tracking of the reflective markers was done using an optoelectric stereophotogrammetric system [81] with 16 Vicon cameras. Detailed information of the system and camera locations can be found in [81]. Belt tension was recorded on the shoulder belt.

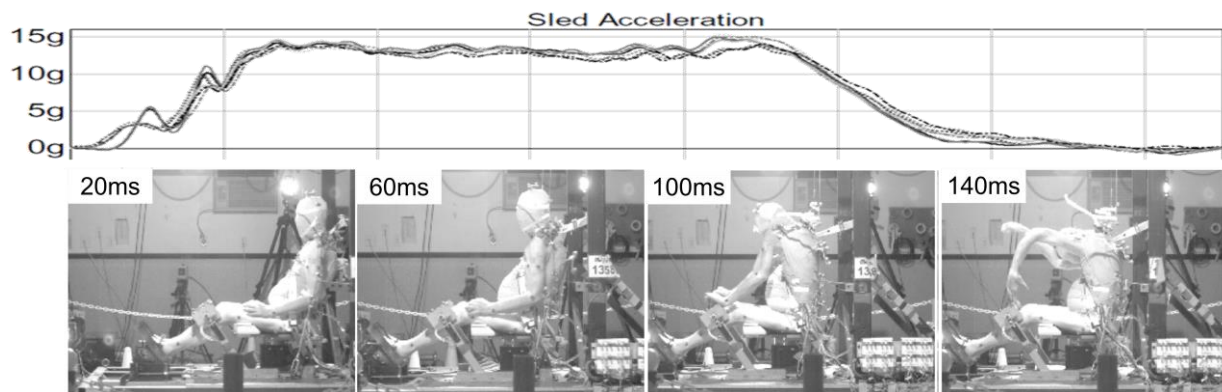


Fig. 2.31 GS1 pulse and photograms of test 1358. Taken from [81]

Output / published data

Kinematic data for each tracking point was generated, nevertheless not all data was published. Shoulder belt tension, torso deformation (derived from the kinematic data) and injury outcome were documented. The torso deformation was assessed by reconstructing the relative displacements between the anterior thorax tracking points to with respect to virtual coordinate systems defined on the T8. Corridors are presented in the Fig. 2.32.

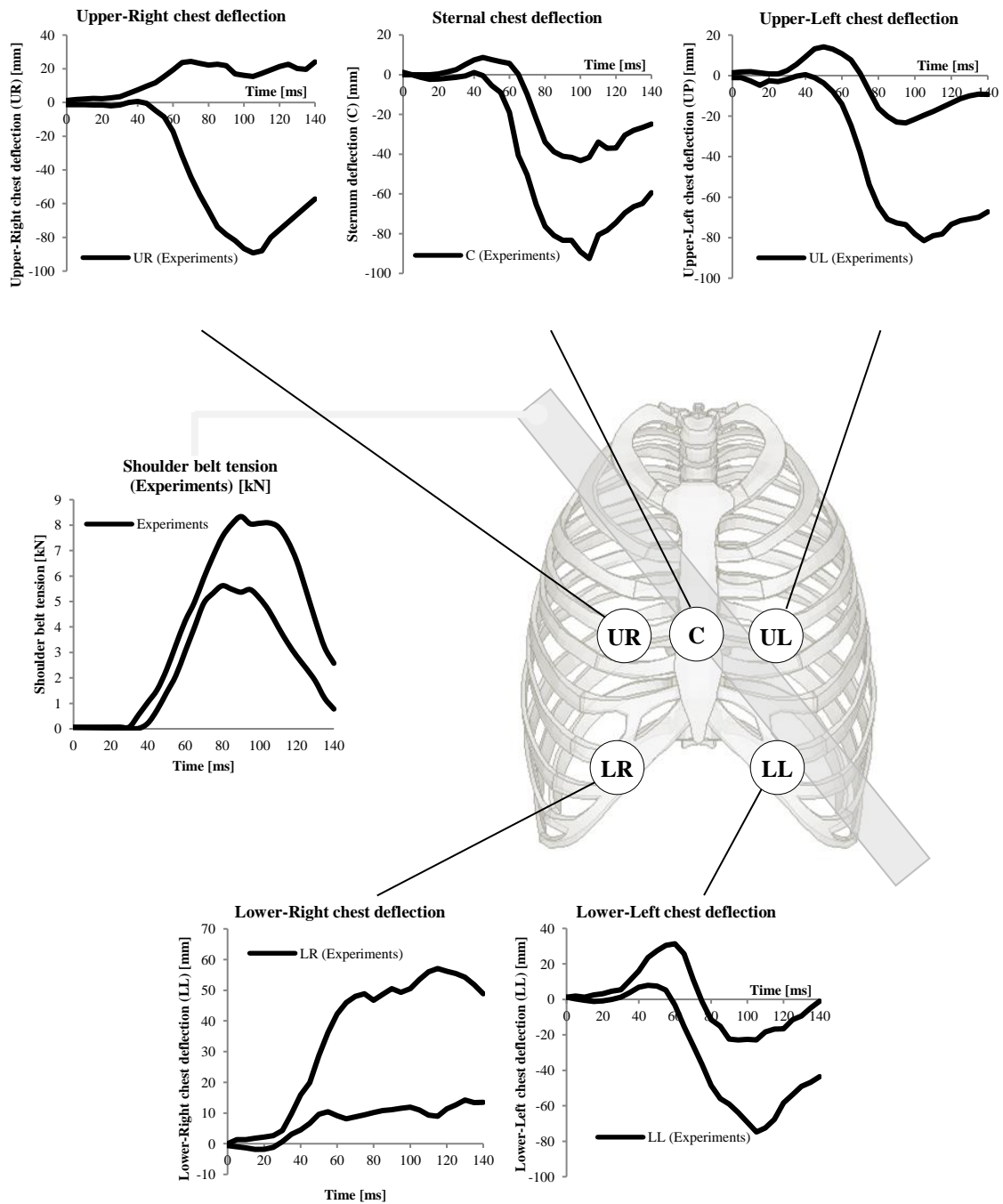


Fig. 2.32 Belt tension and multipoint chest deflection corridors wrt. T8. The simulation results are shown in 2.2.4.4.

2.2 Results

2.2.1 Results Sternum and 3D μ CT Scans

The data was processed by clustering in five groups representing the 20%-, 40%-, 60%-, 80%- and 100%-ile of the cortical thickness distribution as presented in the following table. Image post-processing steps credits: Anja Wagner (LMU).

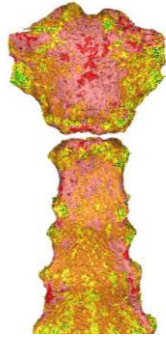
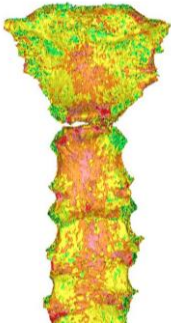

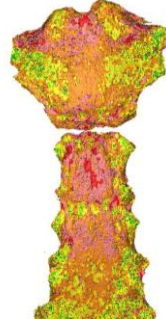
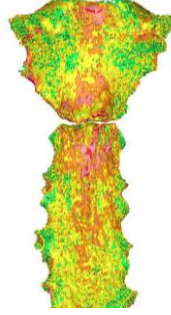
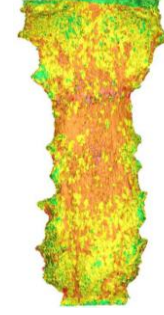
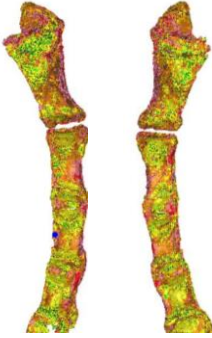
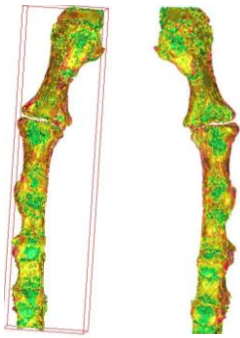
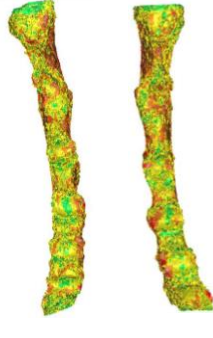
	CAD161 (Sternum 1)	CAD162 (Sternum 2)	CAD163 (Sternum 3)
Frontal View			
Rear View			
Lateral View			
20%-ile			
40%-ile			
60%-ile			
80%-ile			
100%-ile			

Fig. 2.33 Results of the μ CT scans, each color represents a “Thickness group”

The following tables contain the clustered thickness data per surrogate, including upper and lower thickness bounds, average and standard deviation.

CAD161				
Group	Min. [mm]	Max. [mm]	\bar{X} [mm]	σ [mm]
20%-ile	0.01	0.35	0.230	0.087
40%-ile	0.35	0.68	0.531	0.092
60%-ile	0.68	1.01	0.820	0.092
80%-ile	1.01	1.34	1.129	0.088
100%-ile	1.34	1.67	1.456	0.099

CAD162				
Group	Min. [mm]	Max. [mm]	\bar{X} [mm]	σ [mm]
20%-ile	0.10	0.38	0.25	0.08
40%-ile	0.38	0.66	0.51	0.08
60%-ile	0.66	0.94	0.77	0.08
80%-ile	0.94	1.22	1.04	0.08
100%-ile	1.22	1.50	1.32	0.07

CAD163				
Group	Min. [mm]	Max. [mm]	\bar{X} [mm]	σ [mm]
20%-ile	0.10	0.40	0.27	0.27
40%-ile	0.40	0.70	0.56	0.09
60%-ile	0.70	1.00	0.84	0.08
80%-ile	1.00	1.30	1.10	1.10
100%-ile	1.30	1.60	1.40	0.08

Table 2.11 Sterna μ CT scans Cortical thickness groups generated by 3-Matic Software Package. Credits: Anja Wagner LMU.

Hereafter, the data transfer to the HBM begins. However, note that number of surrogates included in this study is not representative for a large population. It is recommended to add further scans in order to enhance the statistical relevance of the current study. Moreover, when analyzing the age dependency of the cortical distribution, no specific trends were found when comparing the CAD161 and CAD163 data (old sterna). Considering the external shape and size similarities with the Thums-original sternum model and the markedly trend into the scientific community to define an elderly group on the range 65 YO, the CAD161 (65 YO) was chosen as base line to extract and transfer the thickness data to the Thums-original, therefore generating a modified “old” version denominated “Thums-elderly”. This personalized model attempts to represent more realistically the dynamic response of a 65 YO sternum. The thickness-groups were manually transferred to the Thums-original as shown below by assigning the average thickness of each thickness group according to the original shell-element locations.

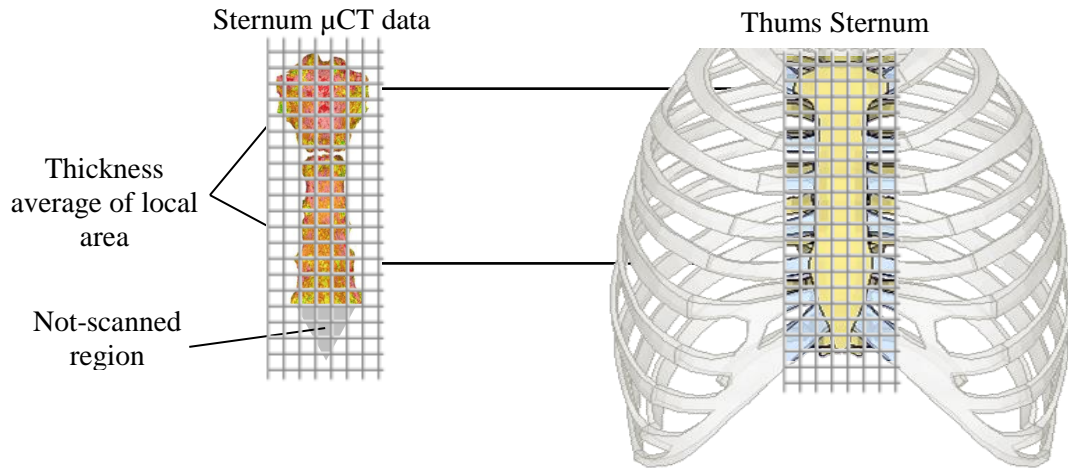


Fig. 2.34 Thickness groups for Thums-elderly sternum. Manual mapping to the FE model

Thickness Group	Thickness [mm]
20%-ile (Green)	0.230
40%-ile (Yellow)	0.531
60%-ile (Orange)	0.820
80%-ile (Lila)	1.129
100%-ile (Red)	1.456

Table 2.12 Thickness groups and thickness values

The influence of the new thicknesses on the mechanic response of the new sternum will be analyzed in 2.1.4.2.1 and 2.2.4.2.1.

2.2.2 Results Ribs and Variable Cortical Thicknesses

As mentioned in the method subchapter, μ CT data processed in order to define variable cortical thickness groups for the 7th rib. A similar approach was taken for the ribs 3rd to 10th. Based on the thickness-groups defined for the 7th rib, each rib was divided in four zones. The thickness values per group are a result of linear scaling of the cortical thickness of each group based on the 7th rib data was applied for the rest of the ribs.

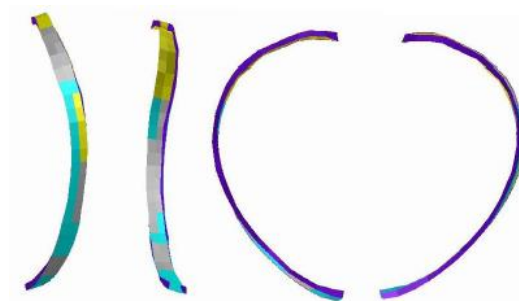


Fig. 2.35 Thickness groups for Thums-elderly (7th rib)

Thickness Group	Thickness [mm]
0-25%ile (purple)	0.4658
25-50%ile (Blue)	0.6683
50-75%ile (grey)	0.7634
75-100%ile (yellow)	1.3973

Table 2.13 Thicknesses assigned to each group (Thums-elderly)

The average thickness per group was assigned to the correspondent shell elements included into each group. The constraints for the scaling factor was the best-match of the bending results of the third rib under 3-point bending test conditions. The resulting thickness per rib and thickness group are shown in the Table 2.14. The thickness values of the 75-100%-ile were tuned out of the linear approach aiming for a closer match with experimental results [82].

Thickness Group	3rd	4th	5th	6th	7th	8th	9th	10th
0-25 %ile (Purple)	0.1553	0.2329	0.3106	0.3882	0.4658	0.4658	0.4658	0.4658
25-50 %ile (Blue)	0.2228	0.3349	0.4461	0.5572	0.6683	0.6683	0.6683	0.6683
50-75 %ile (Grey)	0.2545	0.3817	0.509	0.6362	0.7634	0.7634	0.7634	0.7634
75-100 %ile (Yellow)	1	1.1	1.1	1.2	1.3973	1.3973	1.3973	1.3973

Table 2.14 Elements thicknesses repartition

The thickness distribution for the ribs 8th, 9th and 10th kept the 7th rib values due to the similarities in size and function. Further work should include μ CT scans on a representative group of ribs (all levels). This extrapolation approach was based on data available at the time of development.

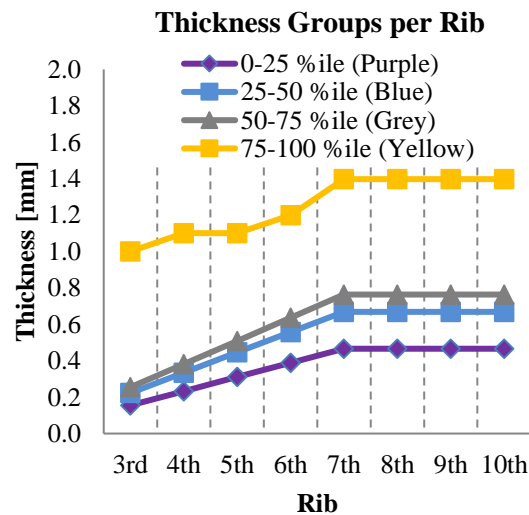


Fig. 2.36 Cortical thickness of the "Thickness Groups" per rib implemented on the Thums-elderly

The extrapolation starting from the 7th rib shows the potential to better represent the response of elderly ribs under AP (Anterior-posterior) loading. It was noted that the yellow region (75-100%ile) is responsible for most of the stiffening of each rib. See the response comparison with the experimental data in the section 2.2.4.2.2.

2.2.3 Results Costal Cartilage Calcification

Into the method subchapter (see 2.1.3), a simulation approach for the representation of costal cartilage calcification is proposed. The assumption for the study was the assessment of the thoracic response under table-top as a realistic restraint system-like loading. The simulation results are presented here. The following effects were noted:

- (i) The increase of stress concentration on the sternum
- (ii) An anterior-posterior shift of the stress concentration on the ribs
- (iii) Higher lower chest deflection

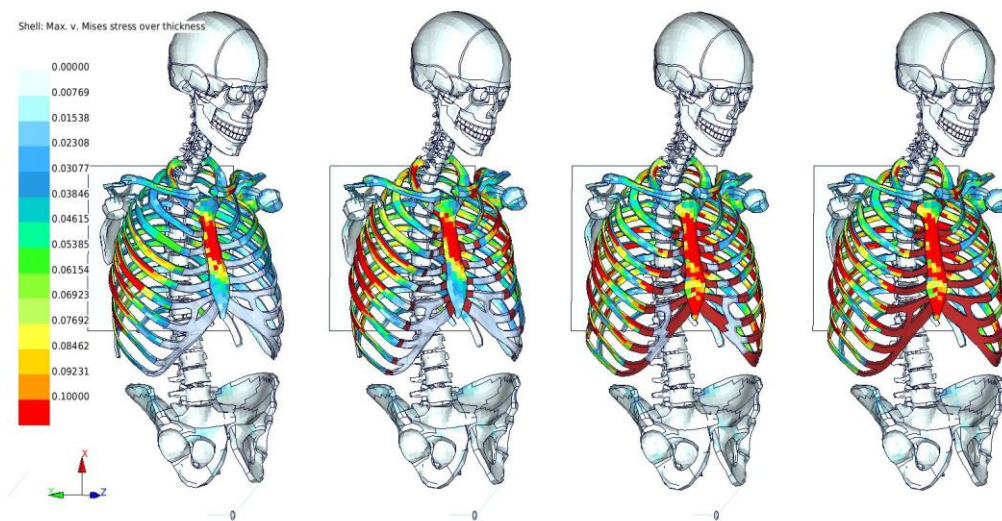


Fig. 2.37 Von Misses (VM) stress distribution in GPa on ribs and sternum. Note the higher VM stresses in the fully calcified model

(i) Higher stress concentration on the sternum: In general, the calcification correlates with an increase of Von Misses stresses on the anterior side of the sternum as show in the following figure. Note also that the ventral region of the sternum suffered also higher stresses. The deformation energy dissipated by the cartilage in the non-calcified model is directly transferred to the ventral region of the sternum in the fully calcified model.

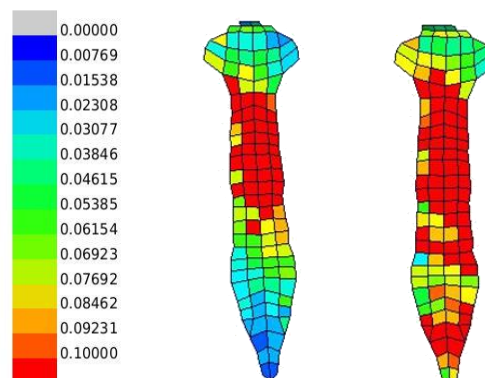


Fig. 2.38 VM-Stress [GPa] distribution on the sternum. Left: Non-calcified model. Right: Fully calcified model

Quantitatively, plotting the peak stresses at the same loading state for both non-calcified and fully calcified models we have:

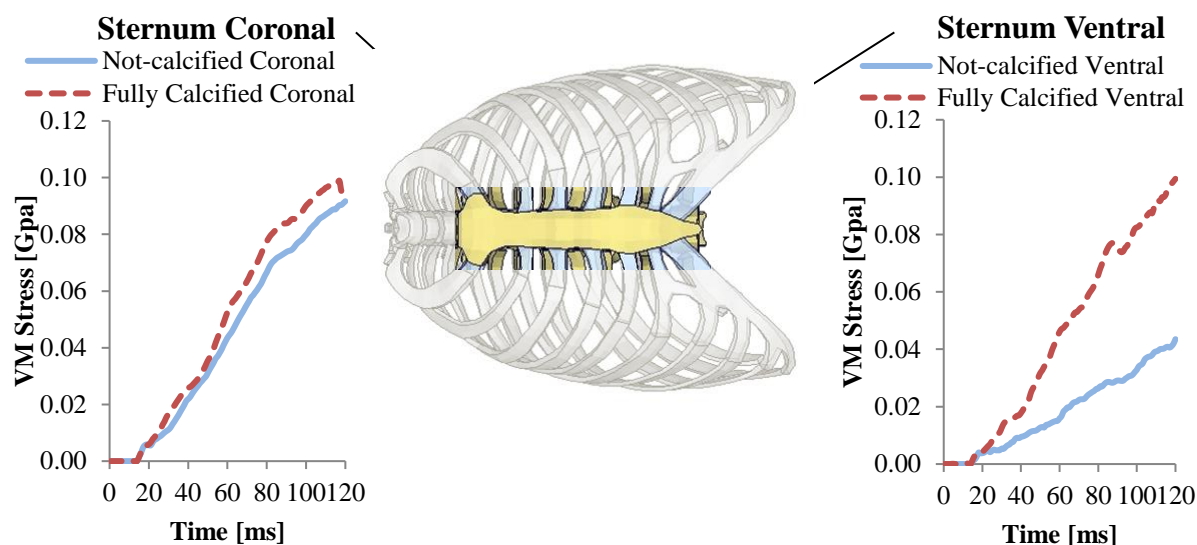
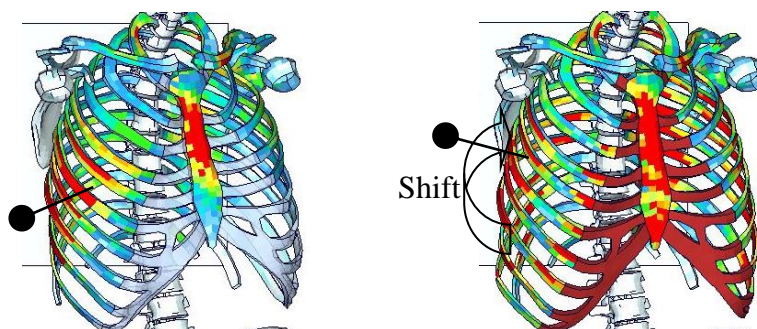


Fig. 2.39 Peak Von Mises stresses of all elements of the anterior cortical layer of the sternum on both 0% calcification (left) and 100% calcification (right) models

(ii) Shift of strain concentration: As shown in the figure below, another effect noted is an anterior-to-posterior shift of the peak stresses on the ribs. The abrupt change of material properties in the interface rib-cartilage in the non-calcified model contributes to keep the peak stresses close to the maximum curvature point of the ribs whereas in the fully calcified model the stiffer interface appears to generate stress concentrations on the interface itself and an anterior-to-posterior shift of the peak stresses along the rib. Possible implications of the shift could be an increased risk of rib fracture in the posterior area due to calcification / age.



Again, quantitatively, the following figures show the stress concentration shift in the 6th right rib for both models. Peak VM stresses from 11 selected reference points along the rib where plotted in order to facilitate the visualization. As above mentioned note also the stress concentration on the rib-cartilage interface (reference point “100”)

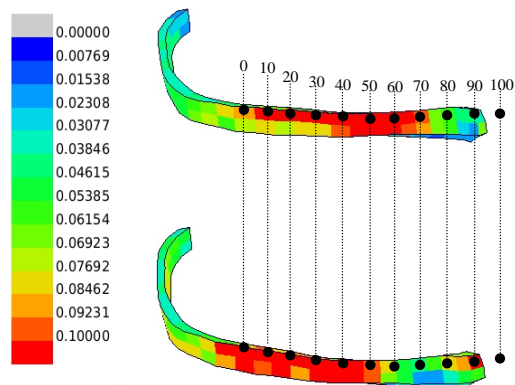


Fig. 2.41 VM-Stress [GPa] shift on the 6th rib. Top: From the 0% calcification model. Bottom: From the 100% calcification model. Note anterior-posterior shift of the stress concentration. The reference points are shown.

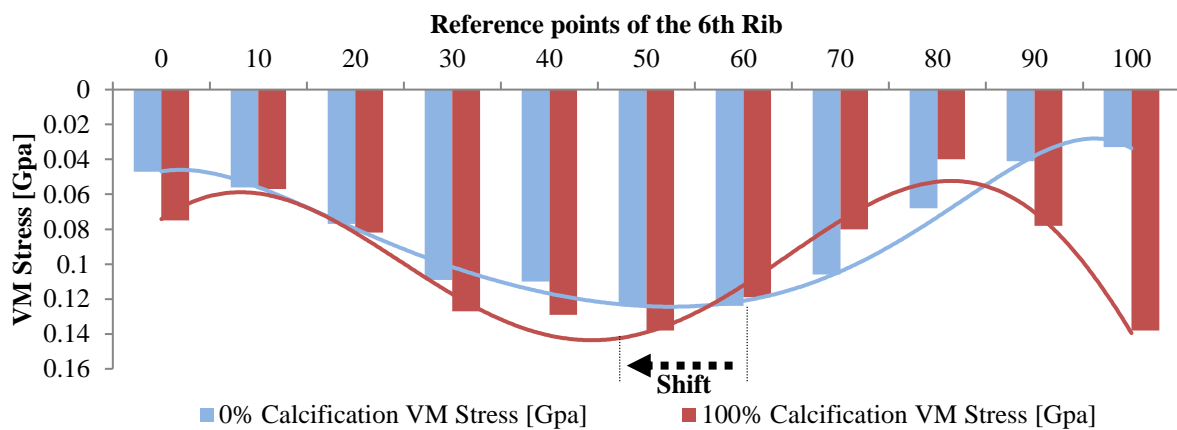


Fig. 2.42 Structural effect of cartilage calcification: Anterior-to-posterior Von Mises stress shift. Note also the stress concentration on the reference point 100

(iii) Higher lower chest deflection: By comparing the chest deflections of five points on the rib cage, it was noted that both lower (left and right) measured values in the fully calcified model chest deflection were higher.

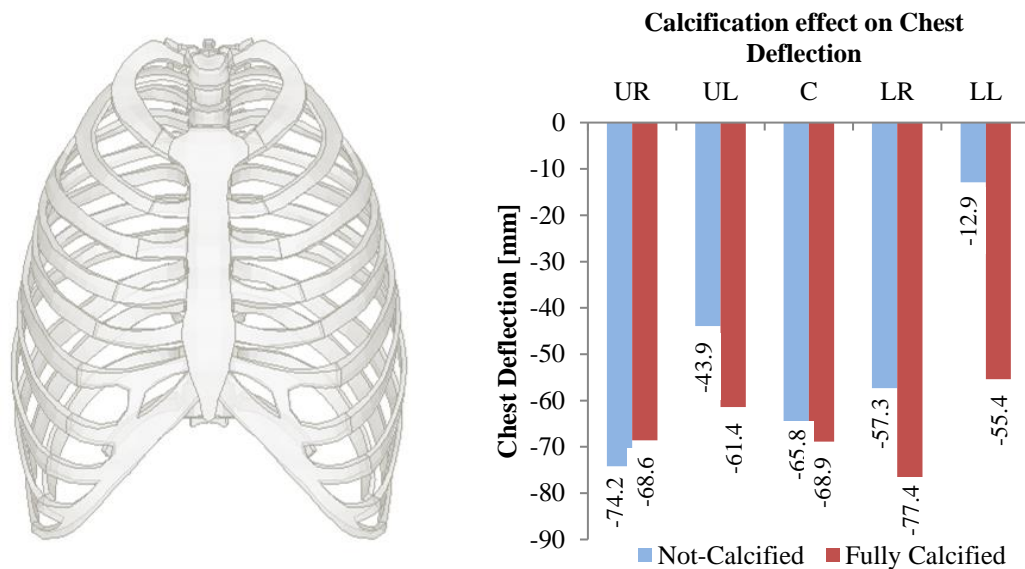


Fig. 2.43 Chest deflections upper left (UL), upper right (UR), center (C), lower left (LL) and lower right (LR). Note the increased lower chest deflection in the fully calcified model

This comparative analysis presents a simulative approach to evaluate the effect of costal cartilage stiffening on the structural behavior of the rib cage. Under the assumption that the calcification can be modeled by stiffening a selected set of elements, this is a simplified method to represent an age-dependency by cartilage calcification with HBMs. The Thums-elderly was hence further modified based on these findings by considering the 100% calcification case as a conservative approach. Reaction forces and central chest deflection are supposed to be relatively constant accordingly to the nature of the table-top test experiment.

2.2.4 Validation Results

Following the loading conditions described in the method section, FE validation models for both Thums-original and Thums-elderly were built. The reference corridors from experimental data are explained also in the method section. Summarizing, models for the following loading conditions were simulated: Table-Top non-impact test for diagonal belt and distributed loading (airbag-like loading), pendulum impact test (frontal, lateral and oblique), clavicle 3-point bending test (3PBT), anterior-posterior (AP) rib loading, sternum 3PBT. As shown in the method section, the test were grouped in validation levels: (i) Material, (ii) component, (iii) body region and (iv) full-scale tests.

2.2.4.1 Material Level

2.2.4.1.1 Sternum and Rib Cortical Bone

Following the description by Kemper et al [61] (see also 2.1.4.1.1) a dog-bone coupon was modeled. Shell elements with thickness equal 0.5 mm were generated with the automatic 2D mesh tool from ANSA®. The element formulation was set to three integration points. The original Thums elastic-plastic material MAT103 (VPS) was set to the model. A fully constraint boundary was set to one end whereas on the opposite end of the model strain rate of 0.0005 strain/ms was used. No specific failure was defined in the biocorridors presented in the method section nor for the simulations. Instead, for comparison purposes, the original Thums failure criteria for cortical bone was switched off. Note that the mesh size was reduced to 0.5 mm (in the middle area) in order to match the small sizes of the dog-bone. Single-element test with size 5 mm and 0.5 mm were also simulated. No significant increase of the stiffness due to the mesh size was found. The Table 2.15 shows the basic material properties of both rib and sternum cortical bone model.

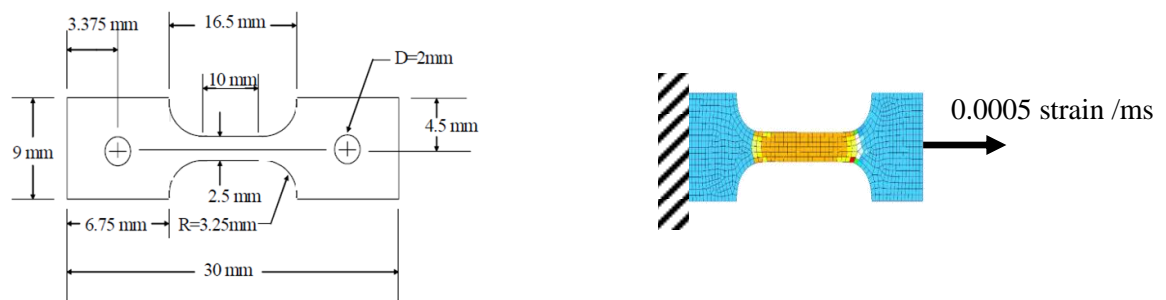


Fig. 2.44 Left: Geometry of the coupons [61]. Right: Simulation Model and boundary condition

Component	Element Type	Young's Modulus [GPa]	Yield's Stress [GPa]
Sternum Cortical Bone	Shell	11.5	0.123
Ribs Cortical Bone	Shell	13	0.0935

Table 2.15 Rib and sternum cortical bone material model properties

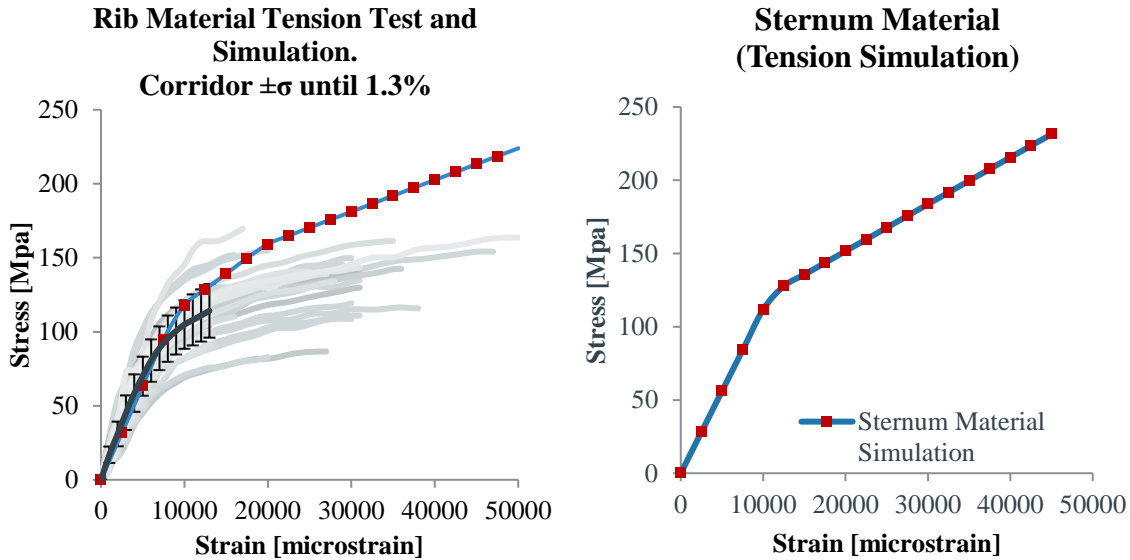


Fig. 2.45 Stress-Strain response of the dog-bone model. Left: Ribs. Right: Sternum.
Both Thums-original and Thums-elderly are represented by the blue red-dotted curve

For the sternum material, the same dog-bone tension test was simulated. The results matched the corridor into one σ . There is no reference of specific tensile test done with cortical bone of human sternum hence no corridor is defined. Material properties similar to the ribs were assumed. The original material card MAT105 “elastic-plastic with damage” in VPS was utilized.

2.2.4.1.2 Cartilage

Retaking the sample description of the method sub-section, a 30 mm long, and 1 mm thick single-element model was generated. The solid element formulation (VPS) was used, under-integrated and with stiffness-based hourglassing control method. The elastic-plastic (MAT16) material from the original Thums was kept for the Thums-original cartilage whereas for the Thums-elderly the Bulk module was increased to 17.5 GPa based on the comments from Forman et al. [8]. A fully constraint boundary was set to the bottom nodes (111111) whereas on the nodes on top the degrees of freedom were only set free in Z (110111). A constant imposed velocity of 0.1 mm/ms was set to the nodes on top. Reaction forces were taken for the post-processing. Engineering stress was assumed. Further parametric analysis on mesh size and necking should be addressed in order to prove this assumption. No specific failure was defined in the biocorridors presented in the method section nor for the simulations. The Table 2.16 shows additionally the material stiffness of both rib and sternum cortical bone model.

Component	Element Type	E [GPa]
Costal Cartilage (Thums-original)	Solid	0.0175
Costal Cartilage (Thums-elderly)	Solid	17.5

Table 2.16 Costal cartilage element type and E

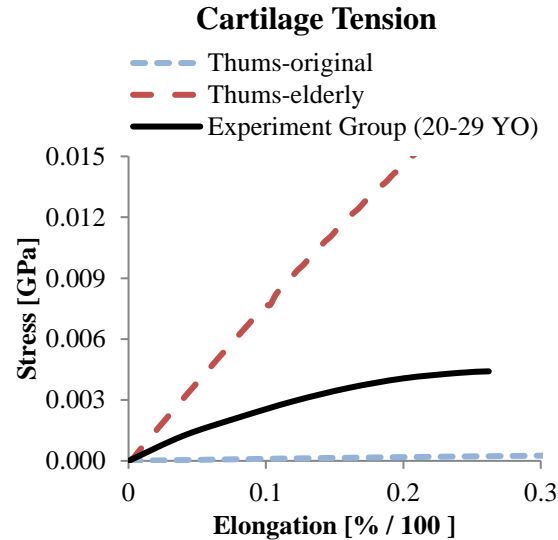


Fig. 2.46 Experiment stress-strain response and simulation of a single-element model with both Thums-original and Thums-elderly material

The simulation results with the Thums-original material is approximately 10 orders lower than the test [63]. Additionally, the simulations with the Thums-elderly material shows a stiffer behavior compared with the experimental data. The following facts have to be taken into account for the analysis: (i) All samples were extracted from Japanese PMHS, (ii) no information about calcification level nor bone mineral density is available, (iii) further information is required to determine the real dimensions of the sample due to inconsistencies between [62] and [63]. Due to these uncertainties, the material parameters were kept as presented and cross checked in a bending component level done by Forman et al. [8] .

2.2.4.2 Component level

This subsection contains the test and simulation results described in the method chapter (see subsection 2.1.4.2)

2.2.4.2.1 Sternum Bending test (Results)

Test setup, response corridors and simulation were described in the section 2.1.4.2.1. The test was simulated in VPS using an isolated sternum model extracted from the Thums-original. The potted ends were simulated as nodal rigid bodies at both ends. One rotational degree of freedom was set to both ends. The servo-hydraulic actuator (12.7 mm diameter) was simulated as a rigid body and a prescribed velocity of -1115 mm/ms in Z direction was assigned. A contact type 34 was chosen for the actuator-sternum interaction. Friction coefficients were set to 0.2. The cortical thickness of the original Thums model has a constant value of 0.7 mm. The material card was set with a Young Modulus of 13 GPa. Material modeling details and a snapshot of the model setup are shown below in the Table 2.17 and Fig. 2.47.

Bone Layer	Material Type (VPS)	Element Type	Young's Modulus [GPa]	Yield's Stress [GPa]	Failure Strain Definition [microstrain]
Cortical	MAT105 Elastic-Plastic	Shell	11.5	0.123	(Failure w/out element elimination)
Trabecular	MAT16 Elastic-Plastic	Solid	G=0.0138 K=0.133	0.0018	100000

Table 2.17 Material properties of cortical and trabecular layers of the sternum model

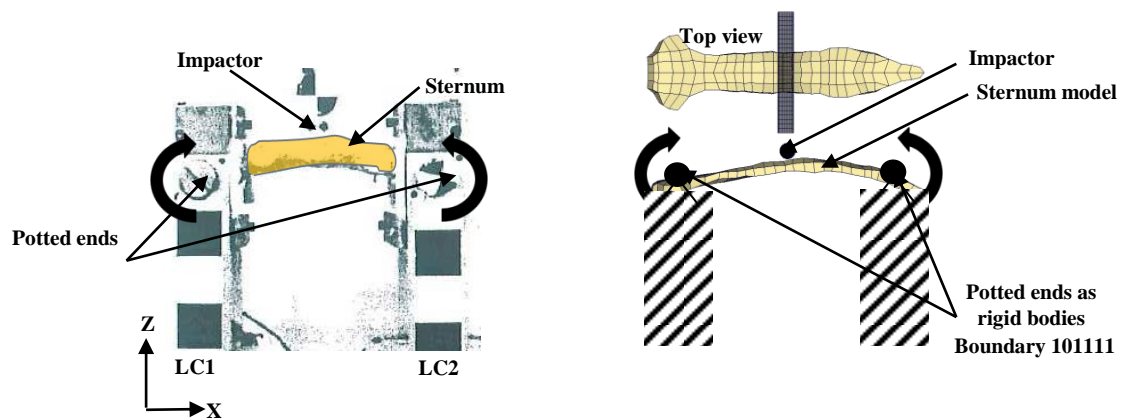


Fig. 2.47 Left: Experiment set up from Kerrigan et al. [64]. Right: Simulation model

Real cortical thickness distribution from the μ CT scan process was set to the sternum model as described in 2.1.1 hence generating a “Thums-elderly” sternum. The response in bending of both sterna compared to the corridor is shown below.

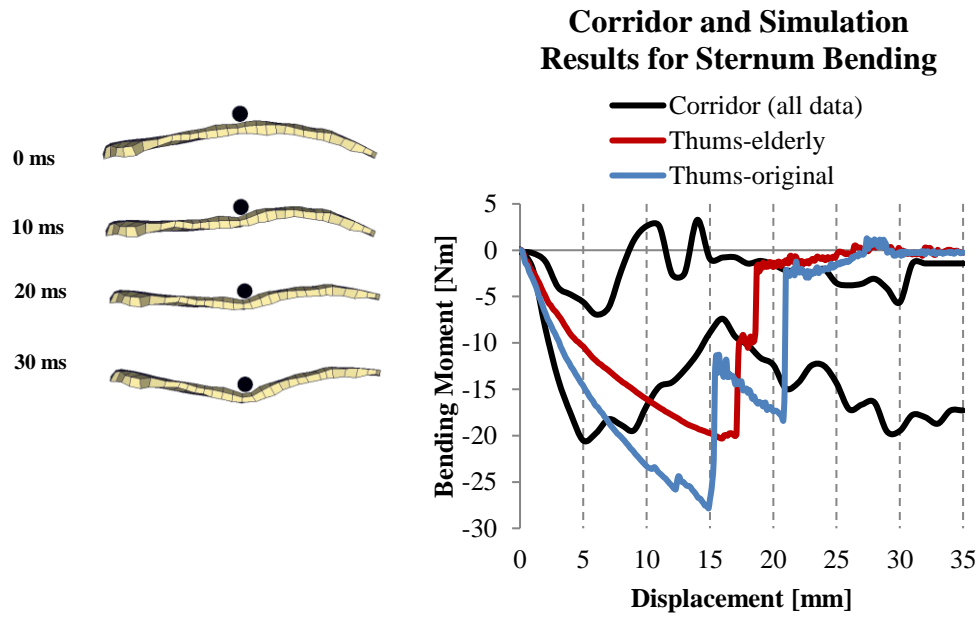


Fig. 2.48 Left: Bending with the Thums-original sternum. Right: Dynamic response corridor for sternum under bending loading

Note that the maximum bending moments depend on the failure criteria specified in the cortical and trabecular material cards. The results shown here correspond to the original failure limits defined into the material cards. In the simulation matrix of the chapter 4 the failure criteria was set off for the cortical bone to ensure comparability between models and loading reduction information above the fracture limits for restraint system analysis.

2.2.4.2.2 Ribs Anterior-Posterior (AP) loading (Results)

Following the description in 2.1.4.2.2, Charpail's [65] anterior-posterior (AP) bending loading was simulated. The results were compared with the linear stiffness, reaction force and internal energy boundary values per rib from the experiment data. The tests were simulated in VPS using isolated ribs extracted from the Thums-original, including both cortical and trabecular layers. Ribs from 3rd to 9th were included into the analysis. The potted ends were simulated as nodal rigid bodies at both ends. The nodal sets were defined based on the descriptions of Charpail et al. in order to represent the real potting conditions. The boundary conditions were set to 111110 for the posterior rigid body (representing the posterior cap), and to 011110 for the anterior rigid body. A prescribed velocity of the anterior rigid body was set to 1.73 m/s along the X axe. Ribs from both Thums-original and Thums-elderly were simulated. Note that the material properties were kept the same, thus only the effect of the cortical thickness distribution will be analyzed. The Table 2.18 includes material modeling details. The Fig. 2.49 shows the model setup.

Bone Layer	Material Type (VPS)	Element Type	Young's Modulus [GPa]	Yield's Stress [GPa]	Failure Strain Definition [microstrain]
Cortical	MAT103 Elastic-plastic	Shell	13	0.0935	18000
Trabecular	MAT16 Elastic-plastic	Solid	G=0.0138 K=0.133	0.0018	100000

Table 2.18 Material properties of cortical and trabecular layers of the rib models

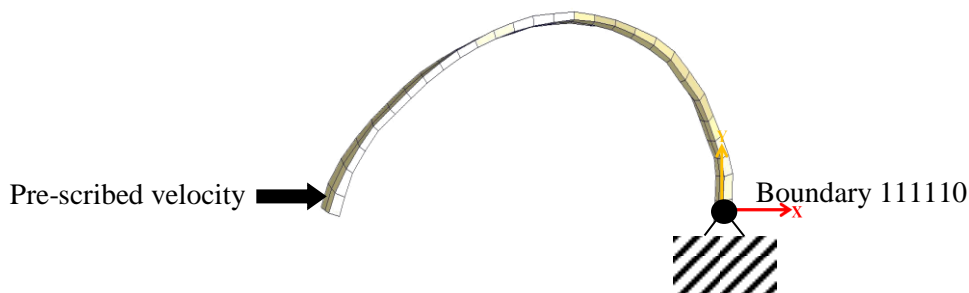


Fig. 2.49 7th Rib under anterior-posterior loading. Boundary conditions and prescribed velocity

Bending moments at the point of maximum curvature were recorded and plotted. It was noted that the point of maximum curvature matches also the most common fracture location in CPR procedures. An analysis of this phenomena done by Lange and Schick (Institute for Legal Medicine of the University of Munich, unpublished) determined the cumulative distribution of rib fracture locations for both sides for a sample of $n = 102$.

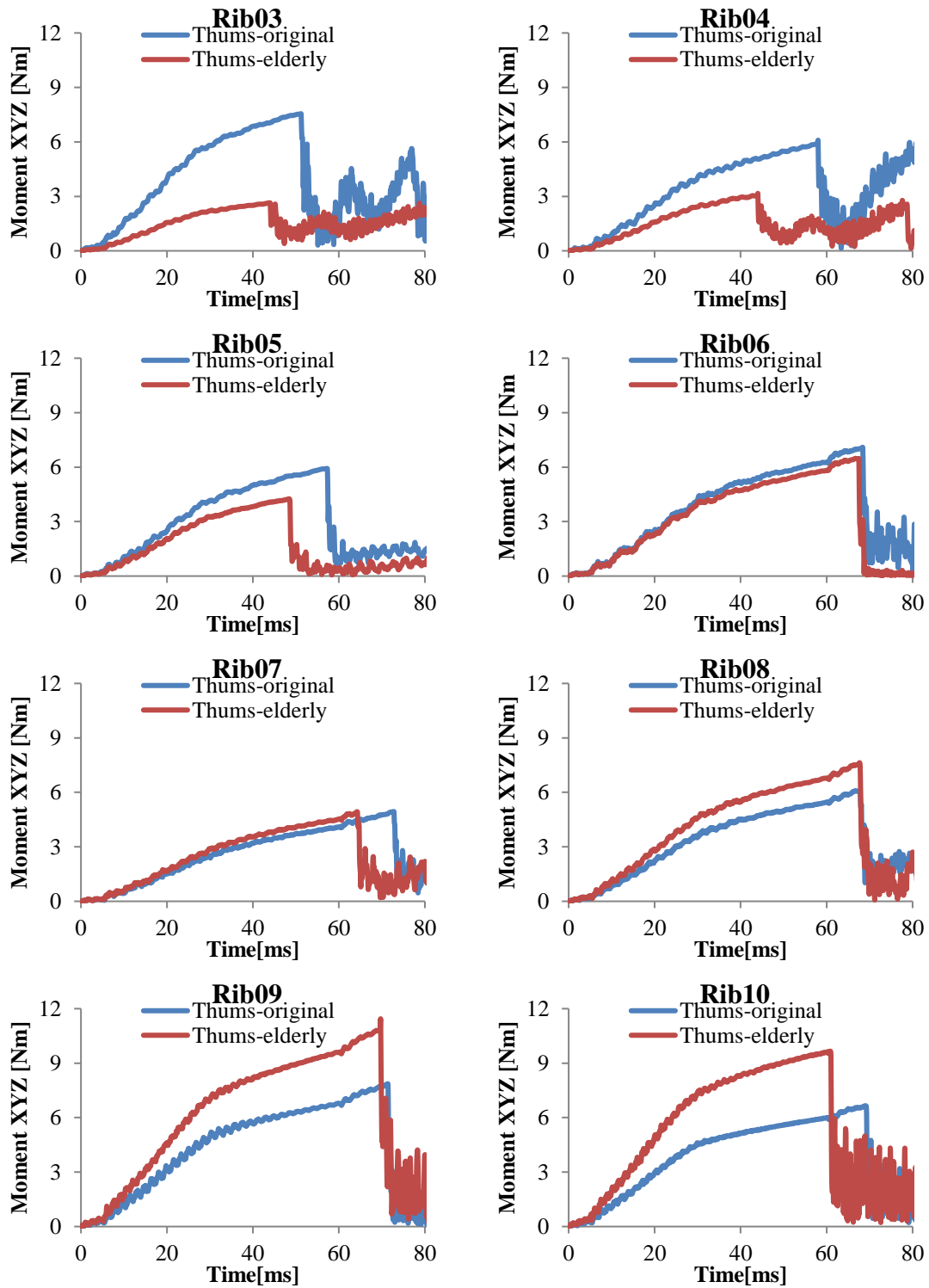


Fig. 2.50 Bending moments per rib level using the test configuration from Charpail et al [65] with Thums-original and Thums-elderly

Reaction forces at the anterior constraint were recorded and plotted. Following the Charpail's procedure, linear regressions were calculated for the range of 15 mm to 25 mm cap displacement in order to generate the K values.

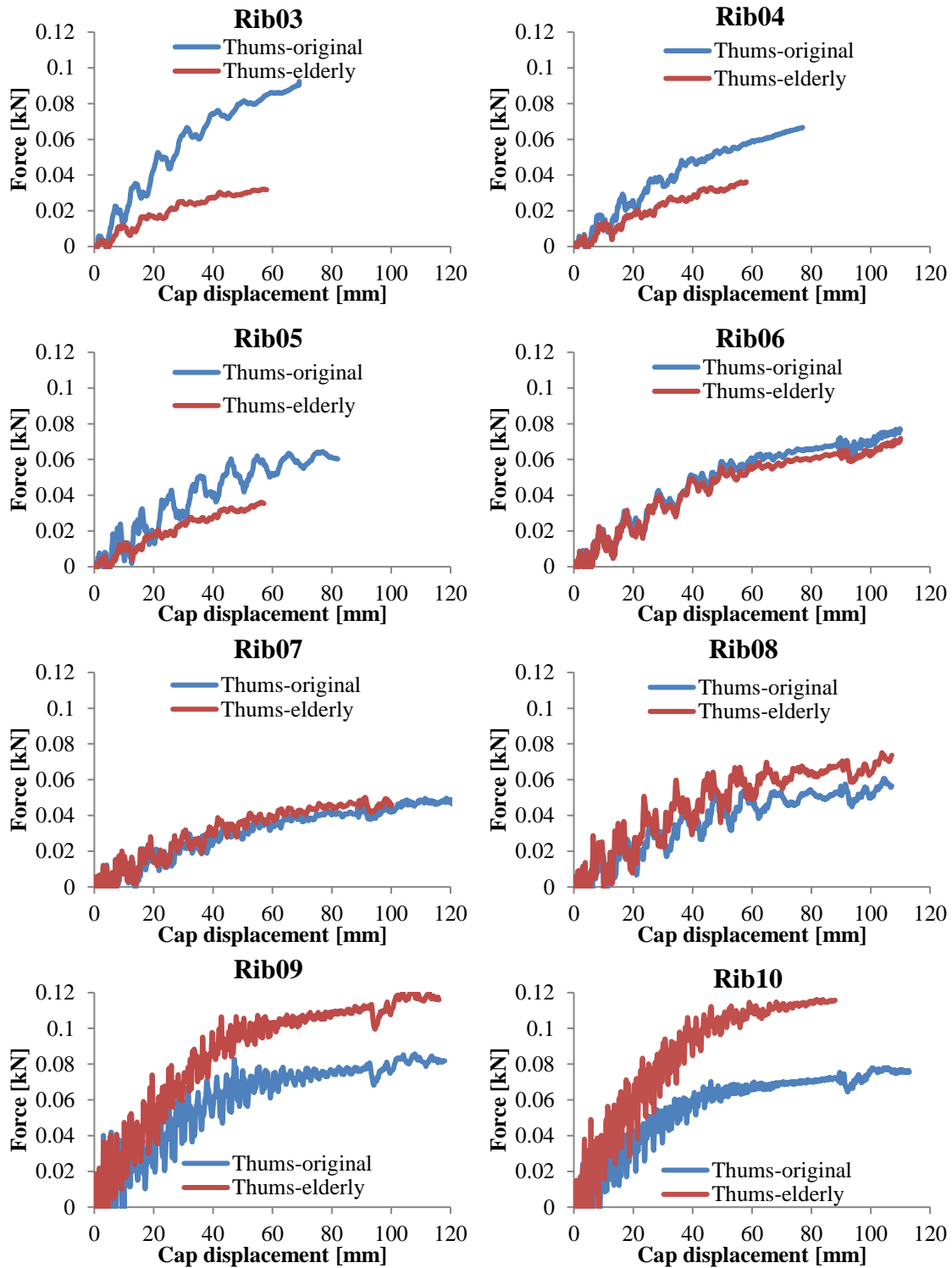


Fig. 2.51 Reaction forces (F_x) under AP bending per rib

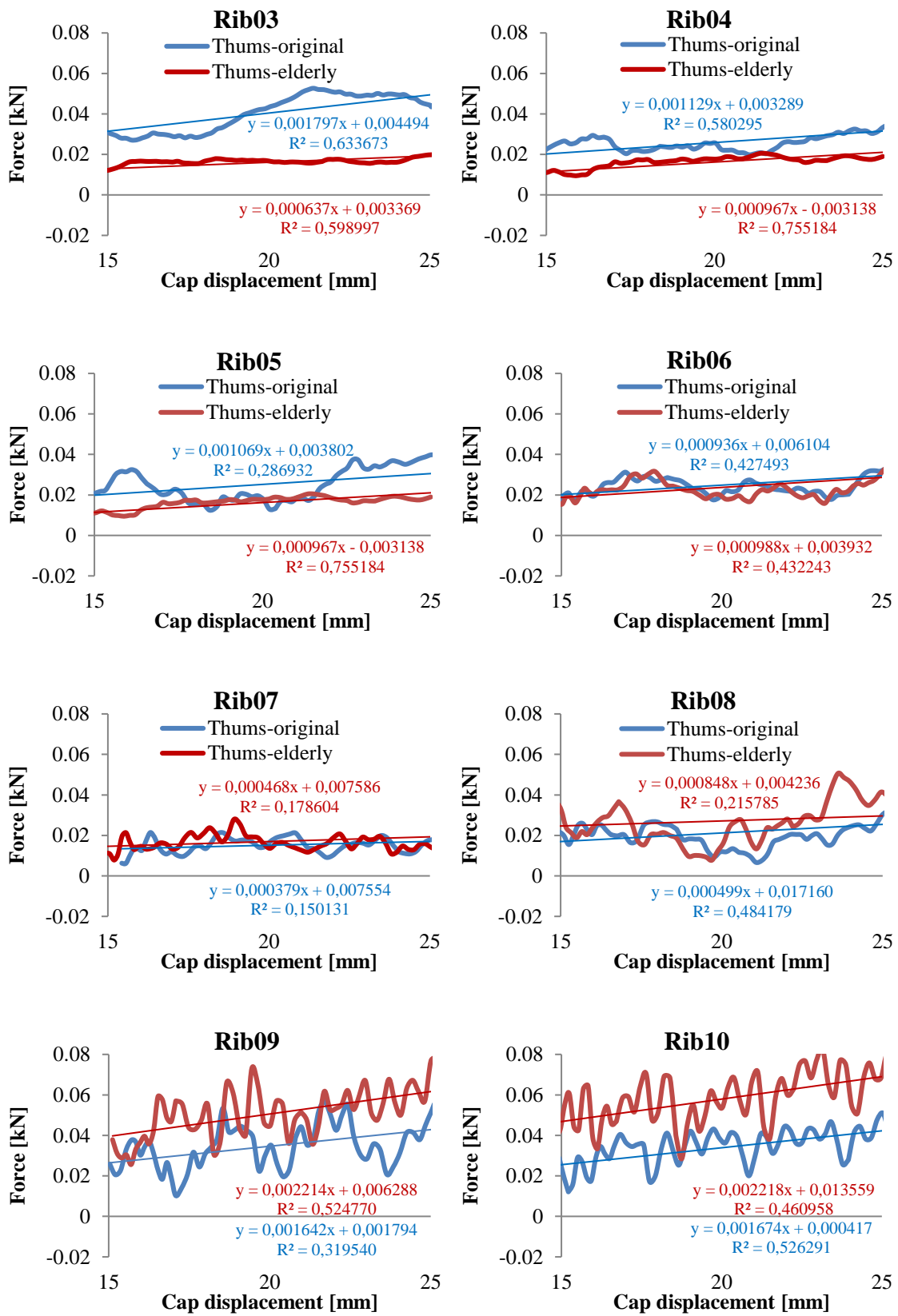


Fig. 2.52 Regression between 15 mm and 25 mm cap displacement for K calculation

As defined in 2.1.4.2.2, the mechanical characterization of the ribs under AP are summarized in the following plots. Both Thums-original and Thums-elderly simulation results are compared to the experiment mean values $\pm\sigma$.

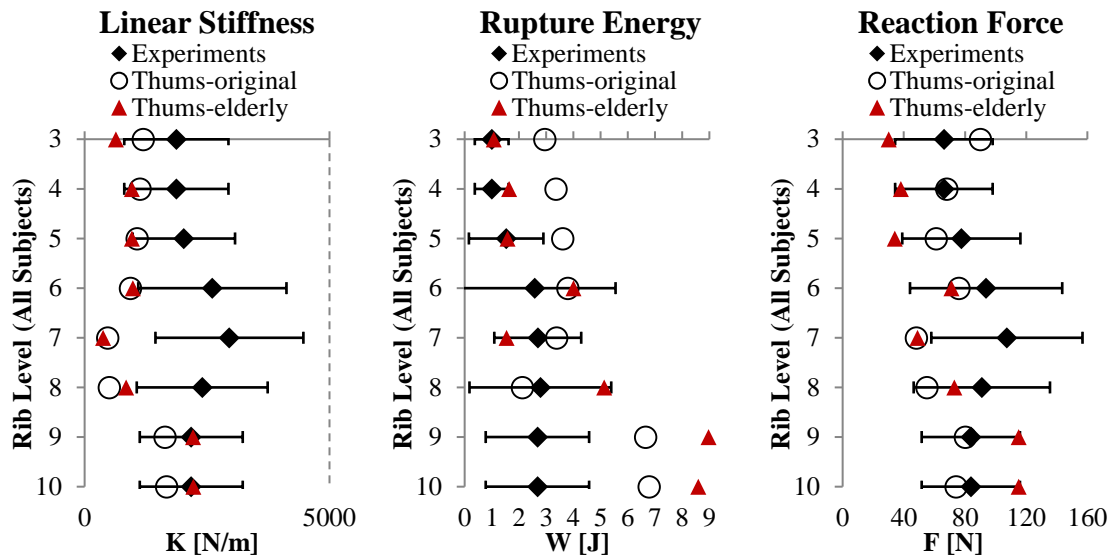


Fig. 2.53 K, rupture energy and reaction forces (mean and $\pm\sigma$ per rib level). Simulation results with Thums-original and Thums-elderly

An analysis of the results can be found in 5.2.

2.2.4.2.3 Clavicle Bending Test (Results)

Corridor and test details are depicted in the method section. The test was simulated in VPS with clavicles extracted from the Thums-original. The same model applies for both Thums-original and Thums-elderly. As for the ribs, the cortical and trabecular layers are simulated as shells and solid elements respectively. Material properties and VPS material and element type are listed below in the Table 2.19.

Bone Layer	Material Type (VPS)	Element Type	Young's Modulus [GPa]	Yield's Stress [GPa]	Failure Strain Definition [microstrain]
Cortical	MAT103 Elastic-plastic	Shell	10	0.200	Not defined
Trabecular	MAT1 Elastic-plastic	Solid	G=0.013 K=0.133	-	Not defined

Table 2.19 Material properties of cortical and trabecular layers of the clavicle model

The impactor and vertical constraints were simulated as elastic-plastic with steel properties (MAT103, $E=200\text{GPa}$). Contact type set to 34 and contact thickness set to 1 mm. Static (μ -static) and dynamic friction (μ -dynamic) coefficients were assumed 0.3. The impact velocity was set to 4 m/s as in the real test. Forces were measured as impactor-on-clavicle contact force whereas in the test the impactor force was recorded. The following plot shows the Thums clavicle response under 3-point bending. The curve response applies for Thums-original and Thums-elderly. No age dependent changes were introduced. Note the linear response.

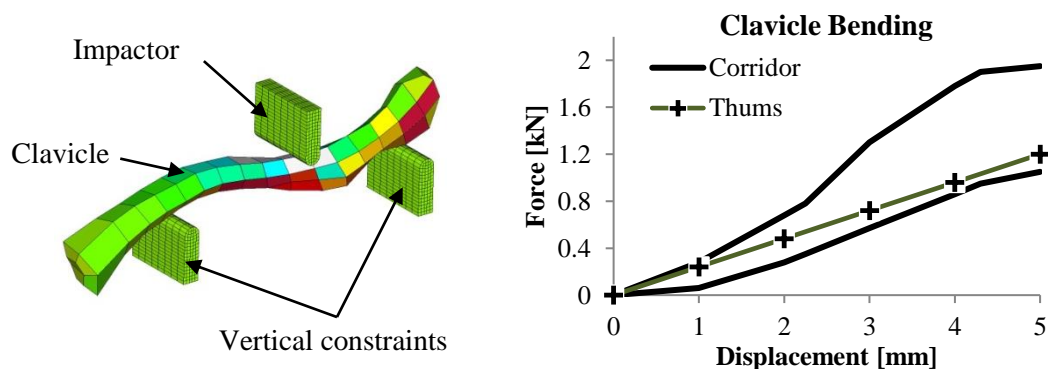


Fig. 2.54 Left: Three-point bending test simulation setup. Right: Bending response of both Thums-original and Thums-elderly

2.2.4.2.4 Costal Cartilage (Results)

The experiments were simulated in VPS following the specimen extraction described by Forman et al. [8] (see 2.1.4.2.4). A costal cartilage segment of from the Thums-original was isolated. Both ends were modeled as nodal rigid bodies. A fully constraint definition (111111) was set on the costochondral end. Following the experiment, the chondrosternal end was set with a prescribed motion with a ramp function of 400 mm/ms.

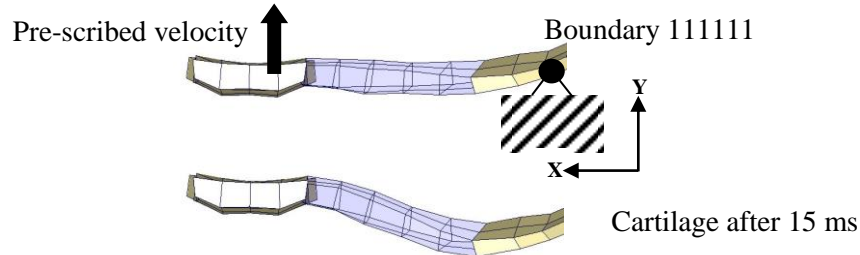


Fig. 2.55 Costal cartilage model with boundary conditions following the description of Forman et al [8]

Component		Element Type	Bulk and Shear Modulus [GPa]	Yield's Stress [GPa]	Failure Strain Definition [microstrain]
Cartilage	Hyaline + Perichondrium	Solid	G = 0.0175 K = 0.082	0.00485	330000

Table 2.20 Material properties of the cartilage model

For the elastic range, the Young's modulus can be calculated by

$$E = 3K(1 - 2\nu)$$

Eq. 2.1

$$E = 2G(1 + \nu)$$

Eq. 2.2

with the G and K from the Thums-original. A Poisson's ratio of 0.41 satisfies the correlation:

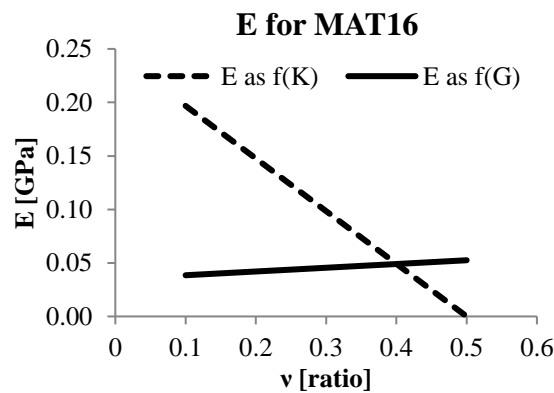


Fig. 2.56 Young's modulus from Thums-original for the increase of stiffness by calcification

The cartilage calcification effect was included in the models by increasing the elastic modulus in the material card from $E=0.0491$ GPa to $E=49.1$ GPa according with the range proposed in [8]. As mentioned in 2.1.4.2.4, the costal cartilage is represented in the Thums models as a single PID merging both hyaline core and perichondrium. The simulation results of cartilage reaction-force under bending is shown in the following plots.

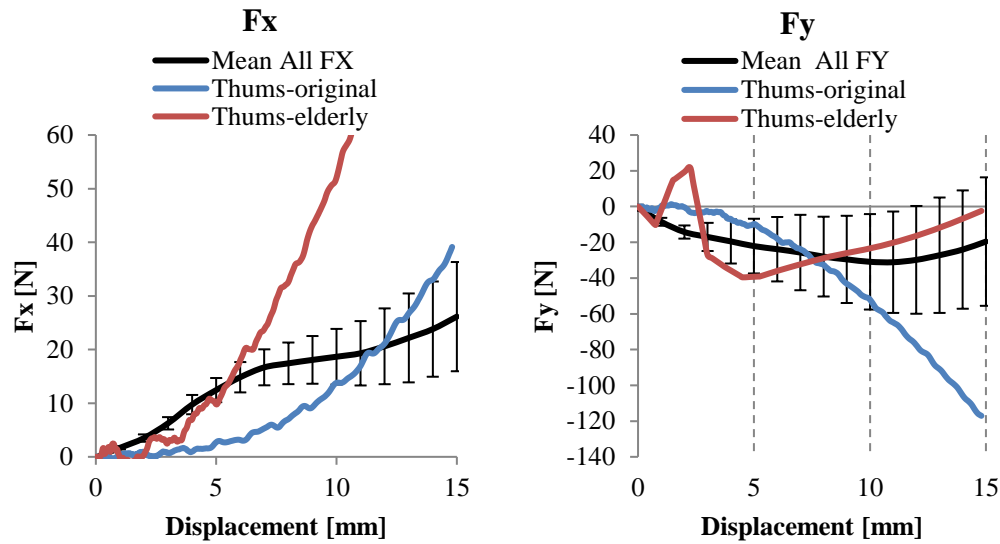


Fig. 2.57 Thums-original and Thums-elderly Fx and Fy reaction forces

Note the early peak in Fy. It is believed that a simulation artifact due to the costochondral constraints and the increased stiffness generates the initial peak at approximately 3 ms. Note also that the corridors do not strictly apply for a complete calcification level as the experiment samples did not exhibit an extreme calcification, instead, the response is showed for comparison purposes of the calcification effect in a component level.

2.2.4.2.5 Internal Organs (Results)

As described in the method section (see 2.1.4.2.5), a test done by Kent et al. [69] was taken as reference. Observing the PMHS average age at time of death ($70 \text{ YO} \pm 3$), the Thums-elderly was taken as baseline model. Two Thums-elderly models were simulated in single diagonal table-top configuration (see section table-top test 2.1.4.3.1). In one of the models, the internal single-mesh that represents the thoracic organs was deleted in order to represent the evisceration. The results are summarized as linear stiffness response as shown in 2.1.4.2.5.

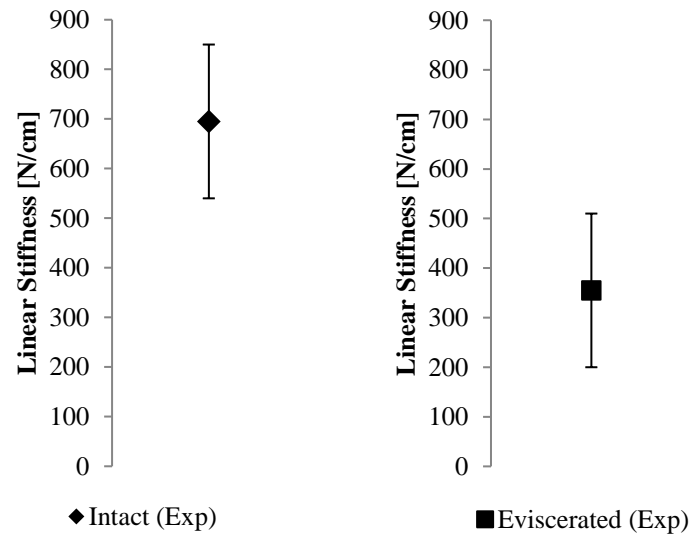


Fig. 2.58 Intact and eviscerated linear stiffness of the experimental data and simulations with the Thums-elderly

Although the stiffness response fits in one σ of the experimental data, the assumption of a single-mesh as a geometrical representation of the individual internal organs generate uncertainties on the inertial behavior of the model, the interaction between organs and force transfer to the internal ribcage surface. In this aspect, further development of the version 3 model is needed.

2.2.4.3 Body region level (Thorax)

In the sub-section 2.2.4.2 is discussed the mechanical response of the Thums-original's thoracic components and the individual effects on the mechanical response when introducing age-dependent factors (variable cortical thickness distribution and costal-cartilage calcification). In order to analyze the combined effect of those factors a "Thums-elderly" was created by introducing the abovementioned modifications in one single model. This sub-section describes the simulation procedure and results of four validation cases for rib cage mechanical response including the table-top test from Kent et al. [60] and blunt impact cases from Kroell et al. [70] and Shaw et al. [72] as explained in the method sub-section.

2.2.4.3.1 Table-Top Test (Results)

The test apparatus described in the method section was simulated. The test plate was simulated as a rigid surface, contact thickness set to 1 mm and friction coefficient to 0.3. Both Thums-original and Thums-elderly models were positioned supine on the plate. No pre-simulation in order to represent the change of lordosis in supine position was run, instead a "pre-fitting" loading (belt and distributed loading cases) was used before the start of the test loading. For the belt loading a 50 mm wide belt was modeled using shell elements and an elastic material representing the fiber-reinforced material used in the real test. The same element formulation and material was used to represent the distributed loading belt. The belt followed a path approximately 30° from the sagittal plane left-to-right engaging the left clavicle superiorly, crossing the sternum on the midpoint (Y-notch point) and leaving the torso at the 9th rib location as defined by [60]. The distributed loading belt was located between the 2nd and 7th rib as shown in the Fig. 2.59.

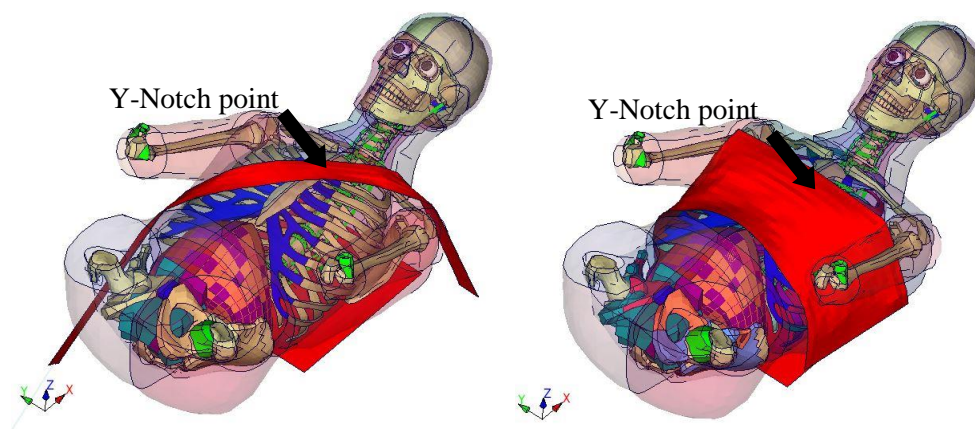


Fig. 2.59 Diagonal belt and distributed load simulations. Note the "Y-notch Point" for chest deflection reference.

The 1 m/s loading rate was set to the ends of both belts in the vertical direction (Z) representing the pulling cables from the real test. Both chest deflection as vertical displacement of the Y-notch point and posterior contact force were calculated. Cross-plot of reaction forces vs. chest deflection were generated in each case. The belt load condition was also simulated with the Hybrid-III (H350) dummy. Posterior force vs. chest deflection cross plot was also generated. Although this additional simulation is independent of the validation process of the HBMs, it was found relevant to show a comparison with the H350 and thus opening the discussion on the biofidelity level of different occupant models.

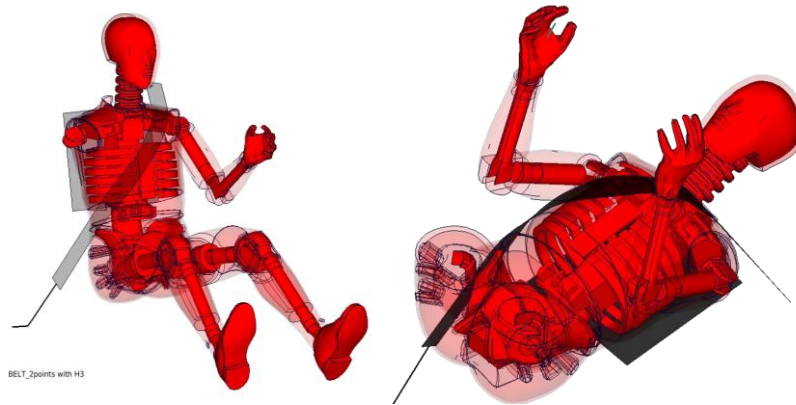


Fig. 2.60 H350 in table-top diagonal belt loading

The following matrix summarizes the simulations done:

Table Top Test	Thums-original	Thums-elderly	H350
Diagonal Belt	X	X	X
Distributed loading	X	X	-

Table 2.21 Simulation matrix for table-top test

Chest depth and normalization factors

In the real test the chest deflection was measured via external potentiometer. Chest deflections were normalized to a 50th %-ile American male (AM) chest depth (229 mm), hence the same method was used to normalize the chest deflection of the three models. The factors are shown in the following table.

Table Top Test	50th %-ile AM	Thums-original	Thums-elderly	H350
Chest depth [mm]	229	230	230	270
Norm. factor	1	0.995	0.995	0.848

Table 2.22 Chest deflection normalization factors

Note that the H350 chest depth is usually defined as the internal rib cage depth equal to 236 mm [46]. This value match the H350's rib cage depth without the outer foam jacket. This assumption intrinsically ignores the influence of the outer jacket on the overall linear stiffness of the H305's ribcage. Therefore, the chest depth of the H350 was normalized including this component (34 mm). For comparison purposes, the not-normalized response was also included.

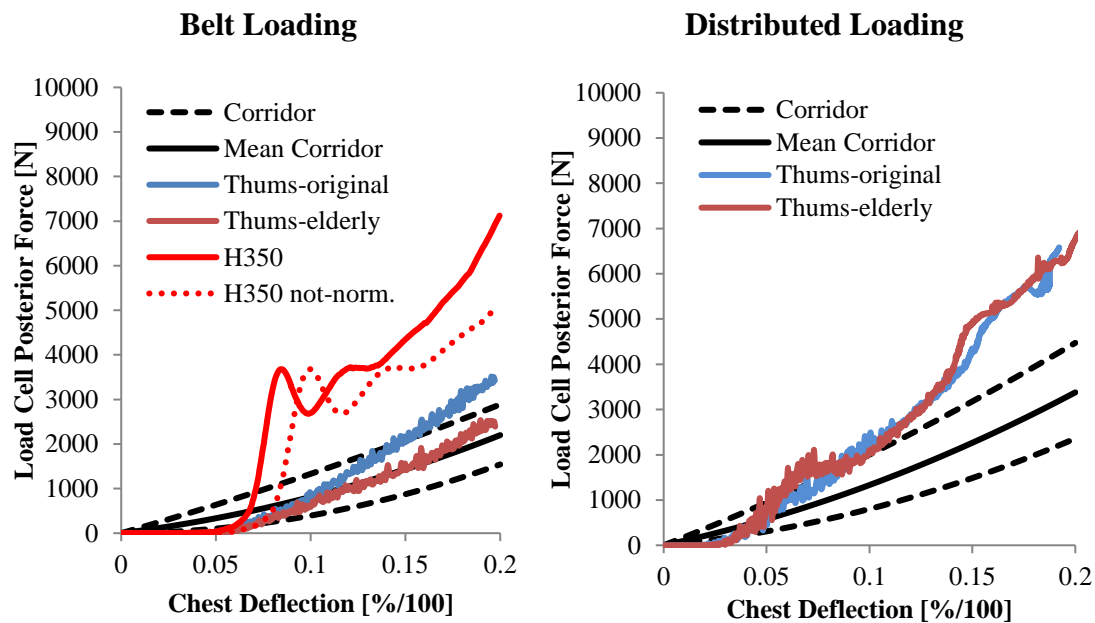


Fig. 2.61 Left: Table-Top diagonal belt test response comparison: Hybrid-III, Thums-original and Thums-elderly. Right: Distributed loading

Note in the belt loading a reduction of around 27 % of the linear stiffness between Thums-original and Thums-elderly when measured after 10 % chest deflection. After 12 % normalized chest deflection both models shown a stiffer response out of the corridor. This effect is related with (i) the internal organ-mesh compression and (ii) with the engage of the abdominal organ-mesh which was not included in the component validation test.

2.2.4.3.2 Frontal Hub Impact Test (Results)

The hub impact test described in the method section was simulated. The impactor was simulated as a cylindrical 152.4 mm diameter rigid body and its weight was set to 23.1 kg via density definition. As defined in the other validation test, contact thickness between impactor and chest was set to 1 mm and friction coefficient to 0.3. Both Thums-original and Thums-elderly models were up-right positioned and impacted in anterior-posterior direction, mid-sagittally at the fourth inter-costal space measured at the sternal height. The impactor velocity was set to 6.9 m/s.

Linear stiffness response was plotted and compared to the experimental corridors developed by [78] as shown below.

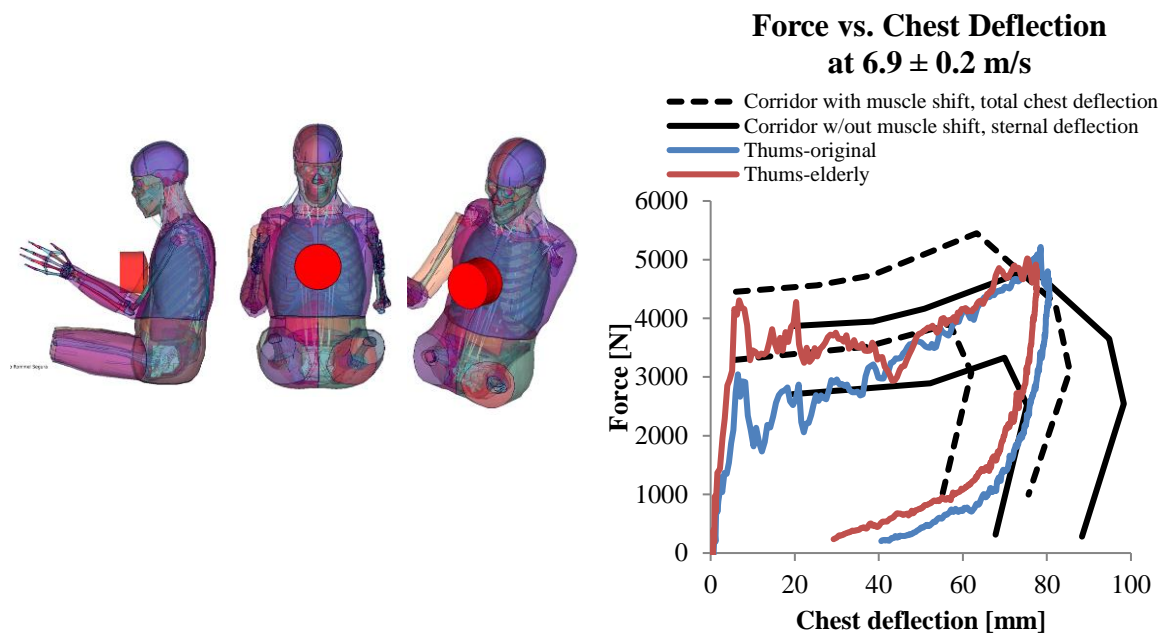


Fig. 2.62 Left: Lateral, frontal and isometric views of the hub impact simulation with both Thums-original and Thums-elderly. Right: Hub impact test: Chest stiffness response comparison

2.2.4.3.3 Lateral and Oblique Hub Impact (Results)

As in the frontal test, the impactor was simulated as a cylindrical 152.4 mm diameter rigid body and its weight was set to 23.1 kg. Contact thickness between impactor and chest was set to 1 mm and friction coefficient to 0.3. Both Thums-original and Thums-elderly models were up-right positioned. The impactor was located to impact the model in lateral-medial direction, mid-sagittally at the fourth inter-costal space measured at the sternal height. For the oblique direction the impactor initial velocity vector was defined with an angle of 60 degrees from the sagittal to the frontal plane. The impactor velocity was set to 4.3 m/s for the lateral test and 2.5 m/s for the oblique test respectively.

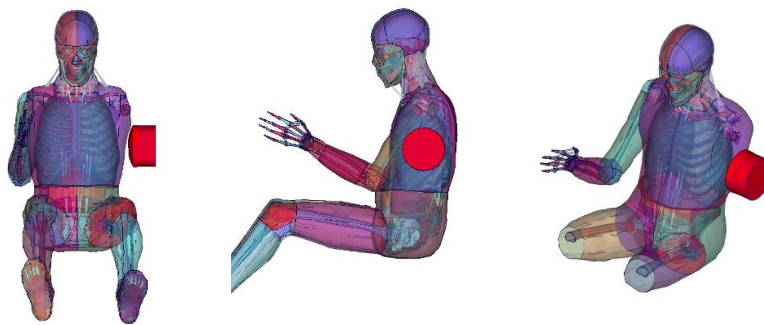


Fig. 2.63 Frontal lateral and isometric views of the lateral hub impact simulation with both Thums-original and Thums-elderly

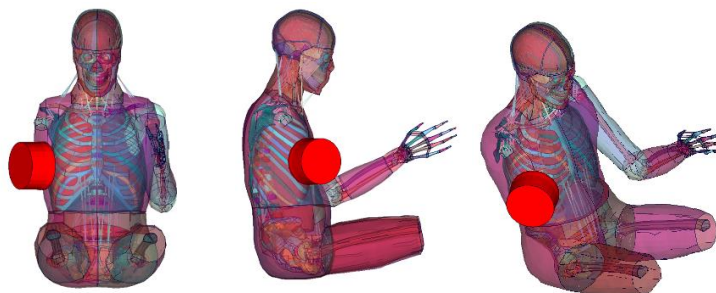


Fig. 2.64 Frontal lateral and isometric views of the oblique hub impact simulation with both Thums-original and Thums-elderly

Contact forces and chest deflection based on relative nodal displacement were plotted. See below the results and corridors in the Fig. 2.65.

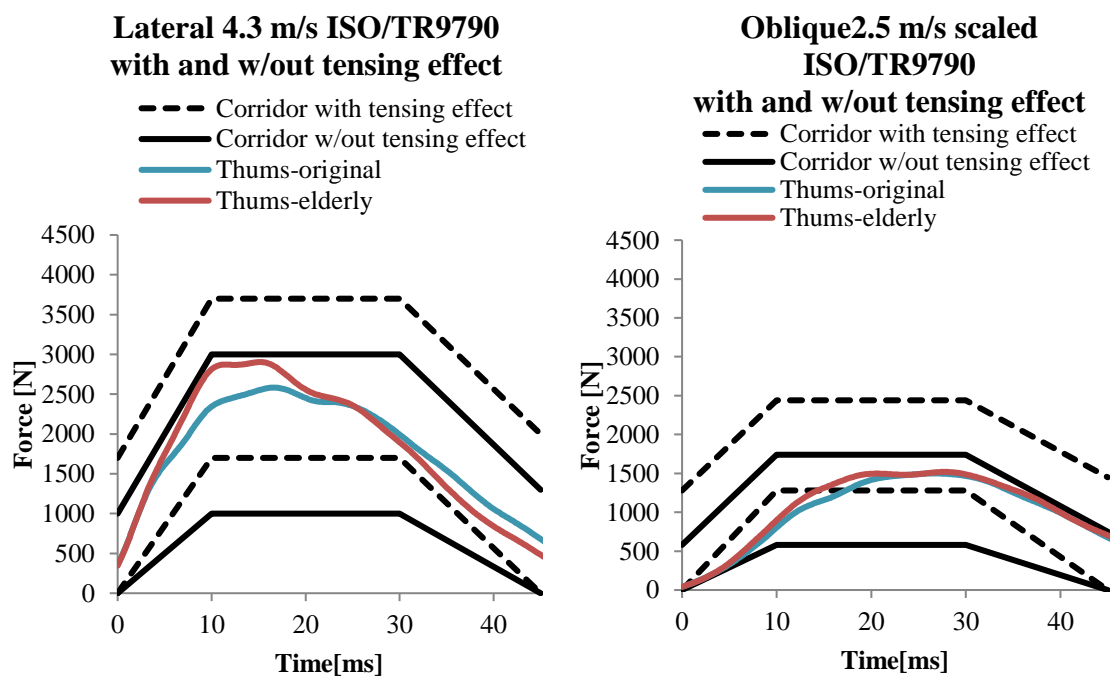


Fig. 2.65 Left: Corridors for and model response for lateral hub impact. Right: Corridors for and model response for oblique hub impact

2.2.4.4 Full-Scale Test (Sled Test / Gold Standard) (Results)

The original buck model was obtained from the UVA-Collaboration website from the THOR-NT FE model project. The access data was a courtesy of Dr. D. Parent (NHTSA). The original LS-Dyna model was converted to VPS. The sled including seat, anchor points, knee bolster and footrest were simulated as single rigid body. Belt material for membrane type elements was taken from the internal model database at Audi AG. Contacts type 33 in VPS for the interface HBM-belts was chosen. A GS1 pulse was set to the model as defined in [81]. The Thums models were positioned matching the coordinates and angles specified in [81]. Belt routing were approximated to the subject 1358 due to the anthropomorphic similarities with the Thums.

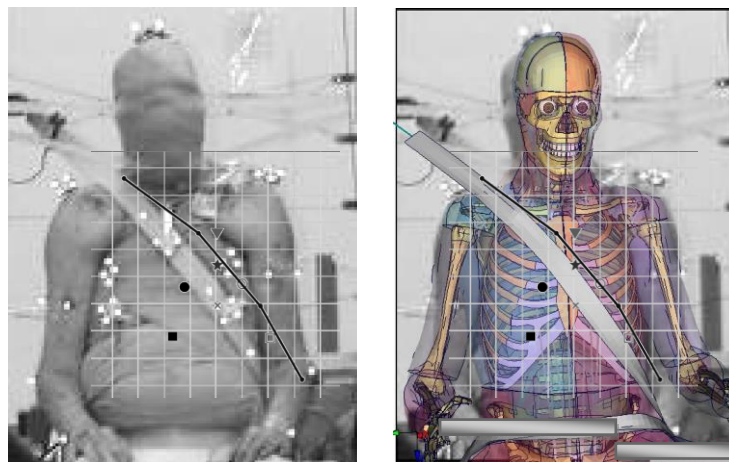


Fig. 2.66 Comparison of the belt routing between subject 1358 and Thums. Path taken from [81]

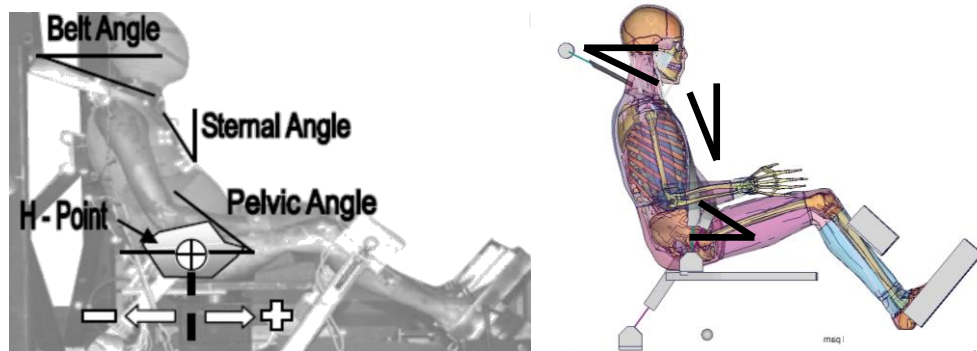


Fig. 2.67 Comparison of GS1 seating position between a PMHS [81] and Thums

	Angle [°]		
	Test		Thums
	Min	Max	
Sternal	17	27	23
Pelvic	23	49	31
Belt	26	29	29

Table 2.23 Angle ranges for positioning as defined in [81] vs. Thums position

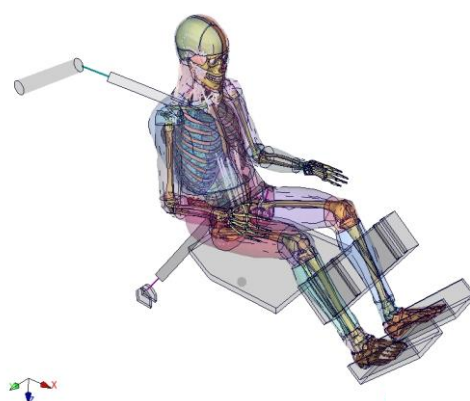


Fig. 2.68 Thums-original / -elderly as positioned in the GS1 simulations

An initial visual check for head and torso excursion was done. A superposition of both cadaver-test and simulation with the Thums are shown in the following diagram:

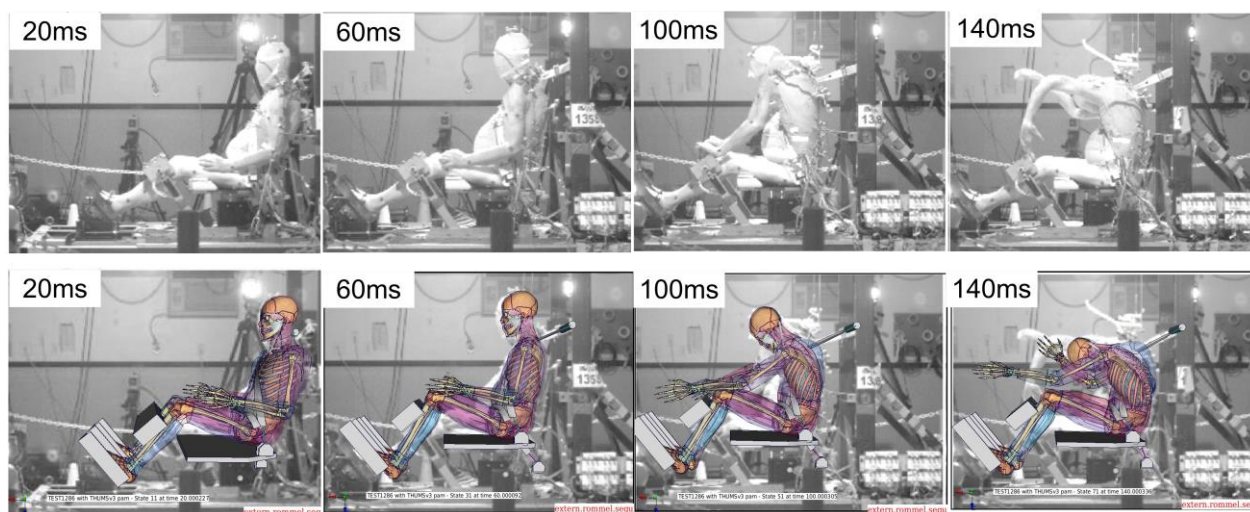


Fig. 2.69 Test and Thums-original forward excursion comparison

Acceleration time histories were calculated including the head COG, sensor points on T1, T8, T12, L2, L4 vertebrae and pelvis. Shoulder tension was recorded using the section-forces card in VPS. Anterior ribcage reference points (upper right, upper left, lower right, lower left and mid-sternal) were assessed by post-processing. Simulation results for belt tension and thorax deformation are presented below.

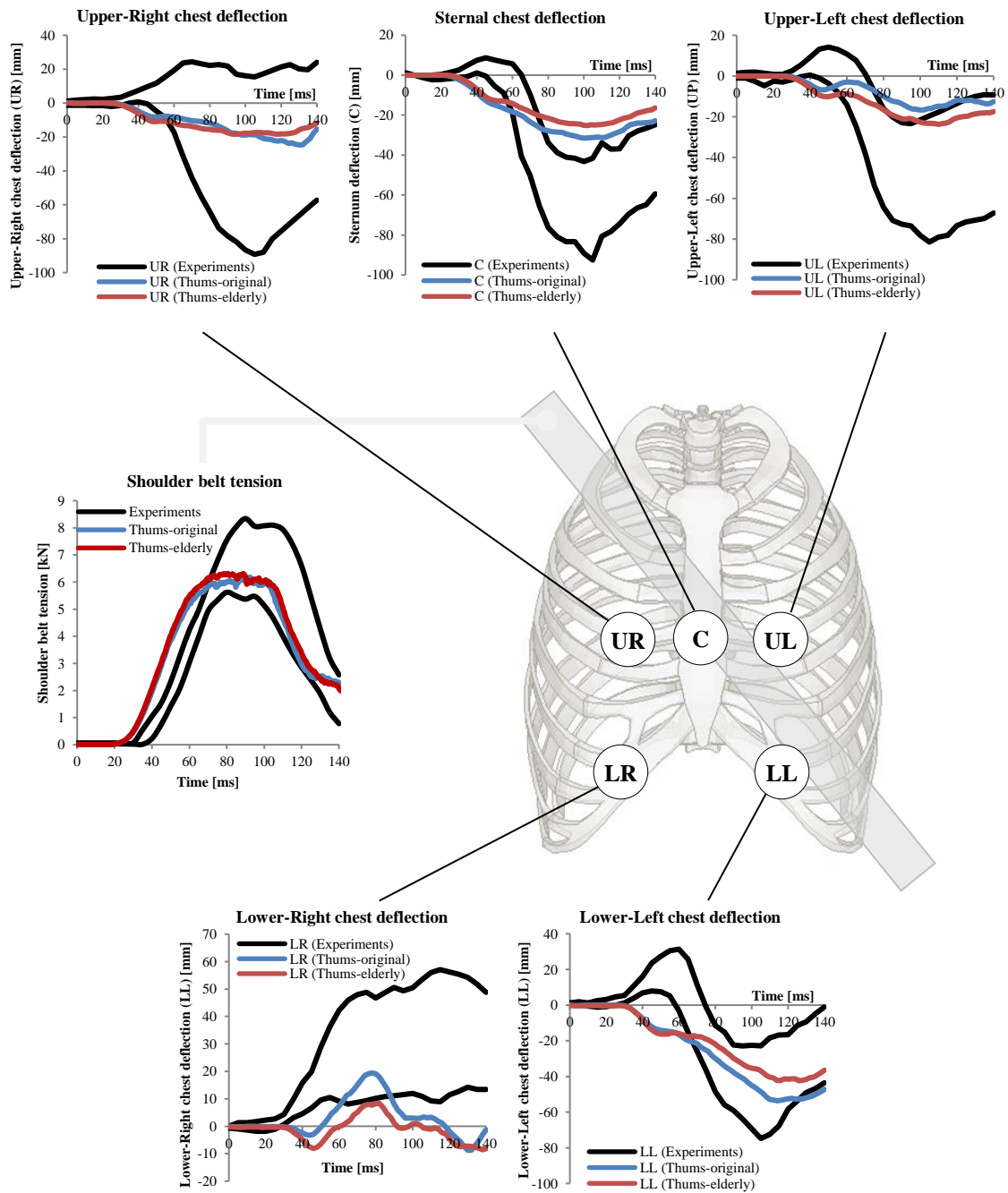


Fig. 2.70 Belt tension and multipoint chest deflection wrt. T8. Thums-original and Thums-elderly simulation results

The GS1 represents the largest sample of PMHS close to the 50th %-ile tested under controlled conditions and replicating a seatbelt restraint-like effect on the human thorax. Both HBMs exhibit a realistic forward excursion. Head and spine trajectories of both models are presented below. Head and spine trajectories from the real test were not published. Rib cage deformation patterns of both models showed to be in a reasonable range compared to the test corridors. One noticeable response involved the lower right chest and the “bulge-out” effect [81]. Mentioned by other authors and reanalyzed by Shaw with the GS1 test, the bulge-out of the lower chest (seatbelt’s opposite side), or “negative deflection”, may increase the sternal moments and consequently the sternal fracture risk. Although both HBMs reproduced the bulge-out effect, the Thums-original showed a peak deflection of -19.2 mm whereas the Thums-elderly peak deflection reached -8 mm (notice the negative sign indicating negative deflection). It is believed that the cartilage calcification causes a coupling effect of the anterior thorax generating a uniform deflection compared to the decoupled-like in Thums-original. The implications could involve an underestimation of the sternal bending moments in belt-like dominated loading.

3 DEVELOPMENT OF ASSESSMENT PROCEDURES

This chapter starts with a review on the basic concepts of occupant restraint, crash severity characterization, design guidelines for restraint systems and current thoracic injury assessment methods for ATDs. An assessment procedure for thoracic injury prediction specifically for HBMs is developed into the subchapter “Method” (3.2). The subchapter “Results” (3.3) presents first (i) four restraint system variants (see 3.3) as a results of the application of design guidelines (3.1.2); these variants constitute the frame for the restraint system effectiveness analysis based on the simulation matrix of chapter 4. Second (ii), the results of the assessment procedure development summarized as a report prototype. An initial validation of the assessment procedure is also presented following the layout of the report prototype.

3.1 Introduction: Occupant Restraint Method

Based on the concepts presented by Kent et al. (2015) [83], the method for the analysis of occupant protection in frontal crash can be divided in two fields: (i) Crashworthiness and (ii) Occupant-Restraint. In the crashworthiness field, the development focuses on the design of crushable structures around the occupant cell minimizing intrusions during a crash and so ensuring a minimum survival space. Crushable structures are in charge of the most kinetic energy dissipation of the collision and controlled deceleration of the vehicle [84]. This field will not be addressed into this dissertation. Into the Occupant-Restraint field, the fundamental concept is the so-called “ride-down” management. This “ride-down” implies a controlled deceleration process of the occupants relative to the vehicle during the crash through the application of restraint systems. This controlled deceleration should ensure that the injury tolerance limits of the occupant will not be exceeded. The restraint system design combines trigger times with load limiting of a variety of components as retractor-, buckle-, anchor-pretensioners and airbags.

Following the aforementioned outline, the methods presented in this chapter are focused on Occupant-Restraint whereas the structural behavior of the vehicle is reduced to an independent variable in form of deceleration pulse of the occupant cell.

3.1.1 Principles, Functions and Components for Occupant Restraint

In a crash, a typical occupant restraint process starts with belt pretensioning followed by a “ride-down” controlled by belt load limiting and airbag leakage. The ride-down is a controlled deceleration process of the occupants relative to the vehicle. The main target is to ensure that the forces generated in the restraint process do not exceed the injury tolerance limits of the occupant. The injury outcome is strongly dependent on the synergy between seatbelt- and airbag-functions. Analyzing separately both functions [83] it is possible to define a “Restraint Management by Seatbelt” and “Restraint Management by Airbag”.

Restraint Management by Seatbelt (Based on Kent concepts [83])

As widely found in the literature [83] [84], the typical example to explain the seatbelt function on the occupant’s kinetic energy dissipation during a crash, is a one-dimensional frontal collision of a vehicle and a fixed rigid barrier. The following graphic illustrates the velocity history of the vehicle and an unrestrained occupant.

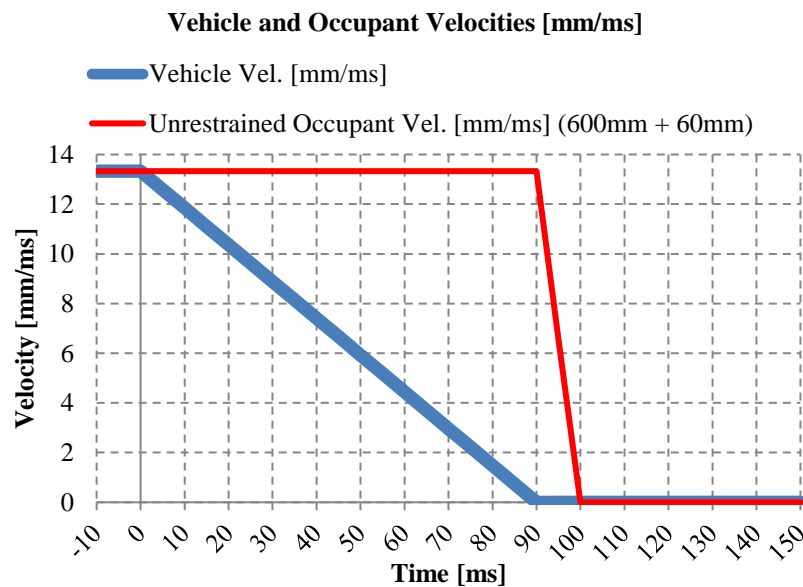


Fig. 3.1 Typical crash vehicle velocity as a function of time. Modified example based on the example from Kent et al. (2015) [83]

The basic principle of a “restraint process” involves the conversion of the initial kinetic energy of the vehicle in deformation work, and the occupant’s kinetic energy dissipation through the work done by the restraining forces. The graphic shows the vehicle’s velocity reduction due to the front-end deformation and the “free flight” of a theoretical unrestrained occupant in the interior of the vehicle.

The graphic represents an example of a vehicle impacting a fixed rigid barrier at 48 km/h (13,33 mm/ms) and an ideal constant deceleration until 90ms. The integral between the impact time “t0” and the velocity equal zero represents the deformation of the vehicle’s front-end as above mentioned. This can be also analyzed according to an equation of linear motion

$$V_f^2 - V_i^2 = 2 * \text{acc} * S$$

Eq. 3.2

Where,

$$V_i = 13,33 \text{ mm/ms}$$

$$V_f = 0 \text{ mm/ms}$$

$$\text{acc} = -0.1481 \text{ mm/ms}^2$$

(calculating the slope of the vehicle's velocity between $t = 0$ and $t = 90\text{ms}$) or,

$$\text{acc} = \sim -15 \text{ g}$$

and

$$S = 600\text{mm} \text{ (Representing the deformation of the vehicle front-end)}$$

Now, analyzing the unrestrained occupant kinematics, if there are no forces present that change the trajectory of the occupant, it will experience a free-fly phase from the beginning of the crash until 90ms. Assuming that the available forward excursion of the vehicle is 600mm (as vehicle deformation), the occupant should impact the vehicle's interior after 90 ms at a velocity of 13,33 mm/ms. The impact under these conditions will produce extreme high accelerations on the occupant. Assuming a deformation of the interior panel of 60 mm, the values of this deceleration will reach $\sim 136 \text{ g}$. For a restrained occupant case (simple restraint, no pretensioner, no force limiting), the velocity plot will look as shown here:

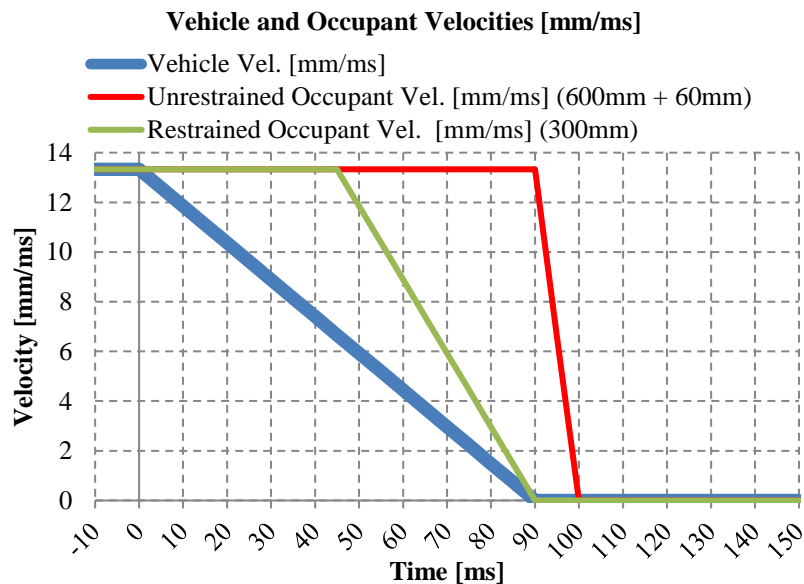


Fig. 3.2 Green: simple belt restraint. All: No pretensioner, no load limiters. The forward excursion is around 300mm.

Where the green line represents a restrained occupant with

$$\begin{aligned} \text{acc} &= -30.2 \text{ g} \\ S &= 149.95 \text{ mm (from } t = 45 \text{ ms to } t = 90 \text{ ms)} \end{aligned}$$

Note that the green line represents the controlled deceleration effect of a standard belt on the occupant engaging at $t = 45\text{ms}$ hence controlling a forward excursion (with constant deceleration) equals to 149.95 mm. Note also the assumption that both vehicle and occupant reach $V = 0$ after 90 ms.

In the introduction it was mentioned that load limiting devices contribute to the ride-down process of the occupant. Including this concept under idealized conditions of belt force load limiting we have:

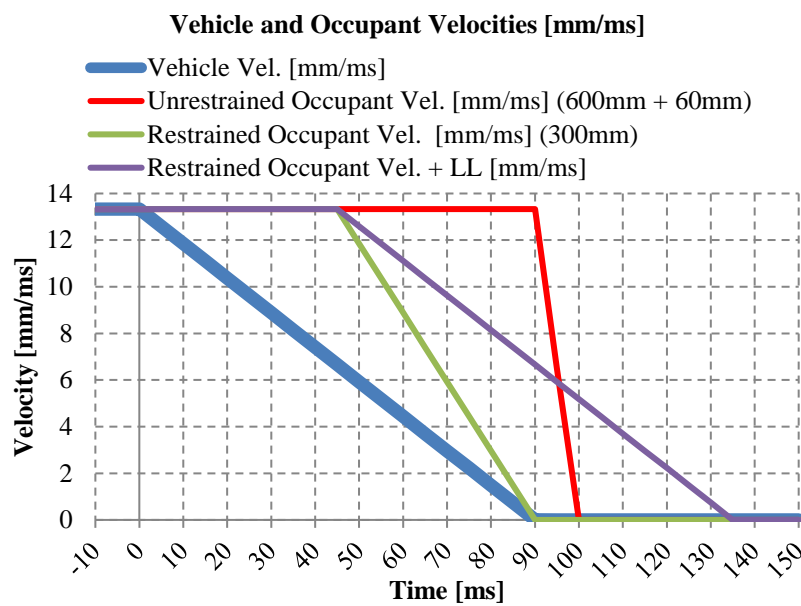


Fig. 3.3 Purple: Effect of a pretensioner. The forward excursion is around 300mm.

Where the purple line represents a restrained occupant with a force limiting belt generating:

$$\begin{aligned} \text{acc} &= -15 \text{ g} \\ S &= 300 \text{ mm (from } t = 45\text{ms to } t = 135\text{ms)} \end{aligned}$$

Note that the forward excursion of the occupant continues after the vehicle complete stops.

Introducing a pretensioner, the combined effect with load limiting shows:

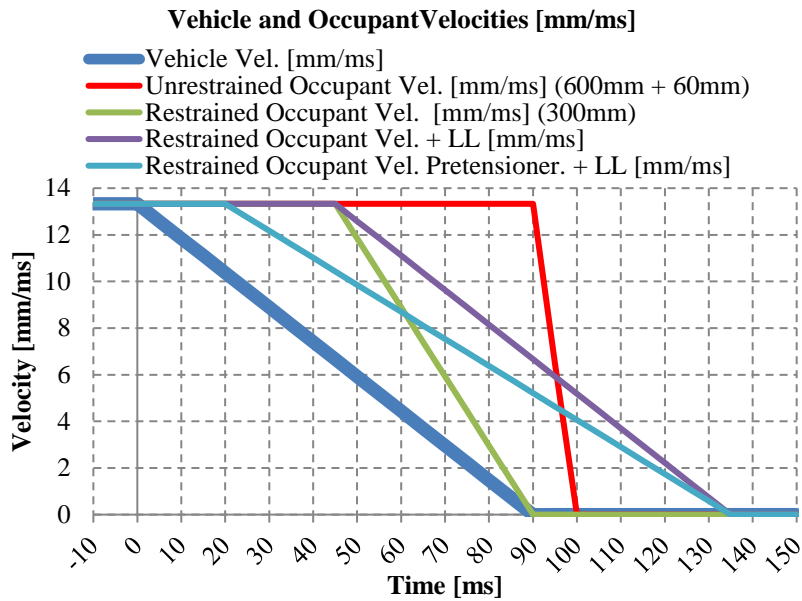


Fig. 3.4 Cyan: Combined effect a pretensioner and load limiters. The forward excursion is again ~300mm

With

$$\text{acc} = -11.81 \text{ g}$$

$$S = 299 \text{ mm (from } t = 20 \text{ ms to } t = 135 \text{ ms)}$$

Note the forward excursion assumption = 300 mm. Note the effect on the deceleration of the occupant.

The aforementioned cases show the effect of pretensioning and load limiting on the occupant restraint management in an idealized case. Considering an example of belt forces from FE simulations of a real crash we have:

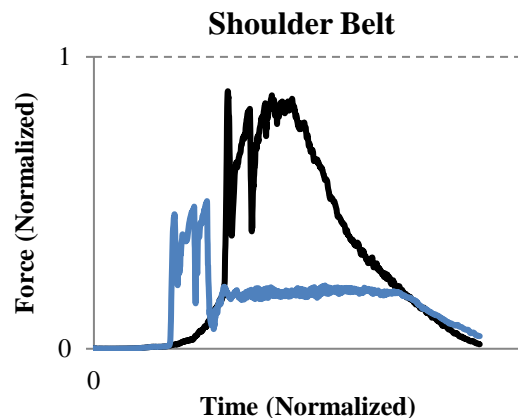


Fig. 3.5 Black: Standard belt with Airbag. Blue: Pretensioned, load limited belt with airbag

The effect of the load limiter (same crash case) on the H350's torso acceleration can be depicted as follows (example taken from [84])

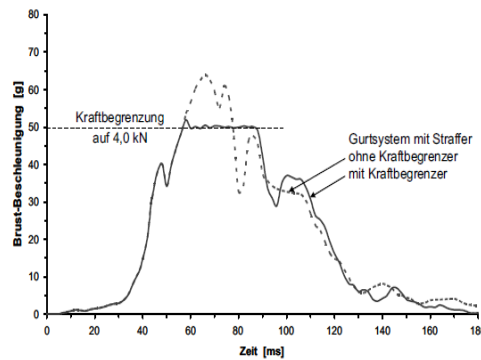


Fig. 3.6 Effect of the load limiter on the occupant acceleration [84]

Summarizing the main concepts, we have:

- (i) Linear deceleration profiles are a simplification in a one-dimensional model
- (ii) The ride down process is dependent on the vehicle's pulse. The deceleration pulse plays a major role in the restraint system design process
- (iii) An early coupling achieved by pretensioning plus load limiting are the basic strategy for the reduction of the occupant deceleration
- (iv) For the velocity plots the maximum forward displacement of the occupant was assumed to be 300 mm. This is the standard reference value for the design of restraint systems. The examples of only-force limiting and only-pretensioning show the optimal deceleration values that, under the mentioned pulse conditions, an occupant can achieve using the maximum forward displacement.
- (v) No rebound was considered in the analysis
- (vi) As showed in the belt force plots, the influence of load limiting and airbag on the belt force and consequently on the occupant ride-down in noticeable beneficial

Restraint Management by Airbags

Based on the concepts of Kent et al. (2015) [83], the key advantages of the restraint management by airbags are the load distribution and the contribution to reduce the seat belt loading on the occupant during the ride-down phase. Likewise, the functions of an airbag in a frontal crash can be classified in the following four groups:

(i) Head-Neck protection: By avoiding contact of the head and neck with the steering wheel or dashboard. As noted also in [83], the combination of belt and airbag is desired to avoid an induced upwards movement against the windshield or roof. This was tested by Berg et al. [85]

(ii) Force distribution during ride-down: Kent cited the study of Patrick et al. [86] where a comparison of injury outcome with PMHS in sled test was run. Similar injury outcome was obtained under two different peak forces 3.3 kN and 8.8 kN. The difference between the experiments was that in the second case (8.8 kN) the force action area was higher, including not just the chest, but shoulders and chest. This is, the injury tolerance to the force is dependent on the area where the force is applied to. The implications involve that the same dissipation levels of the occupant's kinetic energy can be achieved under higher forces without exceeding the injury tolerance limits. As known, an airbag deployment will generate a bigger contact area compared with the contact area of the seatbelts.

(iii) Share loading in ride-down: An analysis from Grosh [87], also cited by Kent, showed opposite trends between chest acceleration and chest deflection when comparing the benefit of an additional airbag against pure-seatbelt loading without airbag under the same test conditions. An additional airbag generates higher torso accelerations but also a reduction of the peak chest deflection. The introduction of the airbag generates a reduction of the belt force but an increment in the overall resultant force, measured as a torso acceleration. Again, higher acceleration levels can be sustained by the occupant without increasing the injury risk (in this case evaluating the chest deflection peak) if the force is distributed over a bigger area. As an example, a reduction on the shoulder belt force, as a consequence of the airbag action, implies that the effects of the belt's "concentrated load" will be lower even if the total work done on the occupant in the ride-down phase is higher. This work is done by the combination of belt and airbag forces.

(iv) Reduction of belt load-limiting values: As aforementioned, belt-like loading is not equal airbag-like loading. Each case would generate different injury mechanisms and consequently the associated injury risk may not be the same. Under the similar loading peaks, the effect on the injury outcome is different. The belt-like loading is associated with a higher injury risk [88], this implies that a reduction of the belt-like loading is desired. From the theoretical point of view, the belt load limiting values can be even reduced to a level where a contact with the steering wheel or panel (due to forward excursion) would be inevitable by replacing the "missing" restraint using an airbag. Note that for a secondary impact, a loose restraint system cannot control the occupant's kinematics.

3.1.2 Design Method

The energy dissipation of the occupant should be maximized by the restraint system. This maximization is nevertheless constrained to the injury tolerance levels. The principles, functions and components to achieve this maximization were addressed in 3.1.1. This section proposes the design guidelines for restraint management. The concepts are materialized in the subchapter “Results” (see 3.3) in four restraint system variants. These variants constitute the frame for the restraint system effectiveness analysis with the simulation matrix of chapter 4.

3.1.2.1 Design Guidelines

The restraint management was approached in 3.1.1 by analyzing the effect of seatbelt and airbag separately. In a real design process, both restraint management types are combined. The parameter configuration of both management types should consider the following design guidelines proposed by Adomeit [89], Kent et al. [83] and the author.

For the restraint system:

- (i) Maximization of the application time of the restraint loading: From the velocity plots in the section 3.1.1, the longer the force application is, the higher is the work applied. The work applied can be understood as the energy dissipated in the ride-down process. Taking as a constraint the fact that the forward excursion space is finite, this maximization is commonly achieved by an early coupling vehicle-occupant using belt pretensioners.
- (ii) Maximization of forward excursion: With longer dissipation path the total work can be generated by lower forces. Lower forces under the same restraint condition type imply also a lower injury risk.
- (iii) Maximization of the restraint force under the tolerance levels of the occupants. If the forces can be maintained under the tolerance levels, it is not necessary to use the complete forward excursion for the energy dissipation, hence decreasing the risk of head contact with the wheel or dashboard.

For the occupant:

- (iv) Maximization of the restraining force distribution.
- (v) Minimization of deformation, deformation rate and accelerations.
- (vi) Loading concentration of on the strongest body regions. Local tolerance limits will be observed.
- (vii) Shoulder loading through torso pitching (from Adomeit [89] on the fundamentals of ride-down management of shoulder and hip trajectories).
- (viii) Avoid submarining: The forward rotation and vertical downward motion of the hip should be avoided [90]. This minimizes the risk of sliding-off of the lapbelt that could end in the abdominal region. The sliding-off could also occur when the lap belt is not engaged

between the superior and inferior iliac spine. Knee airbags are typically involved in this guideline.

(ix) Concentrate the shoulder belt force on the shoulder region by torso forward pitching: Defined by Adomeit [89] [90], the forward motion of the torso generates a concentration of the belt force on the shoulder region. This force-sharing will decrease the belt forces induced into the torso which is preferable.

(x) Minimize yaw rotation (Author): The torso forward pitching concept has to be complemented with the yaw rotation. HBMs represent a more human-like lumbar and thoracic spine deformation compared to the H350, involving more flexibility. One of the consequences is a twisting effect of the thorax which is associated with a higher local deformation on sternum and ribs, hence increasing the thoracic injury risk.

(xi) Deployment timing of belt, airbag, and differences between driver and co-driver (passenger): Kent et al. [91] showed the chest-acceleration time plots of two H350 in driver and passenger positions. Available excursion distances comparing driver vs. passenger require hence different deployment strategies. Assuming similar trigger and inflation times of both airbags, usually the share-loading starts faster in the driver side due to the smaller distance. For the passenger the share-loading starts later generating an initial belt-dominated ride-down and a second acceleration peak when the airbag engages the occupant. For the driver, the acceleration peak occurs under combined belt and airbag loading. For the passenger, the acceleration peak first occurs under belt loading whereas the second one is caused by airbag loading. Trigger times and load limiting may modify this behavior.

(xii) Conservative design: Excessive forward displacement allowed by yielded belt systems would apply no control of the occupant kinematics in a secondary crash. In this study non-reversible restraint systems were assumed, hence this guideline is worth to be mentioned only as additional factor for future studies. It may be also relevant to mention that reversible restraint systems have currently a low penetration into the market.

3.1.3 Crash Severity Criteria and OLC

The vehicle's deceleration pulse is the design baseline for ride-down management. It is desired that the structural behavior of the crushable zones and the interacting structures maximize the energy dissipation by deformation hence minimizing the resultant pulse severity at the occupant cell. A structure-based criterion helps the design engineers to evaluate the performance of the structure and set the boundary conditions for ride-down management in each loadcase. Trigger times and load limiting will be designed and optimized based on the boundary conditions imposed by the pulse. This sub-chapter reviews a criterion for the characterization of crash pulses. This characterization defines subsequently a crash severity scale, which contributes as classification criteria to define the pulse selection for the simulations matrix in the chapter 4.

The deceleration pulse can be analyzed as six-degrees of freedom (DOF) acceleration field effective on occupants that influence the overall restraint system response. As abovementioned, this potential influence can be quantified using a pulse characterization criterion, which determines a "crash severity level" [92]. This metric help to define how "injurious-like" will be pulse for the occupants.

Based on the definition of Kuebler in 2008 [92], several types of crash pulse criteria can be defined:

Criteria Type	Criterion
Kinematic (calculated from pulse)	Maximum acceleration
	Time of maximum acceleration
	Time of dynamic crush
	Difference of velocity
	End time of crash pulse
	Average acceleration
	Sliding mean:
	SPUL: Specific crash-power (Kramer)
Dynamic System-modeled	Frontal Crash Criterion (FCC)
	Occupant Load Criterion (OLC)

Table 3.1 Crash pulse characterization criteria

Occupant Load Criterion (OLC)

Kuebler et al [92] run a correlation analysis with chosen pulse criteria addressed on the table above. A quantification of the correlation between criteria and occupant injury outcome was done. The simulation matrix (multi-body) was built based on a dataset of real USNCAP pulses from diverse brands, vehicle models, driver and passenger occupants. The HIC36 and Chest3ms were defined as injury criteria for the analysis. From this study, polynomial regressions for each pulse criterion were run and the root mean square (RMS) values for each regression were calculated:

Pulse Criterion	RMS			
	Driver		Passenger	
	HIC36	Chest3ms	HIC36	Chest3ms

OLC	51.33	1.81	50.75	1.40
FCC	53.21	1.81	51.41	1.41
Acc max, 3ms	133.42	4.05	139.36	3.19

Table 3.2 Correlation analysis of injury-outcome with pulse criteria as presented in [92]

The OLC, FCC and Acc max, 3ms were included. The evaluation of other pulse criteria as “Time of dynamic crush” and “SPUL” can be found in the paper. The OLC showed the best correlation with the simulated injury criteria. Based on this results, the dataset of crash cases in the chapter 4 will be classified by their respective OLCs. A short review on the basic concepts and assumptions of the OLC follows.

The OLC is a representation of the occupant dynamics as mechanical system. The analysis method consists of the following three phases (based on [92]):

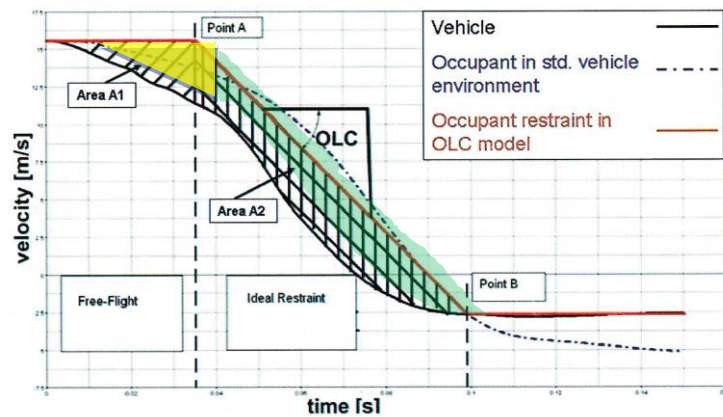


Fig. 3.7 Occupant Load Criterion (OLC). Diagram taken from [92] . Note the 65mm (yellow) and 235mm (green) areas

- (i) Start: The vehicle start decelerating at $t=0$ (Time of impact)
- (ii) Free-Flight: The occupant follows the trajectory of the movement relative to the vehicle with the original velocity until full engagement with the belt. This relative forward translation is assumed to be 65 mm (AREA A1) representing the slack of the restraint system. Before the engagement the restraint system forces on the occupant are assumed to be zero. The distance of 65 mm can be also understood as the distance until the restraint forces start to act significantly on the occupant's forward excursion.
- (iii) Ideal Restrained Ride-Down: When the 65 mm are reached, a complete engagement or coupling is assumed. A constant deceleration of the “ideally restrained” occupant starts until additional 235 mm (AREA A2) of forward excursion is reached. Note that the 300 mm (65 mm+235 mm) forward excursion is the total relative forward displacement of the occupant with respect to the vehicle. The slope of the velocity curve (dv/dt) of the occupant in this phase, also the deceleration, determines the OLC value in g (gravity). Note that the OLC value is independent of the occupant characteristics (mass, length, position etc) and it is only a function of the vehicle pulse.

The assumptions are:

- One-dimensional application of the force (in the crash direction / action of line)
- At the beginning of a frontal crash the restraint forces are negligible until 65mm
- 65 mm represents the slack of the restraint system
- After 65 mm the occupant will be “ideally” restraint
- 300 mm of total forward displacement represents implicitly an ideal vehicle where this excursion distance could be used for energy dissipation

Note that the ride down process is principally dependent on the first phase of the vehicle's pulse. A non-linear vehicle pulse with a hard deceleration at the beginning of the crash will reduce automatically the engage time (the 65 mm area remains constant) and theoretically will help reduce the ride-down deceleration, assuming the same time for occupant velocity = 0 in both cases. This means, a hard vehicle pulse in the first phase after $t=0$ may be beneficial due to a faster coupling of occupant to the vehicle.

3.1.4 Thoracic Injury Criteria: Review and Summary

Based on NHTSA's "Development of Improved Injury Criteria for the Assessment of Advanced Automotive Restraint Systems" [93] and [94]. The first steps to develop injury criteria for the thoracic region in aerospace and aeronautic application began with the famous sled test of the Colonel Stapp under high deceleration [93]. This work and posterior studies performed in the 60's in the US lead to the proposal of an injury limit value (pure acceleration-based) of 60g. Specific applications for the automotive industry (vehicle safety) complemented this "pure kinetic" approach with criteria for chest deformation, among others with the test published by Kroell et al. [70] [76] on hub impact test representing the contact between chest and steering-wheel in frontal crash. These studies opened the way to the first correlations between chest deflection and injury response, also the characterization of human thorax stiffness under different impact rates. The first "biocorridors" for chest deflection under impact were several times reviewed and reanalyzed. Based on Kroell's data, Neathery [78] proposed an injury reference value of 3 inches chest deflection that represented a 50% risk of thoracic AIS \geq 3 of a 50th percentile and 45 YO male. Subsequently revisions from Lau and Viano [95] reformulated the proposal of Neathery and ended with an injury reference value of 35% of chest deflection, which is supposed to be under the injurious threshold of multiple rib fractures and internal organs crushing. If applied to an average chest depth of 229mm for a 50th percentile male, the limit value reach 65mm. Another reference value, presented by Viano in 1977, suggested that after 40% normalized sternal deflection a contact sternum-thoracic spine would occur (Normalized chest deflection = Mid-Sternal Chest Deflection / Total Mid-Sternal Chest Depth).

With the massive introduction of shoulder belts, the focus of loading condition moved from impact to non-impact characteristics. This new conditions were addressed by Mertz [96] by the developed of injury risk curves for the H350 dummy by correlating the dummy's chest deflection measurements with rib fracture risk under reproduced real world accidents. Here the H350 injury risk values of 40% AIS \geq 3 by 2 inches chest deflection were proposed. New field analysis from Horsch derived in new injury risk values of 25% AIS \geq 3 for 40mm chest deflection of the H350. Later on other studies addressed the impact rates and chest deflection rates, where the biofidelity of the H350 under low chest deflection rates (2 to 3.5 due to airbag-driven loading) were criticized, leading to the concept that the H350 underestimate the chest deflection response under such airbag-driven conditions.

The National Highway Traffic Safety Administration (NHTSA) published in 1998 a Notice of proposed rulemaking (NPRM) [93] on new injury reference values and injury criteria based on a dataset of 71 PMHS test under "more" actual / relevant restraint condition (some of them already reported by Eppinger [97] and Morgan [98]). This dataset consist of sled test with five different [94] driver-restraint configurations (3-point belt, 2-point belt and knee bolster, airbag and lap belt, airbag and knee bolster, airbag and 3-point belt) and delta-vs from 23 to 56 km/h. For the posterior data analysis, the PMHS were instrumented with tri-axial accelerometers screwed to the T1 (first thoracic vertebra) and chest bands for the quantification of chest deflection. The chest deflection was calculated later for five locations on the anterior chest (upper left, center and right, lower left and right).

Injury criteria models (also called injury risk curves) were developed using logistic regressions based on the following risk factors (engineering values):

- T1 acceleration (a3ms)
- Maximum normalized central chest deflection (measured at the potentiometer location)
- Maximum normalized chest deflection of one of the 5 reference points
- Maximum chest velocity
- Viscous criterion

In order to determine the likelihood / predictability of the models a $-2\log$ -likelihood ratio was run and the P-values for each model were generated. The data was clustered as “injury” when the injury outcome of the test was an AIS3+ and “non-injury” when the outcome reached was \leq AIS3. The model with best goodness of fit and lower P-values was a linear combination of the T1-acceleration and the maximum deflection of one of the 5 reference points.

An interesting point out of this analysis is the fact (also mentioned in this reference [93] that in just ~25% of the sled test the maximum chest deflection was the one measured on the center of the chest. This could explain why this linear combination, using not only the central chest deflection but the maximum of the five reference points, predicts more accurately the injury outcome. These concepts will be used later on for the injury criteria development of the THOR dummy based on its multi-point chest deflection measuring devices.

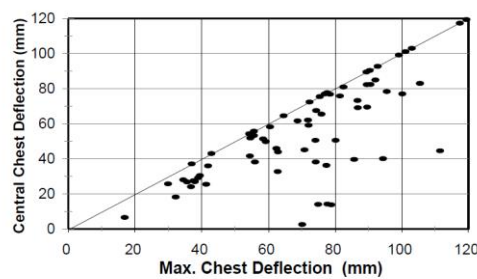


Fig. 3.8 Correlation central chest deflection vs. max. chest deflection [93]

Following the previous steps and using the best combination of injury factors, a CTI (Combined Thoracic Index) was developed to be used with the H350 but not before the dataset data was adapted making some simplifications as the offset of 6 mm [93] of the chest deflection data based on the assumption that the skin-fat deforms (compress) 6 mm before the real rib deflection takes occur.

$$CTI = \frac{A_{max}}{A_{int}} + \frac{D_{max}}{D_{int}}$$

Eq. 3.3

The CTI is a function of the acceleration outcome (A_{int}), acceleration limit value (A_{max}), chest deflection outcome (D_{int}) and chest deflection limit value (D_{max}). The limit values of acceleration and chest deflection when taken into independently (when the other is zero), show that in a condition of high acceleration (but no chest deflection) or vice versa (high chest deflection but no acceleration), the limits go beyond the current injury values defined in the FMVSS 208 for AIS3+ of the H350. Nevertheless, due to impracticable conditions of chest deflection in frontal crash with the H350 the limit values of 60G and 76mm (3 inches) were kept as shown in [93]. A remarkable limitation of the CTI is that no age-dependency factors are included. Note that the variability on the experimental data and the differences of the mechanical response of PMHS compare to living humans requires scaling methods when calculating the injury risk for a living population. Other studies [99] addressed that the injury outcome based on cadaver data has to be adapted based on the biological muscle tonus, bracing and in general muscle activation in crash. In some cases, this “adaptation” have been defined a priori. Citing [93] pp. 47: “Based on all these factors, the 50% probability of injury line (...) was adjusted to represent a 25% probability of injury level for the live human driving population. The adjusted probability of injury curve written in terms of CTI (...)”.

Lau et al. [100] published in 1981 experiments on anesthetized rabbits testing the impact-rate dependency of liver injuries. Under the same maximum compression, a correlation was found between velocity of impact on the rabbit’s liver and the magnitude of the injury. The experimental dataset served as base for the publication of a viscous criterion “VC” in 1985 [101]. The VC is a function of time product of the instantaneous impact velocity with the normalized instantaneous chest deflection. A diagram is shown below. [102].

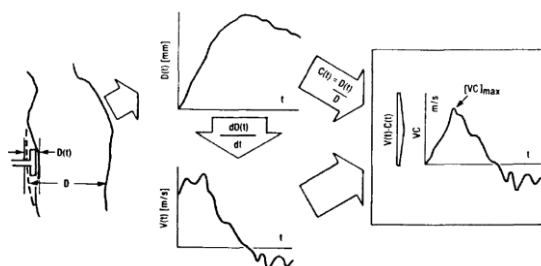


Fig. 3.9 Left: Viscous criteria development diagram [102]

The authors analyzed a battery of blunt impact experiments on PMHS done by Kroell et al. [70]. [71]. A reference value of $VC_{max} = 1$ m/s was proposed for a 25 % AIS4+ thoracic injury risk. A $VC_{max} = 1.3$ m/s was associated to a 50 % AIS4+. The AIS4+ injury risk curve was based on Probit analysis [102]. A range of validity was also defined. The VC_{max} prediction is applicable in a deformation rate range of 3 to 30 m/s. Typical chest deflection rates in frontal crashes varies approximately from 1 m/s to 8 m/s

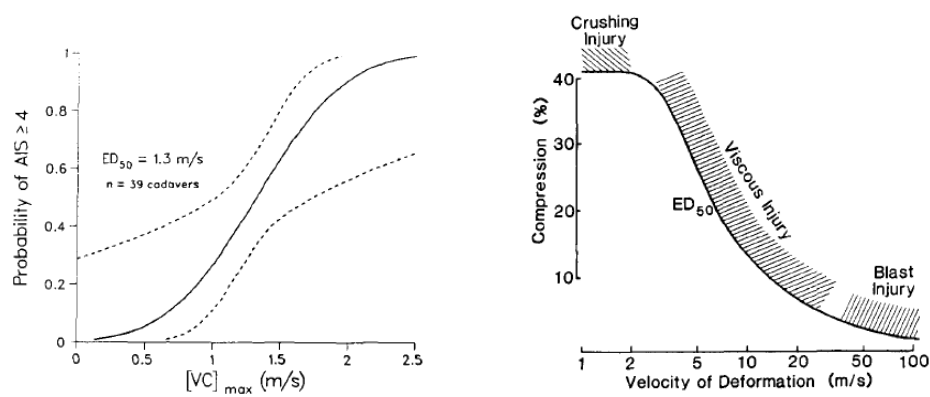


Fig. 3.10 Left: IRC AIS4+ based on VCmax. Right: Applicability range of the criterion [102]

More recent injury criteria

Another important contribution was made by Foret-Bruno et al. (1998) [103] where a field data analysis of 256 cases was carried out. Based on the evaluation of the load limiting effect at the shoulder belt on the injury outcome, four force-based thoracic injury risk curves including age-dependency were generated (Probability of AIS3+ thoracic injuries “P_chest(AIS3+)”):

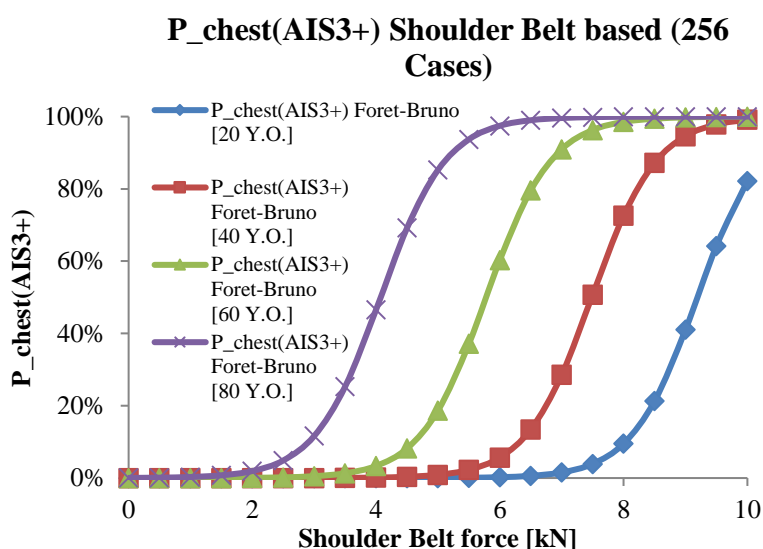


Fig. 3.11 Injury risk curves force-based with age dependency proposed by Foret-Bruno [103]

Other approach seen in the recent years is the development of new injury criteria dependent on the loading mode of a restraint system (belt- or airbag-driven). The concept in background is that the injury mechanism under shoulder-belt loading is not the same as under airbag loading. This implies that a discrimination between the contribution of both types of loading on the chest deflection is needed (in this case the H350's chest deflection). Mertz et al. (2003) [47], Kent et al. (2003) [104] and Laituri et al. (2005) [48] made the first steps presenting independent injury risk curves depending on the loading conditions.

Another one involves matched sled test of H350 vs. PMHS [104]. The dataset covered different restraint systems and acceleration pulse levels. An interesting finding of this analysis was that the measured chest acceleration (alone) could not discriminate the injurious or not-injurious outcome at an AIS3+ level. This is also supported by the study from Grosh (1985) [105] where contradicting trends were found when sled test with only-“belt-dominated” restraints were compared with matched “airbag dominated” test. The additional force induced by the airbag deployment leads to higher torso accelerations but also to a reduction of chest deflection. This is explained by the force distribution effect of the airbag. This means the airbag effect increase the torso acceleration but it does not imply directly that the thoracic injury risk will increase.

Following this restraint system discrimination concept, in 2003 Petitjean et al. [88], and in 2013 Trosseille et al. [106] presented a new injury criterion, the “Deq” (Equivalent Deflection) were the separated contributions of belt- and airbag-loading to the H350’s chest deflection generate a combined injury risk. The mentioned sample of Foret-Bruno et al. was used to build the injury risk curves of the belt-loading type whereas for the airbag-like loading the hub test sample from Kroell et al. [75] was used. The calculation process as presented in [106] can be summarized in a block diagram as follows:

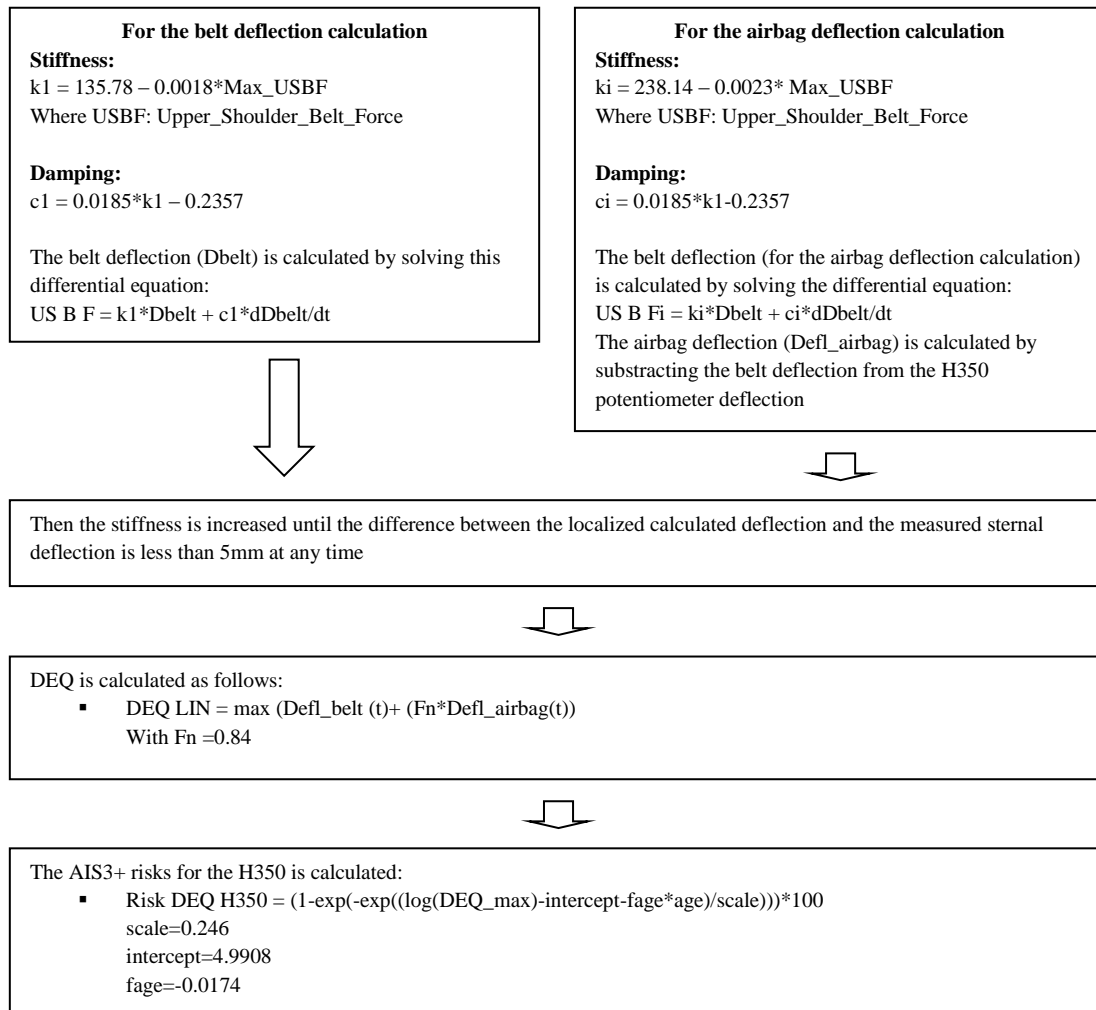


Fig. 3.12 Block diagram for DEQ calculation with the H350 [106]

In 2005 Laituri et al. [48] developed age-dependent thoracic injury risk curves for the H350. Two datasets including impacting- (blunt hub), non-impacting-loading and sled test with PMHS constituted the baseline for the analysis: The first one based on the publications from Kent et al. in 2003 [107] and in 2004 [60], Horsch et al. in 1988 [108] and the second from Kuppa et al. (1998) [109], Kallieris et al. (1995) [110] and Banglmeier et al. (2002) [111]. The two datasets consisted of $n = 153$ and $n = 86$ cases respectively. The injury outcome in this study was defined as the NRF (Number of Rib Fractures). The NRF definition in this study assumes, based on the concepts from Viano et al. (1977) [112] and Foret-Bruno et al. (1978) [113], an over-response of the PHMS in test condition of two or three more rib fractures than a living-human counterpart. A binary output was defined as “injury AIS3+” when $NRF \geq 7$ or “not-injury AIS3+” when $NRF < 7$. Note that the injury levels were defined based in the AIS Codebook from 1990, where the AIS3+ was defined as ≥ 4 rib fractures. The updated codebook definition from 2005 redefines AIS3+ when number of fractured ribs is ≥ 3 .

The following predictors were evaluated by Laituri et al. [48]:

- Age
- Normalized Sternal Deflection (UC)
- Combination of Age and Normalized Sternal Deflection (Transformed)
- Loading Type (Seatbelt or “others”)
- Gender
- Combination of gender and age (Transformed)

Two statistical methods, the Conventional Maximum Likelihood Method (CML) and the Modified Maximum Likelihood Method (MML) [48], were assessed using the Pearson Goodness-of-Fit (P-value) and Goodman-Kruskal (Gamma) methods. The generated models based on PMHS normalized sternal deflection (UC) were later transformed to use H350 chest deflection as independent variable. Therefore, matched test PMHS – H350 were analyzed. A correlation between sternal deflection from PMHS and H350s was done based on datasets reported by Kent et al. (2001) [114], Cesari and Bouquet (1994) [115] and Horsch and Schneider (1988) [108] for a total of $n = 20$. The UC correlated with the H350 chest deflection follows the equation:

$$\overline{UC} = 0.0583 * \delta_{H350}^{0.4612}$$

Eq. 3.4

The evaluation of prediction level of the methods was carried using estimated chest deflections for several speed changes from the Transport Canada (TC) and theoretical field models for each age group [48] based on NASS data. The best prediction level was reached with the MML using the second dataset and the data already transformed in H350 injury risk. Using the untransformed data (UC from PMHS), the following age-dependent injury risk curves were proposed by Laituri.

$$P_{\text{Thorax(AIS3+)}} = \frac{1}{1 + e^{-(12.5972 + 0.058614 \cdot \text{Age} + 26.90118 \cdot UC)}}$$

Eq. 3.5

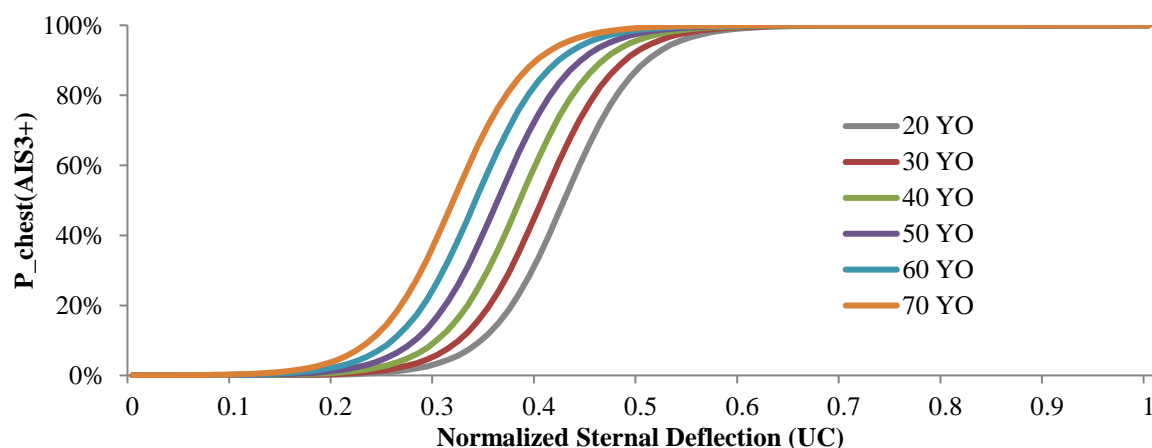


Fig. 3.13 Plotted age dependent injury risk curves developed by [48]. Applicable to PMHS.

A relevant assumption here is that model with the best fit based in H350 chest deflection data also correspond to the best fit using UC. Another interesting finding from this study is that no severe thoracic injury (AIS3+) was found if the normalized chest deflection was > 0.21 .

The above presented criteria present limitations in terms of method and assessment hardware. The predictors are reduced to chest kinematics and/or sternal deflection due to mechanical and sensing possibilities of the H350. New dummies (e.g. Thor) and the HBMs (Human Body Models) offer an extended mechanical output and consequently the possibility to analyze additional injury predictors such as multi-point chest deflection, individual rib strains, bending moments etc. In the THORAX Project [15] this topic was addressed. The project aimed for the development of thoracic injury criteria for the Thor dummy and HBMs. A noticeable development was the NFR criterion (Number of Fractured Ribs).

Based on [116], the NFR was developed based on FE simulations with the Humos2 and real test with the Thor dummy [117]. Matched test PMHS vs. Thor-NT of a representative dataset of frontal loading cases was analyzed. The test included frontal and oblique hub-, table top- and sled-test. The core dataset with $n = 59$ including 26 frontal and oblique impactor test, 9 airbag and inertial load test, 24 sled test. An extended dataset with $n = 71$ including 26 frontal and oblique impactor test, 9 airbag and inertial load test, 8 table-top test, 28 sled test. Some of the cases from this dataset were simulated with the Humos2 aiming for a better understanding of the injury mechanisms and the identification of injury criteria. Rib bending moments produced by anterior-posterior (AP) loading were identified as the principal injury mechanism for rib fractures. This concept was also supported by [65]. In this method, peak bending correlates with peak strain mostly happening on outer surface of the ribs and consequently with the failure (representing the fracture). This suggest that rib maximum strain as predictor for thoracic injuries. An inconvenient of choosing the maximum strain as injury criterion is the fact that higher strain in some specific ribs does not imply directly that the risk of additional rib fractures will increase. This could be defined as certain “independency” of fracture between ribs. In addition, this concept implies that the same injury outcome (e.g. three fractured ribs) could be achieved with different maximum plastic strain limits. This

“failure playground” is the backbone of this method allowing to tune the given measured strain of the Thor-NT ribs in order to best match the correct number of fractured ribs (NFR) found in the PMHS test. In other words, in this method the maximum strain limit (denominated dummy failure strain DFS) is optimized in order to reach the overall PMHS injury outcome from the real dataset, extracting from the matched test the number of ribs that reached the threshold level and using it as an injury predictor. For each case the rib strains of the Thor-NT were recorded and a correlation of PMHS-NFR vs. Thor-NFR was done for a given DFSs (e.g. 0.8%, 1.2%, 2% etc.). A linear correlation is assumed. The correlation quality is given by R^2 in the linear regressions. The best correlation analyzing the core and extended datasets was found with a DFS of 1.6%. The correlation of PMHS-NFR vs. Thor-NFR acts as a transfer function between the NFR from PMHSs as an injury predictor of NFR > 6 (AIS3+). Afterwards the data regression process (details not published) was run based on the injury binary outcome (two injury levels: <6 rib fractures and ≥ 6 rib fractures). A relevant point to mention is that the goal is to represent the number of real fractures and not the exact location of the fractures. From real testing is widely known that similar PMHS under the same loading conditions normally present very different injury patterns. Summarizing, the development process of the NFR (Number of Fractured Ribs) followed these steps:

- (i) Match of the PMHS dataset with Thor-NT test
- (ii) Extraction of the elastic strain histories of the Thor-NT ribs for each test
- (iii) Optimization of the best DFS to match the right PMHS-NFR for the datasets
- (iv) Data regression to generate the injury risk curve for NFR>6 (AIS3+) based on Thor-NFR injury criteria.

In 3.2.3 an adapted version of the NFR method will be applied as an assessment tool for the simulations with the Thums.

Injury criteria for sternal injuries

The mechanical function of the sternum is to maintain the stability of the rib cage acting as a closing of the rib rings 1st to 6th and protecting structure of the heart, aorta, vena cava and thymus gland, which are located just deep to the sternum. In addition, the sternum serves as insertion point of diverse muscles responsible for the movement of the arms, head and neck (e.g. sternocleidomastoid, pectoralis major, sternhyoid and sternohyroid). The causes for sternal injuries in vehicle collisions can be grouped as (i) contact of the chest with the steering wheel or dashboard in belted occupants due to restraint system malfunction, misuse or not use at all and (ii) seatbelt loading itself, so called 'safety belt syndrome [118] which is a typical injury pattern caused by seat belts in vehicle accidents [119] where the loads generated by the restraint system rise above the sternal injurious limits. It is known also that weakened bone in sternum (e.g. by ageing) may produce pathological fractures and contribute to increase the risk of sternal fracture in blunt loading [120]. However, differing from the extensive available data for rib fracture injury criteria, not much attention have been paid to define the injury mechanics and related injury criteria of sternal fractures. As an initial guess, the experiments published by Kerrigan et al. [64] served as reference to define injury reference values.

Bending moments perpendicular to the sagittal plane close to 20 Nm were set as initial guess, as a preamble for the injury reference limits proposed in 3.3.2.

3.2 Method: Thoracic Injury Assessment Procedures for HBMs

As shown in the last subchapter, the methods for thoracic injury risk prediction with the H350 are well established and accepted. Dummy-based metrics as spine acceleration and chest deflection are correlated with specific injury risk values. The correlation is achieved by statistical methods where real test binary data (injury, no-injury) is modeled via regressions. Such standardized assessment methods do not exist currently for the interpretation of HBMs simulations. Following the review on current “dummy-based” thoracic injury criteria, an injury assessment method for HBMs was developed in the framework of this dissertation. This method attempts to rate automatically thoracic injury risks with HBMs. Age dependency was also addressed. The method development involved custom automatic post-processing tools in order to assess automatically HBMs simulation results. Condensed under “HUMAT” (**H**Uman-**M**odels-**A**ssessment-**T**ool), these tools generate automatically an estimation of skeletal thoracic injury risk per simulation, in an attempt to run a direct comparison with the calculated injury risk predicted by a H350 under the same loading conditions. The analysis was divided in two modules: (i) Rib fracture- and (ii) sternum fracture risk. The identification of the injury mechanisms for each module and the injury risk reference values were addressed in this study. The validation of the mentioned tools involves a comparison with the injury results of eight PMHS sled test [81]. The method followed five steps as explained below.

3.2.1 *Split of analysis: Rib fractures (AIS3+) and Sternal fractures (AIS2)*

The prediction of sternal injuries is the final goal. Realistic boundary conditions for the mechanical interaction between sternum, ribs and costal cartilage has to be ensured. A reasonable injury evaluation of the ribcage helps creating a realistic injury environment for the evaluation of sternal fracture risk. Therefore, the current method splits the analysis in AIS3+ (rib fracture based) and AIS2 (sternal fracture based)

3.2.2 Identification of injury mechanisms for ribs and sternum

Injury mechanism for rib fractures (AIS3+)

HBM offers significant advantages for thoracic injury assessment by simulating realistically rib cage deformations. Simplifications like correlation by a single metric with the injury risk (e.g. H350 single point chest deflection) may not be the best method to follow due to the fact that the same chest deflection could be reached under two different rib cage deformation patterns. Two rib cage deformation patterns imply by definition two different injury risks. A realistic rib cage deformation leads to represent realistically the injury mechanisms. In frontal vehicle collisions, anterior-posterior (AP) loading represents the typical condition where the occupants sustain rib fractures.

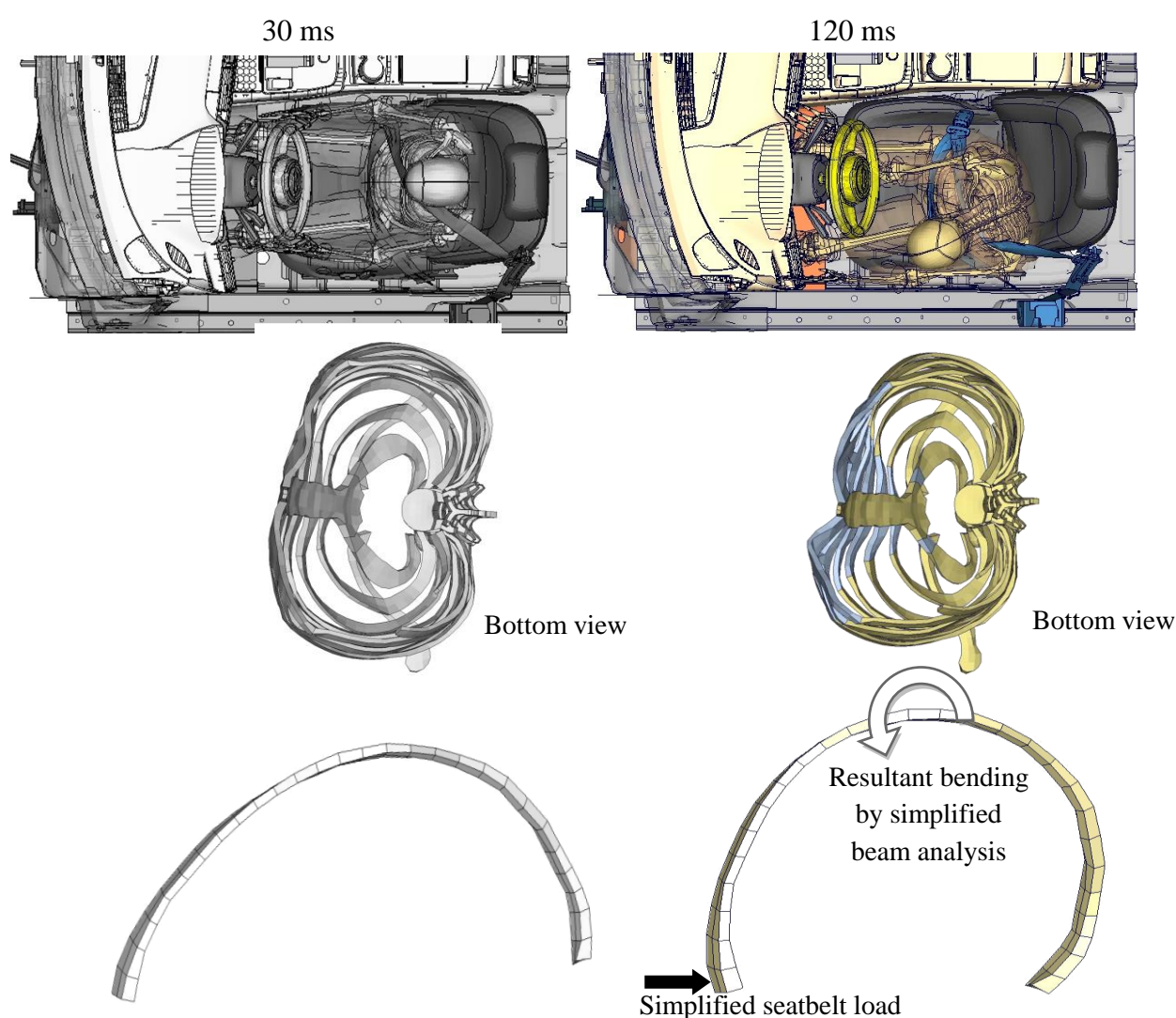


Fig. 3.14 Gray: Undeformed ribcage and 7th rib. Bony color: Ribcage and 7th rib under bending due to seatbelt loading. Simplified representation of the loading configuration involved in an oblique crash

These loading conditions have been explored by Charpail et al. [65] by testing PMHS isolated ribs under controlled conditions (see 2.1.4.2.2). The fracture is generated, as expected, by bending. However, note that the boundary conditions of the rib-ends at the potting points used by Charpail introduce an implicit error due to the unrealistic representation of the costal cartilage and costo-vertebral joints. Another example to illustrate the rib bending was addressed in the THORAX Project (unpublished), where the Humos2 was used to analyze the strain patterns on the ribs under seatbelt loading. Transversal and longitudinal strain time histories were compared and concluded that the phenomenon is clearly dominated by the longitudinal component (along the outer side of the rib), typically associated to the strain pattern in bending.

Injury Mechanism for sternal fractures (AIS2)

Continuing with the description of the section 3.1.4, the causes for sternal injuries in vehicle collisions can be grouped as (i) contact of the chest with the steering wheel or dashboard [23] and (ii) seatbelt loading, denominated also “safety belt syndrome” [118] which is a typical injury pattern caused by seatbelts in vehicle accidents. The safety belt syndrome involves excessive loads generated by the restraint system that rise above the sternal injury limits. Age dependent factors as osteoporosis and cortical thickness reduction can also increase the risk of sternal fracture in this type of loading [120]. Khoriaty et al. [121] also mentioned that the principal sternal injury mechanism is associated with deceleration and blunt chest trauma. The study published by Shaw et al. [122], also cited by Kerrigan et al. [64], suggest that the injury mechanism for sternum fractures under restraint system loading is bending. The stability of the thorax decreases significantly with sternal fractures [123]. Apart from the experiments published by Kerrigan [64], just few data is available for mechanical analysis of the sterna under seatbelt loading. This limitation can be partially overcome by considering HBM simulations. Specifically, the author proposes to consider the table-top (belt loading) and GS1 sled test loadcases from the validation pool (see 2.1.4) as their similarity to real restraint-system loading is evident. In addition, for both loadcases the PMHS injury outcome was documented and published, being the table-top non-injurious and the GS1 injurious in terms of sternal fracture. This difference suggests that comparing the mechanical behavior of the sterna in each loadcase more information will be available to elucidate the injury mechanisms involving sternal fractures.

In order to run the analysis an additional pre-processing was necessary to facilitate the data collection. Five sensors to record three-axial forces and bending moments were defined on the sternal inter-costal-spaces of both Thums-original and Thums-elderly models. Section forces cards from VPS were used. Coordinate systems were created at each section force. The X axis was orientated along the longitudinal sternal axis while the Y axis was set perpendicular to the sagittal plane. For comparison purposes the results were reduced to the inter-costal spaces two and three as long as the highest loaded area by the seatbelt matches one or both locations.

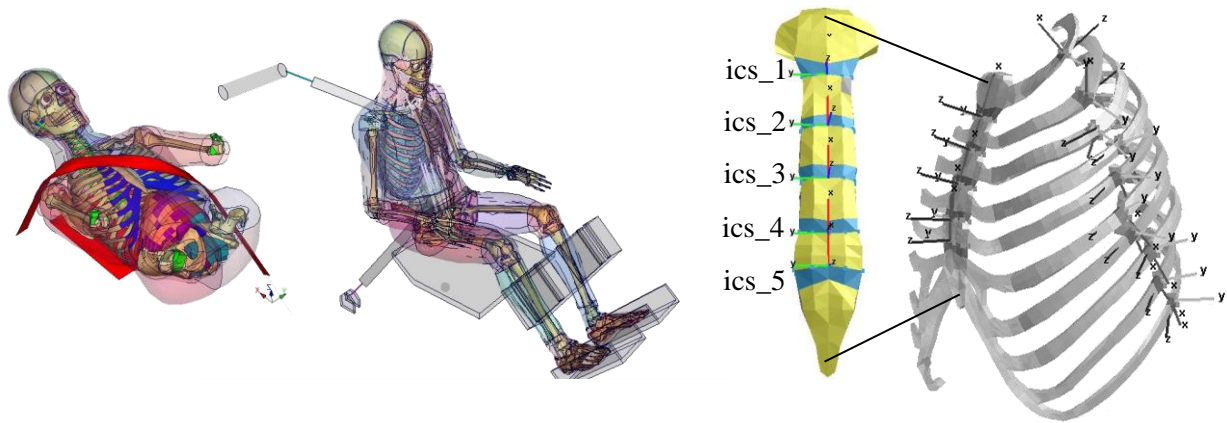


Fig. 3.15 Left: Table-top (belt loading) and GS1 as test loadcases for the injury mechanism analysis. Right: Bending moments measurement locations at the inter-costal spaces (ics) via section-force cards in VPS

The results of the analysis are shown in 3.3.2.

3.2.3 *Correlation of the injury mechanism with injury reference values with and without Age-dependency (Ribs)*

As mentioned in 3.1.4, the NFR method developed for the Thor dummy proposes a direct correlation between AIS3+ thoracic injury risk and the NFR-Thor values generated after the parametric study on maximum DFS (Dummy Failure Strain). By using this correlation as a baseline with the Thums models it would be possible to have an estimation of the AIS3+ thoracic injury risk directly with the HBMs. The first assumption in order to use this method with the Thums_original and Thums_elderly, is that the correlation PMHS-NFR with the Thor-NFR is similar to the correlation PMHS-NFR with Thums_original/elderly-NFR. Future work should cover a complete reconstruction of the THORAX-Project datasets (n = 59) with the Thums models, in order to verify this correlation.

Correlation / Custom weighting for rib fractures (AIS3+)

Differing to the definition on the NFR-Thor based on the maximum strain values on the ribs, the NFR-Thums is proposed to be based on the maximum bending moments under anterior-posterior loading (AP Loading), as defined on identification of the injury mechanism. This method aims for:

- (i) Robustness: By avoiding the simulation artifacts as concentration of the maximum stain values on the costo-vertebral joint region due to inaccuracies on the joint modeling.
- (ii) Transparency: A simple mechanic response per rib that represents the real injury mechanism will reduce the complexity of the analysis in a multi-dimensional design process (Dimensions understood as loadcases, restraint system deployment strategies and age dependency).

The following plots show the time histories of the bending moments on each rib (3rd to 10th) under simulated AP loading. The simulations were performed for both Thums-original and Thums-elderly. The differences of the response of the Thums-original and Thums-elderly are implicitly generated by the different cortical thickness distribution (see 2.2.4.2.2).

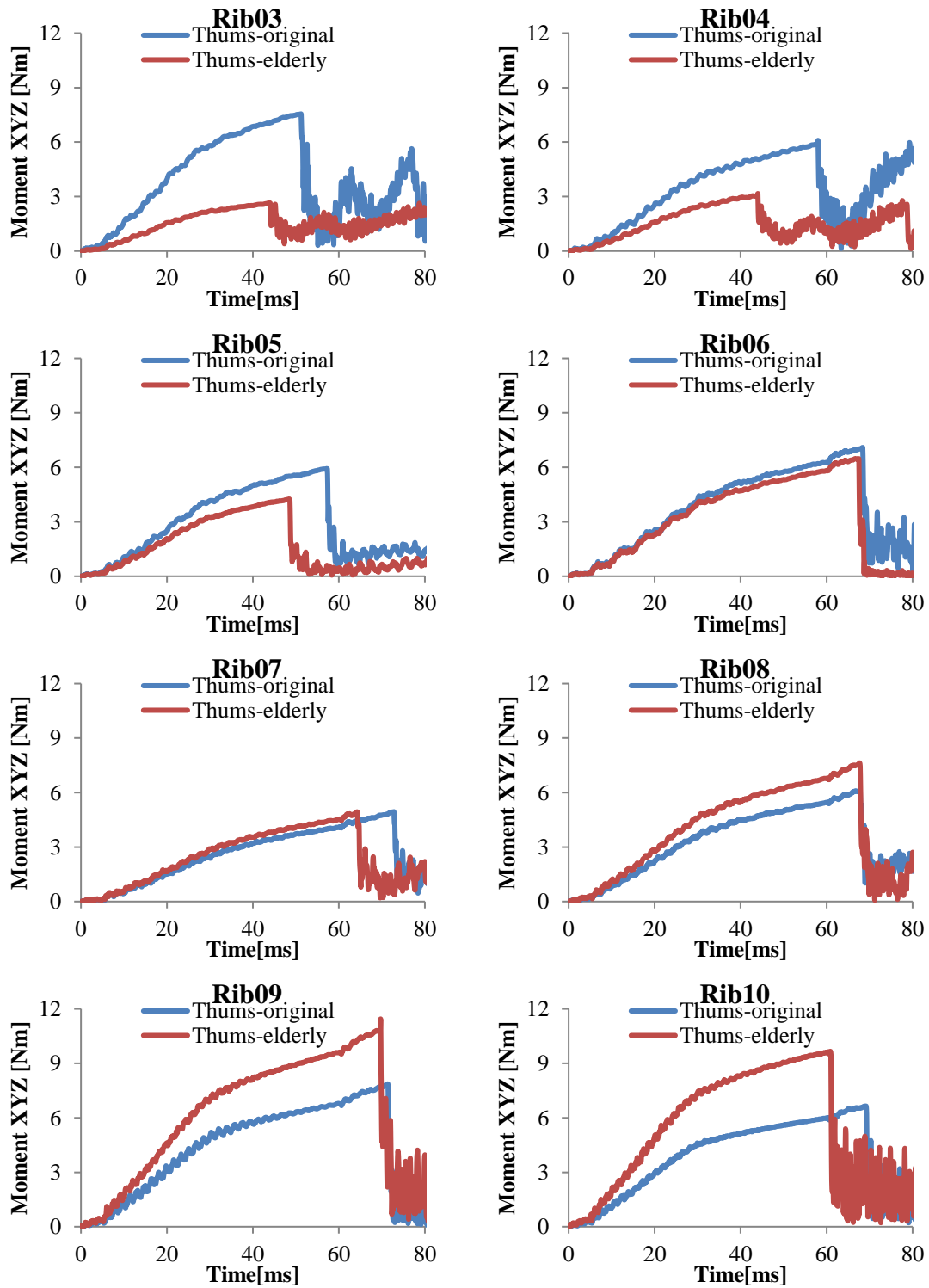


Fig. 3.16 Bending moments per rib level under AP loading

The time histories are extracted from the typical arch-region per rib were the bending moments reach the maximum values in a frontal crash. The section locations (VPS cross section cards element-node based with output on local coordinates) are shown below.

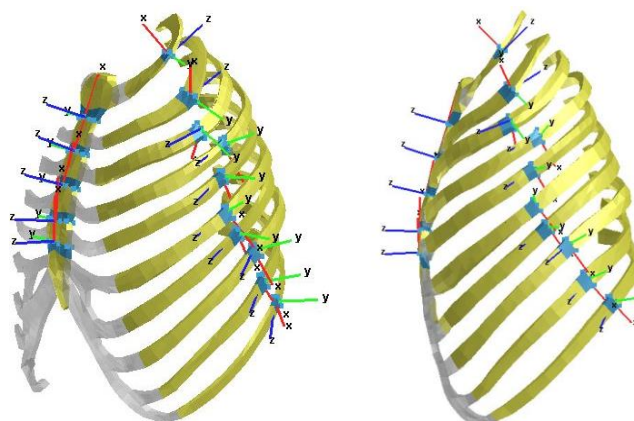


Fig. 3.17 Location of the section forces and coordinate systems for bending output

It was assumed that the maximum bending take place in one specific arch of each rib. The selection of a single measuring per rib simplifies the analysis of the simulation matrix presented into the chapter 4. Although this simplification could miss the real maximum bending moments, the difference between the real peak value and the measured bending is assumed to be under 5%, based on observations in different loadcases and directions in a typical frontal crash simulation.

The peak bending moment of the ribs is defined as the bending value when the failure strain threshold in one element (cortical layer) is reached. Note that the failure strain of the cortical bone (modeled by shells, 5 integration points, constant thickness in the Thums-original, variable thickness in the Thums-elderly, material elastic-plastic 103 VPS) remains constant at 1.8% in both models. Maintaining this plastic strain threshold ensures that the differences of the pure AP bending response of the ribs between Thums-original and Thums-elderly are only the result of the variable cortical thickness distribution of the Thums-elderly. The cortical thickness distribution in the Thums-elderly is one of the age-dependent factors proposed in this dissertation.

The measured peak bending moments are used as limit values for the generation of injury reference curves per rib. Logistic functions were used. At the time of the development of this method, no studies were found (to the author's knowledge) where a statistically relevant correlation of AP rib bending with a risk of fracture per individual rib was determined. Neither a correlation including age dependency factors for each rib. In order to define the factors (β_0 and β_1) of the logistic equations for the injury reference curves an example for the behavior of human bones under bending loading was needed. Kennedy et al. published in 2004 [124] a study on femur dynamic bending (including superficial soft tissue) on a dataset $n = 45$ PMTO, fracture risk curves were generated for normalized cross sectional area and inertia. The observations on the resultant injury risk curves for a 50th percentile male group suggest that 50% of the fracture risk correspond to one half of the maximum bending moment. The assumption based on these observations is that the ribs in AP loading will have a 50% of fracture risk at approx. 50% of the maximum bending moment. Future work should

prove this assumption specifically for ribs in AP loading. The β_0 and β_1 values were selected the abovementioned assumption match the 50% of the “reference” risk at around one half of the maximum moment per rib. For lower ribs (8th, 9th and 10th) it was noticed that high values of bending were reached already in an early stage of the loading. For those higher reference risk value was assumed. The factors and reference curves are shown below.

	Thums-original		Thums-elderly	
	β_0	β_1	β_0	β_1
Rib 3	-11	3	-6	4
Rib 4	-6	2	-6	4
Rib 5	-6	2	-5.5	2.5
Rib 6	-10	3	-9	3
Rib 7	-5	2	-4.5	2
Rib 8	-8	3	-12	3
Rib 9	-10	3	-15	3
Rib 10	-9	3	-9	3

Table 3.3 Regression parameters for the reference curves

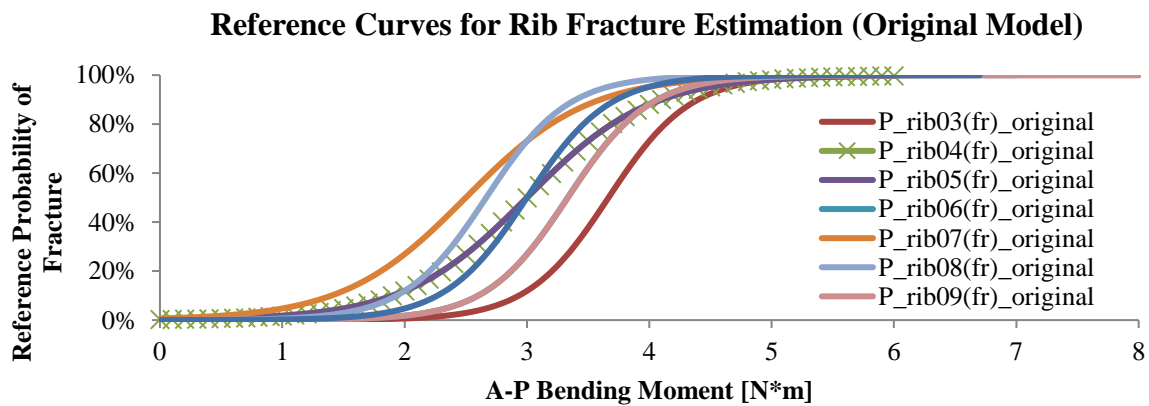


Fig. 3.18 Reference risk curves for Thums-original.

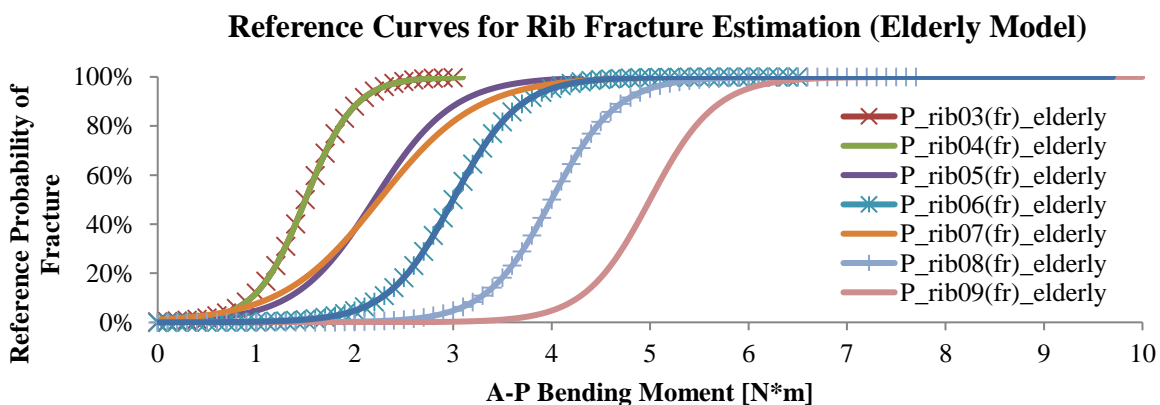


Fig. 3.19 Reference risk curves for Thums-elderly

The reference curves attempt to create a link between a local injury criterion as rib bending with

a global injury criterion as the NFR (in this case applied to the Thums models). The reference curves weight the contribution of each rib to a Thums-NFR value (e.g. zero bending moment in all ribs will generate a Thums-NFR equal to zero and 100% bending in all ribs will generate a Thums-NFR equal to 24. This assumption attempted to represent a virtual “fracture probability” per rib. It is recommended to review the reference curves when new experimental data allows to generate individual- and age-dependent injury risk curves for AP loading. Summarizing, bending is a local criterion, needed to generate a quantifiable global criterion “Thums-NFR”. This specific value correlates in turn with a thoracic injury probability AIS3+.

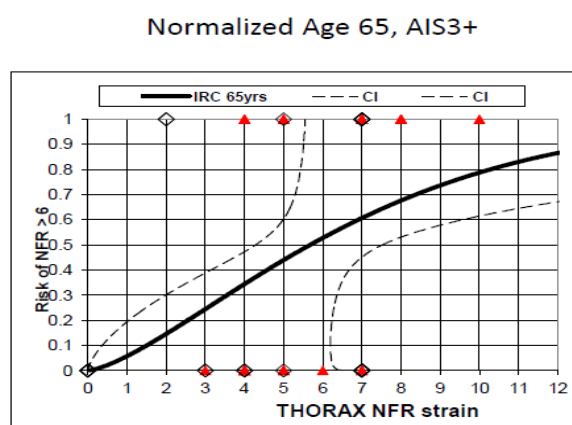


Fig. 3.20 Injury risk curve for NFR>6 (AIS3+) from the core dataset [116]

Note that the reference curves were generated for the ribs 3rd to 10th. This is based on three facts:

- (i) The first two rib and the ribs 11th and 12th are rarely fractured in frontal crashes
- (ii) The bending moments of the ribs 11th and 12th are decoupled of the rib cage deformation, whereas there is not mechanical link with the sternum
- (iii) After analyzing the bending response of the 1st and 2nd ribs models, uncertainties regarding the morphological accuracy aroused

The above mentioned facts motivated a slight correction of the eight contributing ribs from the Thums-original/elderly to the seven contributing rib of the Thor. As an example, a Thor-NFR equal to 1 correspond a Thums-NFR equal to 0.875.

The injury risk curve NFR-based was generated for the average age (age at time of death) of the PMHSs in the core dataset (65 YO) after normalizing the data by chest deflection, impactor speed and PMHS mass. Recapitulating, age dependent factors were then addressed in two levels: (i) direct on the mechanical response of the ribs in AP bending (for maximum bending values and the injury reference curves) and (ii) the correlation with the global thoracic injury risk curves from the THORAX Project specifically for elderly. A one-pager diagram is showed in 3.3.3.

Despite the presentation of the final elderly-IRC at the project's final workshop [116], the development process is still under debate. However, the method represents the state of the art of the combined application of a HBM and currently the most biofidelic dummy in frontal crash (Thor) where individual metrics per rib that analyzed as a whole system to generate a global injury risk.

3.2.4 Energy Plots

The kinetic energy of the full body and internal energy of the sternum PIDs (HBMs) are included into the simulation results for each case in the chapter 4. This contributes to quantify the amount of energy dissipated by deformation in of both sternal cortical and trabecular layers.

3.2.5 Comparison to the H350

A comparison of thoracic injury risks between HBMs and H350 makes only sense on an injury probability level. Direct comparison of engineering values (e.g. spine accelerations or uni-axial chest deflections) are a simplification that should not be considered. For the simulation matrix in the chapter 4, H350's chest deflection was taken as input parameter for AIS3+ thoracic injury risk. Current USNCAP injury risk curve (IRC) developed by Laituri et al. was utilized [48].

$$P_{\text{chest(AIS3+)}} = \frac{1}{1 + e^{[(10.5456 - 1.568(\text{Chest deflection})^{0.4612})]}}$$

Eq. 3.6

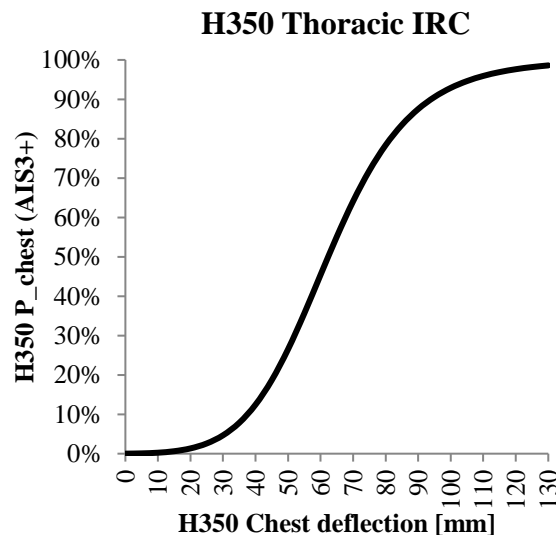


Fig. 3.21 Current H350 USNCAP thoracic injury risk curve

3.3 Results

3.3.1 Restraint System Variants for Simulations (as result of design guidelines)

Following the concepts presented in 3.2, four restraint system variants are proposed in an attempt to crystallize the design guidelines into concrete restraint system configurations. Approached as a whole system, the injury outcome assessed by ATD models or HBMs is the result of the interaction of the restraint components. This interaction is mastered by trigger times, seat belt load limiting and airbag performance (deployment, mass-in, mass-out, leakage etc). The configuration of the restraint variants was outlined by (i) the definition of an adequate pretensioner configuration and, (ii) a first guess on the benefit of load limiting and airbag deployment in the ride-down phase.

Belt Pretensioning

The belt pretensioning is normally activated few milliseconds after the crash. The target is to ensure an optimal occupant coupling with the initial vehicle deceleration by minimizing the belt slack. This phase is dominated by the pretensioner trigger time (Belt_TTF). As defined by [125], the pretensioning can be achieved under different configurations, the most common are:

- Retractor Pretensioner
- Buckle Pretensioner
- Anchor-Point-Pretensioner
- Combination of the above mentioned configurations

The effect of different pretensioning configuration was studied under controlled sled conditions by Zeller [125] (see Table 3.4). The study included mid-sized sedan crash pulses from USNCAP and Euroncap real test with a H350 in passenger position. Restraint components were delivered by Autoliv. The effectiveness of the individual- and combined effects of the pretensioner configurations were rated here in terms of chest forward displacement (see table below). Only USNCAP data were used as the forward displacements were noticeable larger.

Pretensioner Type	Effectiveness
Retractor	++ (280 mm – 300 mm)
Buckle	++ (280 mm – 300 mm)
Combined	+++ (260 mm – 279 mm)

Table 3.4 Rated effectiveness of pretensioner configurations

Note that the higher effectiveness is achieved by the combined variants. However, for analysis simplification and clearness purposes, a single pretensioner at the retractor was chosen for the simulation matrix in the chapter 4. Future work should include additional pretensioner combinations into the simulation matrix presented in the sub-section 4.2.1.1.

Ride-Down

In this phase, the load limiter at the retractor (LLim) keeps the shoulder belt force up to a pre-defined level (current restraint systems use around 4 kN) during the forward displacement of the occupant. As explained in the section 3.1.1 “Principles, Functions and Components” the force limiter controls the ride-down of the occupant by dissipating the occupant kinetic energy along the available forward space in the occupant cell. The belt load limiters can be triggered by convenience in the ride-down phase, in order to achieve the restraint guidelines mentioned in 3.1.1. The mechanical interactions in the sub-system (pretensioner) influence the belt pay-out process (film spool effect, webbing stretch, friction properties among others). In the simulation models, the parameters that control these phenomena were kept constant for all simulated cases. The airbag deployment generates benefits by load sharing with the belt and a wider force transfer area to the anterior chest, while the airbag’s vents deployment ensures the energy dissipation by mass outflow.

Variants

The study case showed the benefits of early coupling, restraint loading reduction and load sharing in terms of chest deflection reduction with the H350 model. The following table summarizes the restraint system triggering variables and load limiter values proposed to be applied for the simulation matrix in 4.1.1.8

Parameter	Meaning	Range
Belt-TTF	Trigger Time Belt Pretensioner	≥ 10 ms
AB-TTF	Trigger Time Airbag	≥ 10 ms
LL-TTF	Load Limiter Deployment Time	\geq Belt-TTF ms
LL1	Load Limiter level 1	3.5 kN (Base)
LL2	Load Limiter level 2	LL1 to 1.85 kN
LL3	Load Limiter level 3	LL1 to 1.00 kN
LL4	Load Limiter level 4	LL1 to 0.60 kN
AB-Vent-D	Airbag Vent Deployment Time	\geq AB-TTF ms

Table 3.5 Restraint System Parameters for deployment strategy used in this study

Trigger times were combined with load limiters guided principally by the strategy “maximization of forward excursion and applied force under the tolerance levels of the occupants”. The crash cases presented in 4.1.1.9 and 4.1.1.8 were simulated under four restraint variants following the mentioned strategy. Please refer to 4.1.2 for an example of the effect by applying the strategy to a real-world accident case. Slight variations of the parameters have been applied in order to fulfill the design guidelines proposed in 3.1.2.1. Although the guidelines do not have a quantitative meaning due to the variability of the loadcases, the following table depicts the most relevant relation between parameters and restraint function

Parameter	Triggering strategy defined by
Belt-TTF => 10ms	<ul style="list-style-type: none"> -Technical state of development for acceleration- and deformation-sensor signal processing -Maximization of the application time of the restraint loading -Maximization of forward excursion -Minimization of deformation, deformation rate and accelerations
AB-TTF	<ul style="list-style-type: none"> -Maximization of the application time of the restraint loading -Ensuring the fastest load-sharing belt-airbag -Minimize yaw rotation
LL-TTF	<ul style="list-style-type: none"> -Maximization of the application time of the restraint loading -Maximization of forward excursion -Maximization of the restraint force BUT under the tolerance levels of the occupants -Minimization of deformation, deformation rate and accelerations -Avoid submarining -Maximizing belt force on the shoulder region by torso forward pitching -Minimize yaw rotation -Conservative design
AB-Vent-D	<ul style="list-style-type: none"> -Maximization of the application time of the restraint loading -Maximization of forward excursion -Maximization of the restraint force BUT under the tolerance levels of the occupants -Maximization of the restraining force distribution -Minimization of deformation, deformation rate and accelerations

-Avoid submarining
-Maximizing belt force on the shoulder region by torso forward pitching
-Minimize yaw rotation
-Conservative design

Table 3.6 Relation restraint parameters and design guidelines

Underlining the strong dependency of the ride-down management and the crash pulse, the following diagram shows the correlation between OLC (normalized) and trigger times (normalized) of some of the crash cases shown in 4.1.1.8. Two restraint system variants “A” and “B” are used to depict the triggering changes.

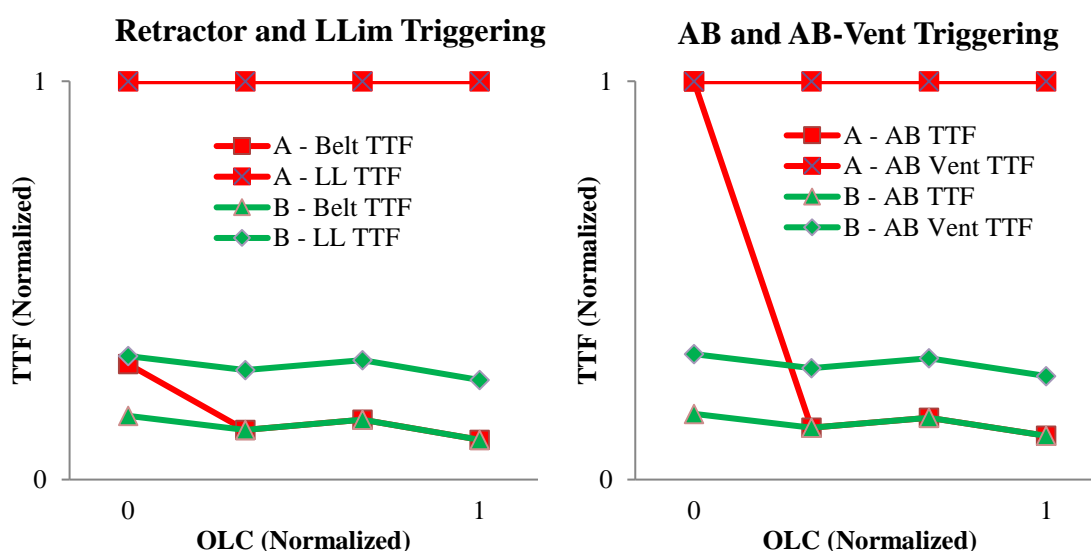


Fig. 3.22 Example of different triggering strategies (A vs. B) for some of the crash cases of the chapter 4.

Note that the triggering strategies have also different load limiting levels as shown in the Table 3.6. The parameters Belt-TTF, LL-TTF, AB-TTF and AB-Vent-TTF are individual for each loadcase.

3.3.2 Sternal Injury Mechanism and Injury Reference Value (IRV)

Developing the analysis under table-top and GS1 conditions proposed in 3.2.2, the results are presented as follows. For clearness purposes, the following table contains the abbreviations used for the post-processing:

Abbreviation	Meaning
T-Top	Table Top (belt loading)
GS1	Gold-Standard-I Sled
orig	Thums-original
elde	Thums-elderly
ics	Sternal inter-costal space
FX	Force in X (local coordinate System)
FY	Force in Y (local coordinate System)
FZ	Force in Z (local coordinate System)
FXYZ	Resultant force
MX	Bending moment in X (local coordinate System)
MY	Bending moment in Y (local coordinate System)
MZ	Bending moment in Z (local coordinate System)
MXYZ	Resultant bending moment

Table 3.7 Abbreviations

The following table shows the sterna deformation in both cases (sagittal view):

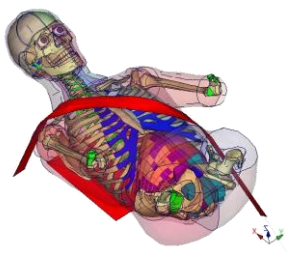




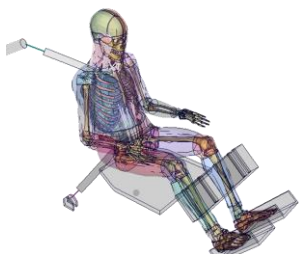




		Loading			
		25 %	50 %	75 %	100 %
Table-Top					
GS1					

Table 3.8 Sternum bending in table-top belt and GS1

The following plots show the differences in sternal loading for both loadcases.

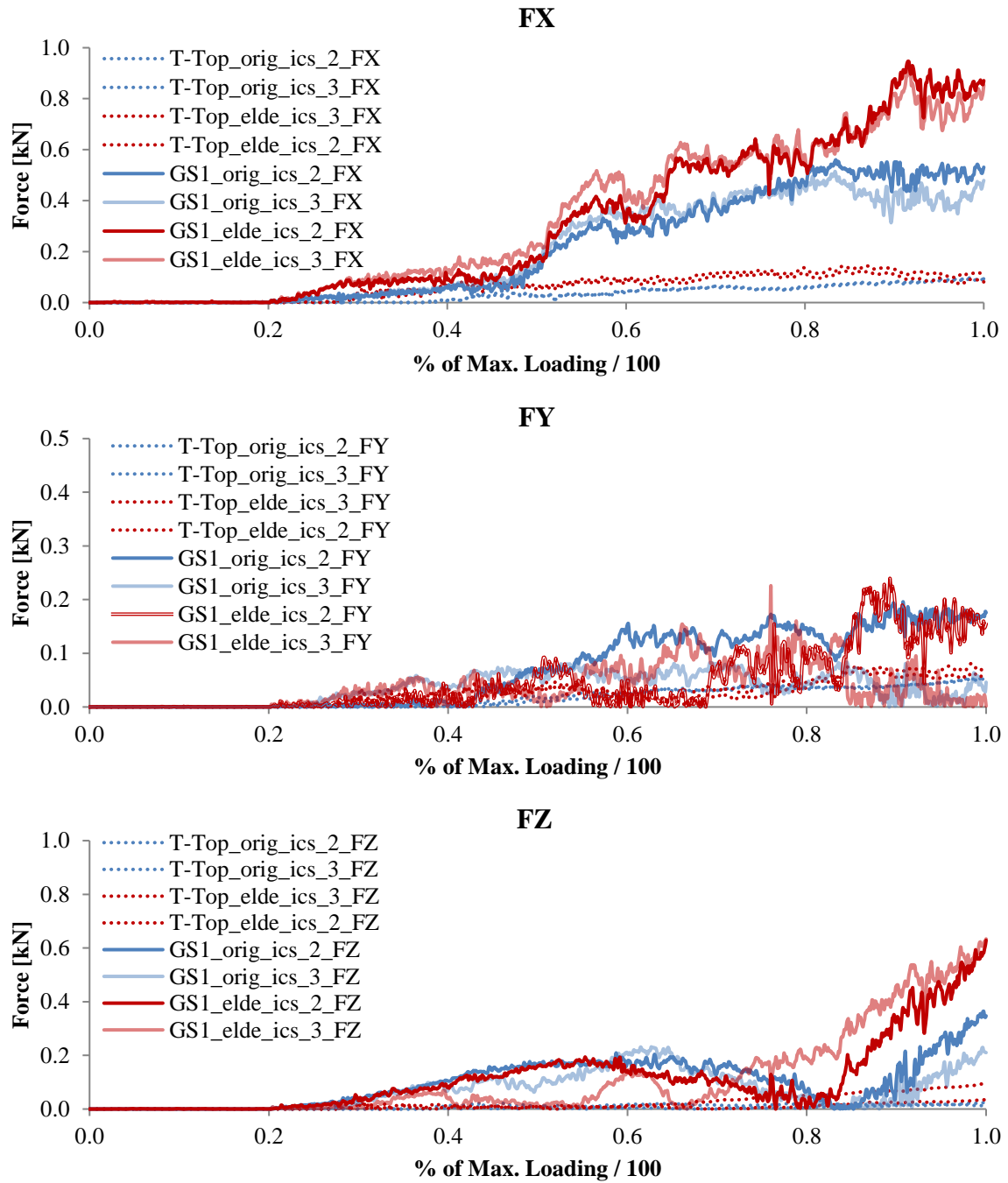


Fig. 3.23 FX, FY and FZ for both Thums-original (orig) and Thums-elderly (elde) in Table-top (dotted line) and GS1 (solid line)

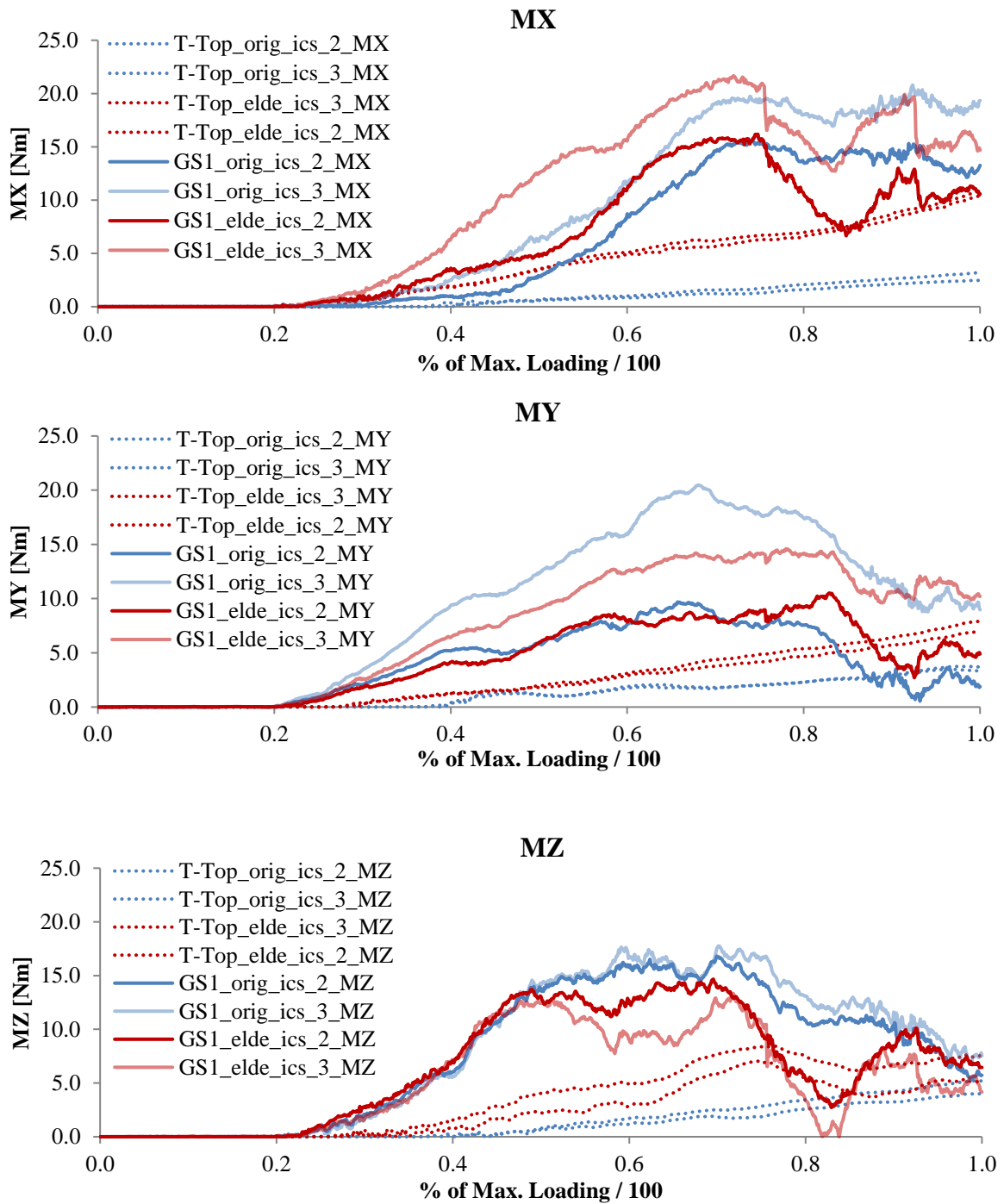


Fig. 3.24 MX, MY and MZ for both Thums-original (orig) and Thums-elderly (elde) in Table-top (dotted line) and GS1 (full line)

As shown in the plots above, the loading phase for both loadcases was normalized based on the 20% chest deflection limit defined in [60] and observation of the loading level and chest deflection in the GS1. The differences in forces and bending moments between Table-top and GS1 loading are summarized in the following diagram and defined for each sensor as “absolute loading difference”:

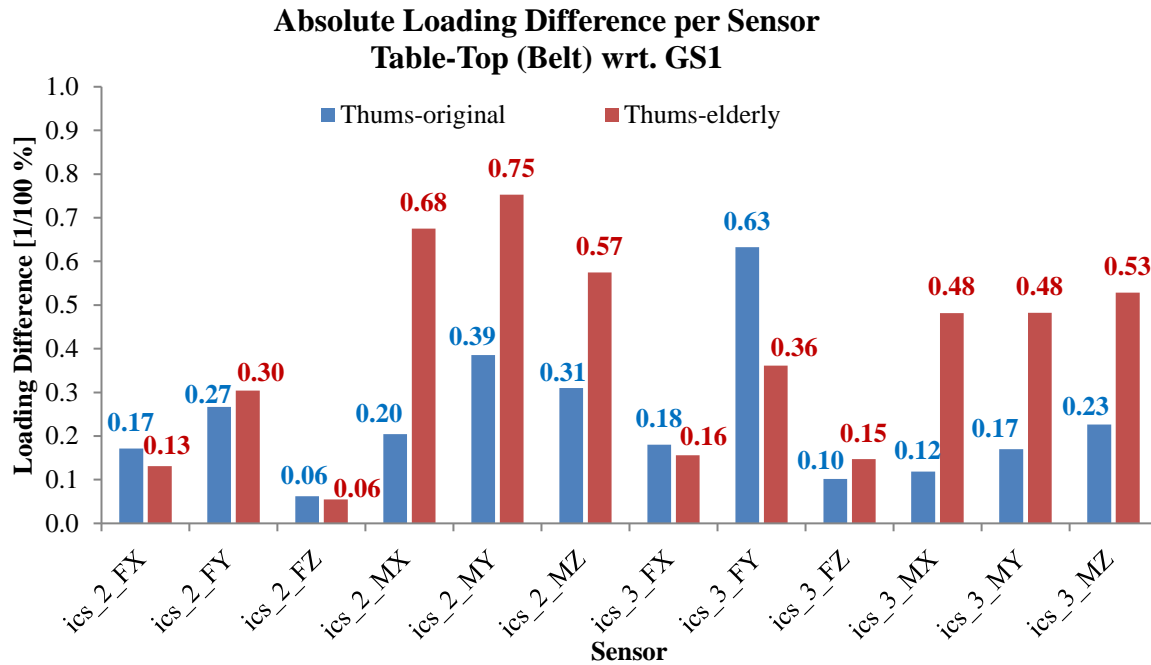


Fig. 3.25 Absolute-loading-difference comparison for all ics_2 and ics_3 in Thums-original and Thums-elderly

The Fig. 3.25 shows that the highest absolute-loading-differences are generated by the bending effect of the seatbelt loading. Note for the Thums-elderly the three loading directions measured on ics_2: 68 % (MX), 75 % (MY), 57 % (MZ) compared to 13 % (FX), 30 % (FY), 6 % (FZ) absolute-loading-difference. These results and the deformation patterns of both cases suggest that the risk of sustaining a sternal fracture better correlates with bending.

Sternal fractures and hypothesis of twisting effect in inertial loading

A correlation between resultant bending moments on the sternum and twisting is proposed here. Ribcage twisting is related with asymmetric loading, e.g. seatbelt-dominated. An increased risk of sternal fractures it's supposed due to a tri-axial bending effect on the stress tensor of the elements in each ics. In addition, age dependent factors e.g. costal cartilage calcification are supposed to increase stresses on sternum due to a higher force transfer from the rib to the sternum dissipating less energy by cartilage deformation. Note also the higher absolute differences in bending are found in the Thums-elderly ics_2 (68%, 75% and 57%) compared to ics_3 (48%, 48% and 53%). The same trend was found with the Thums-original.

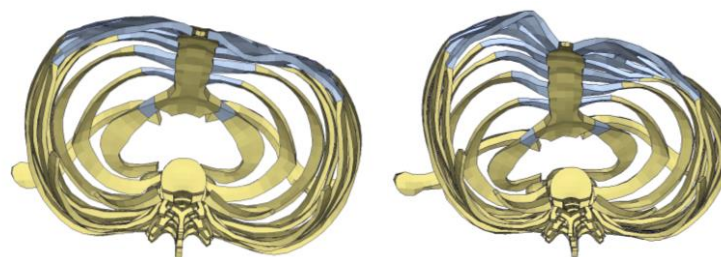


Fig. 3.26 Ribcage's bottom view to illustrate twisting under the same loadcase but different restraint.
Left: AB dominated loading. Right: Seatbelt dominated loading

The last observation suggests a correlation of the ics_2 resultant bending moment and ribcage twisting. This point will be addressed again with the analysis of the simulation matrix in the chapter 4. Other studies addressed the twisting effect of the ribcage by analyzing the chest deflections in several points of the anterior thorax, however, no specifically correlation with an increase of the sternal fracture risk was analyzed. A reduction of sternal fracture risk suggests to be related, among others, with the reduction of twisting. Other relevant studies on twisting, from a kinematic perspective, can be found in [126].

Correlation for sternal fractures (AIS2)

Currently, no experimental data is available to collect a statistically representative sample in order to run a study on sternal fracture risk. As explained in 3.2.2, one approach would be to generate four virtual cases (table-top and GS1 loadcases with both Thums models) as done for the injury mechanism evaluation. A regression on simulated binary injury data would follow. Note that the table-top tests (belt loading until 20% deformation) [60] are right-censored whereas the GS1 [81] (ignoring the not-injured outlier) is left-censored. The abovementioned limitations motivated the use of a more robust method involving an injury reference value for bending on the ICS_2. As mentioned in 3.2.2, the bending moments measured on the ICS_2 represent the highest absolute difference when comparing both non-injurious and injurious cases, hence used here as a predictor. An injury reference value (IRV) matching both table-top and GS1 loadcases (see 3.2.2) is adopted here as $MXYZ = 20$ Nm. This assumption is also supported by the peak values found in the experiment battery of Kerrigan et al. [64]

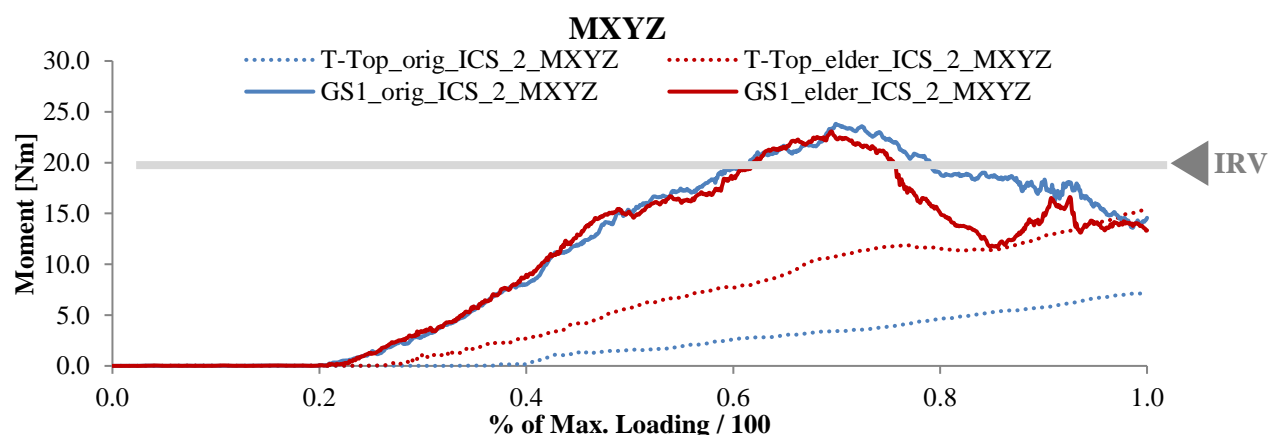


Fig. 3.27 Resultant moments at the ICS_2 for both Thums models and IRV

Possible implications for the restraint system management

Based on the abovementioned concepts, ribcage twisting would increase the risk of sternal fractures thus strategies to reduce it have to be addressed. As defined in 3.1.2.1 an early occupant coupling and the subsequent ride-down management by load limiting will be effective just until the load generate twisting hence triggering MX and MZ on the inter-costal spaces.

3.3.3 Report summary and Method Validation

Following the method development, the post-processing is also split in rib - and sternal fracture risk. A one-pager was designed to summarize peak bending moments and the NFR-based injury risk (Fig. 3.28). The sternal fracture risk assessment is based on the sternal IRV (Fig. 3.27). An additional sternal loading descriptor was summarized in a one-pager (Table 3.10). A battery of PMHS sled test was simulated following two targets: (i) Validate the assessment method and (ii) present the report prototype.

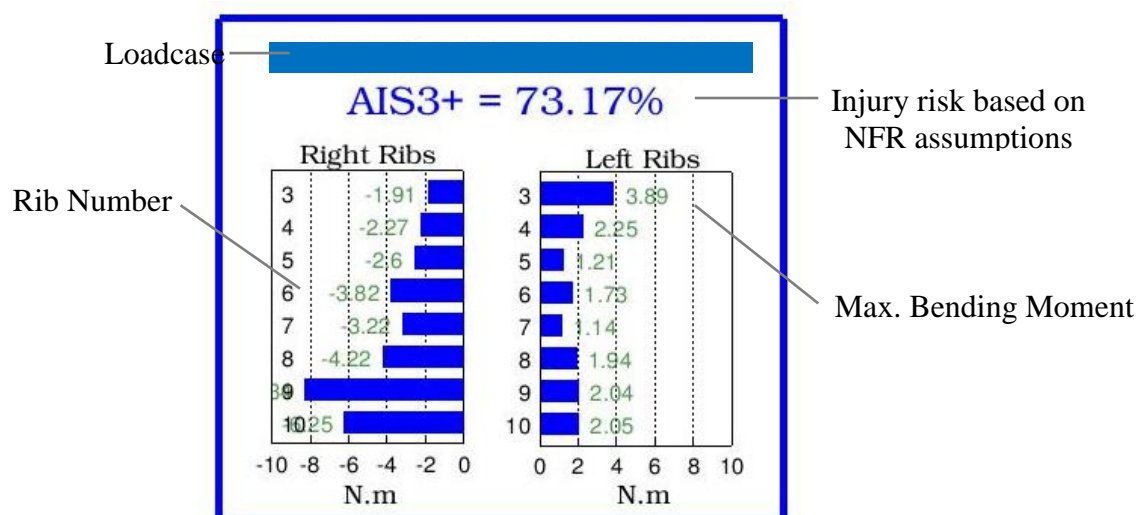


Fig. 3.28 Humat one-pager summary for one validation loadcase

The thoracic injury prediction of Thums-original and Thums-elderly is compared against the injury outcome of the battery of PMHS sled test [81]. H350's thoracic injury prediction was calculated using the USNCAP IRC. For the Thums models, Humat was utilized. The three models were positioned and simulated using the GS1 environment as described in 2.2.4.4.

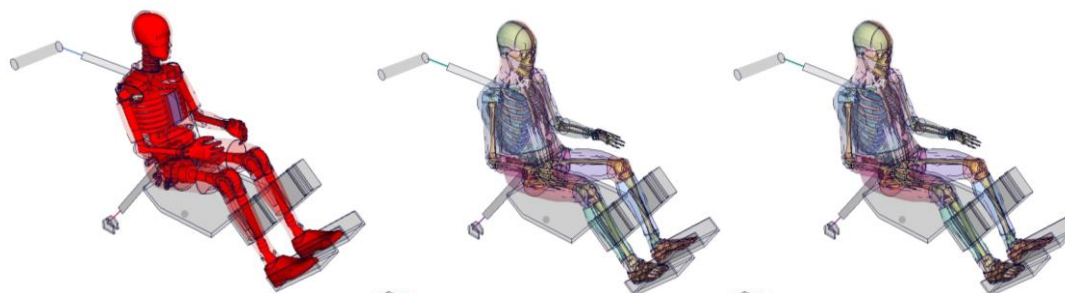


Fig. 3.29 Positioned model in GS1. Left: H350. Right: Thums-original and Thums-elderly

A time line of the simulations is shown in the following photogram:

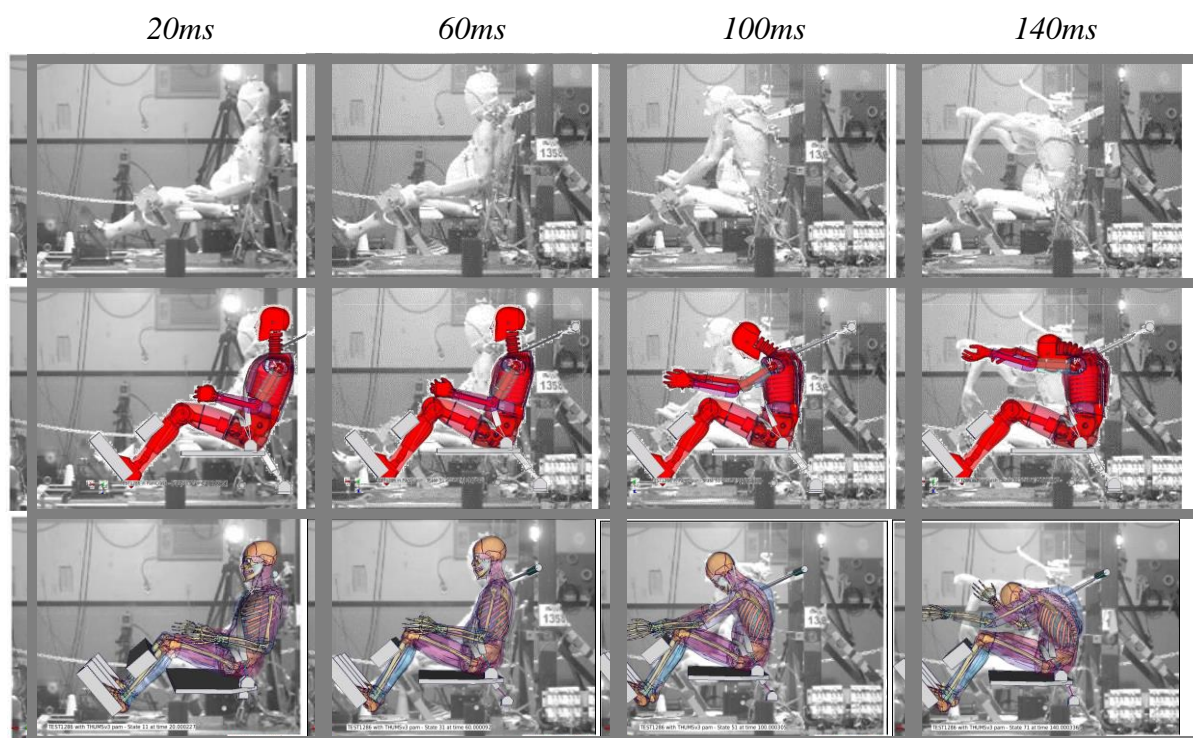


Fig. 3.30 GS1: PMHS Test, H350 (second row) and both Thums (third row)

The comparative analysis is summarized in the following two tables:

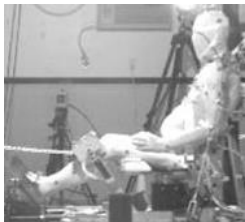
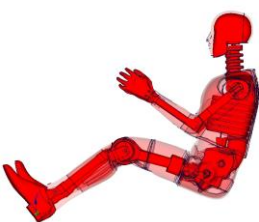
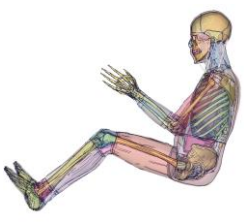
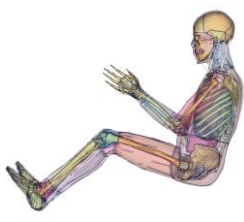
	Experiments	H350	Thums-original	Thums-elderly
Lateral View				
AIS3+	7 of 8	14 % (USNCAP IRC)	73.17% (HUMAT)	76.8% (HUMAT)
Sternal fractures	7 of 8	N/A	Yes (MXYZ = 23.85 Nm)	Yes (MXYZ = 23.05 Nm)

Table 3.9 Experiments, H350 and Thums models injury outcome

Addressing again the sternum loads for Thums-original and Thums-elderly (AIS2 as sternum fracture risk) the following summarizes the simulation results:

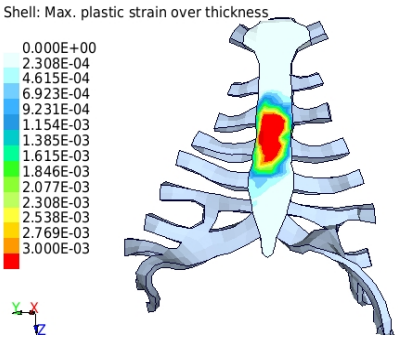
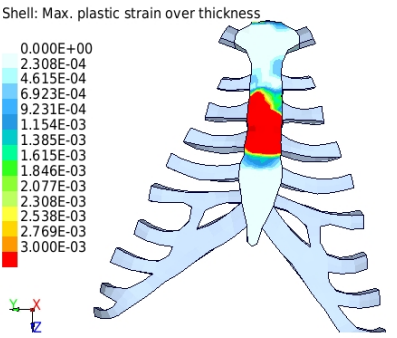
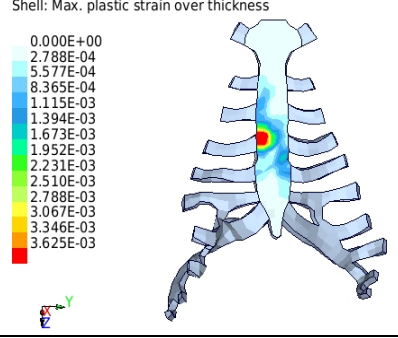
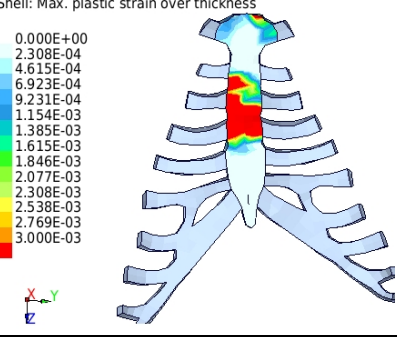
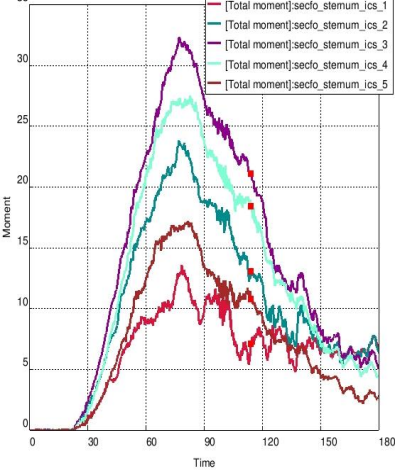
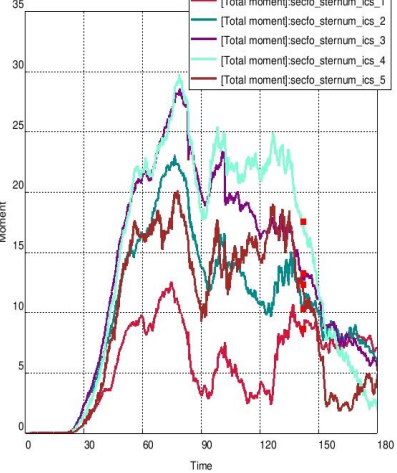
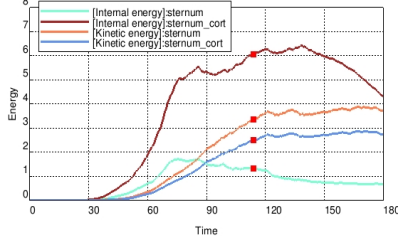
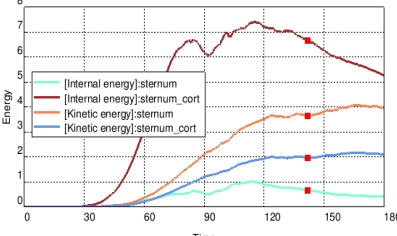
	Thums-original	Thums-elderly	Comments
Anterior View. Ep [GPa]	<p>Shell: Max. plastic strain over thickness</p> 	<p>Shell: Max. plastic strain over thickness</p> 	Anterior view of the sternum. Plastic strain distribution
Posterior View. Ep [GPa]	<p>Shell: Max. plastic strain over thickness</p> 	<p>Shell: Max. plastic strain over thickness</p> 	Posterior view of the sternum. Plastic strain distribution
ICS Bending Moments [Nm]			Bending moments [Nm] vs. Time [ms] in each sternal intercostal-space. From ICS_1 to ICS_5
Energy Plots [J]			Kinematic and internal energy of sternal cortical and trabecular (spongy) bone

Table 3.10 Assessment of sternal loading for both Thums models

A noticeable difference of AIS3+ injury prediction was depicted with the simulations. The age dependent effects seem more evident for the rib injury risk than for the sternal loading. The H350 lack of metrics for sternal loading left the analysis to the HBMs. Both Thums-original and sternal stress distribution (anterior and posterior views) and bending moments at each intercostal space (ICS) are shown in the next page. Energy time histories for both cortical and trabecular layer are also plotted. As discussed in the GS1 validation results, one interesting observation on the lower right chest and the “bulge-out” effect [81] was done. Mentioned by other authors and reanalyzed by Shaw with the GS1 test, the bulge-out of the lower chest (seatbelt’s opposite side), or “negative deflection”, may increase the sternal moments and consequently the sternal fracture risk. Despite both HBMs reproduced the bulge-out effect into the GS1 conditions, the Thums-original showed a peak deflection of -19.2 mm whereas the Thums-elderly peak deflection reached -8 mm (notice the negative sign indicating negative deflection). It is believed that the cartilage calcification causes a coupling effect of the anterior thorax generating a more uniform deflection than the “more-decoupled” Thums-original. The implications could involve an underestimation of the sternal bending moments in a belt-like dominated loading.

4 APPLICATION AND RESULTS: SIMULATION MATRIX AND REAL WORLD ACCIDENT RECONSTRUCTION

A matrix of crash cases was simulated including one accident reconstruction and six field-relevant crash cases. Each crash case was simulated with three different occupant FE-models: H350, Thums-original and Thums-elderly. Four restraint system variants were tested in order to compare the injury prediction of each model in each crash case. The deployment strategy of the restraint variants was based on the design guidelines developed in 3.1.2. Both driver and co-driver (passenger) sides were simulated for a total of 168 simulations (7 crash cases * driver and passenger * 3 occupant models * 4 restraint variants). The results are summarized per case as AIS2 (as sternum fracture) and AIS3+ injury prediction outcome using the report prototype developed in the chapter 3. This chapter is divided in two parts:

- (i) A real-world accident reconstruction including the reconstruction procedure, real injury data and analysis methodology
- (ii) Simulation and analysis of six additional field relevant crash cases

4.1 Crash Case 1: Real-World Accident Reconstruction

A better understanding of the injury outcome in a real frontal accident was needed. Specific cases involving mid-severity crash pulses were evaluated for reconstruction purposes. Although frontal mid-severity crashes are likely to be judged as low injury-risk cases, thoracic injuries still occur. As no OLC data was available for the search, frontal crash severity was defined as the classical proportional correlation to the change of velocity of the vehicle (ΔV) during the crash period including rebound:

$$\Delta V = \max(V(t)) - \min(V(t))$$

Eq. 4.1

Three different ranges of ΔV were defined based on a study from Ressle [127] in order to quantify a crash severity scale. The medium severity range constituted the first criteria for the accident database filtering.

Crash Severity Scale	ΔV [km/h]	Equivalent Standard Case
Low	0 - 15	-
Medium	16 - 39	e.g. FMVSS 208 (32-40 km/h) 0° and 30°
High	> 40	e.g. EURONCAP (64 km/h)

Table 4.1 Frontal crash severity scale, and equivalent cases addressing occupant injury risk evaluation

4.1.1 Method and Simulations

This section addresses the criteria for the database clustering, accident description, accident reconstruction method and restraint system variants utilized for the simulations. This accident reconstruction was already published by the author in [128].

4.1.1.1 AARU Database and Search Parameters

The AARU (Audi Accident Research Unit) is an interdisciplinary research team between Audi AG and the Clinic of the University of Regensburg (Bavaria, Germany). The analysis of traffic accidents includes research activities involving accurate accident reconstruction and detailed analysis of injury outcomes. The AARU supported the database search providing a sample of mid-severity real world accidents. The filtering focused frontal collisions with passenger cars. Side crash and rollovers were excluded. The search criteria are summarized here:

- (i) Frontal collisions (nearly 100% overlap)
- (ii) Car models from 2008 and newer
- (iii) Medium Crash severity ($\Delta V \approx 20$ km/h)
- (iv) Driver or/and Passenger with medium thoracic injury severity (AIS 2) or higher
- (v) Reconstructability criteria.

The filtering result showed seven accidents matching the search requirements. The reconstructability factor led to choose a collision between a Skoda Octavia Kombi and an Audi A4. The crash analysis was focused on the Audi A4. This case was chosen and reconstructed.

4.1.1.2 Accident Description

The accident outline where daylight (11:15 a.m.), dry road, urban and velocity limit 50 km/h. A Skoda Octavia Kombi (red) drives into the crossroad without braking with an estimated initial velocity of about 50 km/h. From the right side an Audi A4 (blue) collided into the right side of the Skoda Octavia with an estimated initial velocity of 50 km/h and full overlap. Afterwards the Skoda Octavia breaks through a soft coppice. See the following diagrams.

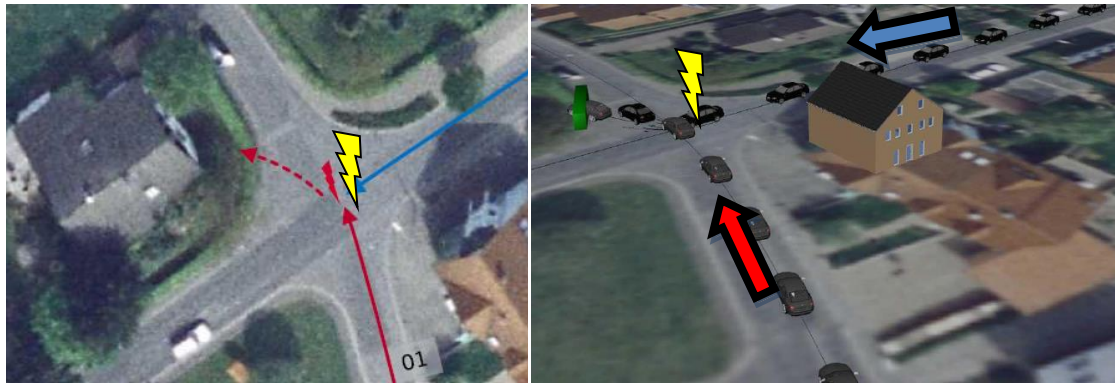


Fig. 4.1 Selected accident scheme (AARU). Skoda Octavia (red), Audi A4 (blue) [128]

4.1.1.3 Occupant's Injury Summary (Audi A4)

The driver sustained injuries with MAIS 1. The passenger sustained injuries up to MAIS 2 due to a sternum fracture. The following table explains the anthropometric characteristics, age and injury severity of both driver and passenger.

Occupants A4 Data	Driver	Passenger
Age [years]	61	59
Height [m]	1,70	1,57
Weight [kg]	77	61
Injury severity	MAIS 1	MAIS 2

Table 4.2 Anthropometric characteristics, age and injury severity of the occupants in the Audi A4

4.1.1.4 Kinematic Reconstruction Step

The AARU carried out a PC-Crash [129] accident reconstruction using as input data the trajectories and final locations of both cars out of the database. The results were the initial velocities and directions at the collision time. These values are set for the FE structural simulations. The PC-Crash iterations resulted in the following results:

Variable	Skoda Octavia	Audi A4
Initial Velocity [km/h]	50	50
Collision Velocity [km/h]	33	42
ΔV [km/h]	26	24
Velocity Tolerance	$\pm 5\text{km/h}$	$\pm 5\text{km/h}$

Table 4.3 Initial kinematic conditions obtained with PC-Crash simulations

And for the trajectories:

Fig. 4.2 Collision trajectories for the selected accident. Skoda Octavia (red) vs. Audi A4 (blue) Credits: Thomas Schenk (AARU) [128]

4.1.1.5 Structural Simulation Step

The initial kinematic conditions and trajectories were used to set the initial and boundary conditions. As both Skoda and Audi models involved in the accident share the same platform into the VW Group, a similar structural behavior was assumed. Therefore, the collision was simulated with two Audi A4 FE Models. Assumptions for the structural simulation were as follows:

- (i) Simulations were done using gravity
- (ii) Braking after the t_0 (Collision time) was neglected
- (iii) Road surface friction properties were neglected
- (iv) Skoda Octavia FE Model taken as A4 FE Model

The simulations were run in VPS. The two FE A4 models were positioned as shown:

Fig. 4.3 Left: FE models. Right: Resulting trajectories from PC-Crash [128]

A qualitative deformation analysis shows similar deformation patterns between the real crash and the FE model. Realistic energy absorption and dissipation due to material's plastic deformations and failure in the simulations are assumed to represent realistically the kinematical conditions of the occupant-cell during the crash.



Fig. 4.4 Structure deformation comparison. Left: Real accident. Right: Simulation. Credits: Adrian Langner (ASTech) [128]

Resultant pulse

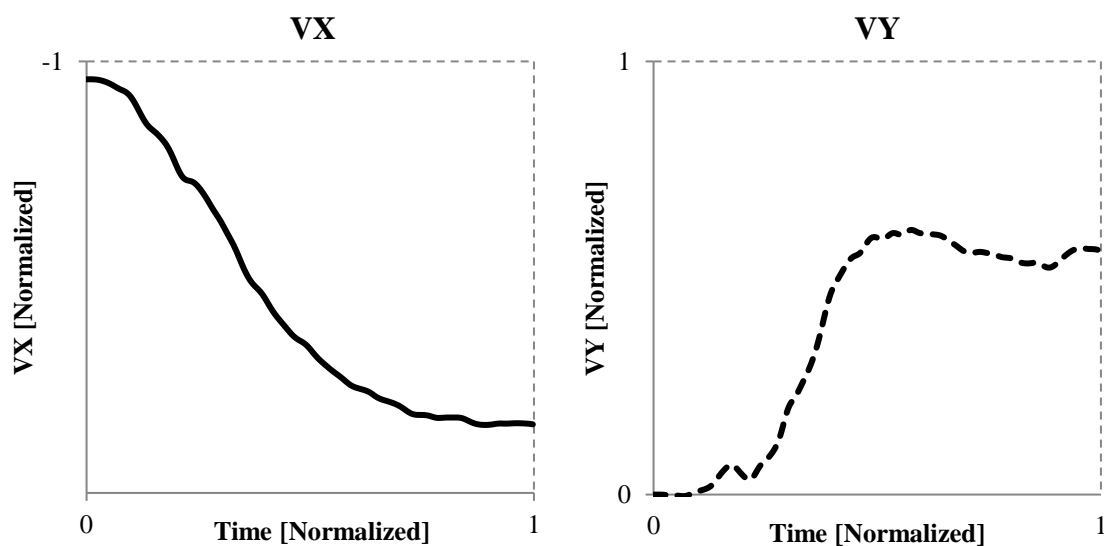


Fig. 4.5 Resultant velocity pulses (normalized) from the structural simulation

4.1.1.6 Sensor Simulation Step

The accident report showed that both occupants were buckled up and the belt pre-tensioners were activated. Airbags were not triggered. These deployment conditions are expected to occur in cases from low to mid crash severities. The assumption is that the occupants are well restrained by the combined action of the pretensioner and force limiters.



Fig. 4.6 Right: Interior view of the Audi A4 after the crash [128]

The crash pulse defines the fire times of the restraint system. In a real crash case, algorithms running into the crash control units analyze the input signal (crash pulse and front-end deformations) delivering as output a pre-set of trigger times for the restraint components. From the simulation, the pulse was analyzed with an external control unit hence generating the virtual triggering that would have been generated in the real crash. No deviation between real and virtual trigger times was assumed. Pulse and the virtual trigger times define the kinematic and restraint system input for the occupant-cell simulation step.

4.1.1.7 Occupant-Cell Simulation Step

Deceleration pulses were obtained from the structural simulation and set to an isolated occupant cell by pre-scribed motion cards in VPS. Virtual trigger was set to the first restraint system variant. Three additional triggering strategies and load limiter level were simulated. Isolated occupant cell simulation allows a computing-time reduction by 1/8 compared to the structural simulation. See next figure.

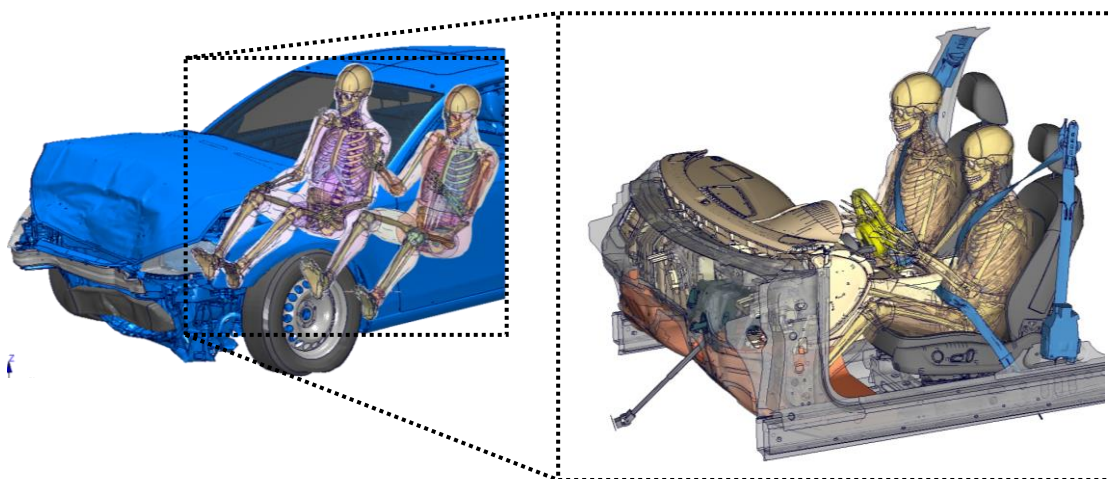


Fig. 4.7 HBMs in driver and passenger side. Occupant-cell shown in gray. Roof, A- and B-pillars were blended for visualization

Assumptions for the occupant-cell simulations:

- (i) Both occupants were considered as 50th percentile American Male (AM)
- (ii) The initial positions of the occupants and seats into the car were assumed to be as the USNCAP (2014) testing protocol establish
- (iii) Pre-crash muscle reaction was assumed to be negligible
- (iv) Undeformed occupant-cell. From the visual inspection (accident report) no relevant structural deformations of the occupant-cell were found

4.1.1.8 Matrix of Simulations

Occupant-cell simulations of driver and passenger seat positions with the H350, Thums-original and Thums-elderly were simulated under four restraint system variants.

Occupant	Restraint System			
	A	B	C	D
H350 Driver	X	X	X	X
H350 Passenger	X	X	X	X
Thums-original Driver	X	X	X	X
Thums-original Passenger	X	X	X	X
Thums-elderly Driver	X	X	X	X
Thums-elderly Passenger	X	X	X	X

Table 4.4 Accident reconstruction simulation matrix

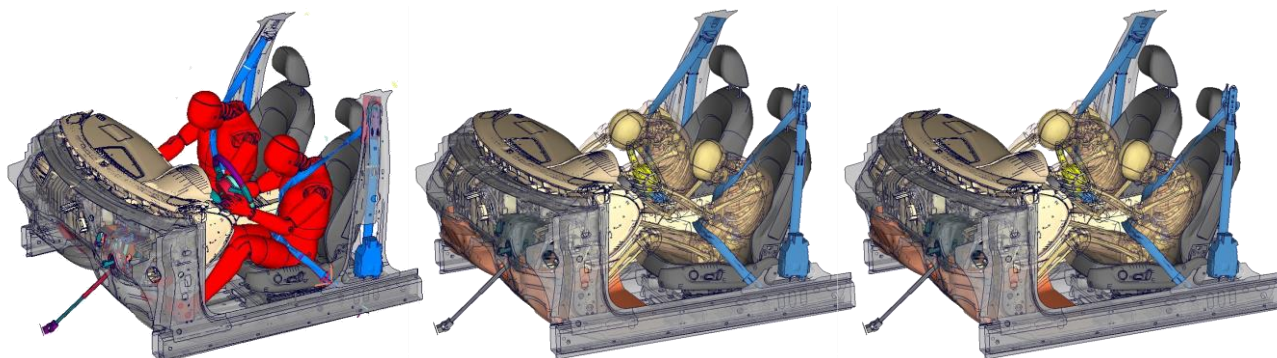


Fig. 4.8 Simulations with H350, Thums-original and Thums-elderly in driver and passenger positions

4.1.1.9 Restraint System Variants A, B, C and D Explanation

The deployment strategy is summarized as follows:

Variant	Belt Load Limiter Level	Airbag Vent Deployment
A	3.5 kN (Linear)	No
B	From 3.5 kN to 1.85 kN	Yes
C	From 3.5 kN to 1.0 kN	Yes
D	From 3.5 kN to 0.6 kN	Yes

Table 4.5 Restraint System variants description

The conventions red, yellow, green and blue were defined for visualization of the results in this sub-section, the section 4.1.2 and sub-chapter 4.3. Triggering of pretensioners, load limiters and airbag deployment are -in almost all cases- similar for the variants B, C and D, being the main difference the load limiting level.

4.1.2 Results Crash Case 1: Accident Reconstruction

The above mentioned restraint system variants were simulated (see 4.1.1.9). The variant “A” represents the restraint trigger times and belt load-limiting conditions of the real accident. In order to illustrate the loading reduction achieved, a summary of the deployment strategy, shoulder belt forces (normalized) and resultant moments at the ics_2 are presented in the next page. Following these results, simulation results on injury prediction are shown, including driver and passenger sides, injury severities AIS2 and AIS3+ for the Thums models and AIS3+ for the H350.

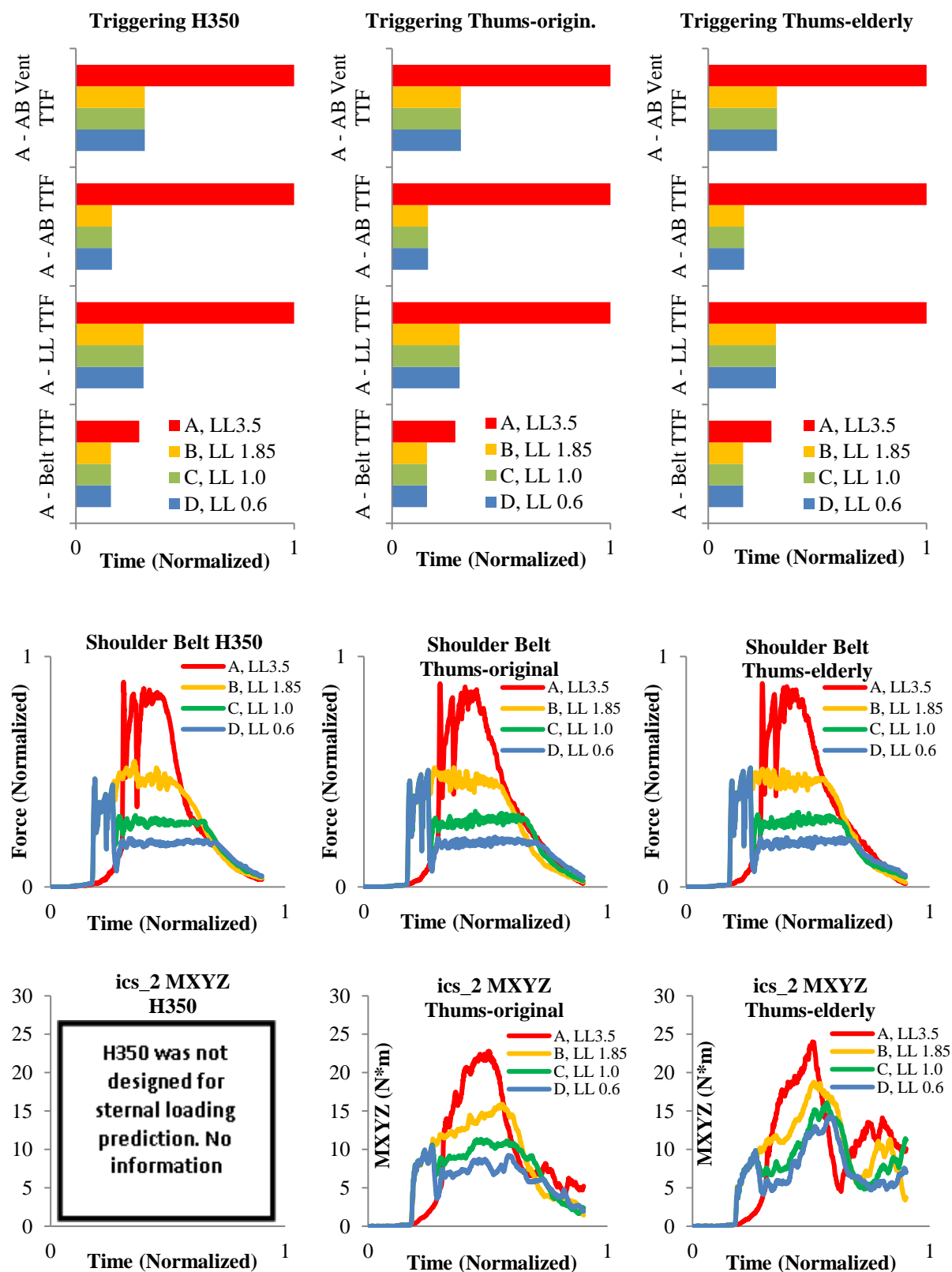


Fig. 4.9 Normalized trigger times and belt loading for all models in passenger position. Sternal loading reduction in terms of inter-costal-space-2 resultant moment. Note that the H350 was not designed for this type of loading assessment. The loading reduction cannot be assessed with the H350

Injury prediction for:	Restraint System Variant			
	A	B	C	D
<i>H350 Driver (AIS3+) %</i>	1.14	1.62	1.1	0.75
<i>Thums-original Driver (AIS3+) %</i>	39.63	2.98	2.42	2.7
<i>Thums-elderly Driver (AIS3+) %</i>	55.91	24.23	22.97	20.75

Table 4.6 Crash Case 1: Drivers AIS3+ Prediction

Thums-original Driver (AIS2 as sternum fracture risk)

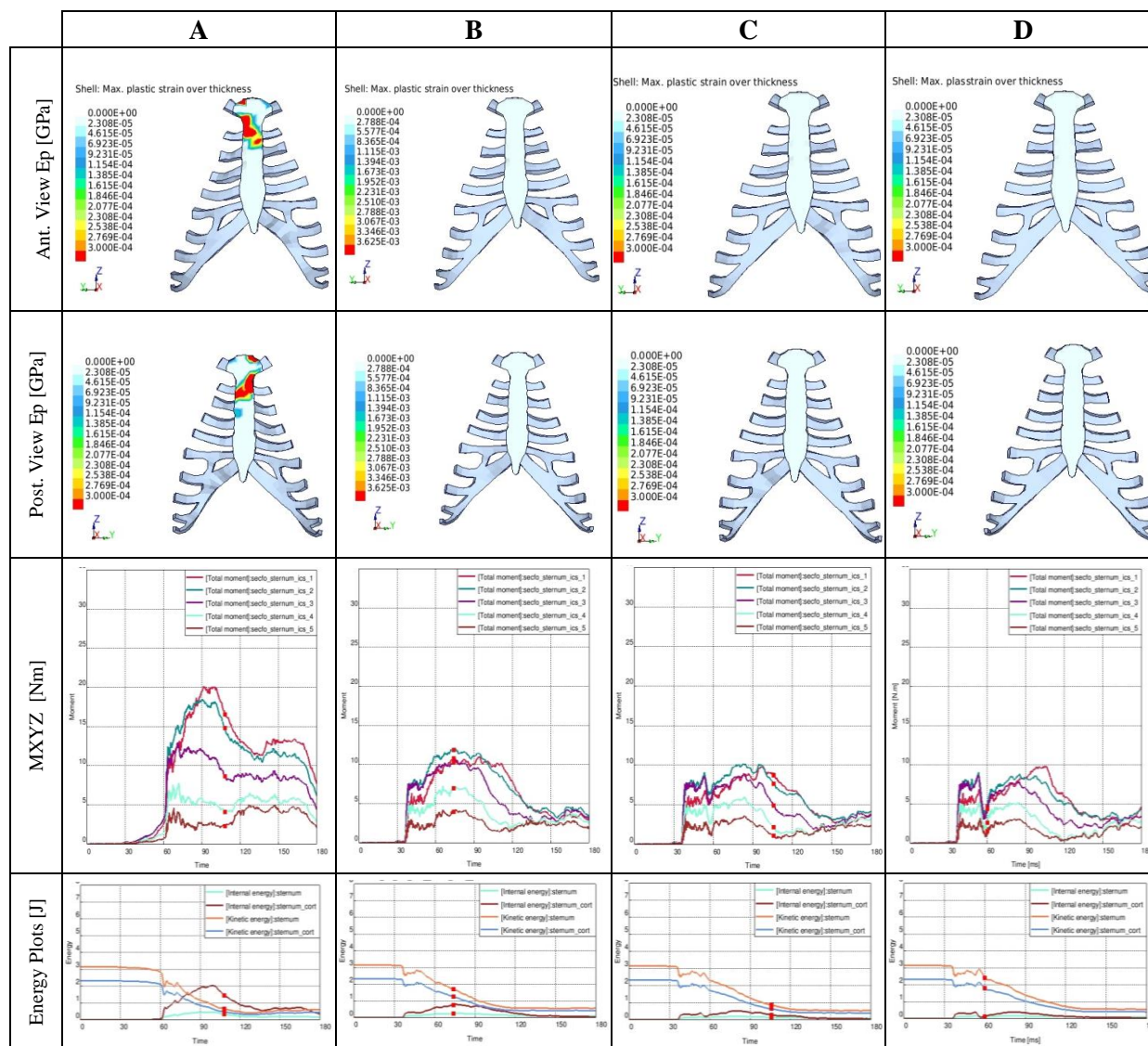


Table 4.7 Crash Case 1: Driver, Thums-original sternal loading

Thums-elderly Driver (AIS2 as sternum fracture risk)

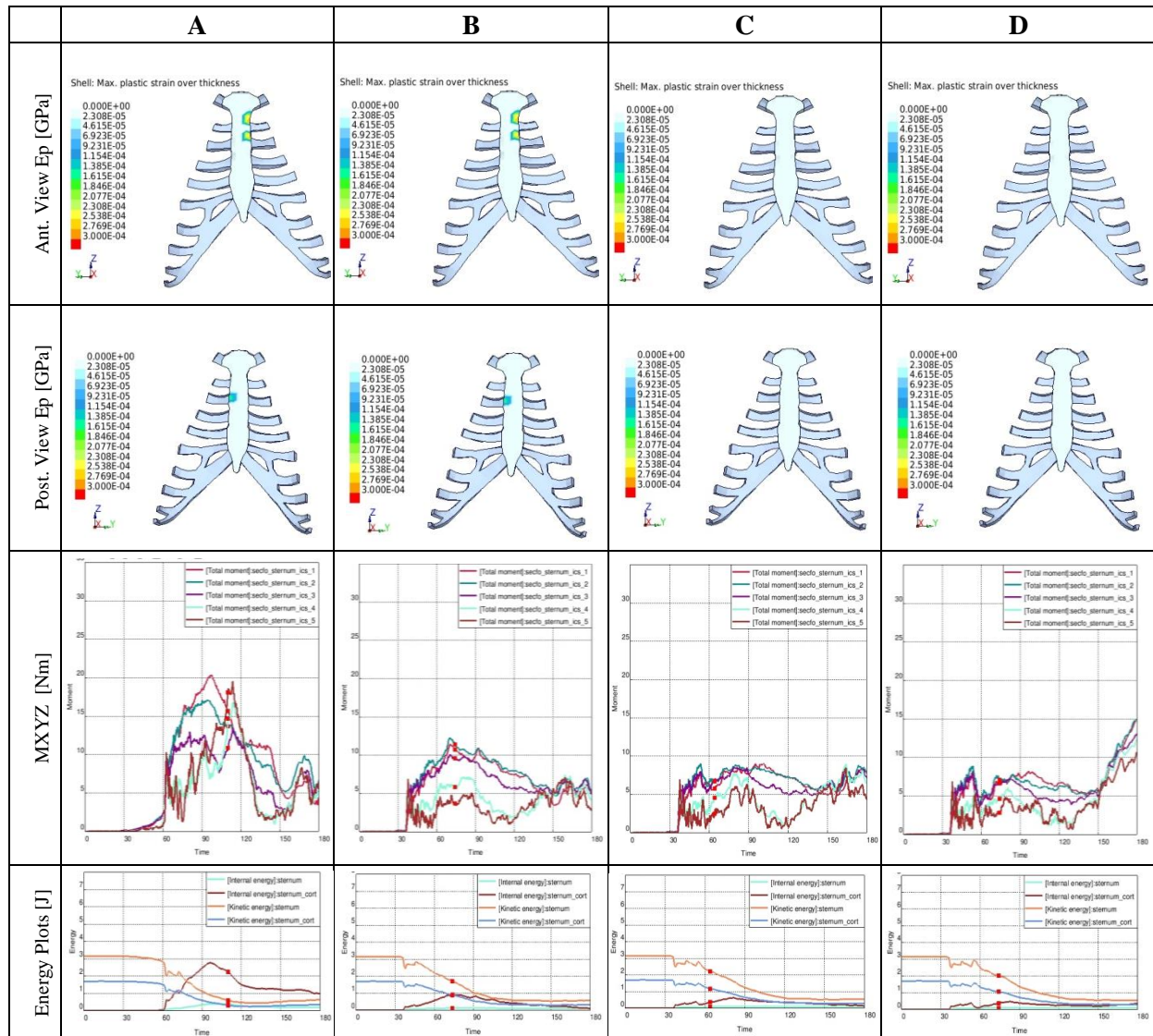


Table 4.8 Crash Case 1: Driver, Thums-elderly sternal loading

Injury prediction for:	Restraint System Variant			
	A	B	C	D
<i>H350 Passenger (AIS3+) %</i>	0.651	0.518	0.349	0.351
<i>Thums-original Passenger (AIS3+) %</i>	39.4	2.97	2.25	1.37
<i>Thums-elderly Passenger (AIS3+) %</i>	53.11	27.09	29.36	27.3

Table 4.9 Crash Case 1: Passengers AIS3+ Prediction

Thums-original Passenger (AIS2 as sternum fracture risk)

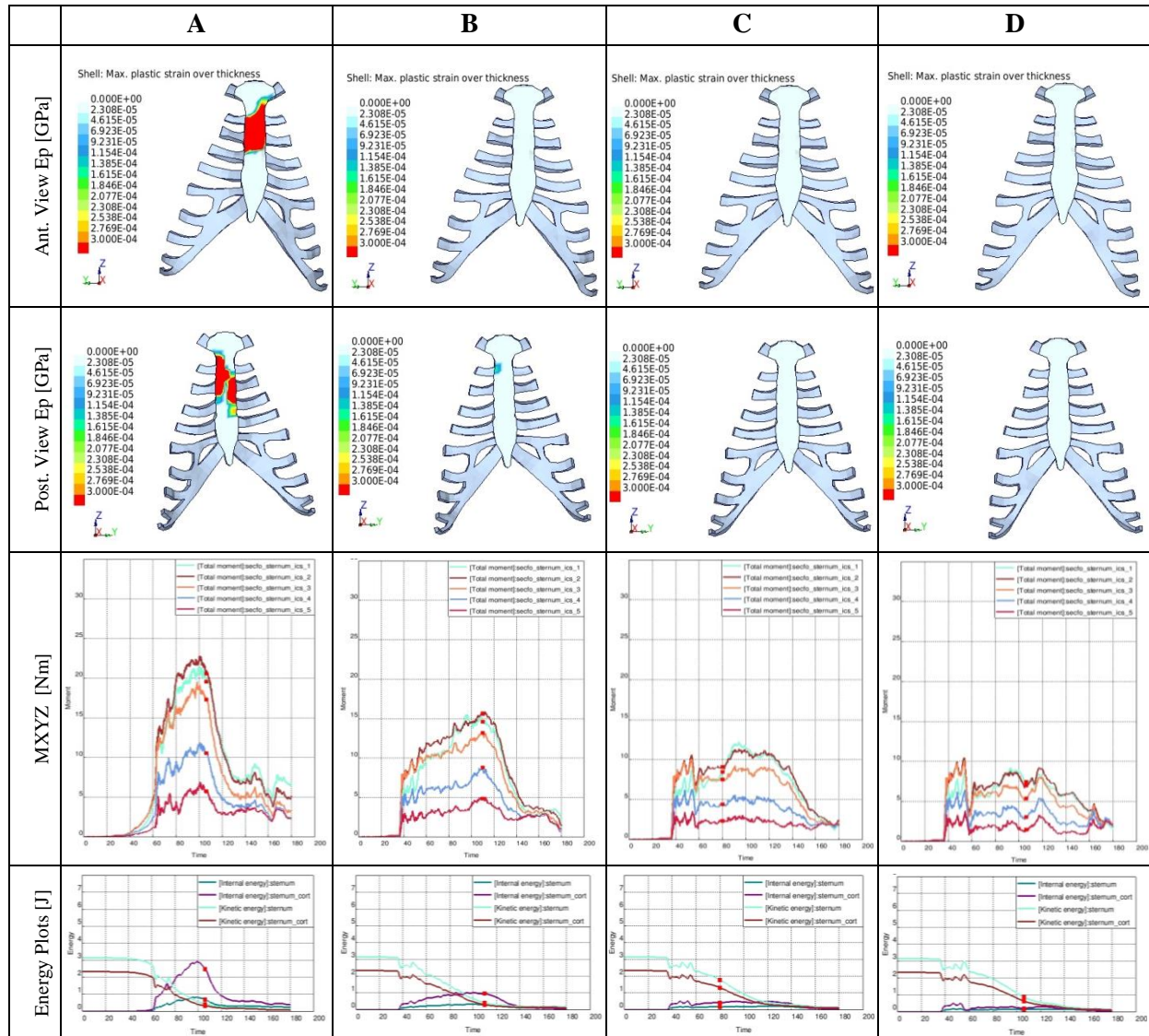


Table 4.10 Crash Case 1: Passenger, Thums-original sternal loading

Thums-elderly Passenger (AIS2 as sternum fracture risk)

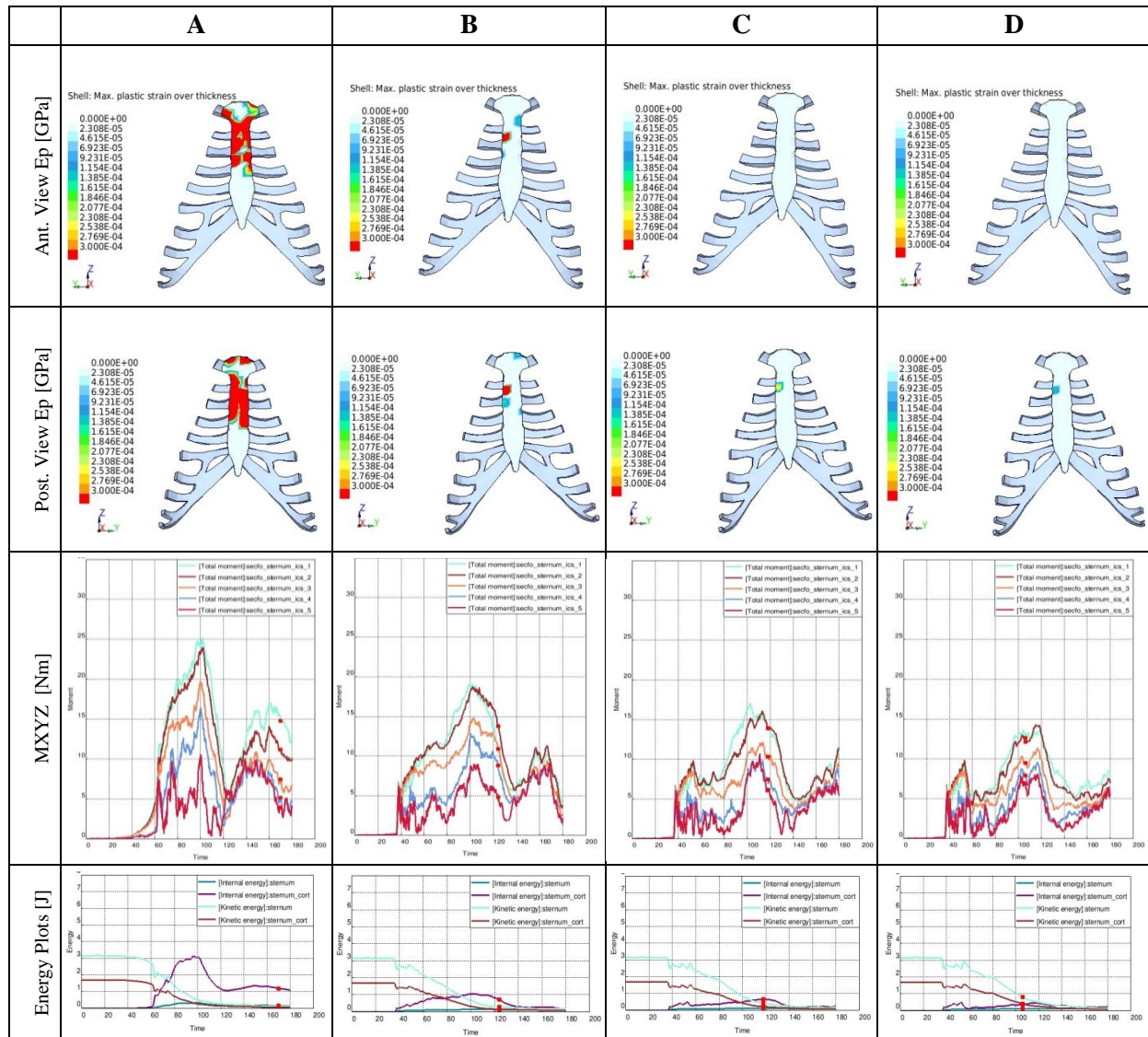
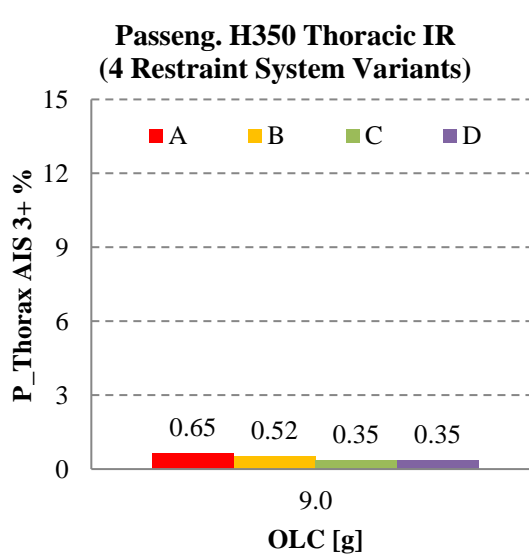
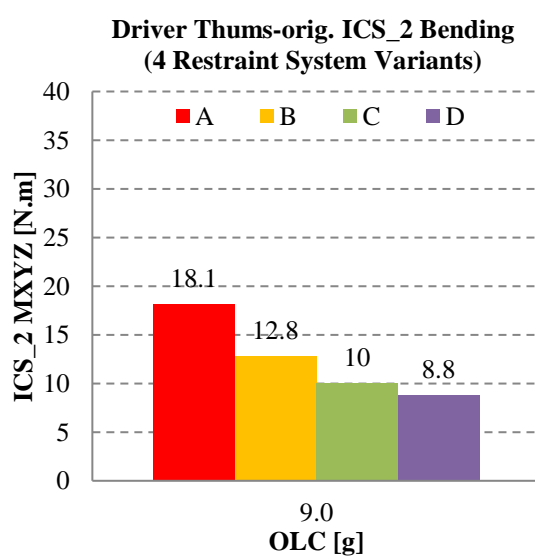
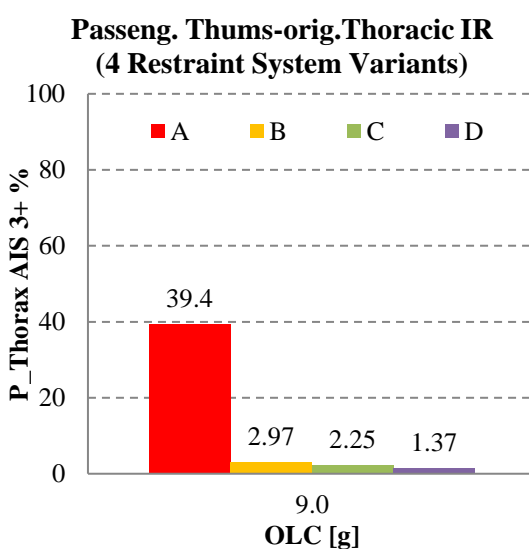
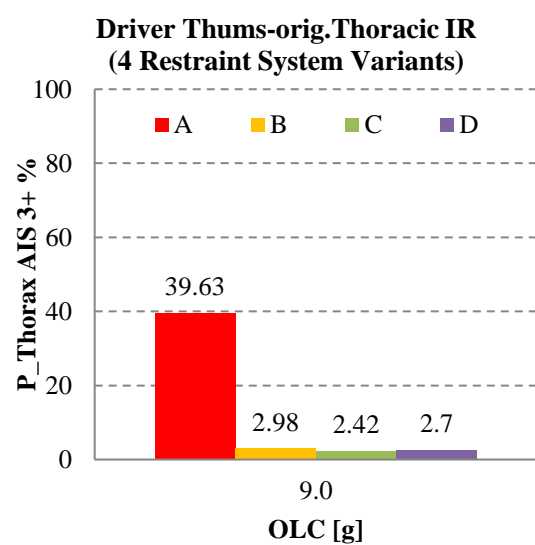
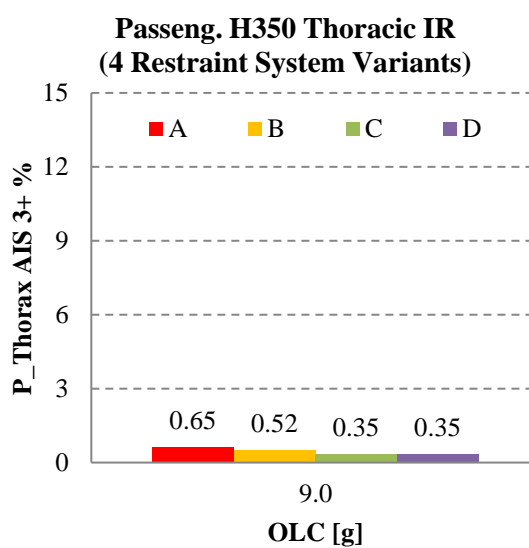
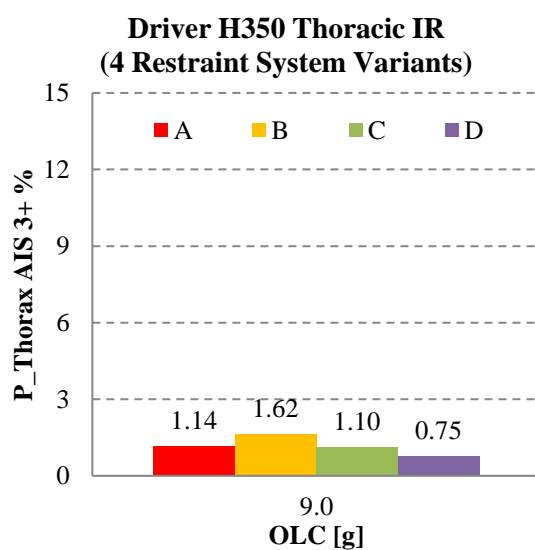
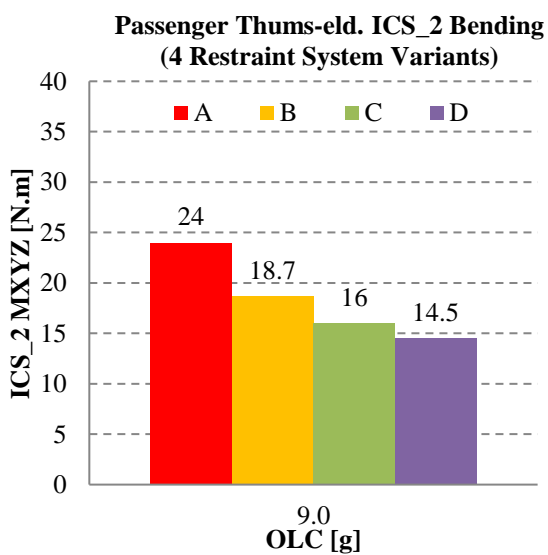
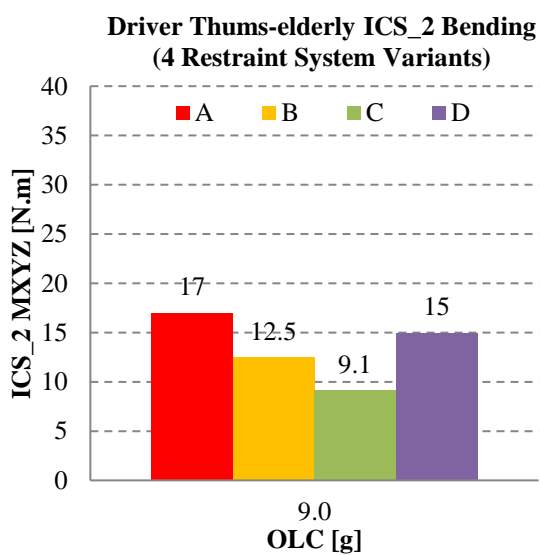
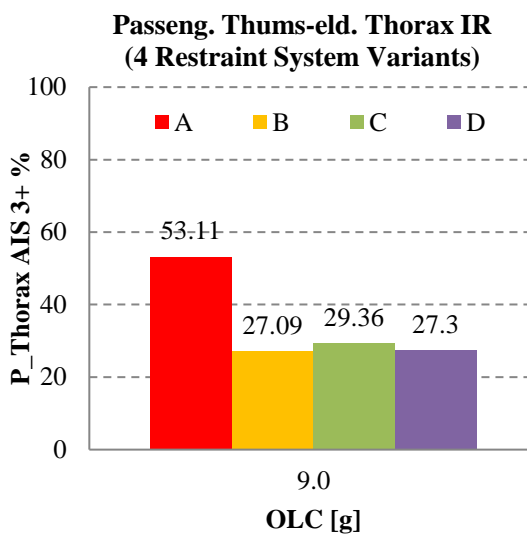
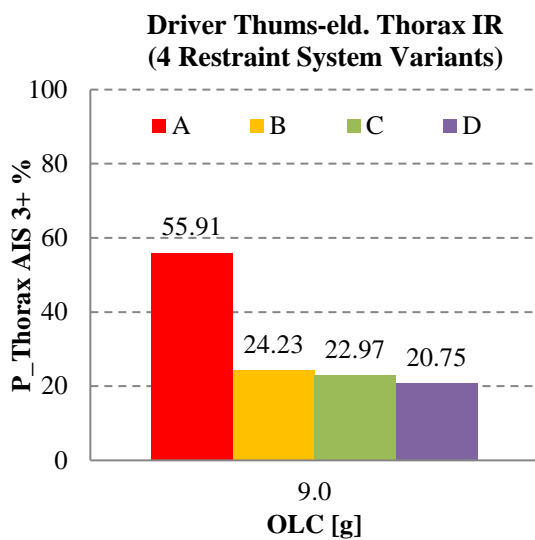


Table 4.11 Crash Case 1: Passenger, Thums-elderly sternal loading

Plots for all occupants, real world accident





Ribcage Twisting and ICS_2 bending reduction

As mentioned in 3.2.2 and 3.2.3 the method to evaluate the sternum fracture risk involves an injury reference value for bending on the ICS_2. Recapitulating, the bending moments measured on the ICS_2 seems to be also a metric to quantify the effect of the ribcage twisting on the sternal fracture risk. Nevertheless, it was considered relevant to show a qualitative comparison of ribcage twisting for H350, Thums-original and Thums-elderly (passenger side) for the four restraint variants.

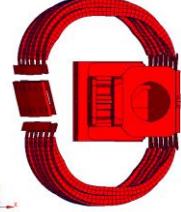





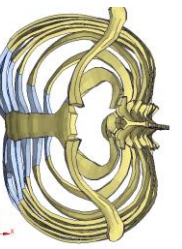
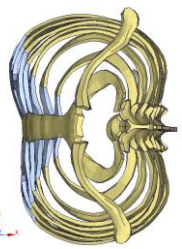

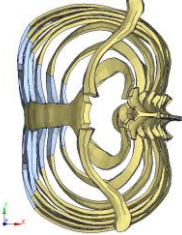
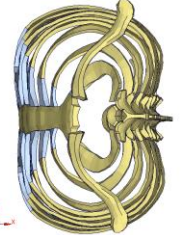
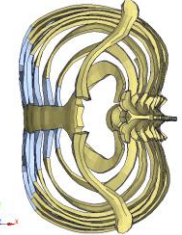
	A	B	C	D
H350 Passenger				
Thums-original Passenger				
Thums-elderly Passenger				

Table 4.12 Ribcage twisting for visualization under four restraint variants

The following observation were found also relevant for the analysis:

(i) The Thums-original and Thums-elderly show similar kinematics, predicting the similar forward excursion when measured at the head COG, T1, T8 and hip reference point (H-point). The HBMs predicted higher head and torso excursion compared to the H350 model in both driver and passenger positions. It is believed that the more flexible lumbar spine in the HBMs generated this difference. The H350 spine is in contrast rigid, articulated only with a rubber flexible joint at the thoracic spine height. This observation also suggests that, due to the more flexible nature of the HBMs, a restraint variant that optimizes the forward excursion in an

attempt to reduce the H350's thoracic injury outcome (e.g. chest deflection), may increase the risk of head contact with the dashboard when evaluated with HBMs.

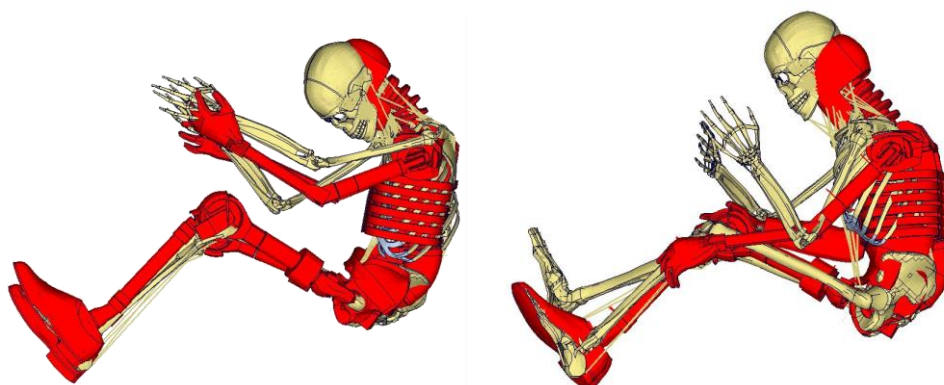


Fig. 4.10 Driver and passenger positions. Overlap with Hybrid-III (red) and HBM (Bony color)

(ii) Summarizing the AIS3+ results, the H350 passenger model predicted a thoracic injury probability of 0.65 % compared with the 39.4 % of Thums-original and 53.11 % of Thums-elderly with the original accident restraint conditions (restraint variant A). The injury prediction of the H350 in both cases is extremely low, suggesting an underestimated bias as the one probed with the Gold Standard Sled Test.

(iii) As for the AIS3+, a remarkable difference was also found in the peak bending moments evaluated on the ICS_2 between driver and passenger. For the Thums-elderly driver (restraint system variant A) a value of 18 Nm suggests a response just under the proposed injury reference value (the driver sustained no sternal injuries). The Thums-elderly passenger simulation showed a loading reaching 24 Nm, surpassing the proposed injury reference value (the passenger did sustain a sternal fracture).

(iv) Comparing both HBMs in the passenger position, no significant differences were found by comparing the peak bending moments. Nevertheless, when the time histories of the sternal bending are compared, clear differences at the same load limiting level are present as shown below.

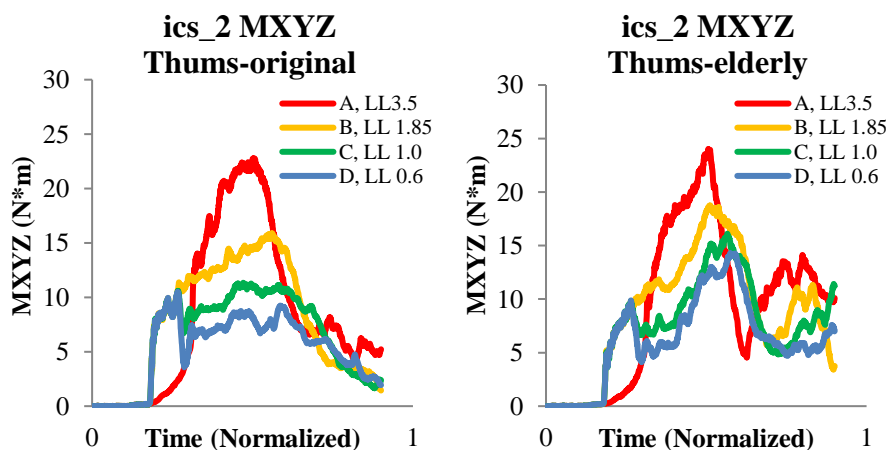


Fig. 4.11 Accident reconstruction, ICS resultant moments for both Thums models and four restraint variants

(v) The accident acceleration pulse presented a dominant lateral component (see 4.3.4). As shown in the Fig. 4.10, the H350 thoracic seems to be unaffected by this component. The effect of the lateral pulse is believed to increase the ribcage twisting of both HBMs.

4.2 Crash Cases 2 to 7

A group of bench loadcases in addition to the accident reconstruction (see 4.1) was simulated in VPS®. Pulses from structural simulations based on a GIDAS subset defined in [127] were utilized for occupant cell simulations. Six loadcases with $OLC \geq 10g$ were chosen from the subset: Rear-end crash at 20 km/h, 35 km/h, 50 km/h and 70 km/h; head-on crash full overlap at 48 km/h; head-on crash partial overlap 40 km/h and 64 km/h; and cross road case at 60 km/h. See the Table 4.13.

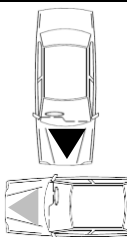
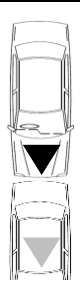
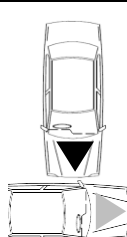

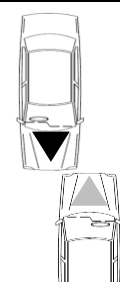
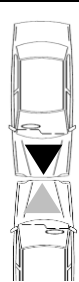
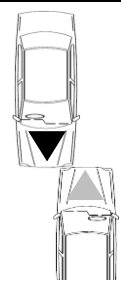
OLC:	9*	10	14.1	15.8	18	27.6	30.4
Vrel [km/h]:	20	50	60	70	80	96	128
Overlap:	100 %	100 %	100 %	100 %	40 %	100 %	40 %
Collision Type:							
Comments:	Accident Reconstruction	Rear-end Collision	Frontal Collision Vrel=60Km/h against left side (90°) V=45Km/h	Rear-end Collision	Frontal (Head on) Collision	Frontal (head on crash partial overlap) Collision	Frontal (head on crash partial overlap)

Table 4.13 Characteristic crash cases including an accident reconstruction*. Based on [127]

A crash-severity range from 9 to 30,4 OLCs (including the accident reconstruction) constituted a bench pool for injury patterns analysis. An overview of the simulation matrix and results per loadcase follows.

4.2.1 Method and Simulations

The simulation method replicates the procedure presented in 4.1. The six bench cases were simulated for driver and passenger side with the H350, Thums-original and Thums-elderly models. Four restraint system variants (see 3.3.1, 4.1.1.9 and 4.1.2) per case were tested for total of 144 simulations. The variants are summarized into the following matrix of simulation.

4.2.1.1 Matrix of Simulations

Overview of the simulation pool.

	OLC 9				OLC 10				OLC 14.1				OLC 15.8				OLC 18				OLC 27.6				OLC 30.4			
	Variant				Variant				Variant				Variant				Variant				Variant				Variant			
Occupant	A	B	C	D	A	B	C	D	A	B	C	D	A	B	C	D	A	B	C	D	A	B	C	D	A	B	C	D
H350 Driver	X	X	X	X	X	X	X	X	X	X	X	X	X	X	X	X	X	X	X	X	X	X	X	X	X	X	X	X
H350 Passenger	X	X	X	X	X	X	X	X	X	X	X	X	X	X	X	X	X	X	X	X	X	X	X	X	X	X	X	X
Thums original Driver	X	X	X	X	X	X	X	X	X	X	X	X	X	X	X	X	X	X	X	X	X	X	X	X	X	X	X	X
Thums original Passenger	X	X	X	X	X	X	X	X	X	X	X	X	X	X	X	X	X	X	X	X	X	X	X	X	X	X	X	X
Thums elderly Driver	X	X	X	X	X	X	X	X	X	X	X	X	X	X	X	X	X	X	X	X	X	X	X	X	X	X	X	X
Thums elderly Passenger	X	X	X	X	X	X	X	X	X	X	X	X	X	X	X	X	X	X	X	X	X	X	X	X	X	X	X	X

Table 4.14 Simulation matrix. Gray: Accident reconstruction.

4.2.2 Results Crash Case 2

Injury prediction for:	Restraint System Variant			
	A	B	C	D
<i>H350 Driver (AIS3+) %</i>	2.551	2.363	1.341	1.064
<i>Thums-original Driver (AIS3+)%</i>	4.330	2.610	3.040	1.720
<i>Thums-elderly Driver (AIS3+)%</i>	20.480	24.610	23.040	23.180

Table 4.15 Crash Case 2: Drivers AIS3+ Prediction

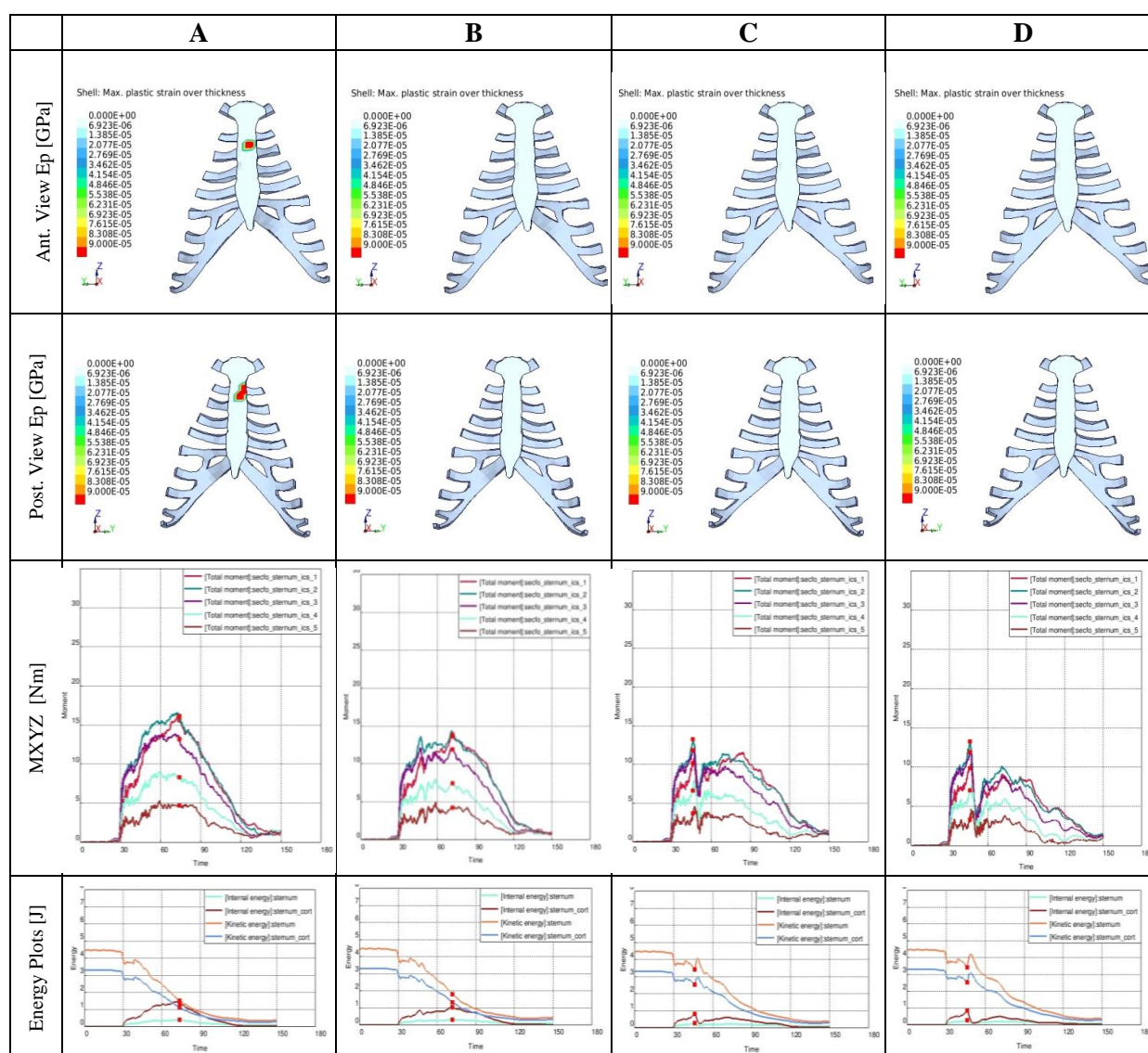
Thums-original Driver (AIS2 as sternum fracture risk)

Table 4.16 Crash Case 2: Driver, Thums-original sternal loading

Thums-elderly Driver (AIS2 as sternum fracture risk)

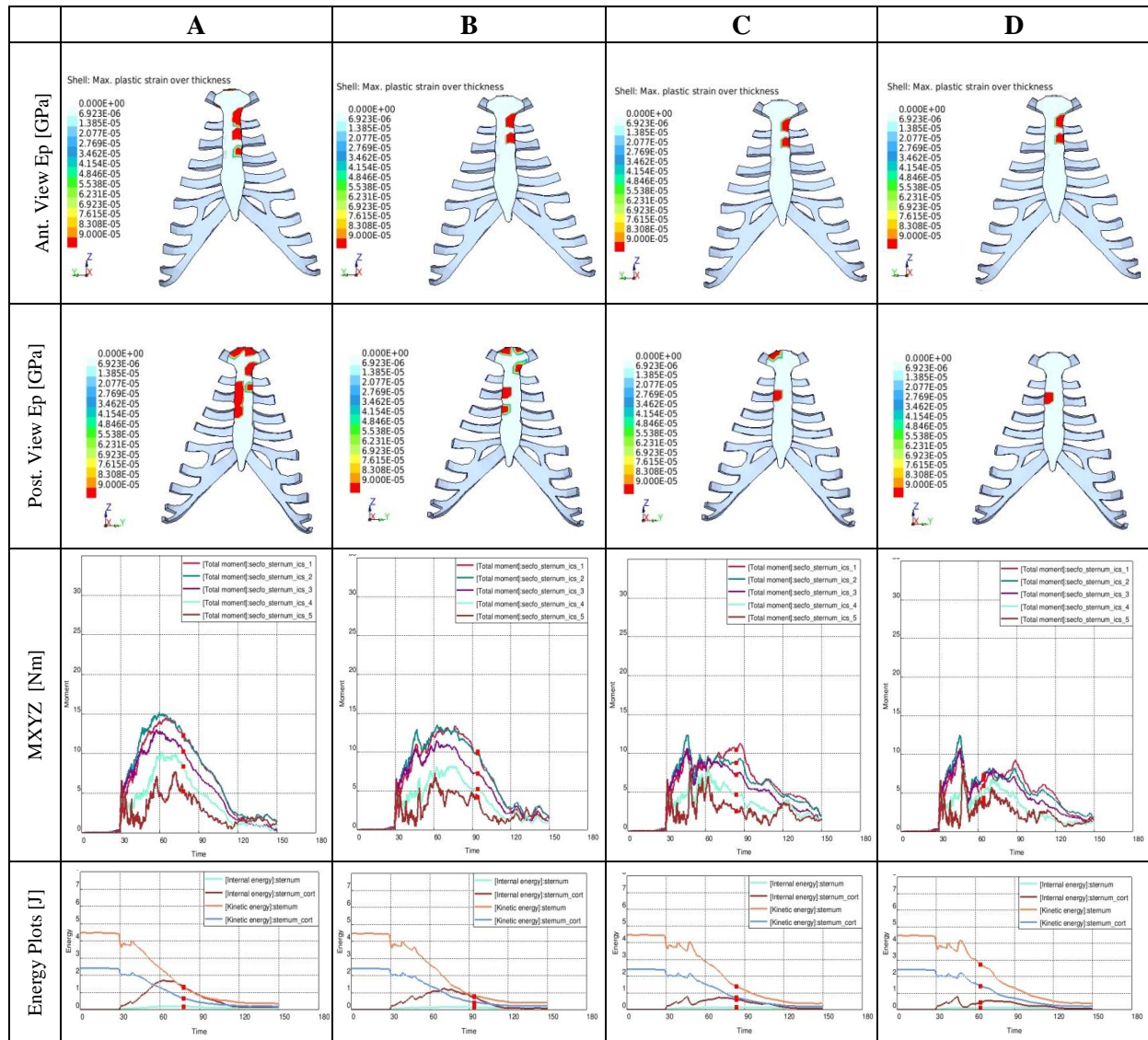


Table 4.17 Crash Case 2:Driver, Thums-elderly sternal loading

Injury prediction for:	Restraint System Variant			
	A	B	C	D
<i>H350 Passenger (AIS3+) %</i>	0.828	0.808	0.599	0.602
<i>Thums-original Passenger (AIS3+)%</i>	13.420	5.280	1.000	0.930
<i>Thums-elderly Passenger (AIS3+)%</i>	30.880	30.340	27.970	23.640

Table 4.18 Crash Case 2: Passengers AIS3+ Prediction

Thums-original Passenger (AIS2 as sternum fracture risk)

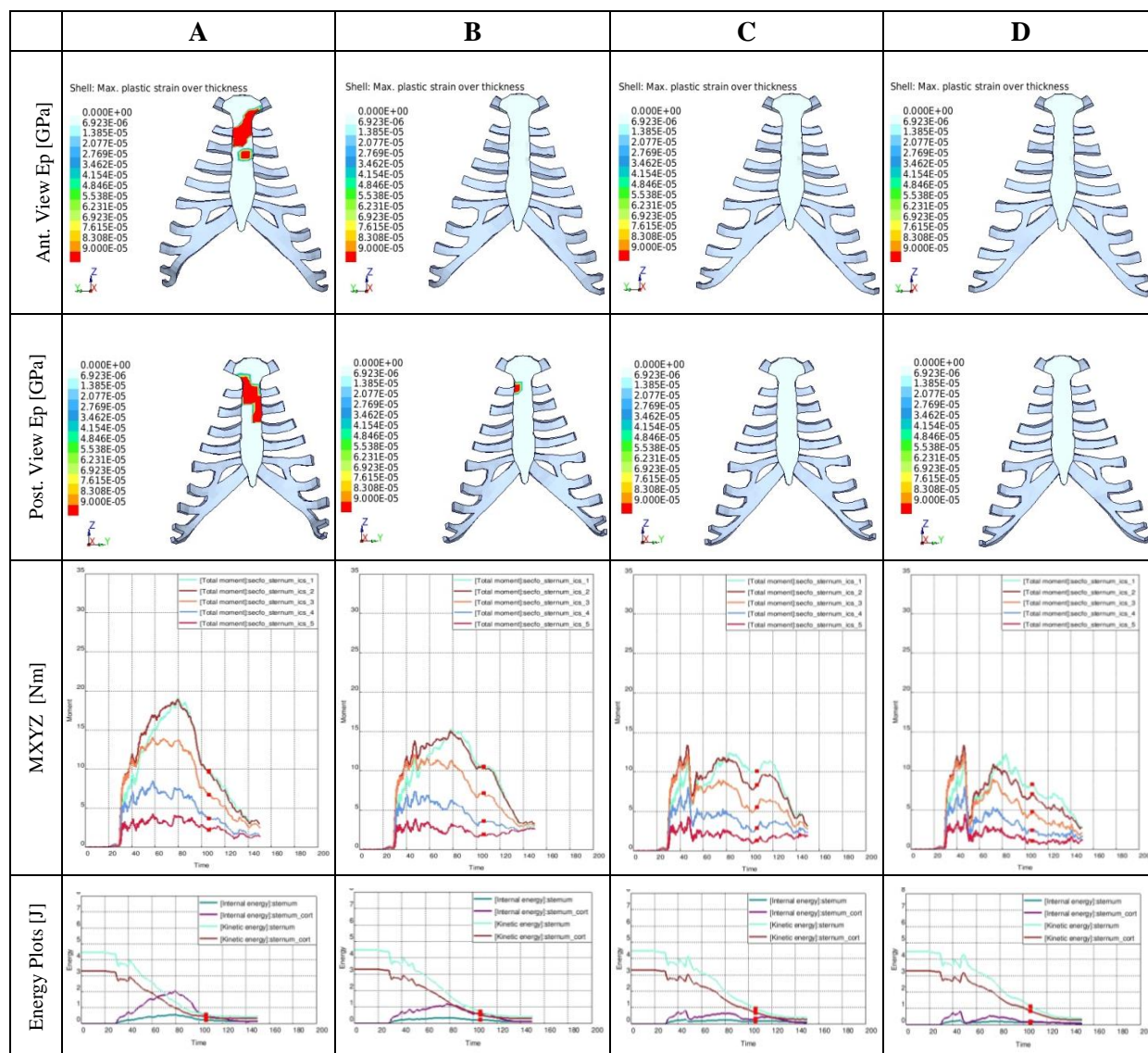


Table 4.19 Crash Case 2: Passenger, Thums-original sternal loading

Thums-elderly Passenger (AIS2 as sternum fracture risk)

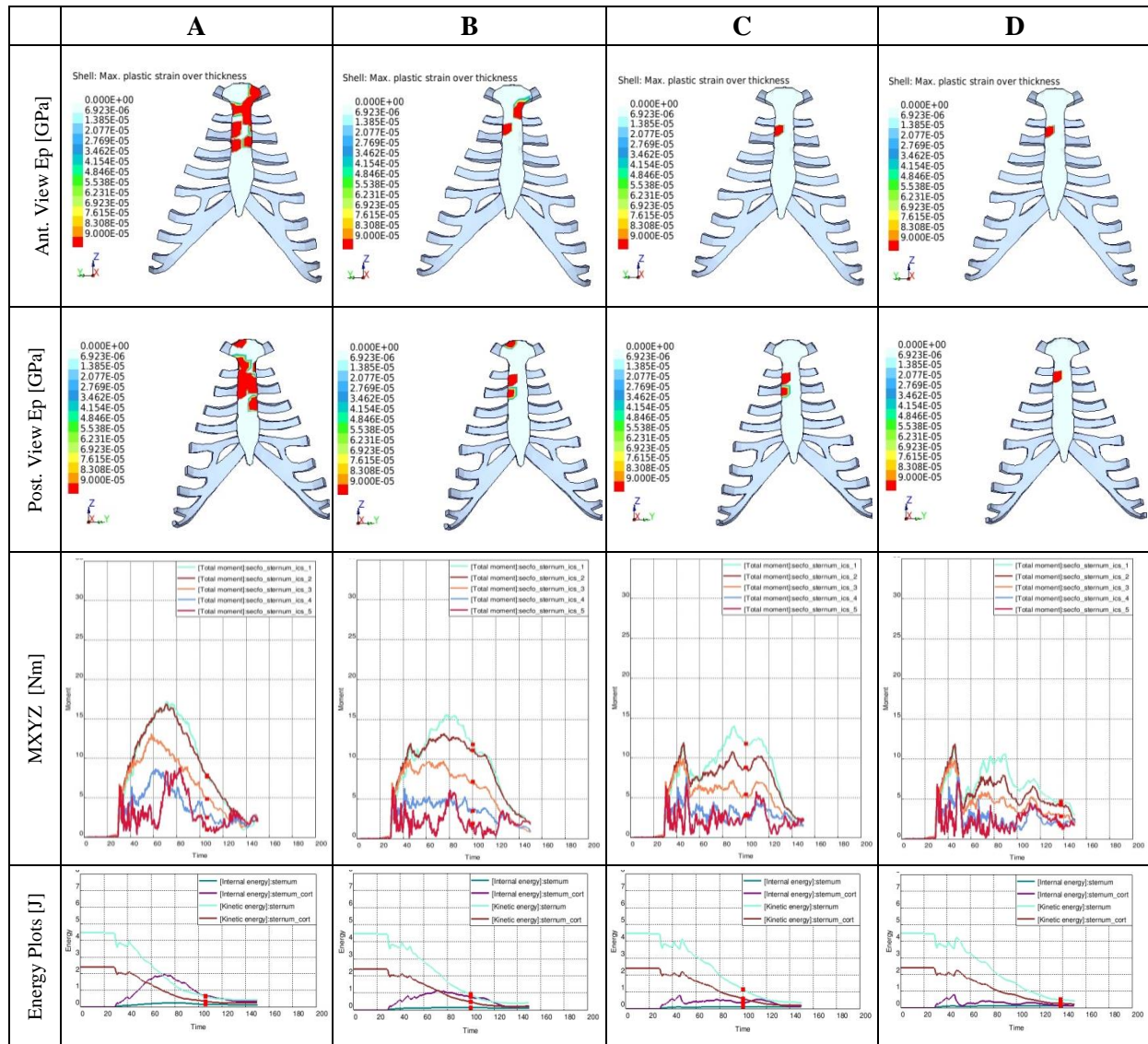


Table 4.20 Crash Case 2: Passenger, Thums-elderly sternal loading

4.2.3 Results Crash Case 3

Injury prediction for:	Restraint System Variant			
	A	B	C	D
<i>H350 Driver (AIS3+) %</i>	3.904	2.223	1.722	1.685
<i>Thums-original Driver (AIS3+) %</i>	45.720	34.860	31.100	22.510
<i>Thums-elderly Driver (AIS3+) %</i>	68.580	58.270	56.620	55.780

Table 4.21 Crash Case 3: Drivers AIS3+ Prediction

Thums-original Driver (AIS2 as sternum fracture risk)

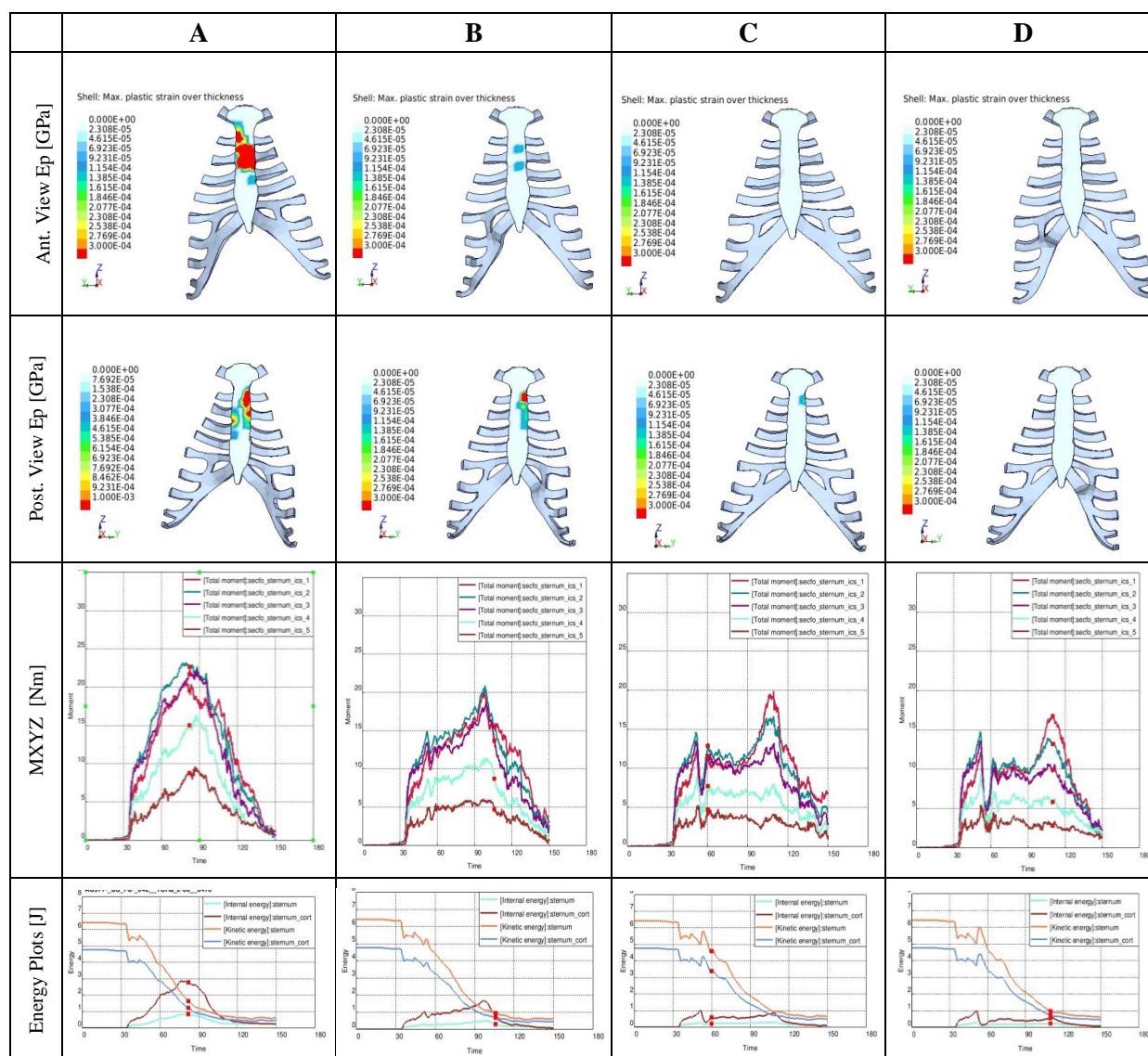


Table 4.22 Crash Case 3: Driver, Thums-original sternal loading

Thums-elderly Driver (AIS2 as sternum fracture risk)

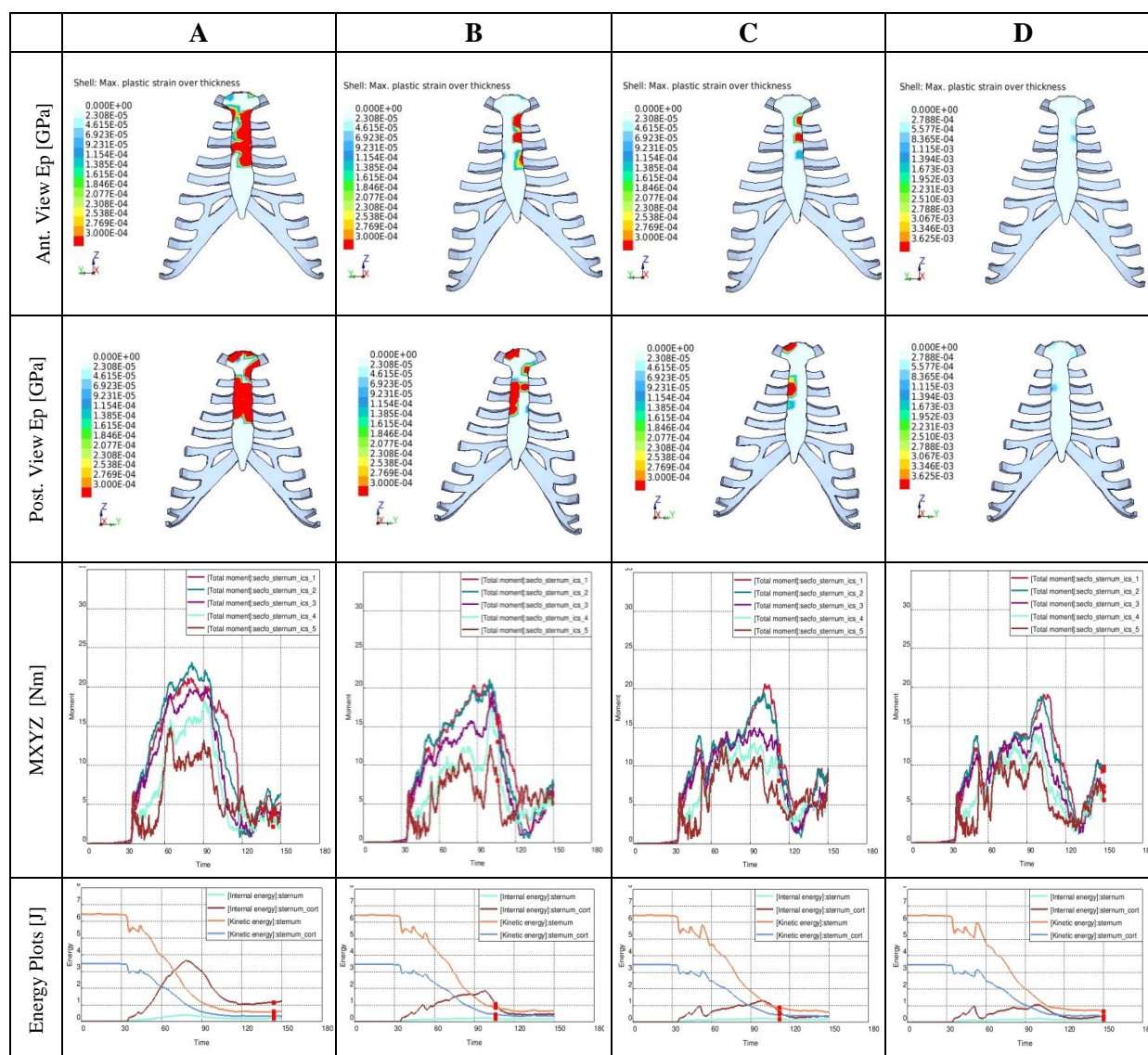


Table 4.23 Crash Case 3:Driver, Thums-elderly sternal loading

Injury prediction for:	Restraint System Variant			
	A	B	C	D
<i>H350 Passenger (AIS3+) %</i>	1.101	1.151	0.758	0.489
<i>Thums-original Passenger (AIS3+)%</i>	38.120	21.190	9.770	10.440
<i>Thums-elderly Passenger (AIS3+)%</i>	49.950	37.740	42.230	23.640

Table 4.24 Crash Case 3: Passengers AIS3+ Prediction

Thums-original Passenger (AIS2 as sternum fracture risk)

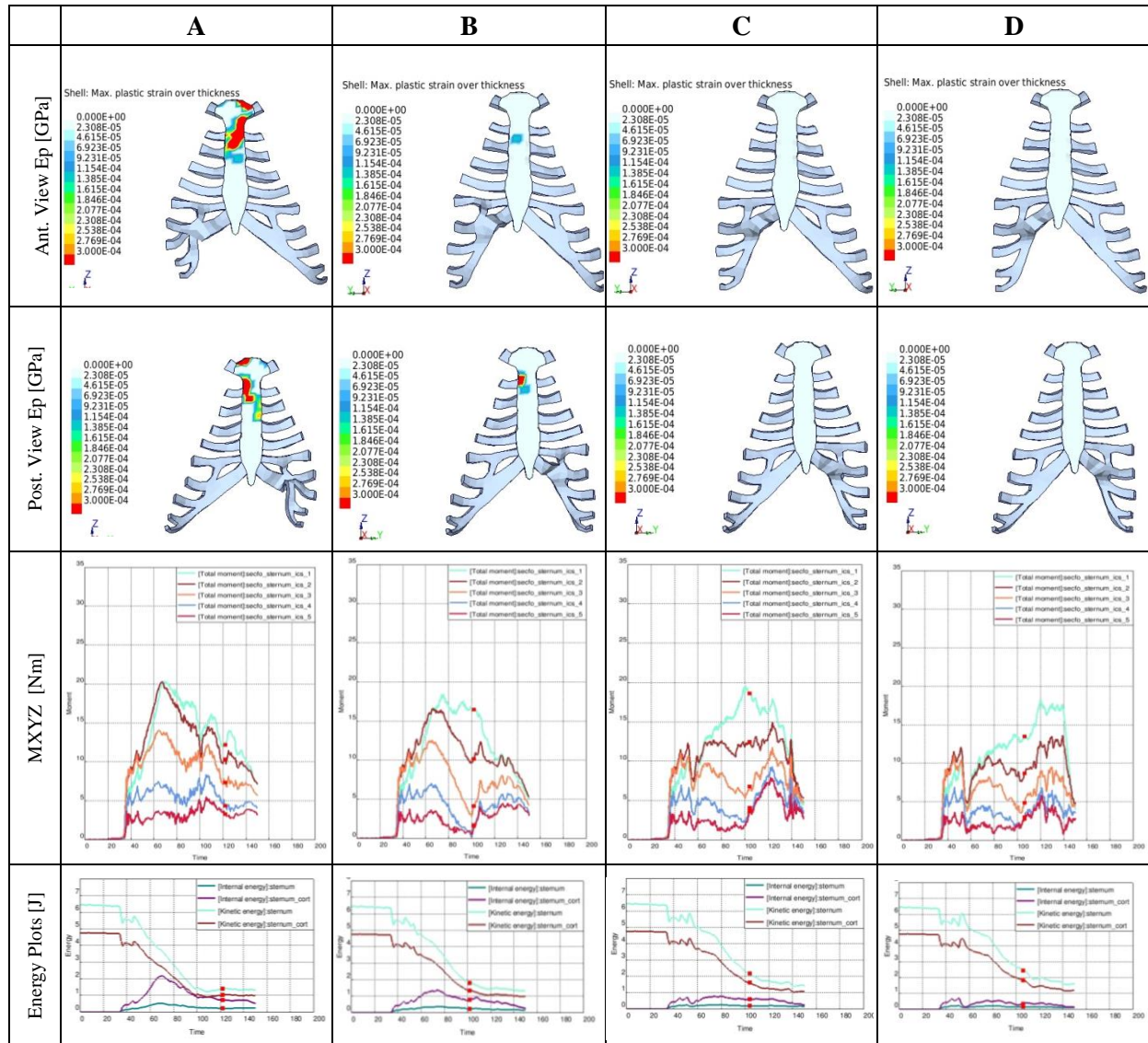


Table 4.25 Crash Case 3: Passenger, Thums-original sternal loading

Thums-elderly Passenger (AIS2 as sternum fracture risk)

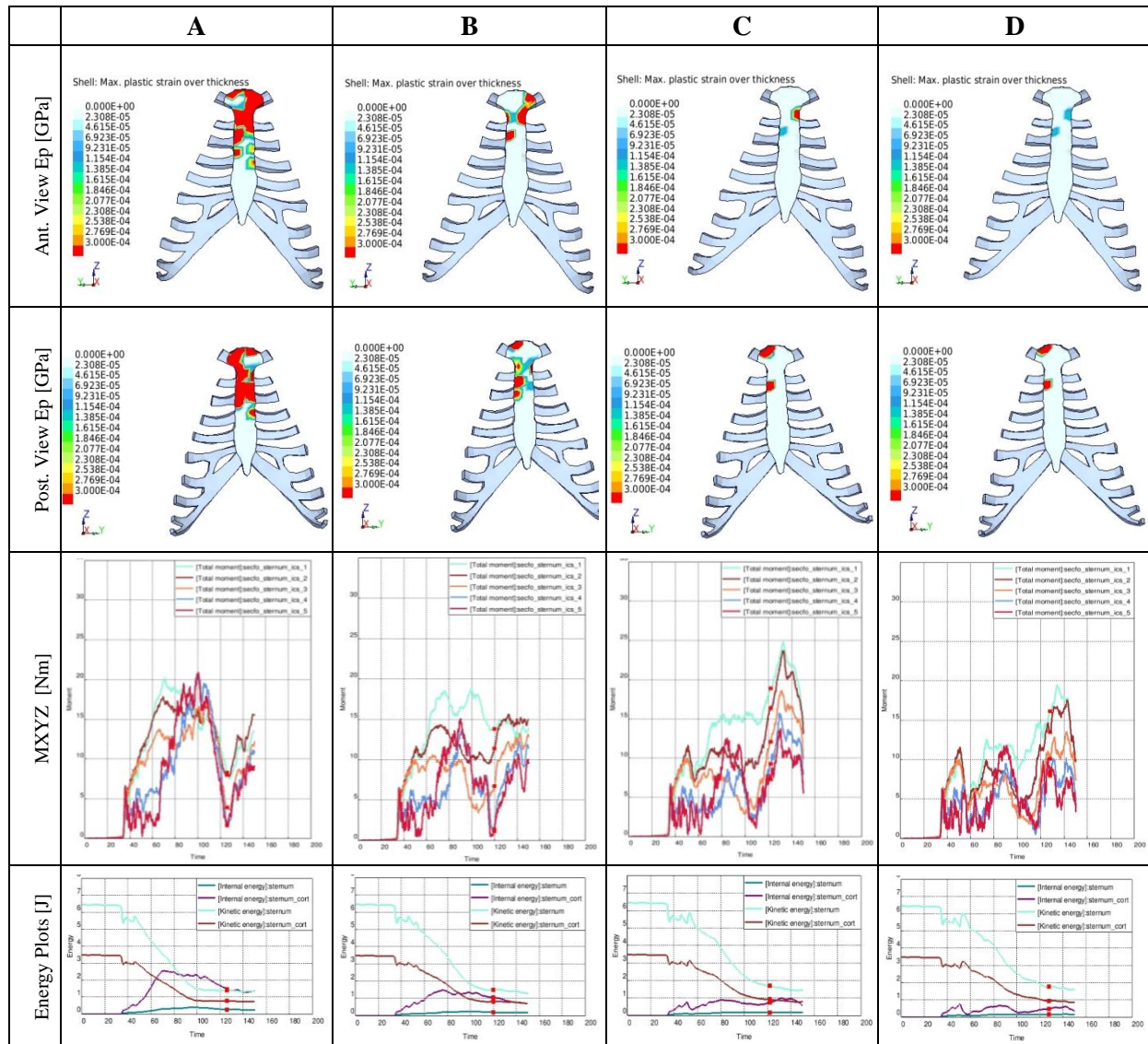


Table 4.26 Crash Case 3: Passenger, Thums-elderly sternal loading

4.2.4 Results Crash Case 4

Injury prediction for:	Restraint System Variant			
	A	B	C	D
<i>H350 Driver (AIS3+) %</i>	4.086	2.928	1.796	1.638
<i>Thums-original Driver (AIS3+)%</i>	21.510	19.490	4.410	10.740
<i>Thums-elderly Driver (AIS3+)%</i>	38.530	26.150	26.810	27.270

Table 4.27 Crash Case 4: Drivers AIS3+ Prediction

Thums-original Driver (AIS2 as sternum fracture risk)

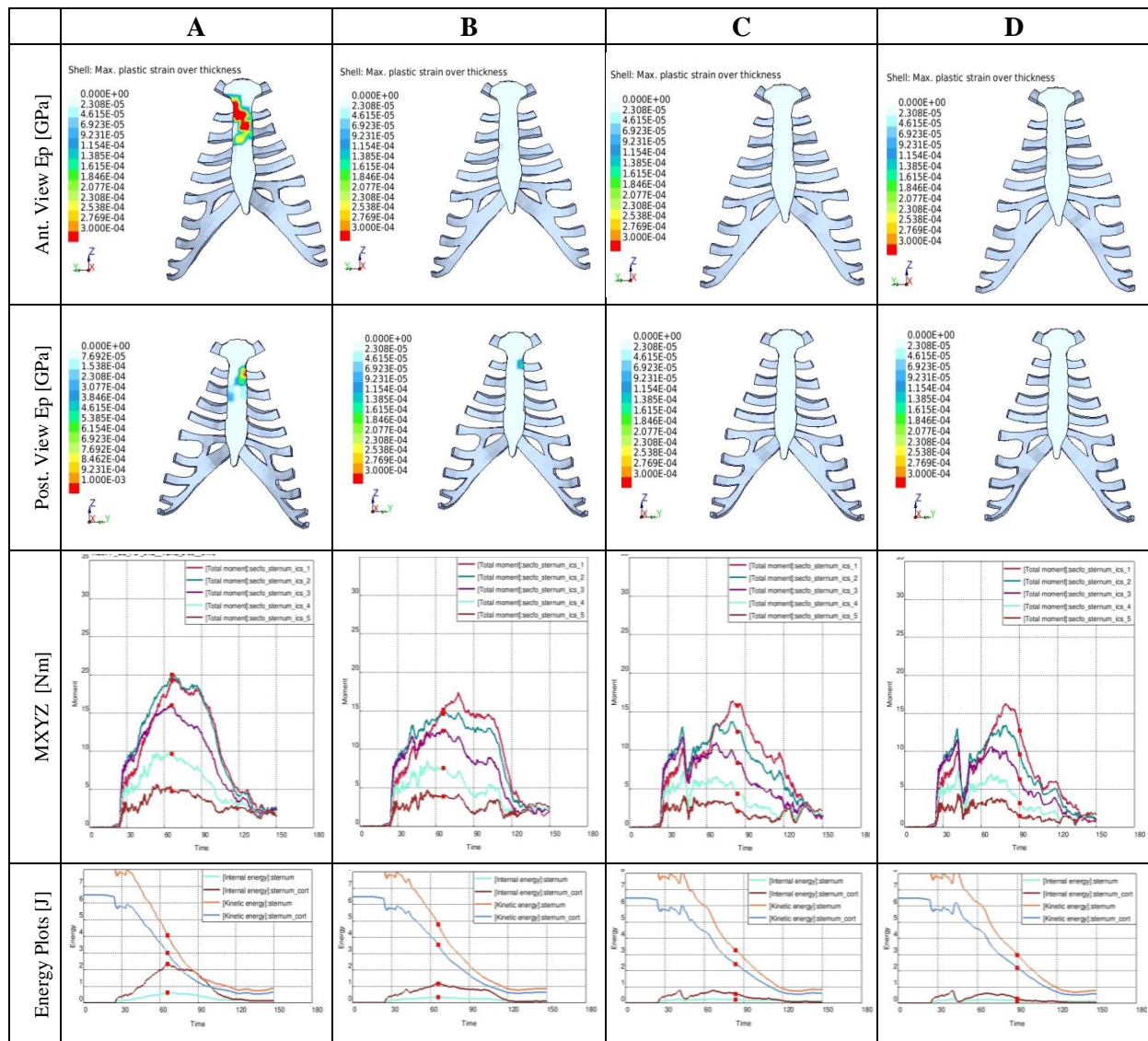


Table 4.28 Crash Case 4: Driver, Thums-original sternal loading

Thums-elderly Driver (AIS2 as sternum fracture risk)

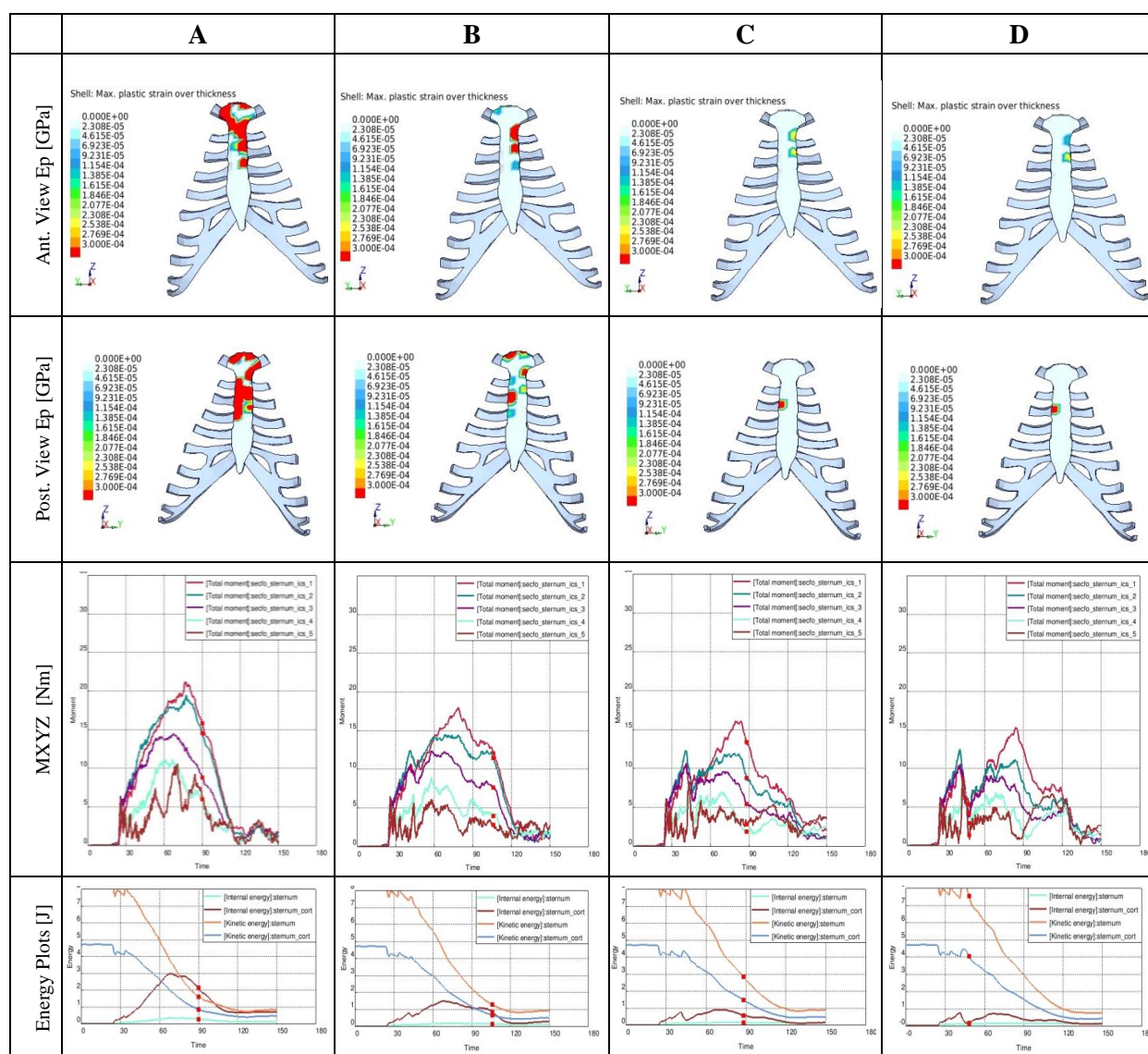


Table 4.29 Crash Case 4:Driver, Thums-elderly sternal loading

Injury prediction for:	Restraint System Variant			
	A	B	C	D
<i>H350 Passenger (AIS3+) %</i>	1.268	0.958	0.639	0.548
<i>Thums-original Passenger (AIS3+) %</i>	28.290	4.460	2.010	2.630
<i>Thums-elderly Passenger (AIS3+) %</i>	37.950	32.630	28.220	27.520

Table 4.30 Crash Case 4: Passengers AIS3+ Prediction

Thums-original Passenger (AIS2 as sternum fracture risk)

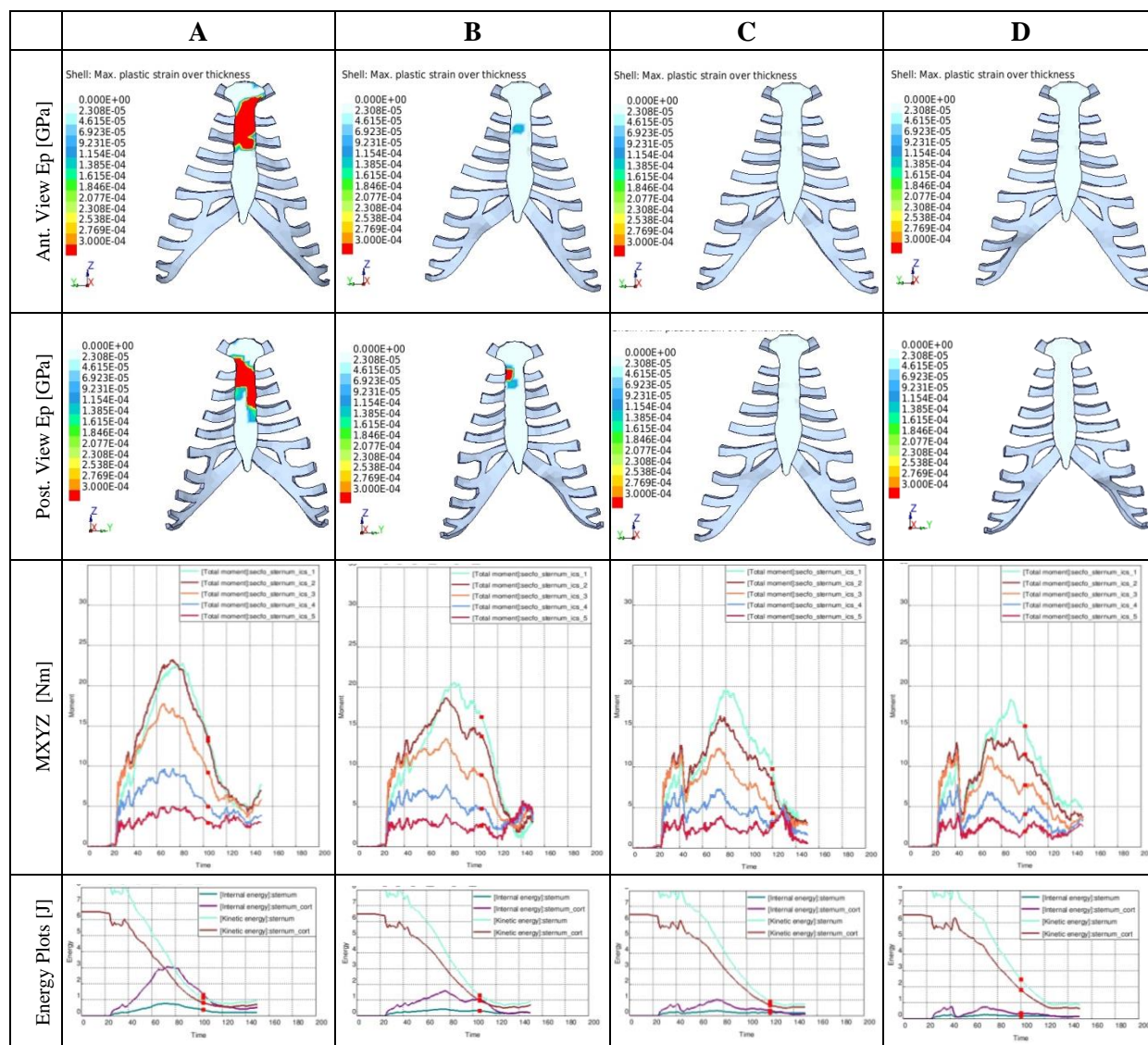


Table 4.31 Crash Case 4: Passenger, Thums-original sternal loading

Thums-elderly Passenger (AIS2 as sternum fracture risk)

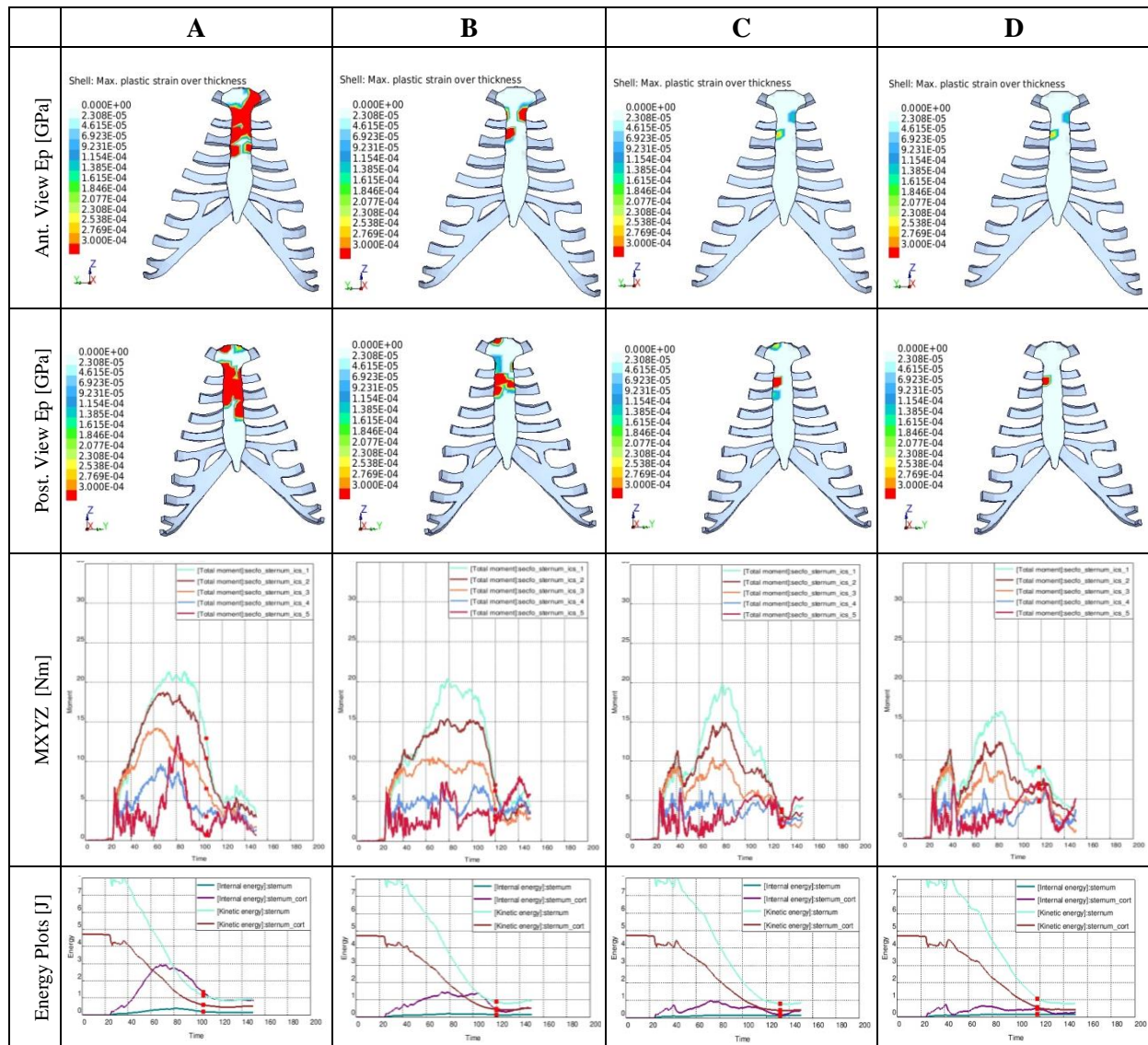


Table 4.32 Crash Case 4: Passenger, Thums-elderly sternal loading

4.2.5 Results Crash Case 5

Injury prediction for:	Restraint System Variant			
	A	B	C	D
<i>H350 Driver (AIS3+) %</i>	4.920	4.367	3.789	3.159
<i>Thums-original Driver (AIS3+) %</i>	56.970	37.430	41.140	45.160
<i>Thums-elderly Driver (AIS3+) %</i>	73.780	50.060	49.200	48.730

Table 4.33 Crash Case 5: Drivers AIS3+ Prediction

Thums-original Driver (AIS2 as sternum fracture risk)

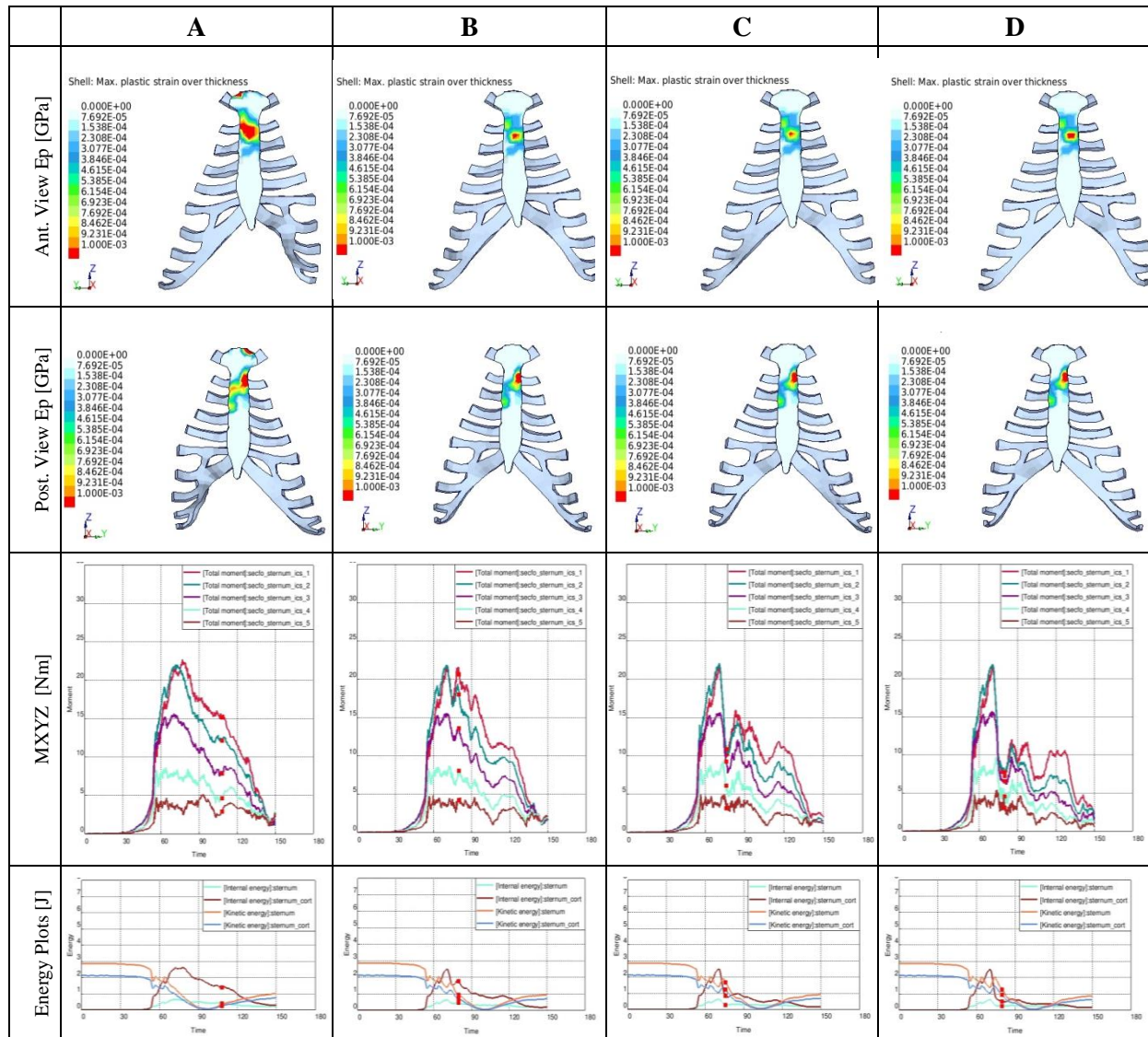


Table 4.34 Crash Case 5:Driver, Thums-original sternal loading

Thums-elderly Driver (AIS2 as sternum fracture risk)

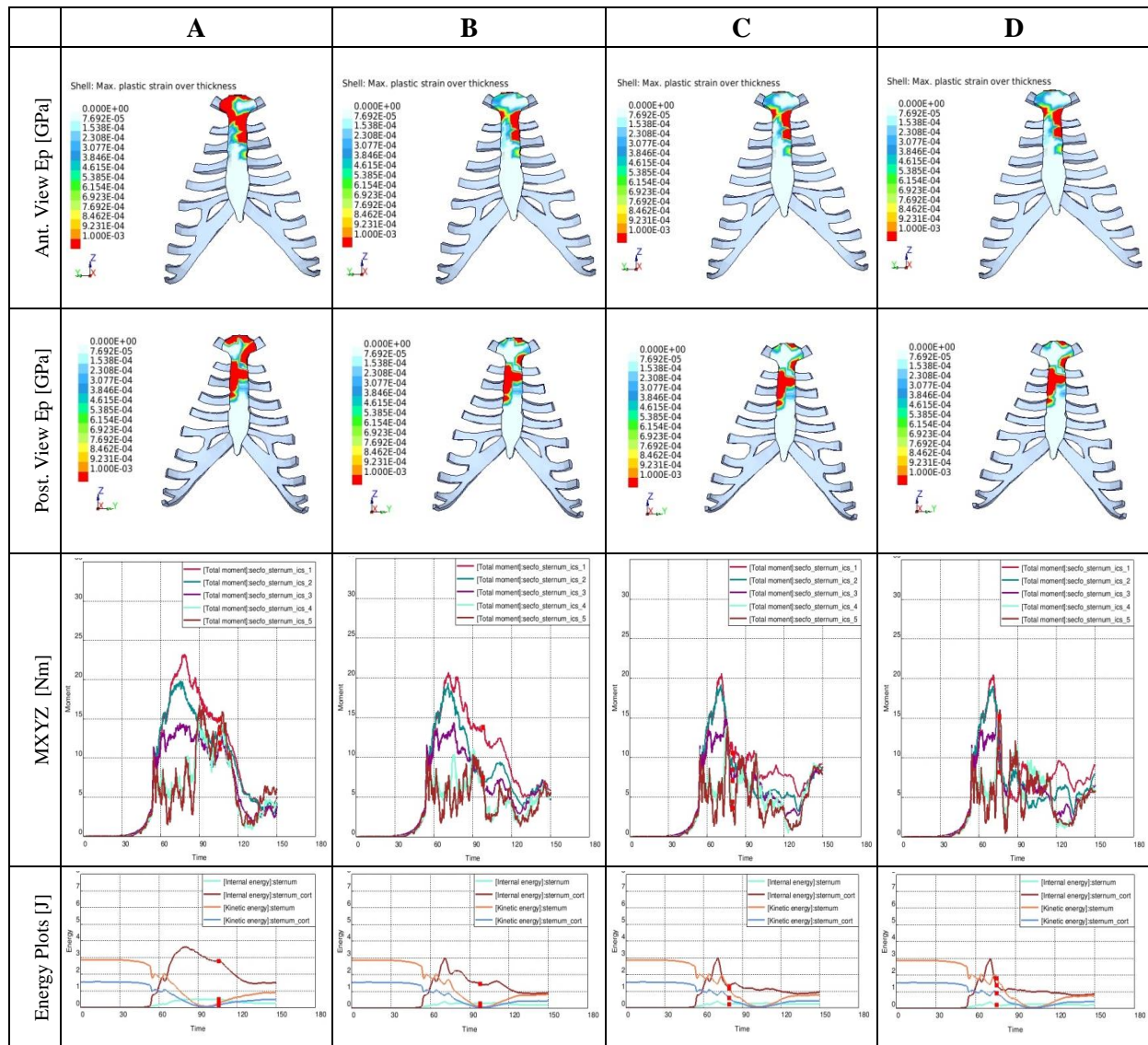


Table 4.35 Crash Case 5:Driver, Thums-elderly sternal loading

Injury prediction for:	Restraint System Variant			
	A	B	C	D
<i>H350 Passenger (AIS3+) %</i>	2.133	1.375	1.364	1.379
<i>Thums-original Passenger (AIS3+) %</i>	66.780	37.390	27.530	26.840
<i>Thums-elderly Passenger (AIS3+) %</i>	65.910	40.600	43.020	46.740

Table 4.36 Crash Case 5: Passengers AIS3+ Prediction

Thums-original Passenger (AIS2 as sternum fracture risk)

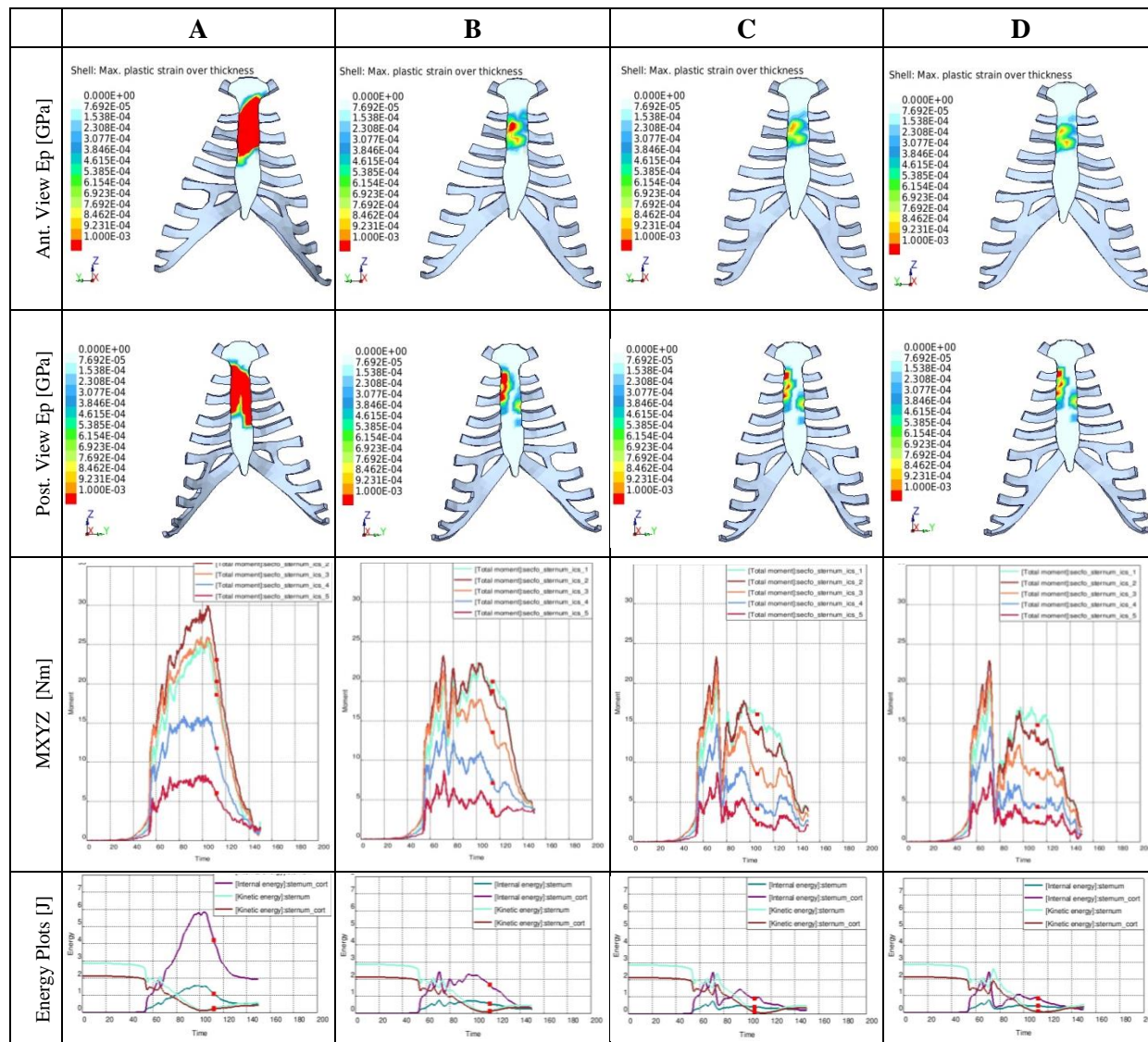


Table 4.37 Crash Case 5: Passenger, Thums-original sternal loading

Thums-elderly Passenger (AIS2 as sternum fracture risk)

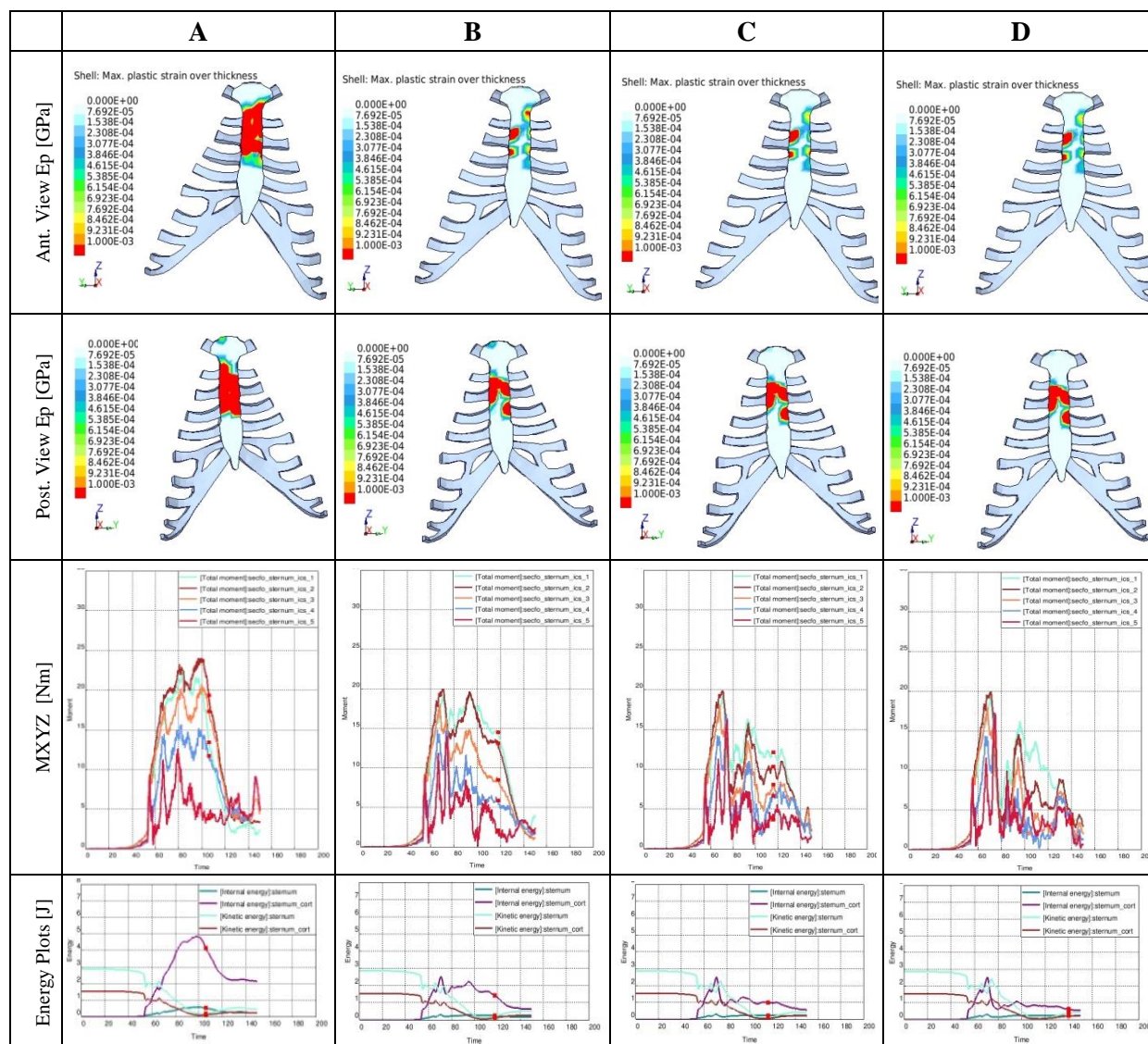


Table 4.38 Crash Case 5:Passenger, Thums-elderly sternal loading

4.2.6 Results Crash Case 6

Injury prediction for:	Restraint System Variant			
	A	B	C	D
<i>H350 Driver (AIS3+) %</i>	5.814	3.384	2.577	PHC
<i>Thums-original Driver (AIS3+) %</i>	65.740	44.070	PHC	PHC
<i>Thums-elderly Driver (AIS3+) %</i>	71.310	59.450	PHC	PHC

Table 4.39 Crash Case 6: Drivers AIS3+ Prediction

Thums-original Driver (AIS2 as sternum fracture risk)

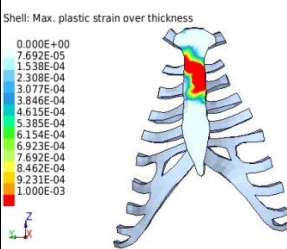
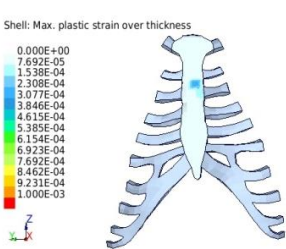
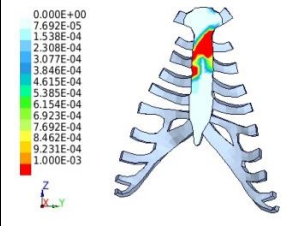
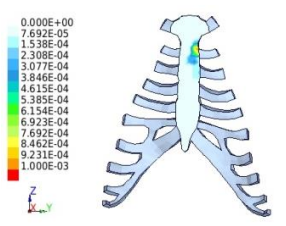
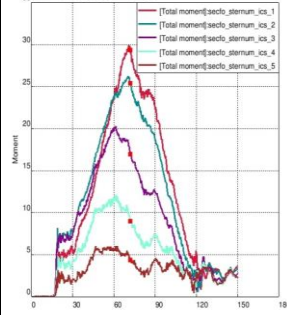
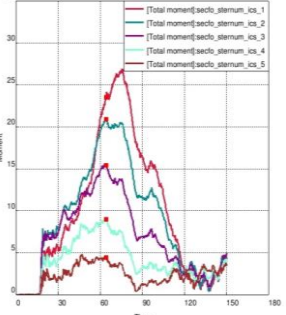
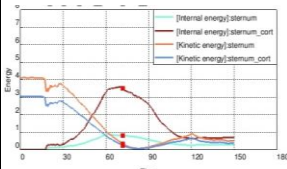
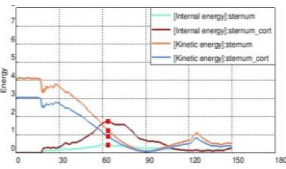
	A	B	C	D
Ant. View Ep [GPa]			Possible Head Contact	PHC
Post. View Ep [GPa]			PHC	PHC
MXYZ [Nm]			PHC	PHC
Energy Plots [J]			PHC	PHC

Table 4.40 Crash Case 6: Driver, Thums-original sternal loading

Thums-elderly Driver (AIS2 as sternum fracture risk)

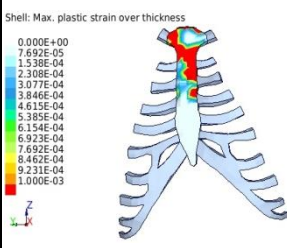
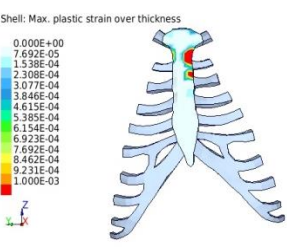
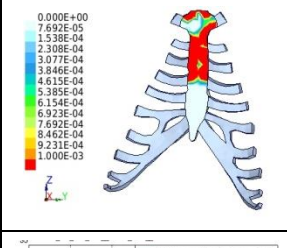
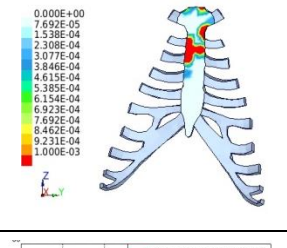
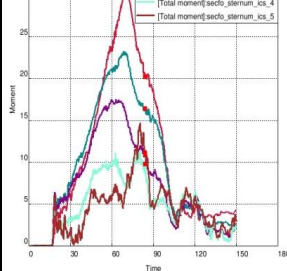
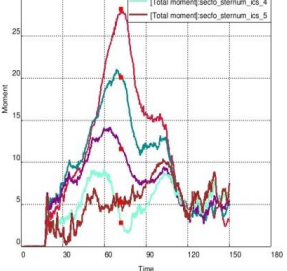
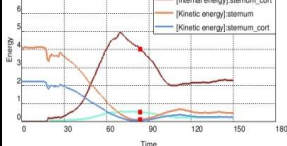
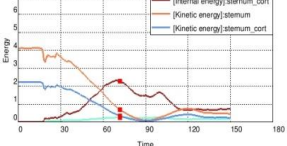
	A	B	C	D
Ant. View Ep [GPa]			PHC	PHC
Post. View Ep [GPa]			PHC	PHC
MMYZ [Nm]			PHC	PHC
Energy Plots [J]			PHC	PHC

Table 4.41 Crash Case 6:Driver, Thums-elderly sternal loading

!

Injury prediction for:	Restraint System Variant			
	A	B	C	D
<i>H350 Passenger (AIS3+) %</i>	1.851	1.955	1.259	PHC
<i>Thums-original Passenger (AIS3+) %</i>	60.510	23.650	PHC	PHC
<i>Thums-elderly Passenger (AIS3+) %</i>	63.570	45.730	PHC	PHC

Table 4.42 Crash Case 6: Passengers AIS3+ Prediction

Thums-original Passenger (AIS2 as sternum fracture risk)

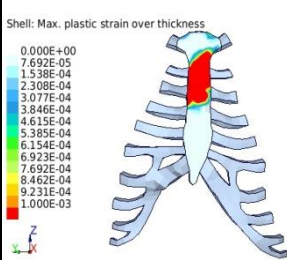
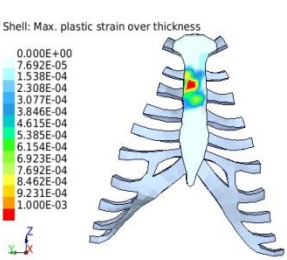
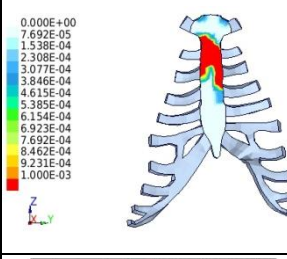
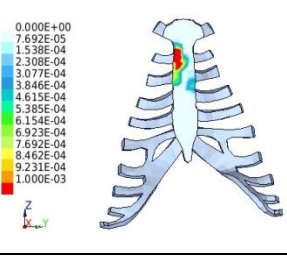
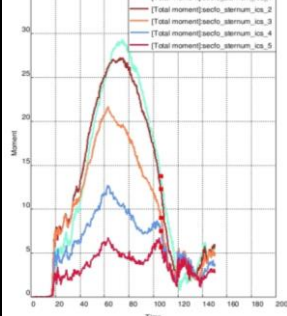
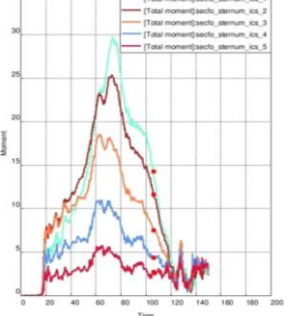
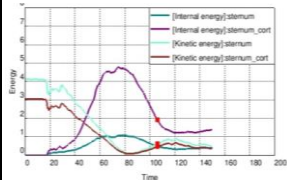
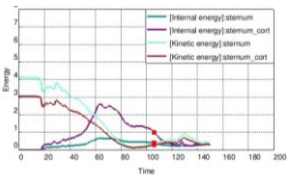
	A	B	C	D
Ant. View Ep [GPa]			PHC	PHC
Post. View Ep [GPa]			PHC	PHC
MXYZ [Nm]			PHC	PHC
Energy Plots [J]			PHC	PHC

Table 4.43 Crash Case 6: Passenger, Thums-original sternal loading

Thums-elderly Passenger (AIS2 as sternum fracture risk)

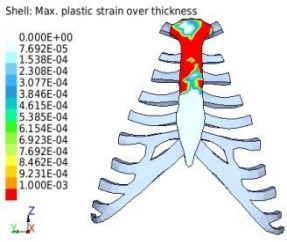
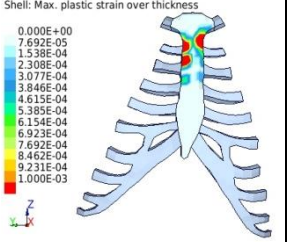
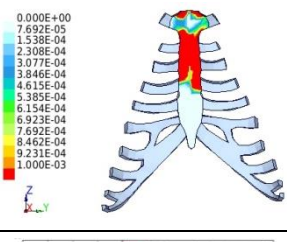
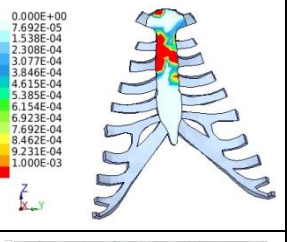
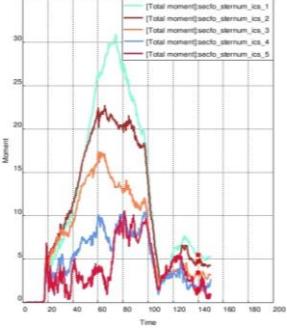
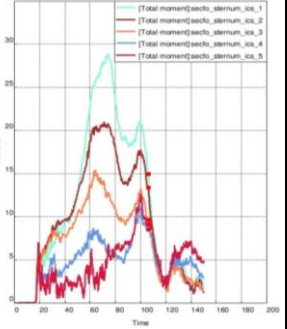
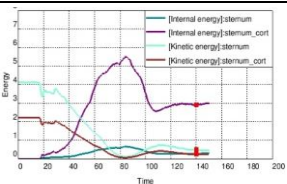
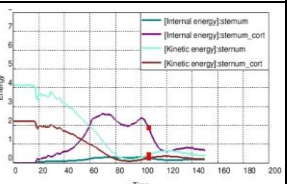
	A	B	C	D
Ant. View Ep [GPa]			PHC	PHC
Post. View Ep [GPa]			PHC	PHC
MMYZ [Nm]			PHC	PHC
Energy Plots [J]			PHC	PHC

Table 4.44 Crash Case 6:Passenger, Thums-elderly sternal loading

4.2.7 Results Crash Case 7

Injury prediction for:	Restraint System Variant			
	A	B	C	D
<i>H350 Driver (AIS3+) %</i>	11.765	9.691	9.187	PHC
<i>Thums-original Driver (AIS3+) %</i>	86.860	73.110	PHC	PHC
<i>Thums-elderly Driver (AIS3+) %</i>	86.400	81.680	PHC	PHC

Table 4.45 Crash Case 7: Drivers AIS3+ Prediction

Thums-original Driver (AIS2 as sternum fracture risk)

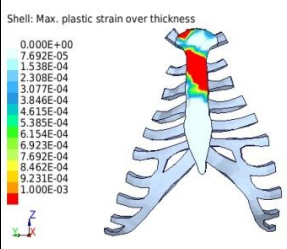
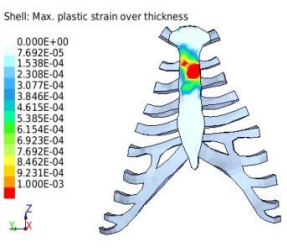
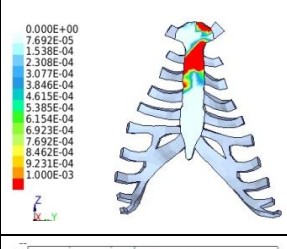
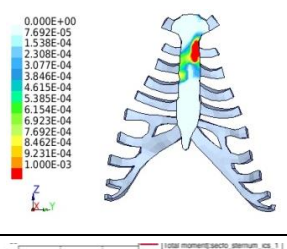
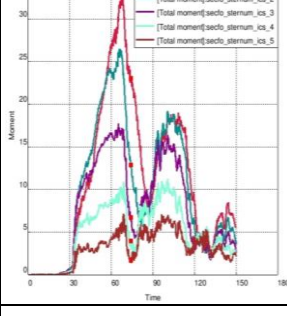
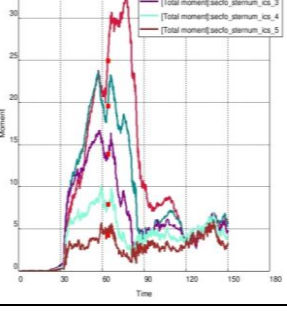
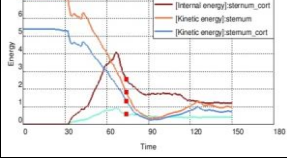
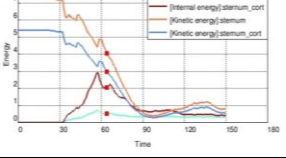
	A	B	C	D
Ant. View Ep [GPa]			PHC	PHC
Post. View Ep [GPa]			PHC	PHC
MXYZ [Nm]			PHC	PHC
Energy Plots [J]			PHC	PHC

Table 4.46 Crash Case 7:Driver, Thums-original sternal loading

Thums-elderly Driver (AIS2 as sternum fracture risk)

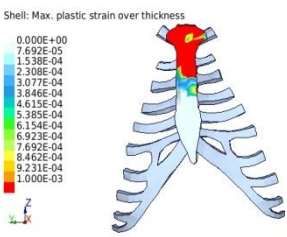
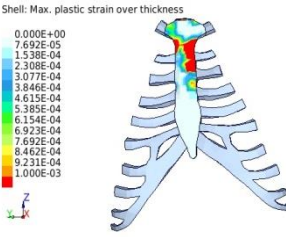
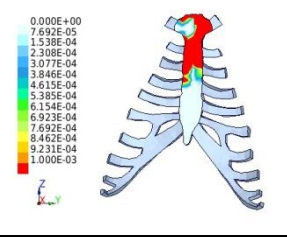
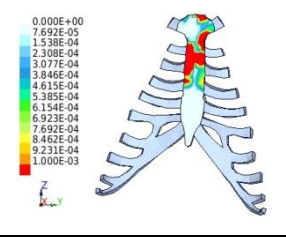
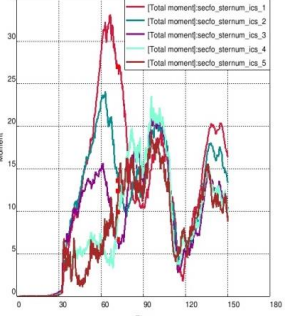
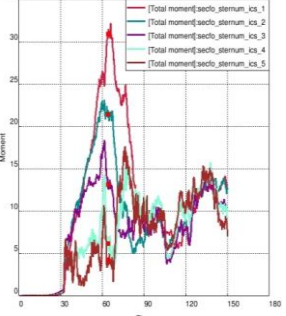
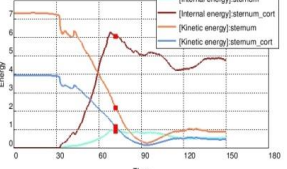
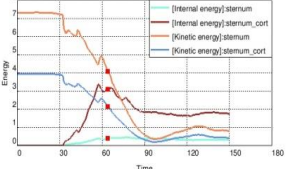
	A	B	C	D
Ant. View Ep [GPa]			PHC	PHC
Post. View Ep [GPa]			PHC	PHC
MXYZ [Nm]			PHC	PHC
Energy Plots [J]			PHC	PHC

Table 4.47 Crash Case 7:Driver, Thums-elderly sternal loading

Injury prediction for:	Restraint System Variant			
	A	B	C	D
<i>H350 Passenger (AIS3+) %</i>	2.209	3.559	3.345	PHC
<i>Thums-original Passenger (AIS3+) %</i>	73.560	76.020	PHC	PHC
<i>Thums-elderly Passenger (AIS3+) %</i>	86.990	85.400	PHC	PHC

Table 4.48 Crash Case 7: Passengers AIS3+ Prediction

Thums-original Passenger (AIS2 as sternum fracture risk)

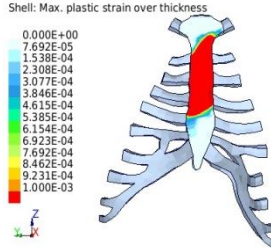
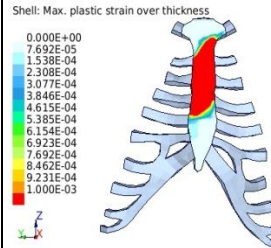
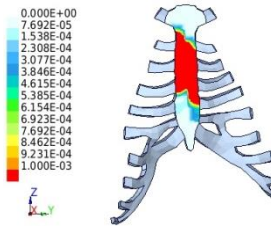
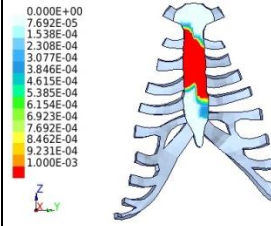
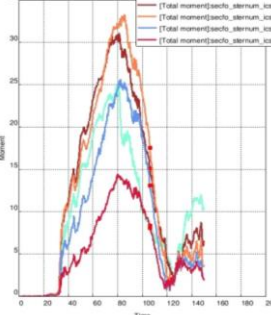
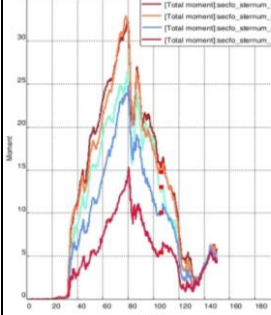
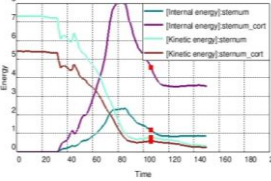
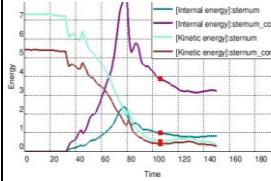
	A	B	C	D
Ant. View Ep [GPa]			PHC	PHC
Post. View Ep [GPa]			PHC	PHC
MMXYZ [Nm]			PHC	PHC
Energy Plots [J]			PHC	PHC

Table 4.49 Crash Case 7: Passenger, Thums-original sternal loading

Thums-elderly Passenger (AIS2 as sternum fracture risk)

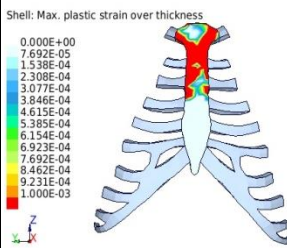
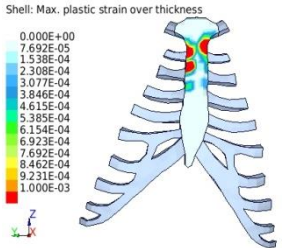
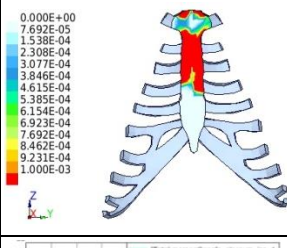
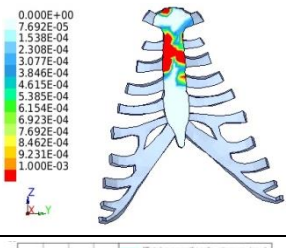
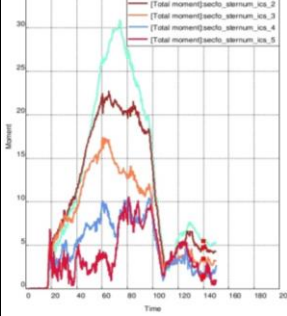
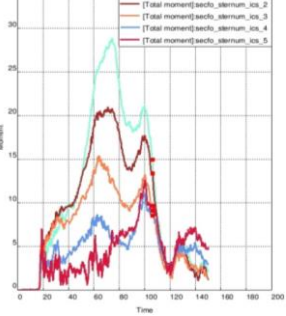
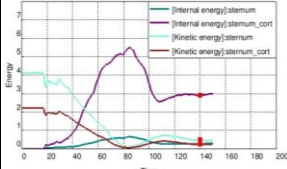
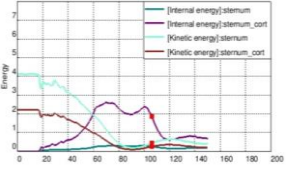
	A	B	C	D
Ant. View Ep [GPa]			PHC	PHC
Post. View Ep [GPa]			PHC	PHC
MXYZ [Nm]			PHC	PHC
Energy Plots [J]			PHC	PHC

Table 4.50 Crash Case 7: Passenger, Thums-elderly sternal loading

4.3 Summary of Results: All occupants, all crash cases

Injury and load prediction for all passengers, restraint variants and loadcases are presented below. Comments are included for the most relevant observations. The results are analyzed in 5.4.

4.3.1 H350 Driver and Passenger

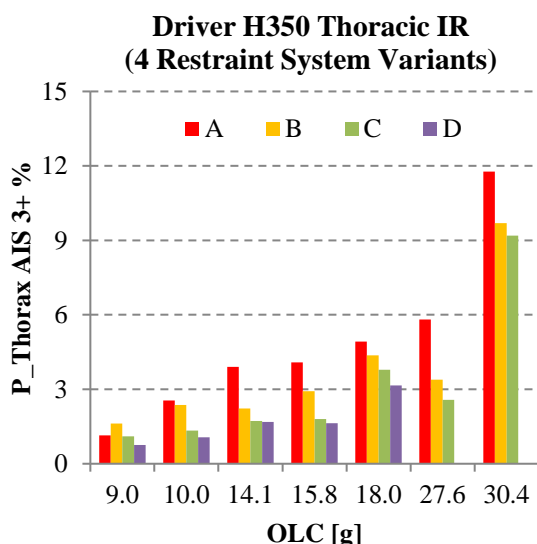


Fig. 4.12 Driver H350 thoracic injury risk for all restraint system variants

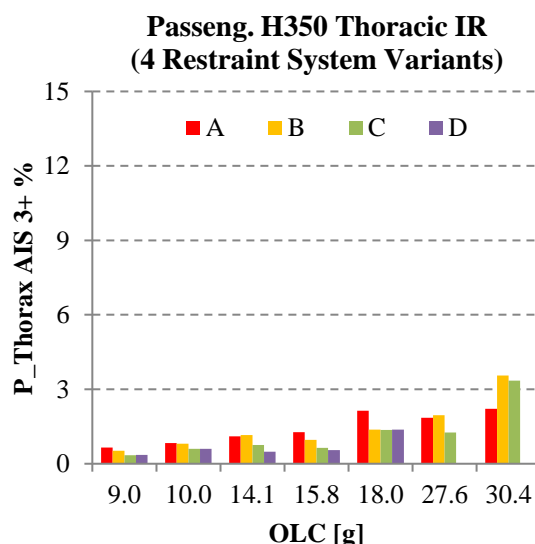


Fig. 4.13 Passenger H350 thoracic injury risk for all restraint system variants

Comments

Fig. 4.12 and Fig. 4.13. The H350 AIS3+ risk differs between driver and passenger, being markedly higher for the driver. This suggests that the risk of medium severity injuries will be lower for the passenger side. The injury outcome of the accident reconstruction shows the opposite: Driver AIS1 and passenger AIS2. HBMs show a comparable risk of both driver and passenger sides. The sternal loading is higher for the HBMs passenger (Fig. 4.14 to Fig. 4.17).

In addition, the H350 AIS3+ injury prediction shows, as expected, a clear trend was the strategy of lower load limiting plus airbag-dominated restraint reduce the injury probability, independent of the crash severity. In the crash cases 6 (OLC 27,60g) and 7 (OLC 30,40g) the results of the strategy D was no longer considered due to the high risk of head-to-steering wheel contact.

For the passenger side, the H350 prediction showed the restraint variants B and C to be ineffective. This outcome is dependent on the chosen configuration for the crash case 7, where the load limiting levels are kept, but not the original trigger strategy for the other loadcases.

4.3.2 Thums-original Driver and Passenger

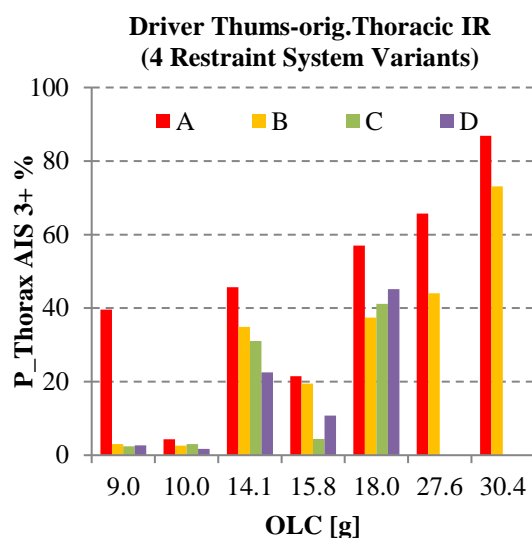


Fig. 4.14 Driver Thums-original thoracic injury risk for all restraint system variants

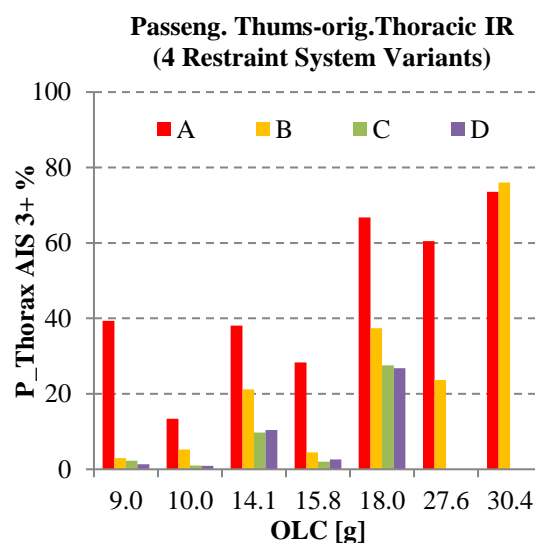


Fig. 4.15 Passenger Thums-original thoracic injury risk for all restraint system variants

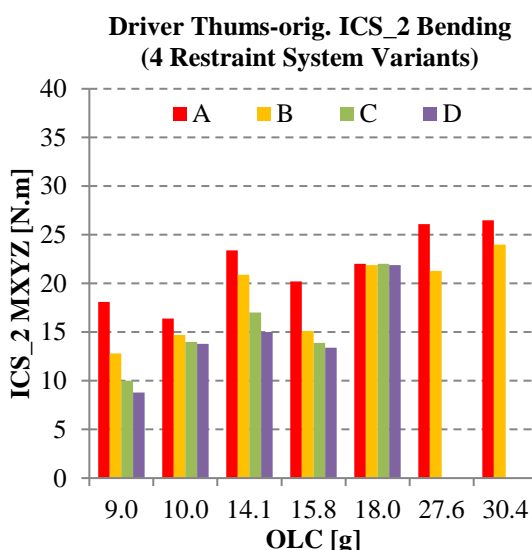


Fig. 4.16 Driver Thums-original ICS_2 bending for all restraint system variants

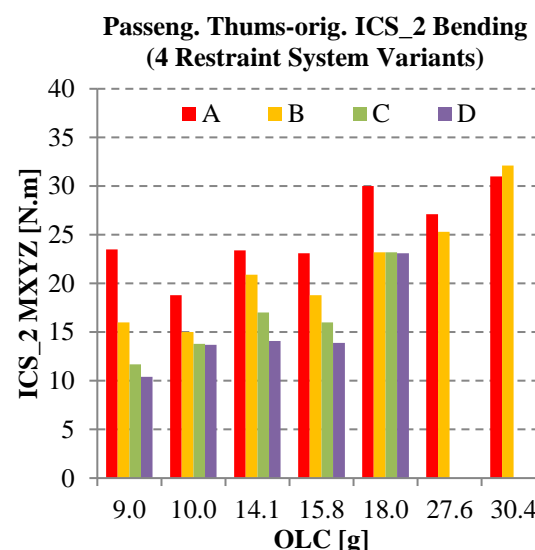


Fig. 4.17 Passenger Thums-original ICS_2 bending for all restraint system variants

Comments

In the accident reconstruction case, the sternal loading (defined as ICS_2 MXYZ) for the variant “A” shows higher load levels sustained by the HBMs passenger. In the real accident the passenger sustained a sternal fracture. The driver’s injury outcome was AIS1. The Thums-original shows a comparable AIS3+ risk of both driver and passenger sides. The sternal loading is higher for the HBMs passenger, variant A (Fig. 4.14 to Fig. 4.17).

4.3.3 Thums-elderly Driver and Passenger

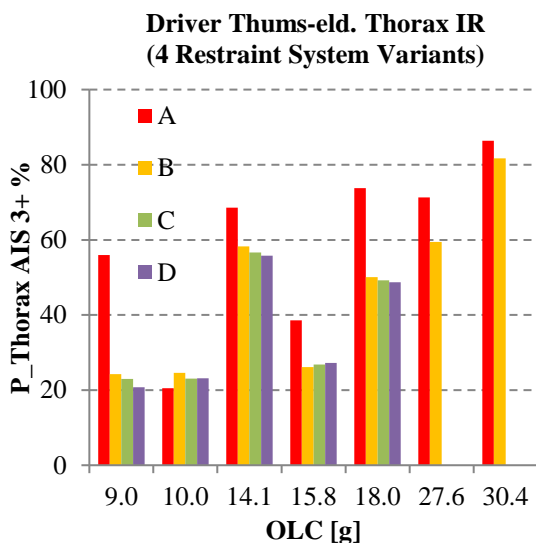


Fig. 4.18 Driver Thums-elderly thoracic injury risk for all restraint system variants

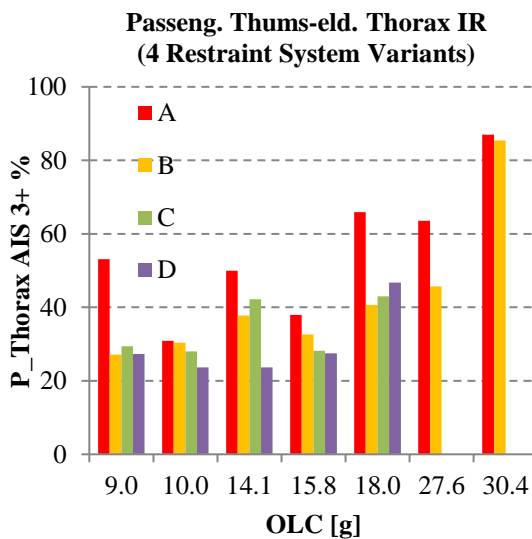


Fig. 4.19 Passenger Thums-elderly thoracic injury risk for all restraint system variants

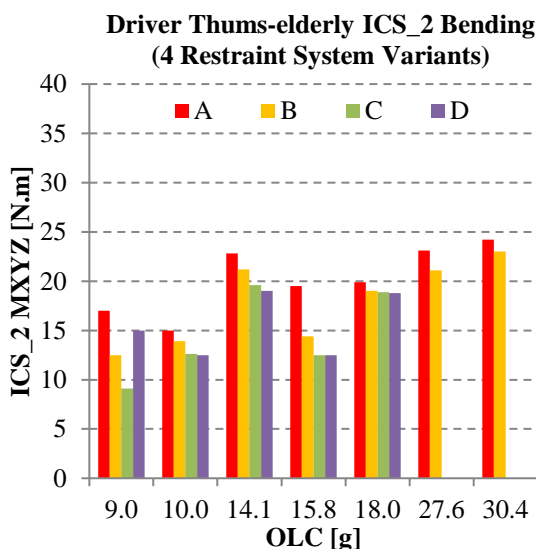


Fig. 4.20 Driver Thums-elderly ICS_2 bending for all restraint system variants

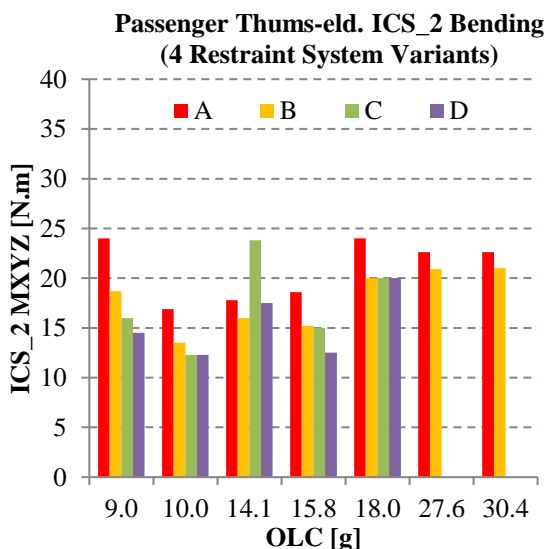


Fig. 4.21 Passenger Thums-elderly ICS_2 bending for all restraint system variants

Comments

Same trends were found here for the AIS3+ and sternal loading compared to the Thums-original. The load reduction showed to have less effectiveness on the Thums-elderly. This could be interpreted as an ageing effect. As for the H350 simulations, the crash cases 6 (OLC 27,60g) and 7 (OLC 30,40g) with restraint variants C and D were no longer considered. Those cases represented high risk of head-to-steering wheel contact (PHC).

4.3.4 Correlations

Linear regressions for injury outcome with respect to crash severity are plotted. All occupants are included. A “rate of benefit” have been defined based on the slope of the regression when an intercept with the vertical axis constraint on zero is imposed. This satisfies also the constraint null injury outcome at zero loading.

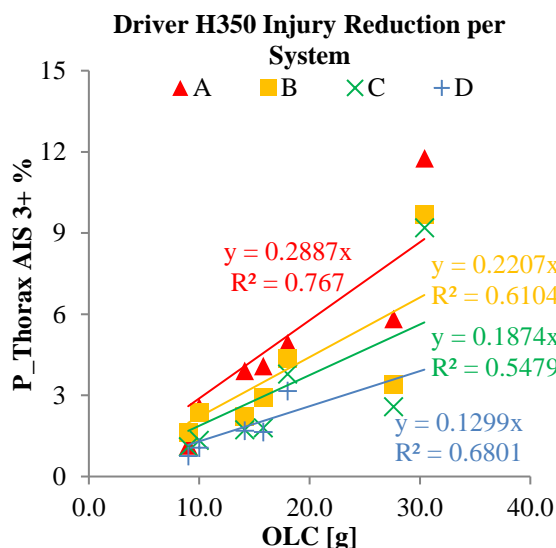


Fig. 4.22 Driver HJ350 injury reduction per system

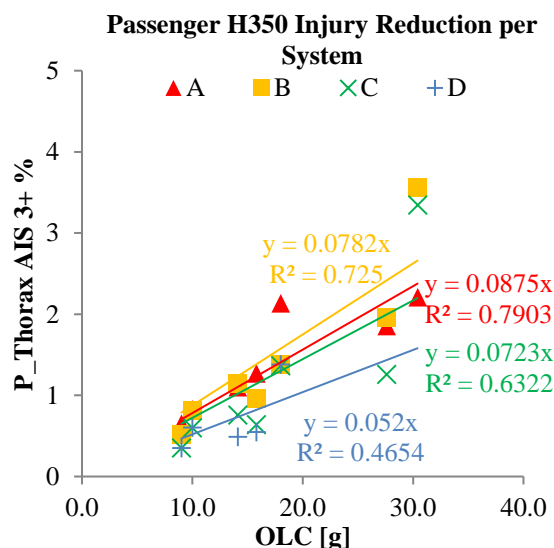


Fig. 4.23 Passenger HJ350 injury reduction per system

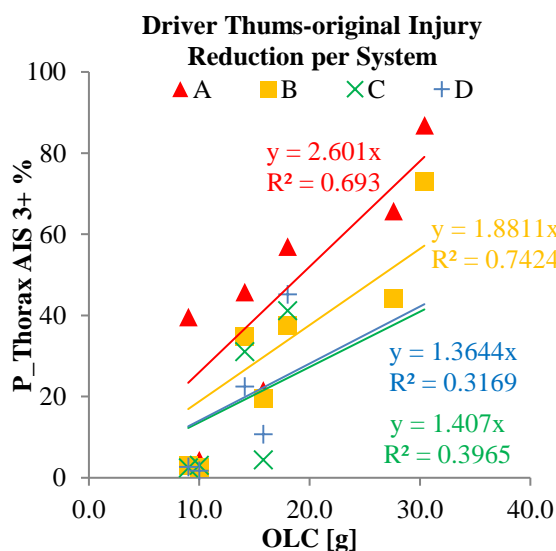


Fig. 4.24 Driver Thums-original injury reduction per system

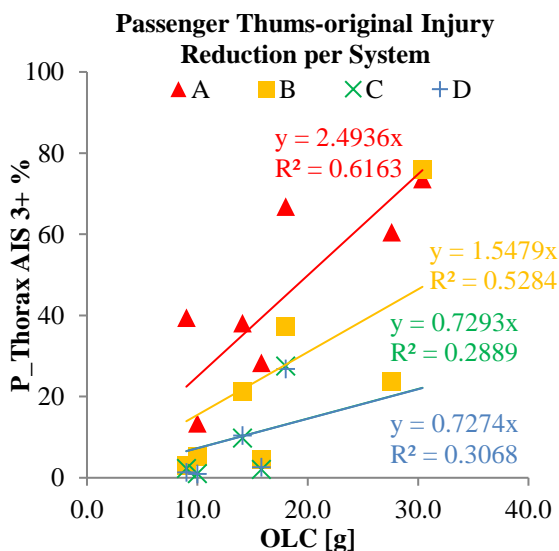


Fig. 4.25 Passenger Thums-original injury reduction per system

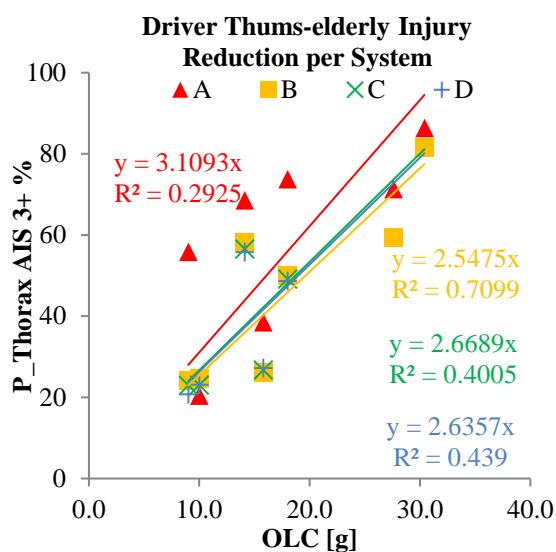


Fig. 4.26 Driver Thums-elderly injury reduction per system

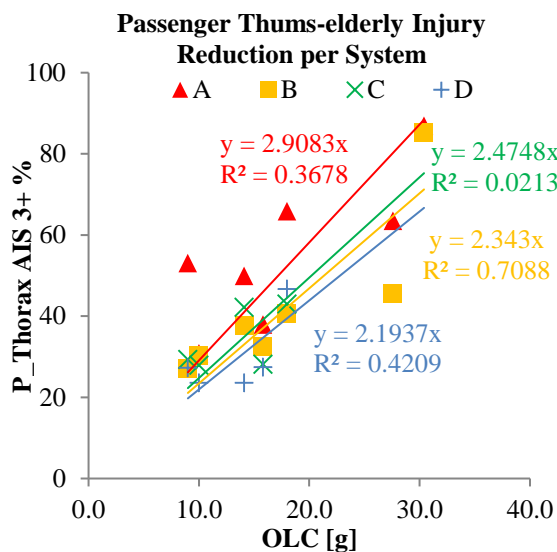


Fig. 4.27 Passenger Thums-elderly injury reduction per system

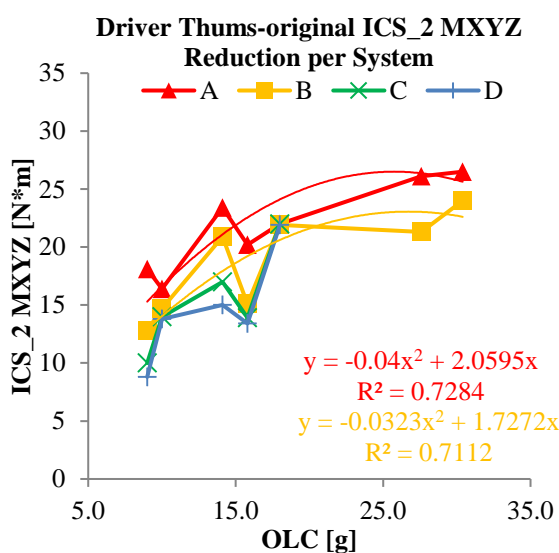


Fig. 4.28 Driver Thums-original ICS_2 MXYZ reduction per system

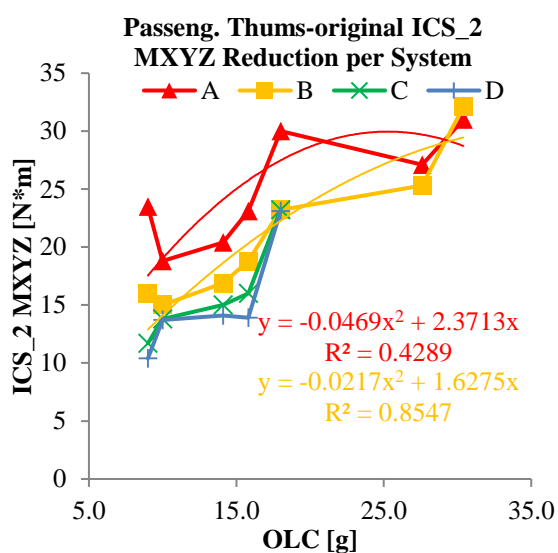


Fig. 4.29 Passenger Thums-original ICS_2 MXYZ reduction per system

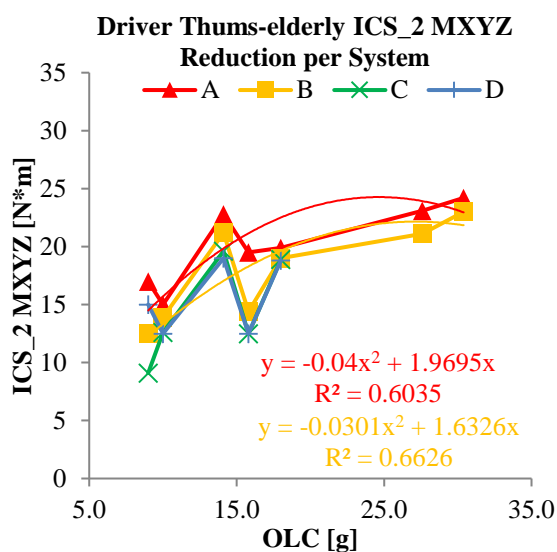


Fig. 4.30 Driver Thums-elderly ICS_2 MXYZ reduction per system

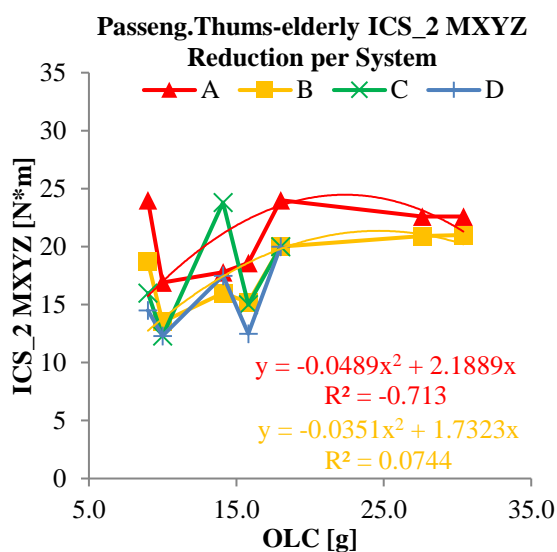


Fig. 4.31 Passenger Thums-elderly ICS_2 MXYZ Reduction per system

Note the outliers on the crash case 3 (OLC 14.1). The injury prediction at this stage can be interpreted based on the VY pulse. The hypothesis for this loadcase is, the variants B and C generate a larger belt pay-out. The occupant will be “laterally” unrestrained when the VY peak is reached. Lateral pulses are associated with higher ribcage twisting and consequently sternum bending. This effect is not / could not be seen with the H350 due to its design restrictions to frontal crash. The HBMs showed to be in this case an effective tool to assess the influence of combined pulses. Specifically, the influence of lateral pulses in a frontal crash. Similar effects can be seen in the loadcases with considerable VY pulses: 1 (9g), 3 (14.1g), 5 (18g) and 7 (30.4g). See the normalized pulses in the next page. This observation will be addressed again in 5.4.

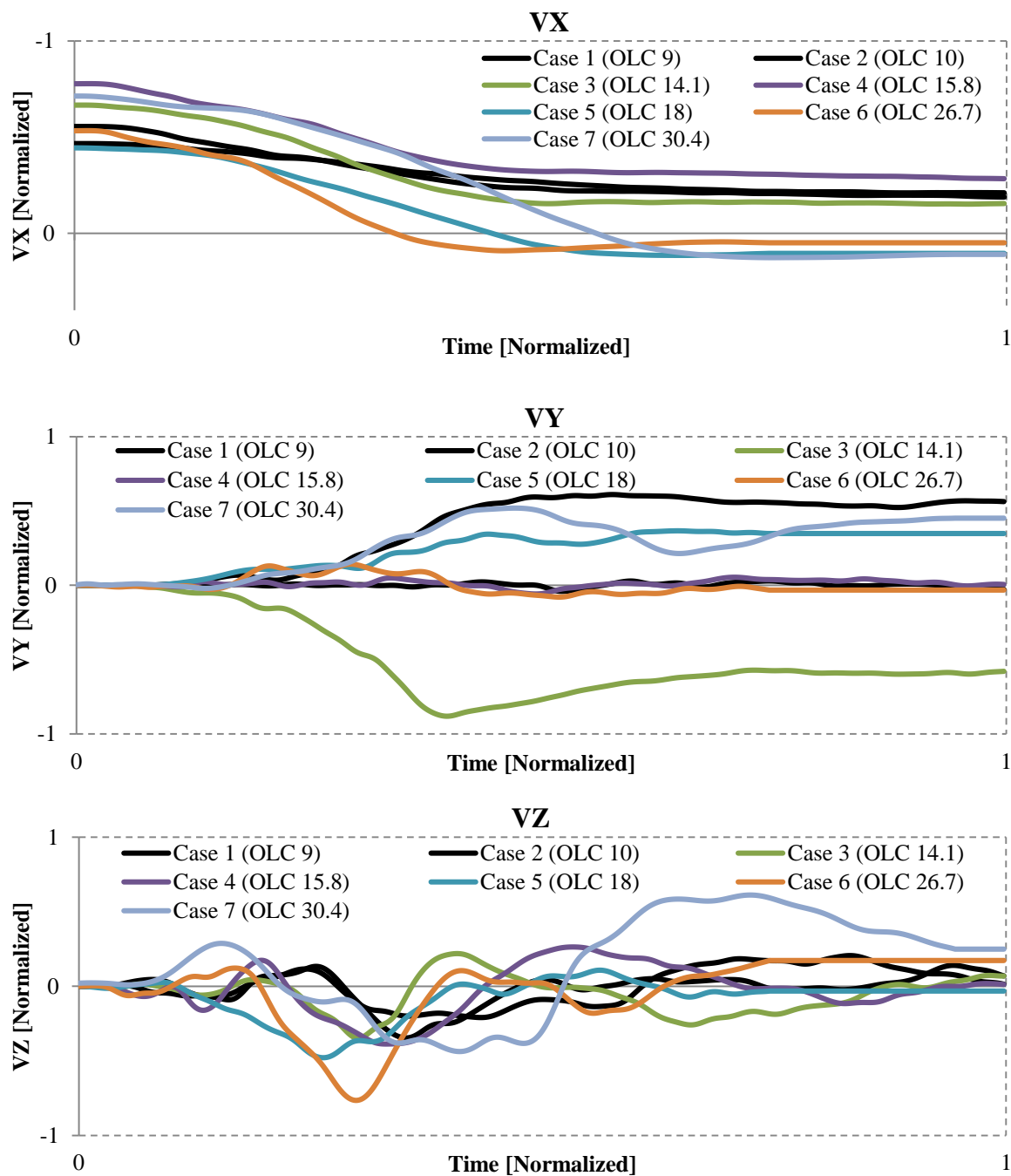


Fig. 4.32 VX, VY and VZ pulses of all loadcases

5 DISCUSSION

Current restraint systems in frontal-crash are designed, assessed and optimized based on the Hybrid-III dummy (H3) injury prediction. Although the prediction capabilities of the dummy have boosted the performance of restraint systems in high crash severities worldwide, implicit dummy-design limitations question its applicability for moderate-injury prediction in lower crash severities. The hypothesis is whether moderate injuries as sternal fractures can be predicted based on the H3, or whether the assessment needs to be complemented with more accurate and biofidelic tools as human body models (HBMs) into a variety of crash cases in a simulation environment. The fact that a H3 hardware does not have a transducer to convert the metrics of thoracic deformation into an engineering metric for sternal loading suggests a gap of information. This gap could potentially lead to an erroneous optimization of the restraint system in terms of sternal injury risk minimization. In order to analyze the hypothesis, three main dimensions have been addressed and discussed in 5.1 to 5.4:

- (i) Development of a novel elderly human model called Thums-elderly (based on the Thums-original) in order to address age-dependency factors and realistic geometrical properties of the cortical bone.
- (ii) Development of injury-risk assessment methods HBMs-dedicated.
- (iii) Comparison of the driver and passenger injury prediction of the dummy model and both HBMs (Thums-original and Thums-elderly) in a wide range of crash severities including a real-world accident reconstruction. The comparison addressed four different restraint systems including three adaptive restraint system variants.

5.1 Relevance of sternal fractures

As shown in the epidemiological review, sternal fractures and related injuries to “seatbelt syndrome” are common in frontal crashes. In addition, a growing elderly population and its higher vulnerability to injury seems to underline the necessity of a deeper look into the injury causations and possible countermeasures. Detailed analysis on severe and moderate thoracic injuries can be carried out with both dummy and HBMs in order to show their capabilities on injury prediction under a multi-dimensional analysis. Ridella et al. [1] found that the most

frequent moderate thoracic injuries for a population >45 YO are sternal fractures while rib fractures are the most common severe thoracic injuries. A correlation between sternal fractures and ageing is suggested. In addition, repercussions of an ageing society on the traffic accident panorama have been gaining more relevance in the research field and soon into the vehicle safety development. Even though sternal fractures are not normally associated to life threatening effects, its implications in terms of life quality and associated rehabilitation costs motivates the investigation efforts to find assessment methods and injury references needed to optimize restraint systems thus a complete protection of the occupants can be ensured inclusive in low and moderate crash severities.

5.2 Development of an elderly model and validation

As mentioned before, the current H350 was not designed to accurately measure sternal loading nor predict a risk of sternal fracture. This assessment gap can be closed by the application of Human body models (HBMs) as more biofidelic and accurate design tools. Nevertheless, the inclusion of ageing into the analysis required an additional model as ageing effects could not be addressed with the original HBM “Thums-original” as it represents the mechanical response of a 50th percentile male approximately 40 YO [51]. Therefore, a novel “Thums-elderly” was developed.

The guideline for this development was to introduce (i) realistic cortical thickness distribution in sternum and ribs, and (ii) represent and proof that cartilage calcification plays a considerable role on the mechanical response of the ribcage. A realistic mechanical response and injury prediction for sternum and ribs cannot be separated as both components are interacting structures under restraint loading. A correct mechanical output of ribs and cartilage will ensure realistic boundary conditions of load transfer to the sternum. The influence of the cartilage calcification has been evaluated under table-top-belt loading as shown in 2.1.3, where the peak stresses were incremented up to 59% in the anterior-ventral region of the sternum. In addition, an anterior-posterior shift of the peak stresses on the ribs was found as a different pattern of chest deflection when measured at five points at the anterior chest. Although three calcification levels were tested, a fully calcified state was chosen for the analysis. A drawback of considering full calcification is the assumption of absence of low density area surrounding the calcified regions, where a higher risk of cartilage fracture is expected. In addition, as mentioned by [130], the calcification appears to be generated first on the external layer (perichondrium) which was not represented with the model as the costal cartilage is modeled as a single PID in the Thums models. However, by considering a full calcification of both hyaline layer and perichondrium, the assumption of a single calcified PID was found to be reasonable. Note that for this study the cortical thickness was not modified in order to isolate the effect of the cartilage calcification. Instead, this topic was addressed by the introduction of real cortical thickness distribution into the Thums based on μ CT scans. The novel data was generated in collaboration with the Institute for Legal Medicine and the Mineralogy Research Department of the Ludwig-Maximilians-University of Munich [52]. The data of one selected subject was transferred to the model and tested subsequently in component, body region and full body conditions. The representativeness of

three μ CT scans is clearly a limitation. However, it is a step forward to a realistic representation of the bone geometry considering that no μ CT data is public available for this specific application. Note that the age at time of death of the selected subject was 65. A similar approach was done with the rib cortical thicknesses where the input data was based on a single “elderly” rib. It served as reference for the extrapolation of iso-thickness regions to the third to tenth ribs as presented in 2.1.2. Summarizing, the Thums-elderly represents an approach where the effects both cartilage calcification and realistic cortical thickness distribution on the mechanical response were addressed. As the Thums-original was kept as base line and no morphological modifications were addressed, a direct comparison of both models was possible as both represent the same global geometry. This method allows to isolate the analysis of the influence of the Thums-elderly modifications. Both models were tested with a validation pool of thirteen loadcases as shown in 2.1.4 to ensure biofidelity and compare the influence of the ageing factors in isolated components under controlled testing conditions.

A premise for choosing the validation setups was to find relevant and representative loading conditions for frontal crash. This ensures implicitly that the injury mechanisms in frontal crash will be addressed. The experiment data was organized in a multi-level validation method including material (or “tissue”) -, component- and body-region level. A final full-body test was added as realistic inertial restraint-like loading. Bio-corridors and “bio-boundaries” were created for sternum- and rib bending based on the available experiment data. In several cases the experiment data was not clearly depicted and / or the test results presented extreme variability. For the material level tests, no experimental data of tensile test with sternal bone was found, hence it was assumed to be similar to rib material response as shown in 2.1.4.1.1. A similar situation was faced for tensile test with calcified costal cartilage. However, the simulation results proved to be at least in the same order of magnitude, showing clearly a stiffer response for the Thums-elderly cartilage material. It was decided to cross-check the simulation results in a component level thus the mechanical output could be set in reasonable limit. This was addressed with the bending test proposed by Forman (see 2.1.4.2.4) which showed the lateral forces into the response corridor for both original and calcified cartilages. Even though the response corridors did not depict the response of a fully calcified cartilage; the data was still useful as a reference for no calcification. Forman’s cartilage component test attempted to quantify the contribution of the perichondrium to the resultant stiffness in bending. As calcification seems to be generated first on the perichondrium, when removed, the stiffness in bending would decrease up to 50%. This fact motivated the scaling of the response corridors by factor two in order to account for the perichondrium effect. As no data for fully calcified sterna was experimentally generated, it was assumed that the response corridor would serve as lower boundary reference for vertical forces. The next component test involved the characterization of the sterna in bending. These tests were noticeably the only effort found in the literature where boundaries for human sterna mechanical response were defined. As explained in 2.1.4.2.1, the boundary conditions of the test (pin joints at potted ends) may add a non-restraint-like constraint. This configuration generates an additional loading state, tension or compression depending on the convexity of the sterna that consequently generates an early failure compared to a pure bending loading condition. The effect of the real μ CT can be seen in 2.2.4.2.1 where the peak bending moments change from

27 Nm to 20.16 Nm, matching the boundary of 20.56 Nm set in the corridor. Note that the material properties and failure limits were kept, isolating the effect of the real cortical thickness distribution. However, it should be also noted that a shift of about 9 mm of vertical displacement, before the bending peak, was found between the experimental data and the simulation models. It was decided not to use the failure limits based on the experimental data due to the high variability and uncertainty nature of those. This approach will contribute to comparability and load reduction analysis with the restraint systems used in the chapter 4. As for the sterna, bending was also the loading condition for the mechanical characterization of the ribs as presented in 2.1.4.2.2. Anterior-posterior loading was chosen due to the similarity to the deformation pattern seen in frontal crash simulations. The experiment results were summarized in linear stiffness, rupture energy and anterior reaction forces. It was noted that the 7th rib showed a considerable underestimation of the linear stiffness, in contraposition, the 9th and 10th an overestimation of the rupture energy. In general, lower ribs showed a stiffer mechanical response in Thums-elderly compared with the Thums-original. It is believed that the effect of the ribs shape and cortical thicknesses account for most of the differences, as (i) the material properties were validated under tensile test as above mentioned and (ii), the rib geometry as maximum depth and curvature did not match the values of many of the real tested ribs. It was also noted that the results are strongly dependent on the boundaries chosen for the linear stiffness calculation hence the method was kept constant for all ribs.

Nevertheless, the results showed to be in a reasonable range compared to the experimental data. The next analyzed component was the clavicle, also tested in bending as realistic representation of seatbelt loading. As mentioned, for the clavicle no age-dependent effects were introduced thus the results of both Thums-original and Thums-elderly are the same. It should be noted that the linear response of the clavicle model may not be strictly representative although the results fit into the experimental corridor. Another relevant aspect into the component level was the internal organs validation. In the Thums model version 3 the internal organs are modeled as a whole single-mesh where no individual organ geometry nor individual materials have been modeled. As mentioned in 2.1.4.2.5, a direct comparison of test with individual organ vs. the response of the mentioned single-mesh makes less sense than validating it as a whole component. Results from eviscerated and not-eviscerated table-top test served as reference showing the resultant linear stiffness into the limits of the experimental data for both cases. The stiffness reduction with respect to the mean values of the experimental data account to 51% and 65% for the simulations. The simulations were run with the Thums-elderly as best match for the age at time of death of the PMHS tested.

The above described test characterized the individual component but not the resultant mechanical interaction for the thoracic body region. Therefore, table-top test and hub impact test were chosen for validation where the response of the complete torso was characterized. Wrapping up the test description of 2.1.4.3, a difference between blunt impact and non-impact loading was underlined, whereas a non-impact loading offers a better understanding of PMHS thorax deflection under realistic loading rate conditions (restraint system-like). This approach avoids undesired inertial effects of blunt loading. Two non-impacting table top test (belt- and distributed loading-like) were simulated and compared with the PMHS test data. It was shown that for the belt loading a reduction of around 27% of the linear stiffness after 10% sternal deflection comparing Thums-original and Thums-elderly. This suggests that an elderly thorax would be less stiff than a young one, taken the table-top belt testing conditions and similar

morphology. The H350 was also tested under table-top belt, showing a remarkable higher stiffness compared to the Thums models. The chest depth normalization was also addressed as the outer foam jacket of the H350 would shift the results. Both results (normalized and not normalized) showed peaks around 6860 N (not-normalized), 4975 N (normalized) compared with the Thums-original peak anterior reaction force of 3420 N at 20% sternal deflection. In addition, a H350's early peak force around 10% deflection suggests an unrealistic linear stiffness up to 10% despite the correct force-deflection rate showed after this peak. It is believed the thoracic stiffness of the H350 under low deflection rates is unrealistic. This phenomenon was also depicted in this loadcase. The low deflection rate actually represents an average chest deflection on belt restrained PMHS under frontal 48 km/h sled loading conditions as explained by Kent in [60]. Despite that hub impact test experiments were originally designed to represent a direct impact of the chest against the steering-wheel (as typical loading condition before the development and massive introduction of airbags), it was still considered for validation due to its reproducibility characteristics and large amount of published data. Frontal, lateral and oblique hub impact simulations showed a realistic response of both HBMs, specially addressing the plateau response at 4000 N between 5 mm and 80 mm sternal deflection. In all hub tests, both corridors with and without muscle tensing effect were included into the comparison. Both models behave in-between matching both overlapping corridors. Another topic to be analyzed is the increased stiffness in high rate loading cases generated most probably by the outer surface representing the muscle and fat layers of the torso. This topic was not addressed in the validation cases and should be included for future analysis. The validation loop was closed with the Gold-Standard-I (GS1) sled test (see 2.1.4.4). Boundary conditions for model positioning, belt routing and anchor points showed to be deciding for the injury outcome. Both Thums-original and Thums-elderly were carefully positioned and "instrumented" following the real experiments procedure. It was found that the peak values and timing of the shoulder belt force matches satisfactorily the experiment data accounting for 6.11 kN and 6.30 kN for Thums-original and Thums-elderly respectively at 83 ms peak force (experiment 90ms) and a force plateau of around 35 ms long for all cases. The main comparison with the experiments involved ribcage deformation patterns quantified with multi-point chest deflection measurements. One noticeable response involved the lower right chest and the "bulge-out" effect [81]. Mentioned by other authors and reanalyzed by Shaw with the GS1 test, the bulge-out of the lower chest (seatbelt's opposite side), or "negative deflection", may increase the sternal moments and consequently the sternal fracture risk. Although both HBMs reproduced the bulge-out effect, the Thums-original showed a peak deflection of -19.2 mm whereas the Thums-elderly peak deflection reached -8 mm (notice the negative sign indicating negative deflection). It is believed that the cartilage calcification causes a coupling effect of the anterior thorax generating a more uniform deflection than the "more-decoupled" Thums-original. The implications could involve an underestimation of the sternal bending moments in belt-like dominated loading. The GS1 represents the largest sample of PMHS close to the 50th percentile tested under controlled conditions and replicating a seatbelt restraint-like effect on the human thorax.

5.3 Development of Assessment Procedures

Benchmark cases were needed in order to analyze the injury prediction of the H350, Thums-original and the recently developed Thums-elderly. Methods for crash case selection, design guidelines for restraint management and the definition of restraint system variants were also required. While methods for thoracic injury risk prediction with dummies are well established and accepted, such standardized assessment methods do not exist currently for the interpretation of HBMs simulations. Therefore, a method was developed. The discussion starts with the design guidelines chosen for the restraint system configuration as follows.

The concepts presented by Kent et al. [83] served as outline for the restraint system configuration. The leading concept involved the definition of restraint parameters ensuring a restraint management process where the energy dissipation is maximized into the injury tolerance levels of the occupants. As explained in 3.3.1, the maximization of the restraint application time, loading, and load share are standard design guidelines accounting for the restraint system optimization. An additional and novel concept proposed in this study is the sternal twisting. In 3.2.2 the concept of sternum twisting was developed by comparing two loadcases (non-injurious and injurious in terms of sternal fractures) where the bending moments at the second inter-costal space suggested to be a reliable criterion to quantify the risk of sternal fractures. This approach represents the real injury mechanism and would not be affected by simulation artifacts as unrealistic stress concentration due to geometrical inaccuracies of the sterna.

For the restraint systems, an important simplification was made for configuration and analysis: Despite the possibility of including combination of seatbelt components, it was assumed to use only retractor pretensioning without combination with buckle or anchor point pretensioning in order to simplify the analysis on triggering, load limiting and interaction with the airbag system. This assumption simplifies the analysis in five dimensions. In addition, it is known that most of the current restraint systems in the market apply this component strategy. Choosing the parameters of load limiting implied also a simplification involving the linearity (or step-wise) load limiting processes. It is also known that non-linear load limiters could bring additional benefits in contrast to the step-wise method. Nevertheless, the linear load limiters simplify the analysis when comparing the results in different loadcases. Future work may add some dimensions to the analysis in terms of non-linear load limiting. Summarizing, it is believed that a benchmark accounting restraint systems retractor-pretensioned, including four linear load limiting levels, variable trigger times for airbag and airbag vent deployment are rather representative of the current and near future restraint system management to be found into the real fleets worldwide.

As above mentioned, while methods for thoracic injury risk prediction with dummies are well established and accepted, for HBMs such methods were not existent. The need for an automatic assessment tool motivated the development of custom automatic post-processing tools in order to assess automatically HBM simulations. This denominated “HUMAT” (HUMAN-Models-Assessment-Tool) generates automatically an estimation of skeletal thoracic injury risk per simulation, in an attempt to run a direct comparative analysis with the calculated H350’s injury risk prediction. The development was approached by splitting the

analysis into two modules: (i) rib fracture- and (ii) sternum fracture risk. As mentioned in the Thums-elderly development, the injury prediction of rib fractures and sternal injuries dependent one on each other in terms of load transfer between components and correct representation of the injury mechanisms. Nevertheless, as the nature of the injury mechanism is individual for both, the assessment was split based on the quantification of the injury mechanism. The correct interaction between components was addressed in the validation phase whereas the specific injury mechanisms and the correlation of simulation metrics with an injury risk or injury reference value was done individually for each module.

While current dummy output metrics are based on a single central chest deflection, HBM's sensors for rib fracture risk calculation and bending moments measured at each rib generate a 24-sensor-based mapping of the ribcage deformation. This approach addresses ribcage twisting, bulge-out effects, split of belt – airbag contribution to the chest deflection and quantifies the injury mechanism itself. A direct correlation to an injury risk was assumed by adapting the NFR method developed for the Thor dummy to the HBMs, addressing the above mentioned advantages of the bending moments approach with one modification: Instead of limits for localized plastic strains, the injury metric was directly based on the bending moments. This allows a robust and direct interpretation of the injury mechanisms avoiding undesired simulation artifacts as unrealistic stress concentrations and model-specific mesh quality. Into the development process other assumptions were done including same PMHS-NFR / Thor-NFR and PMHS-NFR / Thums-NFR correlation, maximum plastic strain of 1.8 % for cortical bone (both models) and injury reference values to weight the individual risk of fracture based on bending. Nevertheless, this mechanical approach will ensure that the risk of injury will be linked directly to the severity of the injury mechanism, generating a reasonable frame for the analysis of sternum fracture risk. Addressing the second module, the mechanical characterization of the sternum was first approached with the validation test published by Kerrigan et al. [64] under constrained bending as explained in 2.1.4.2.1. Supporting the assumption of a bending-dominated injury risk mechanisms, references on seatbelt syndrome and related epidemiological analysis directed the attention to this specific type of loading. As mentioned in 3.2.2, just few data is available for injury risk analysis of sterna under seatbelt loading. This limitation was approached by considering HBM simulations. The author proposed to consider the table-top (belt loading) and GS1 sled test loadcases from the validation pool (see 2.1.4) as boundaries for the analysis. Characteristics as restraint system loading, detailed documentation of loading conditions and injury outcome for both loadcases demonstrated to be a useful reference for setting injury reference values for sternal fractures. Note that, (i) the injury references are simulation derived and model-specific, and (ii) the table-top test (belt loading until 20% deformation) [60] are right-censored test whereas the GS1 [81] (ignoring the not-injured outlier) is left-censored. The analysis involves first the definition of the critical areas on the sternum. The injury patterns in [81] suggested that the intercostal spaces (ICSs) are critical areas for sternal fractures and therefore assumed to be reference locations for simulation output. Hence five sensors were defined on the sternal ICSs of both Thums-original and Thums-elderly models. Another relevant step on the analysis involved the calculation of the denominated “absolute loading difference” (see 3.2.2) which helped to depict that specifically the bending moments at second ICS better explained the difference in loading between the non-injurious and injurious load modes. Quantitatively,

comparing the second and third ICSs for bending in the three local axis, it was found with the Thums-elderly an absolute-loading-difference of 68%, 75% and 57% (MX, MY and MZ) compared to 13%, 30% and 6% (FX, FY and FZ) in GS1 vs. Table-top loading conditions. These facts supported the assumption that, under restraint-like loading, the sterna of both Thums-original and Thums-elderly will fail in a range of resultant moments close to 20 Nm when measured at the second intercostal space (ICS_2). This is also supported by [81] where the fracture locations were typically located at the edge path of the seatbelt when projected on the sternum.

The injury prediction of both modules were evaluated against the real injury outcome of a battery of PMHS GS1 sled test published by Shaw et al. [81] where all but one subject sustained AIS3+ thoracic injuries, including sternal fractures. As shown in 3.3.3, the test was simulated with the H350, Thums-original and Thums-elderly. The injury outcome revealed a 14% AIS3+ injury prediction with the H350 model, a 75% and 81% with the Thums-original and Thums-elderly respectively. For a quick reference, values approaching 100% would be the desired prediction. For the sterna, the bending moments measured with both HBMs reached 23 Nm suggesting a high risk of sternal fracture. The H350 it is not applicable for this type of assessment as this dummy was not designed to accurately measure sternal loading nor predict a risk of sternal fracture. Consider that in [48] AIS2+ injury risk curves for H350 are not relevant for the sternal injury risk analysis as they consider only the risk of rib fractures for AIS2 probabilities.

5.4 Results: Discussion on Simulation Matrix Outcome

As mentioned in the last sub-chapter, benchmark crash cases were needed in order to analyze the injury prediction of the three occupant models (H350, Thums-original and Thums-elderly). The candidate cases were classified using the occupant load criterion (OLC) as it includes the rate of energy to be dissipated by the occupant, instead of one-dimensional criteria as Delta-V or maximum acceleration. The crash cases were simulated for both driver and passenger sides and four restraint system variants for a total of 168 simulation cases (7 crash cases, driver and passenger, three occupant models and four restraint variants). The results are summarized per case as AIS2 (as sternum fracture) and AIS3+ injury prediction outcome.

The crash case 1 was an OLC 9g real-world accident. The case was reconstructed and assessed with methods developed on chapter 3. The simulation results showed noticeable differences on the AIS3+ prediction between models. While the H350 predicted 1% and 0,6% for driver and passenger respectively, the Thums-elderly reached the 39% and 53%. It is believed that a slight over prediction of the rib injury could be generated as the protective effect of muscle tensing is not specifically addressed with the current HBMs. After this prediction the driver (AIS1 injured) would have had a risk of almost 40% of suffering three or more rib fractures. Muscle activation and its role in the injury outcome is a topic still in an early research phase and will be addressed mid- and long term. It was also noted that while the H350's injury prediction was rather constant for both sides, the HBMs showed a

considerable difference between driver and passenger in the injury prediction. It is also believed that the deformation pattern under this asymmetric loading (high lateral pulse and diagonal belt) is noticeably with the more realistic deformation of the HBMs (in terms of ribcage twisting) rather than with the stiff H350. As the lateral pulse imposes different loading conditions for driver and passenger, the injury outcome is expected to be different, supporting the abovementioned observation with the HBMs. For sternal loading, the analysis was outlined by the injury outcome of the real accident, where the passenger sustained a sternum fracture. As mentioned before, the H350 is not applicable for sternal loading analysis, thus the comparison could only be carried out with the HBMs. As for the rib fracture injury risk, a remarkable difference was also found in the peak bending moments evaluated on the ICS_2 between driver and passenger. For the Thums-elderly driver (restraint system variant A), a value of 18 Nm suggests a response just under the proposed injury reference value (the driver sustained no sternal injuries). The Thums-elderly passenger simulation showed a loading reaching 24 Nm, surpassing the proposed injury reference value (the passenger did sustain a sternal fracture).

Comparing Thums-original and Thums-elderly, no significant differences were found suggesting that, under this OLC level and restraint variant A, the risk is still age independent. As defined in 3.3.1, three additional restraint system variants were tested in order to compare the effect of different restraint strategies on the injury prediction per model. On AIS3+ level the H350 showed an injury risk reduction in a rather marginal decreasing trend for both driver and passenger reaching a 1.14%, 1.62%, 1.1% and 0.75% with the systems A, B, C and D respectively. For the passenger similar results were reached. The HBMs showed the same reduction trend, just with the observation that the injury risk calculated with the Thums-elderly showed a more reasonable trend 53.1%, 27.1%, 29.4% and 27.3% (systems A, B, C and D) than the 39.4%, 3%, 2.3% and 1.4% of the Thums-original. It is believed that the rib fracture risk, calculated with the Thums-original, may over-calculate the benefit of load reduction on the rib fracture risk due to a stiffer behavior under low crash severities compared to the Thums-elderly. The effect of the restraint variants on the sternal loading was only possible with the HBMs. The variant D proved to be the most effective in reducing the peak loadings ICS_2 on the Thums-original by 9.5 Nm (driver) and 13.1 Nm (passenger). Although the Thums-elderly showed a similar trend, the variant C (LL 1kN) proved to be more effective for the driver side with a reduction of almost 8 Nm in contrast to the variant D where the benefit reached a moderate 2 Nm. This phenomenon can be observed in the time histories of the sternal bending for the driver Thums-elderly results in 4.1.2. The explanation involved an external factor where the left hand of the model was shortly engaged by the airbag deployment, modifying the left scapula-arm joint kinematics, deriving in an increased clavicle-sternal load transfer by the end of the simulation. Without this exception, the resultant bending moments of the variant D would have most likely remained lower than C's.

A similar comparative analysis was done in a wider panorama with the additional six crash cases. The injury reduction trend reached with the restraint systems variants B, C and D proved to be beneficial also in different OLC levels. Linear regressions per occupant and restraint variant were calculated in order to quantify the rate of AIS3+ reduction along the OLC scale, showing an injury rate reduction (AIS3+%/g) from 0.22 to 0.13 for the H350 driver, 0.087 to 0.052 for the H350 passenger, 2.6 to 1.36 for the Thums-original driver, 2.49

to 0.72 for Thums-original passenger, 3.1 to 2.63 for Thums-elderly and 2.9 to 2.19 for Thums-elderly passenger, all comparing the restraint variant “A” with the best restraint performance variant, in most of the cases, the variant D. The intersect to the injury axis was set to zero ensuring comparability between variants and no injury probability at zero loading. However, loading and kinematic response of the HBMs were strongly dependent on each lateral pulse (VY-pulse), for both driver and passenger positions. As shown in 4.3.4, the cases 1 (OLC 9g), 3 (OLC 14.1g), 5 (OLC 18g) and 7 (OLC 30.4g) exhibit considerable VY-pulses in contrast to the remaining cases. By cross-checking the HBM’s injury prediction (both AIS3+ and AIS2 as sternal fracture risk) with the VY-pulse severities it was found that the simulation results reached higher injury risk levels in the cases with higher VY-pulses despite lower OLC values (see 4.3.2 and 4.3.3). This effect was not seen with the H350 where a monotone linear correlation of the injury risk with the OLC did not depict the effect of the VY-pulse. Facts as frontal-crash dedicated design and unrealistic torso stiffness caused principally by the rigid one-joint thoracic spine, question the H350’s prediction quality in frontal crashes with Y-pulse components. This suggests the HBMs as more reliable tool with the capability to assess the influence of lateral pulses in frontal crash. A carefully evaluation of the H350’s prediction relevance is recommended in current regulation and consumer test crash cases involving Y-pulses (e.g. ODBs, oblique test, small-overlap etc.). Addressing the injury prediction of all models in both driver vs. passenger positions, it was noted that, despite the H350 showed a rather comparable AIS3+ prediction for both sides in the accident reconstruction case, the trend along the complete OLC range showed lower risk for the passenger side. This is contrasted with the AIS3+ prediction of the Thums-original and Thums-elderly where the differences between driver and passenger were notably low. The effect of the restraint variants B, C and D was for almost all cases beneficial except for the crash case 7 (OLC 30.4) where in two runs (H350 passenger and Thums-original passenger) the injury risks were slightly higher compared to the variant A. It is believed that this effect is the consequence of a slight change in the restraint strategy (earlier triggering and longer timer for load limiting) in an attempt to minimize the risk of head contact against the dashboard due to excessive forward excursion. This phenomenon was noted with the variants C and D for the crash cases 6 and 7. The cases were denominated “PHC” (Probable-Head-Contact) and taken out from the analysis. Those cases helped understanding the limits for the maximization of controlled excursion even when sternal loading was further minimized. This observation also suggests that, due to the more flexible nature of the HBMs, a restraint variant that optimizes the forward excursion in an attempt to reduce the H350’s thoracic injury outcome (e.g. chest deflection) may increase the risk of head contact with the dashboard when evaluated with HBMs. The sternal loading was approached only with the HBMs as done with the accident reconstruction. Plotting the difference driver vs. passenger for both HBMs, the results suggest a higher loading prediction for passenger side as shown in 4.3.4. Just few cases and variants were out of the trend (negative values mean that the Thums-elderly’s loading prediction showed higher values than the Thums-original). Outliers on the crash case 3 (OLC 14.1) were found as seen in the AIS3+ risk. The increment of sternum loading is believed to be strongly linked to the VY-pulse and showed to be higher for the driver side in all restraint variants with the Thums-original. The same trend was observed for the variants A, B and D with the Thums-elderly. The age-dependency analysis along the OLC range was split in driver and passenger. For the driver side it was noted that the Thums-elderly’s sternum showed higher

sensitivity to the load reduction (restraint variants C and D) than the Thums-original one in low severity pulses (OLCs 9g and 14.1g). For the passenger a similar trend was found with the observation that, in the high severity cases 6 and 7 (OLCs 27.6 g and 30.4 g, restraint variants A and B), the Thums-original loading prediction was up to 11 Nm higher than the Thums-elderly's. It is believed that the sternal loading could diverge under high severity pulses due to the mechanical influence on the cartilage calcification and the resultant coupling of the anterior ribcage. This point has to be further investigated in the future. A strong dependency of the sternal loading on the Y-pulse for both HBMs was also found (see Fig. 4.28 - Fig. 4.31) supporting the trends of the AIS3+ prediction. As above mentioned, the H350's lack of metrics to assess sternal loading suggests also the HBMs as complementary tool for moderate-injury risk assessment involved in pure frontal- or combined-pulses (VX – VY).

6 CONCLUSIONS AND FUTURE WORK

6.1 Relevance of sternal fractures

Sternal fractures and related injuries to “seatbelt syndrome” are the most frequent moderate thoracic injuries for a population of 45 years and above [1]. Growing elderly population (see 1.3) and its higher vulnerability to injury underlines the necessity of a deeper look into the injury causations and possible countermeasures.

Thoracic injury prediction in frontal crash is currently assessed with the Hybrid-III dummy (H3). Implicit factors such as a not human-like rib cage morphology and lack of a transducer to convert the metrics of the thoracic deformation into an engineering metric -for sternal loading-, leads to the conclusion that a design gap could exist in terms of sternal injury prediction.

6.2 Development of an elderly model and validation

Ageing society represents concrete challenges for restraint systems design. As new tools are needed for a more accurate analysis on injury mitigation of a vulnerable population. An “elderly” human body model based on the Thums® v3 model was developed. The “Thums-elderly” addresses realistic “elderly” cortical thickness distribution μ CT-based in sternum and ribs. In addition, costal cartilage ageing was represented by progressive calcification. Table top test (belt loading) served as test-bench to determine the role of cartilage calcification on the mechanical response of the ribcage under restraint system loading.

A method for the validation of Thums-original and Thums-elderly models was developed by grouping test data in four levels: (i) Material, (ii) component, (iii) body region and (iv) full-scale (sled). The relevance of the validation test in each level was based on its representativeness of thorax loading conditions in frontal crash. The tests presented in this study included tensile coupon tests for cortical rib bone and cartilage. At local level (or component level) clavicle 3-point bending test (3PBT), anterior-posterior (AP) individual rib loading and sternum 3PBT. At body region level table-top non-impact test for diagonal belt

and distributed loading (airbag-like loading), pendulum impact test (frontal, lateral and oblique). As full scale test the Gold-Standard-I (GS1) configuration was chosen.

Age dependent factors showed lower peak and stiffness values with the Thums-elderly model in component- and body-region response specifically for cartilage, sternum and upper ribs. In contraposition, the lower ribs showed (7th to 10th) a stiffer mechanical response when compared to the Thums-original component- and full-scale validation levels.

6.3 Development of Assessment Procedures

Benchmark crash cases of the chapter 4 were classified using the occupant load criterion (OLC) as it includes the rate of energy to be dissipated by the occupant, instead one-dimensional criteria as delta-V or maximum acceleration.

Benchmark crash cases accounting for restraint systems retractor-pretensioned, including four linear load limiting levels, variable trigger times for airbag and airbag vent deployment are representative of the current and near future restraint system management to be found into the real fleets worldwide.

The concepts presented by Kent et al. [83] served as outline for the configuration of the restraint system variants B, C and D. It was attempted to combine the restraint parameters to ensure a restraint management process where the energy dissipation is maximized into the injury tolerance levels of the occupants, including tolerances for sternal fractures. The restraint variants showed to be effective on successive sternal loading reduction as shown in the chapter 4.

The lack of standardized methods specific for HBM thoracic injury risk prediction motivated the development of a custom group of assessment tools denominated “Humat”. The development was approached by splitting the analysis into two modules: (i) Rib fracture- and (ii) sternum fracture risk.

The NFR method developed for rib fracture assessment with the Thor dummy was adapted to the HBMs, adopting bending moments as input metric instead plastic strains in an attempt to quantify directly the relevant loads generated by injury-mechanisms and avoid simulation artifacts. This approach proved to generate a reasonable frame for the analysis of sternum fracture risk.

The sternum fracture risk was approached by HBM simulations as shown in 3.2.2. The concept of sternal twisting was studied by comparing two loadcases (non-injurious and injurious in terms of sternal fractures) where the bending moments at the second inter-costal space (ICS_2) suggested to be a reliable criterion to quantify the risk of sternal fractures. An injury reference value of resultant moments at the ICS (MXYZ ICS_2) of 20 Nm was proposed.

The assessment methods and models were validated against the injury outcome of an array of PMHS sled test (see 3.3.3) The response of the HBMs in terms of rib- and sternal fracture risk were noticeable closer to the real injury outcome, in contraposition to an underestimation of the injury risk with the Hybrid III dummy 50th %-ile (H350).

6.4 Results: Conclusions on Simulation Matrix Outcome

A matrix of benchmark 168 crash cases was simulated including both, driver and passenger sides and four restraint system variants assessed with the H350, Thums-original and Thums-elderly. The crash cases included one real-world accident reconstruction and six field relevant crash cases.

In the real-world accident reconstruction, the restraint variant A, assessed with the H350 passenger, represents an effective configuration where the injury prediction remained under 12% of AIS3+ thoracic injury risk. The same restraint variant evaluated with the HBMs in terms of sternum loading showed specifically a high risk of sternal fracture by comparing the simulation results and the injury reference value of 20 Nm.

In the real-world accident reconstruction, the Thums-elderly including cartilage calcification and real cortical thickness distribution from μ CT scans showed slightly higher sternal bending moments than the Thums-original. By successive reduction of loading the restraint variants B, C and D showed to be effective by minimizing the sternal MXYZ to 13.1 Nm and 9.5 Nm for Thums-original and Thums-elderly respectively, reducing the bending levels under the specified injury reference value of 20 Nm. The effect of the same restraint variants on the H350 (on AIS3+ level) showed a marginal benefit.

In the real-world accident reconstruction, as the lateral pulse imposes different loading conditions for driver and passenger, the injury outcome is expected to be different. This effect is shown with the HBMs in terms of AIS2 (as sternal fracture) prediction in contrast with the rather constant H350's injury prediction for both sides.

The AIS3+ injury risk outcome with the “adaptive” restraint systems variants B, C and D proved to be beneficial also in different OLC levels. Rates of AIS3+ (AIS3+%/g) along the OLC scale were calculated showing reduction from 0.22 to 0.13 for the H350 driver, 0.087 to 0.052 for the H350 passenger, 2.6 to 1.36 for the Thums-original driver, 2.49 to 0.72 for Thums-original passenger, 3.1 to 2.63 for Thums-elderly and 2.9 to 2.19 for Thums-elderly passenger.

Along the complete OLC range, successive load reduction with the restraint variants B, C and D showed with the HBMs a concrete reduction of the sternum loading hence reducing the risk of sternal fracture risk. The same variants evaluated with the H350 showed a marginal reduction of AIS3+ injury risk delivering no further information specific related to sternal injury risk reduction.

Loadings and kinematic response of the HBMs were strongly dependent on the lateral component of the pulse (VY-pulse), for both driver and passenger positions. This effect was not seen with the H350 questioning its prediction quality in frontal crashes with Y-pulse components. This suggested the HBMs as more reliable tool with the capability to assess the influence of lateral pulses in frontal crash. A careful evaluation of the H350's prediction relevance in current regulation and consumer test crash cases involving Y-pulses (ODBs, oblique test, small-overlap etc.) is recommended.

Along the OLC scale, the Thums-elderly showed to be more sensitive in terms of sternal loading reduction (restraint variants C and D) than the Thums-original in low severity pulses (OLCs 9g and 14.1g). For the passenger a similar trend was found with the observation that in the high severity cases 6 and 7 (OLCs 27.6g and 30.4g, restraint variants A and B) the Thums-original loading prediction was up to 11 Nm higher than the Thums-elderly. This suggests that age dependent injury patterns (represented by the Thums-elderly) are dependent on the pulse severity.

6.5 Future Work

Relevance of moderate injuries as sternal fractures and will gain more importance as an optimization target of restraint systems in the coming years. Inclusion of age-dependent factors in regulations and consumer tests, autonomous driving and a changing panorama of vehicle crashworthiness and restraint scenarios will demand more accurate assessment tools and methods for occupant injury mitigation. New generations of dummies as the Thor and human body models of fourth generation as Thums v4 and GHBMC offer to cover this demand. Furthermore, muscle-activated HBM versions accounting for the influence of muscle reaction under pre-crash and low crash severities will add some dimensions to the analysis generating the chances for simulating scenarios that are more complex.

Specifically, for future development of elderly models, the following topics may be relevant for a more realistic mechanical response:

- (i) Realistic cortical thickness distribution along the cortical layers of the skeleton model
- (ii) Age-dependent material properties
- (iii) Global morphological changes due to ageing process
- (iv) Realistic representation of the internal organs
- (v) Costo-vertebral joints modeling and influence in thoracic mechanical response
- (vi) Influence of the muscle activation on injury outcome
- (vii) Influence of overweight and obesity on injury outcome

The inclusion of the above mentioned topics will facilitate the parameterization of future HBMs hence helping the modeling of personalized models in terms of anthropometry and constitutive materials. Complementary validation cases for multidirectional loading at material level, age-dependency characterization in local- (or component), body region- and full-scale-levels may contribute to the injury risk analysis of individual components.

Approaching the assessment procedures for HBMs, the integration of the methods presented in this dissertation with head injury risk assessment is recommended. Regarding rib injury risk assessment, it is recommended to simulate the loadcase pool used as database for the injury reference values generated with the Thor dummy into the THORAX project. Although detailed data remains officially unpublished, it may represent a valid method to create HBM-specific injury reference values. In addition, multipoint chest deflection methods for thoracic injury analysis may offer advantages in terms of comparability with the Thor dummy in the future. Nevertheless, special attention has to be paid to the conversion of the chest deflection metrics to an injury risk. For the assessment of sternal fracture risk, experimental data at local (component) level is needed to quantify injury reference values per gender and age. In addition, the influence of the sternal shape (global morphology) is a topic for future work. A specific aspect on the sternal mechanical response is the influence of the manubrium-sternal joint stiffness on the limit value for bending. An experiment sample able to represent statistically relevant data on this topic still has to be generated.

The simulation matrix presented in the chapter 4 may serve as a benchmark, in realistic crash scenarios, for a comparison of the Thor dummy and HBMs of fourth generation in terms of injury prediction. Additional loadcases, including regulation and consumer test may help to better depict the field relevance of the model's Y-pulse sensitivity addressed in the chapters 4 and 5. A weighting of the OLC based in the Y-pulse severity would help to differentiate in short term the H350 injury outcome. In addition, new restraint systems including airbelts, asymmetric airbags and new airbag-configurations in the occupant cell may further expand the analysis proposed in this document.

7 SUMMARY / ZUSAMMENFASSUNG

English version: The second leading cause of occupant fatalities in traffic accidents are thoracic injuries. Sternal fractures are the most typical moderate thoracic injury in frontal crash. Until now there is no clear understanding about the sternal injury mechanisms and how to minimize the risk of sternal fracture of the occupants. The design and assessment of advanced restraint systems capable to minimize such injuries is currently based on the Hybrid-III 50th percentile (H350) dummy in frontal crash. Despite the great benefits achieved with the H350 dummy, the inclusion of transducers and specific metrics for sternal loading were not part of its design purposes nor the representation of age-dependent factors. This suggests a gap of information in the design process of a restraint system. This gap could lead to an erroneous optimization of the system in terms of sternal injury risk minimization. It was hypothesized that the restraint design process needs to be complemented with more accurate and biofidelic tools, as human body models (HBMs), in terms of sternal loading minimization. A comparative analysis was needed.

Three dimensions have been addressed in order to analyze the hypothesis: (i) Development of a novel elderly human model called Thums-elderly (based on the Thums-original) in order to address age-dependency factors and realistic geometrical properties of the thoracic cortical bone. This development included novel μ CT data from PMHS and a multi-level validation process.

(ii) Development of thoracic injury risk assessment methods for HBMs aiming for a direct comparison against dummy predictions. (iii) Comparison of the driver and passenger injury prediction of the dummy model and both HBMs (Thums-original and Thums-elderly) in a wide range of crash severities including a real-world accident reconstruction. A total of 168 occupant simulations were run and analyzed. The comparison addressed four different restraint systems including three adaptive restraint system variants.

The assessment methods were grouped on rib fracture risk and sternal fracture risk. Sternal fracture risk was approached using HBM simulations by comparing two loadcases (non-injurious and injurious in terms of sternal fractures). Bending moments at the second inter-costal space (ICS_2) suggested to be a realistic criterion to quantify the risk of sternal fractures. An injury reference value of resultant moments at the second ICS “MXYZ ICS_2”

of 20 Nm was proposed. Out of the benchmark crash cases, it was found that the H350 may underestimate the risk of thoracic injuries and sternal fractures particularly in frontal crash cases with considerably high lateral pulses. This is inherent to the H350 design purposes (frontal-crash dedicated dummy), nevertheless the dummy is currently still an injury prediction tool in assessment programs with crash cases precisely addressing lateral pulses as oblique barriers, offset deformable barriers, small-overlaps and accident reconstructions. For sternal fracture risk, the H350 is a not applicable tool, as this dummy was not designed to accurately measure sternal loading nor predict a risk of sternal fracture. An example of this fact was shown with the restraint system variant A (accident reconstruction case): A rather low AIS3 injury risk with the H350 indicated a safe design (at least for severe injuries) while no metrics of sternal loading or fracture risk were generated. The same variant tested with the HBMs showed an increased risk of sternal fracture. Restraint system variants (B, C and D) showed loading reduction with the HBMs up to non-injurious levels (under 20Nm). The same variants showed rather a marginal benefit with the H350. Lateral pulses are also believed to have an influence on the injury outcome of the front passengers, as the restraint system force transfer will be different due to the asymmetry of the belt paths. This effect is shown with the HBMs in terms of AIS2 (as sternal fracture). Regarding the effects of introducing age dependent factors (represented by the Thums-elderly), a reduced thorax stiffness was found in local- (component-) and body-region validation loadcases, specifically for cartilage, sternum and upper ribs. As the analysis was restricted to morphological dependency rather than material or failure limits, a “fragility” of the elderly model was not clearly represented. Nevertheless, the structural deformation is believed to be realistic due to the improvement achieved by introducing real cortical thicknesses from μ CT data, especially on the sternal region. The Thums-elderly showed to be less sensitive, in terms of sternal loading, to successive shoulder belt force reduction than the Thums-original in high severity pulses.

Sternal fractures and other moderate injuries will play an important role in the near future as optimization target in restraint system design. Sternal loading and sternal fracture risk need to be accurately predicted in order to assess the mitigation capabilities of a specific restraint system. While current dummies seem to be insufficient to reach the needed accuracy, HBMs show potential to assume this task. A simulation matrix with different crash severities and restraint system variants was built for benchmark purposes. The benchmark showed that current H350 dummies are not capable to discriminate noticeable improvements at sternal loading level, whereas HBMs do. Ageing and its effect on sternal fracture risk cannot be neither correctly represent with dummies. In order to represent ageing effects, HBMs need to be improved (e.g. realistic cortical thickness distribution and cartilage calcification). The injury prediction of an improved “elderly” HBM (Thums-elderly) showed to be strong dependent on the crash severity, although, it showed a less sensitive response to restraint loading reduction compared to the HBM without age-dependent factors (Thums-original).

Deutsche Version: Nach Kopfverletzungen sind Thoraxverletzungen die zweithäufigste Todesursache bei Verkehrsunfällen. Darunter sind Brustbeinfrakturen die häufigsten mittelschweren Thorax-verletzungen in Frontalaufprall-Unfällen. Gegenwärtig gibt es weder eine eindeutige Erklärung bzgl. des Verletzungsmechanismus von Brustbeinfrakturen noch klare Strategien, um deren Risiko in der Insassenschutzauslegung zu minimieren. Die aktuelle

Auslegung im Frontalaufprall basiert auf Messwerten des Hybrid-III 50th Prozent (H350) Dummys. Dessen Verletzungs-prognose anhand der gemessenen Werte lassen eine eingeschränkte Bewertung der Effektivität des Rückhaltesystems erstellen. Der Dummy und dessen Messtechnik mangelt an Sensoren spezifisch für die Bewertung von Brustbeinverletzungen. Darüber hinaus wurde eine altersabhängige Prognose nicht dazu mitentwickelt. Diese Fakten weisen auf eine inkomplette Analyse in der Insassenschutzauslegung für die Minimierung der Brustbeinverletzungen hin. Die Hypothese lautet deshalb, dass diese „Lücke“ des Hardware- und virtuellen Entwicklungsprozesses durch genauere und biofidelere Modelle (es entspricht Menschmodellen) gelöst werden kann. Eine vergleichende Analyse von Dummy vs. Menschmodell ist dazu erforderlich.

Die Analyse der Hypothese erfolgte anhand drei Schritten: (i) Entwicklung eines neuen Menschmodells „Thums-elderly“ (basiert auf Thums-original), um altersabhängige Faktoren und realistischerer Kortikalis (Kortikalschicht) der Rippen nachzubilden. Diese Entwicklung enthält neuartige μ CT Daten von PMHS und die Ergebnisse eines Mehrebenen-Validierungsprozesses. (ii) Entwicklung der Auswertungsmethoden spezifisch für Menschmodelle gezielt um die Vergleichbarkeit zur Dummy-Prognose zu gewährleisten. (iii) Vergleichende Analyse Dummy vs. Menschmodell auf Fahrer- und Beifahrerpositionen in einem breiteren Spektrum von Unfallschweren. Ein Realunfall wurde ebenfalls rekonstruiert und analysiert. Insgesamt wurden 168 Insassensimulationen durchgeführt und ausgewertet. Der Vergleich adressiert ebenso vier Rückhaltesystemvarianten, drei davon adaptiv.

Die Auswertungsmethode der Simulationen mit Menschmodellen wurde in Rippenfrakturen und Brustbeinfrakturen unterteilt. Biegeversuche und Gurtstraffung wurden mit dem Menschmodell nachsimuliert, um Verletzungskriterien für Brustbeinfrakturen zu definieren und zu quantifizieren. Binäre Versuchsergebnisse (Verletzung oder Nicht-Verletzung) dienten als Referenz. Die Biegemomente auf ICS_2 (zweiter interkostalraum) zeigten sich als realistisches Kriterium). Als Verletzungsreferenzwert (IRV) ist ein resultierendes Biegemoment auf ICS_2 (MXYZ ICS_2) von 20 Nm vorgeschlagen. Anhand der simulierten Lastfälle wurde festgestellt, dass der H350 zu einer Unterprognose des Risikos der Thoraxverletzungen tendiert, insbesondere in Frontallastfällen mit erheblichen Lateralpulsen. Diese Unterprognose erklärt sich teilweise dadurch, dass der Dummy spezifisch für Frontalcrashanwendung ausgelegt wurde. Jedoch wird der Dummy aktuell noch als Auswertungstool in Gesetz- und Verbraucherschutzlastfälle eingesetzt, obwohl die oben genannten Lateralpulse präsent sind (z.B. Oblique- und Offset-deformable Barrieren, Small-overlaps und Unfallrekonstruktionen). Für eine Prognose der Brustbeinverletzungen ist der H350 weder dazu ausgelegt noch wurden Verletzungsrisikokurven spezifisch dafür entwickelt. Ein Beispiel dafür ist die Verletzungsprognose in der Unfallrekonstruktion (siehe Rückhaltesystem Variante A, Kapitel 4.3): Bei der Betrachtung der Ergebnisse liefert die Prognose des Dummys ein niedriges AIS3+ Verletzungsrisiko. Diese Prognose entspricht prinzipiell einer robusten Performance des Rückhaltesystems. Dabei ist zu beachten, dass keine Informationen bzgl. der Brustbein-belastungen bzw. dem Verletzungsrisiko generiert sind. Auf der anderen Seite weist die Simulation mit dem Menschmodell (ebenso Rückhaltesystem Variante A) ein höheres Verletzungsrisiko des Brustbeins auf. Darüber hinaus zeigten die Rückhaltesystemvarianten B, C und D eine stetige Reduktion der Belastung

bis zu einem optimalen Punkt unter dem Verletzungsreferenzwert (20 Nm). Die gleichen Varianten mit dem H350 zeigen eine minimale Verbesserung, allerdings immer auf ein AIS3+ Niveau bezogen. Die Prognosegüte des Menschmodells weist zusätzlich darauf hin, dass die Verletzungs-wahrscheinlichkeit auch in Abhängigkeit der Insassenposition (Fahrer oder Beifahrer) zu betrachten ist, insbesondere bei Lastfällen mit Lateralpulsen, bei welchen die asymmetrische Konstellation der Schulter-gurtverlauf einem anderen Deformationsmuster des Brustkorbes entsprechen muss. Dieser Effekt ist nur mit dem Menschmodell quantifizierbar, wenn auf dem Beifahrerbrustbein gemessene Biegemomente vom Fahrerbrustbein abweichen. Bzgl. altersabhängigen Effekten weist die Anwendung von einem altersabhängigen Menschmodell (Thums-Elderly) eine reduzierte Steifigkeit auf. Dies geht aus der Validierung der Körperregion des Brustkorbs und einzelnen Komponenten insbesondere Knorpel, Brustbein und obere Rippen hervor. Die vergleichende Analyse mit dem Thums-elderly war beschränkt auf eine morphologische Abhängigkeit. Altersabhängige Materialparameter wie Fließkurven und Versagenskriterien blieben unverändert. Eine typische „Zerbrechlichkeit“ wurde mit dem modifizierten Modell nicht komplett abgebildet. Nichtsdestotrotz erreicht das Thums-elderly ein realistisches Deformationsmuster anhand der Anwendung von μ CT Daten für die Kortikalis (Kortikalschicht) der Rippen und des Brustbeins. Das Thums-elderly weist zusätzlich eine geringere Sensitivität bei sukzessiver Senkung des Niveaus des Gurtkraftbegrenzers im Vergleich mit Thums-original auf. Allerdings ist dieser Effekt nur bei Lastfällen mit „härteren“ Pulsen zu erkennen.

Brustbeinfrakturen und andere mittelschwere Verletzungen werden eine wichtige Rolle als Optimierungsziel bei der Auslegung zukünftiger Rückhaltesysteme spielen. Dazu ist eine realistische Prognose dieser Verletzungen notwendig, um eine korrekte Auslegung und Optimierung des Rückhaltesystems durchzuführen. Aktuelle Dummies sind nicht in der Lage, eine realistische Prognose dieser Verletzungen zu generieren. HBMs zeigen ein deutliches Potential, um diese Aufgabe zu übernehmen. Eine Simulationsmatrix mit einem breiten Spektrum von Crasheschweren und Rückhaltsystemen wurde als Benchmarkbasis aufgebaut. Die Ergebnisse aus dem H350 zeigen bei einer stetigen Reduktion der Rückhaltbelastung keine Reduktion des Brustbeinverletzungsrisikos. Mit HBMs zeigt diese Reduktion jedoch eine deutliche Minimierung dieses Risikos. Eine Altersabhängigkeit des Brustbeinverletzungsrisikos ist nicht von aktuellen Dummies prognostizierbar. Nur optimierte HBMs werden altersabhängige Effekte korrekt nachbilden. Faktoren wie eine realistischere Kortikalschicht und ein korrektes Verknöcherungsmuster der Knorpel sind erforderlich. Die Verletzungsprognose eines optimierten „altersabhängigen“ HBM (Thums-elderly) zeigt eine starke Abhängigkeit von der Crasheschwere, es zeigt jedoch eine geringere Sensitivität nach einer Reduktion der Rückhaltbelastung im Vergleich zu dem nicht-altersabhängigen HBM (Thums-original).

REFERENCES

- [1] S. Ridella, J. D. Rupp and K. Poland, "Age-Related Differences in AIS 3+ Crash Injury Risk, Types, Causation," *IRCOBI*, 2012.
- [2] J. States, „The Abbreviated and Comprehensive Research Injury Scales,“ in *Stapp Car Crash Journal 13*: 282-294, 1969.
- [3] T. Gennarelli and E. Wodzin, The Abbreviated Injury Scale 2005. Update 2008, Association for the Advancement of Automotive Medicine, 2008.
- [4] N. Yoganandan, A. M. Nahum and J. W. Melvin, "Accidental Injury: Biomechanics and Prevention," Third ed., New York, USA, Springer Science+Business Media, 2005.
- [5] T. Taylor, „www.innerbody.com,“ [Online].
- [6] J. C. B. Grant, A. M. R. Agur und A. F. Dalley, Grant's Atlas of Anatomy, Lippicott Williams & Wilkins, 2013.
- [7] R. O. Ritchie, M. J. Buehler and P. Hansma, "Plasticity and toughness in bone," *Physics Today*, pp. 41-47, June 2009.
- [8] J. L. Forman and R. W. Kent, "Modeling costal cartilage using local material properties with consideration for gross heterogeneities," *J Biomech*, pp. 910-916, 2011.
- [9] P. H. Abrahams, J. D. Spratt, M. Loukas, A.-N. van Schoor und R. T. Hutchings, McMinn and Abrahams' Clinical Atlas of Human Anatomy E-Book, Elsevier Health Sciences, 2013.
- [10] J. Waschke, T. M. Boeckers und F. Paulsen, Sobotta Lehrbuch Anatomie, Elsevier, Muenchen; Urban & Fischer, 2015.
- [11] M. DK and D. V. J, "Normal organs weights in men: Part II - The brain, lungs, liver, spleen, and kidneys," *Am J Forensic Med Pathol.*, 2012.
- [12] European Commission, „Towards an European road safety area: policy orientations on road safety 2011 – 2020,“ European Commission, 2009.
- [13] M. a. T. European Commission, Road Safety in the European Union, 2015.
- [14] „Coordination of Vehicle and Road Safety Initiatives,“ 2013. [Online]. Available: www.biomechanics-coordination.eu.
- [15] „THORAX - Thoracic Injury Assessment for Improved Vehicle Safety,“ [Online]. Available: www.thorax-project.eu.
- [16] J. Carroll, D. Hynd and P. Lemmen, "Cover D5 – Main Summary Report, Matrix of serious thorax injuries by occupant characteristics, impact conditions and restraint type and identification of the important injury mechanisms to be considered in THORAX and THOMO," 2009.
- [17] R. Nirula and F. Pintar, "Identification of vehicle components associated with severe thoracic injury in

- motor vehicle crashes: A CIREN and NASS analysis," *Accid Anal Prev*, pp. 137-41, 2008.
- [18] C. R. M. P. E. M. Cuerden R., „A review of the European 40% offset frontal impact test configuration,“ *Proceedings of the 20th Int. Tech. Conf. Enhanced Safety Vehicle*, 2007.
 - [19] G. Mulligan, An introduction to the understanding of blunt chest trauma. Biomechanics of Impact Injury and Injury Tolerances of the Thorax-Shoulder Complex, Backaitis, S. SAE publication PT-45, 1994, pp. pp.11-36..
 - [20] „Insurance Institute for Highway Safety / Highway Loss Data Institute,“ 2016. [Online]. Available: www.iihs.org/iihs/ratings/ratings-info/frontal-crash-test.
 - [21] United Nations, World population prospects:The 2010 revision, Volumen I: Comprehensive Tables, New York: Department of Economic and Social Affairs, Population Division, 2011.
 - [22] Organization for Economic Cooperation and Transport, Ageing and transport – mobility needs and safety issues, Paris: OECD PUBLICATIONS, 2001.
 - [23] R. J. Beck, A. N. Pollak and S. J. Rahm, Thoracic trauma. Intermediate Emergency Care and Transportation of the Sick and Injured., Boston: Jones and Bartlett., 2005.
 - [24] Marin, J.J., Wheeler, A.P. Critical Care Medicine: The Essentials, Hagerstown: Lippincott Williams & Wilkins, 2006, p. pp. 580..
 - [25] J. Myers, R. Tannehill-Jones und M. Neighbors, Principles of Pathophysiology and Emergency Medical Care, Albany, N.Y: Delmar Thomson Learning, 2002.
 - [26] J. Carroll, D. Hynd and P. Lemmen, Cover D5 – Annex I, Matrix of serious thorax injuries by occupant characteristics, impact conditions and restraint type and identification of the important injury mechanisms to be considered in THORAX and THOMO.
 - [27] „CCIS,“ [Online]. Available: <http://www.ukccis.org>.
 - [28] J. Brookes, R. Dunn and I. Rogers, "Sternal fractures: a retrospective analysis of 272 cases," *Journal of trauma*, pp. 46-54, 1993.
 - [29] R. Breederveld, P. Patka and J. van Mourik, "Fractures of the sternum," *The Netherlands journal of surgery*, pp. 133-135, 1988.
 - [30] T. Wedde, Quinlan, JF, A. Khan, H. Khan, F. Cunningham and J. McGrath, "Fractures of the sternum: the influence of non-invasive cardiac monitoring on management," *Archives of orthopaedic and trauma surgery*, pp. 121-123.
 - [31] G. J. Cooper, B. P. Pearce, M. C. Stainer and R. L. Maynard, "The biomechanical response of the thorax to nonpenetrating impact with particular reference to cardiac injuries," *Journal of trauma*, pp. 994-1008, 1982.
 - [32] K. Kroell, D. Allen, Y. Warner und T. Perl, „Interrelationship of velocity and chest compression in blunt thoracic impact to swine II,“ in *Stapp Car Crash Journal*, Warrendale, PA, USA, 1986.
 - [33] J. R. L. Hamilton, C. Dearden and W. H. Rutherford, "Myocardial contusion associated with fracture of the sternum: important features of the seat-belt syndrome," *Injury: The British journal of accident surgery*, pp. 155-156, 1984.
 - [34] B. T. Jolly and R. Martinez, "Sternal fractures and associated injuries in belted and unbelted occupants," *Proceedings of the 40th annual conference of the Association for the Advancement of Automotive Medicine (AAAM)*, pp. 519-520, 1996.
 - [35] K. Knobloch, S. Wagner, C. Haasper, C. Probst, C. Krettek, P. M. Vogt, D. Otte and M. Richter, "Sternal fractures are frequent among polytraumatized patients following high deceleration velocities in a severe vehicle crash," *Injury, international journal of the care of the injured. Elsevier Ltd.*, pp. 36-43, 2008.
 - [36] D. Yeh, J. Hwabejire, M. DeMoja, H. Alam, D. King and G. Velmahos, "Sternal fracture – An analysis of the National Trauma Datenbank," *J Surg Res*, 2014.
 - [37] Cahrs, *Safety companion*, Cahrs, 2015.
 - [38] NHTSA, „Federal Motor Vehicle Safety Standards and Regulations,“ [Online]. Available: <https://icsw.nhtsa.gov/cars/rules/import/FMVSS/>.

- [39] UNECE, "WP.29 Outcomes," [Online]. Available: www.unece.org/trans/main/wp29/presentation_regulations.html.
- [40] NHTSA, „Safercar.gov / NCAP Test Procedures,“ [Online]. Available: http://www.safercar.gov/NCAP_Test_Procedures.
- [41] Euroncap, "EURONCAP / Protocols," [Online]. Available: <https://www.euroncap.com/de/fuer-ingenieure/protocols>.
- [42] "GLOBALNCAP," [Online]. Available: www.globalncap.org.
- [43] Volvo, *Volvo -Children & Cars Safety Manual-*.
- [44] "humanetics / Crash Test Dummies," [Online]. Available: www.humaneticsatd.com/crash-test-dummies.
- [45] NHTSA, „NHTSA / Research / Vehicle Research and Testing / Hybrid III 50th Percentile Male,“ [Online]. Available: [www.nhtsa.gov/Research/Vehicle+Research+&+Testing+\(VRTC\)/Hybrid+III+50th+Percentile+Male](http://www.nhtsa.gov/Research/Vehicle+Research+&+Testing+(VRTC)/Hybrid+III+50th+Percentile+Male).
- [46] FTSS, "Hardware Manual Hybrid III 50th Male Dummy 78051-218X FVMSS208, 49CFR Part 572, Subpart E," 2005.
- [47] H. Mertz, A. Irwin and P. Prasad, "Biomechanical and scaling bases for frontal and side impact injury assessment reference values," *Stapp Car Crash J* 47, pp. 155-188, 2003.
- [48] T. Laituri, P. Prasad, K. Sullivan, M. Frankstein and R. Thomas, "Derivation and Evaluation of a Provisional, Age Dependent AIS 3+ ThoracicRisk Curve for Belted Adults," *SAE*, 2005.
- [49] R. Segura, F. Fuerst und D. Fressmann, „THUMS Validation in PAM-CRASH for Thoracic Loading Simulation in Accidents with mid Crash Severity,“ *VDI Verein Deutscher Ingenieure e.V. / Fahrzeugsicherheit*, 2011.
- [50] P. Ciarlet, N. Ayache and J. Lions, *Computational Models for the Human Body*, Gulf Professional Publishing, 2004.
- [51] T. M. Corporation, *Documentation Total Human Model for Safety AM50 Occupant / Pedestrian Model*, Japan, 2010.
- [52] "LMU. Department for earth and environmental sciences. Section for mineralogy, petrology and geochemistry," [Online]. Available: www.en.mineralogie.geowissenschaften.uni-muenchen.de.
- [53] "GE. Phoenix-vtomex-s," [Online]. Available: www.gemeasurement.com/inspection-ndt/radiography-and-computed-tomography/phoenix-vtomex-s.
- [54] E. Del-Pozo, M. Kindig, Arregui-Dalmases, C, J. Crandall, S. Takayama, S. Ejima, K. Kamiji and T. Yasuki, "Structural response and strain patterns of isolated ribs under lateral loading," *Int J Crashworthiness. Vol 16, No.2.*, pp. 169-180.
- [55] A. Lau, M. L. Oyen, R. W. Kent, D. Murakami and T. Torigaki, "Indentation stiffness of aging human costal cartilage," *Acta Biomater.* 4, pp. 97-103, 2008.
- [56] O. Rejtarova, D. Slizova, P. Smoranc, P. Rejtar and J. Bukac, "Costalcartilages, a clue for determination of sex," *Biomed Pap Med Fac Univ Palacky Olomouc*, pp. 241-243, Dec 2004.
- [57] S. Bahrami, U. Plate, R. Dreier, A. DuChesne, G. H. Willital and P. Bruckner, "Endochondral ossification of costal cartilage is arrested after chondrocytes have reached hypertrophic stage of late differentiation," *Matrix Biology*, pp. 707-715, 2001.
- [58] C. Cunningham, L. Scheuer and S. Black, *Developmental Juvenile Osteology*, Academic Press, 2016, p. 248.
- [59] W. F. McCormick, "Mineralization of the costal cartilages as an indicator of age: Preliminary observations," *J Forensic Sci.* 25, pp. 736-741, 1980.
- [60] R. Kent, D. Lessley and C. Sherwood, "Thoracic Response to Dynamic, Non-Impact Loading from a hub, distributed Belt, and Double Diagonal Belts," *Stapp Car Crash Journal*, 48, pp. 495-519, 2004.
- [61] A. Kemper, C. McNally, E. Kennedy, S. Manoogian, A. Rath, T. Ng, J. Stitzel, E. P. Smith and S. Duma, "Material Properties of Human Rib Cortical Bone," *Stapp Car Crash Journal*, 49, pp. 199-230, 2005.
- [62] H. Yamada, *Strength of Biological Materials*, Baltimore, MD, US: Williams & Wilkins, 1970.

- [63] R. Ko and M. Takigawa, "The tension test upon the costal cartilage of a human body," *J. Kyoto Pref. Med. Univ.* 53, pp. 93-96, 1953.
- [64] J. R. Kerrigan, D. Bose, Z. Li, C. Arregui-Dalmases and E. Del-Pozo, "Response of the sternum under dynamic 3-point bending," *Biomed Sci Instrum*, pp. 440-445, 2010.
- [65] E. Charpail, X. Trosseille and P. Petit, "Characterization of PMHS Ribs: A New Test Methodology," *Stapp Car Crash Journal*, 49, pp. 183-198, 2005.
- [66] M. Beaugonin, J. Yang, D. Kallieris, M. Schoenpflug and O. Ries, "HUMOS2 Project, Deliverable D20: Injury Mechanisms Database," 2004.
- [67] J. S. Shah, K. H. Yang, W. N. Hardy, H. K. Wang and A. I. King, "Development of a computer model to predict aortic rupture due to impact loading," *Stapp Car Crash Journal*, 45, pp. 161-182, 2001.
- [68] N. Hayamizu, I. Watanabe, T. Ishihara and K. Miki, "Measurement of impact response of pig lung," Toyota Central R&D Labs. Inc., Japan, 2003.
- [69] R. W. Kent, D. Murakami and S. Kobayashi, "Frontal Thoracic Response to Dynamic Loading the Role of Superficial Tissues, Viscera and the Rib Cage".*Proc. of 2005 IRCOB Conference.*
- [70] C. Kroell, D. Schneider and A. Nahum, "Impact tolerance and response of the human thorax," *Proceedings of 15th Stapp Car Crash Conference*, pp. 84-134, 1971.
- [71] C. Kroell, D. Schneider and A. Nahum, "Impact tolerance and response of the human thorax, Part II," *Proceedings of 18th Stapp Car Crash Conference*, 1974.
- [72] J. M. Shaw, R. G. Herriott, J. D. McFadden, B. R. Donnelly and J. H. Bolte, "Oblique and lateral impact response of the PMHS thorax," *Stapp Car Crash J.* 50, pp. 147-167, 2006.
- [73] D. Cesari and R. Bouquet, "'Behaviour of human surrogates thorax under belt loading," *Proceedings of 34th Stapp Car Crash Conference*, pp. 73-81, 1990.
- [74] R. Eppinger, J. Marcus and R. Morgan, "Development of dummy and injury index for NHTSA's thoracic side impact protection research program," *Society of Automotive Engineers*, 1984.
- [75] C. Kroell, D. Schneider and A. Nahum, "'Impact tolerance and response of the human thorax," *Proceedings of 15th Stapp Car Crash Conference*, pp. 84-134, 1971.
- [76] C. Kroell, D. Schneider and A. Nahum, "Impact tolerance and response of the human thorax Part II," *Proceedings of 18th Stapp Car Crash Conference*, 1974.
- [77] T. E. Lobdell, C. K. Kroell, D. C. Schneider and W. E. Hering, *Impact Response of the Human Thorax in Human Impact Response*, New York, USA: Plenum Press, 1973.
- [78] R. Neathery, "Analysis of Chest Impact Response Data and Scaled Performance Recommendations," *Proceedings of the 18th Stapp Car Crash Conference*, 1974.
- [79] D. Viano, "Biomechanical responses and injuries to blunt lateral impact," *Proceedings of 33rd Stapp Car Crash Conference*, pp. 113-142, 1989.
- [80] ISO/TR9790(E), "Road vehicles – Anthropomorphic Side Impact Dummy – Lateral Impact Response Requirements to Assess the Biofidelity of the Dummy," ISO/DTR 9790-7 Document N455 – Revision E, 1999.
- [81] G. Shaw, D. Parent, S. Purtsezov, D. Lessley, J. Crandall, R. W. Kent, H. Guillemot, S. A. Ridella, E. Takhounts and P. Martin, "Impact Response of Restrained PMHS in Frontal Sled Tests: Skeletal Deformation Patterns Under Seat Belt Loading," *Stapp Car Crash Journal*, vol. 53, pp. 1-48, 2009.
- [82] J. Boutillier, "Three-point bending test. Internship report,," Munich, 2012.
- [83] N. Yoganandan, A. M. Nahum und J. W. Melvin, „Restraint System Biomechanics,“ in *Accidental Injury: Biomechanics and Prevention*, 3rd Hrsg., New York, USA, Springer Science+Business Media, 2005.
- [84] F. Kramer, „Passive Sicherheit von Kraftfahrzeugen,“ Wiesbaden, Germany, Vieweg & Teubner, 2009.
- [85] F. Berg, B. Schmitt, J. Eppler, R. Matterns and D. Kallieris, "Results of full-scale crash test, stationary tests and sled tests to analyze the effects of airbags on passengers with or without seat belts in the standard sitting position and in out-of-position situations," *Proceedings of the international research council on the biomechanics of impact (IRCOBI)*, 1998.

- [86] L. Patrick, C. Kroell and H. Mertz, "Forces on the human body in simulated crashes," *Proceedings of the 9th Stapp Car Crash Conference*, pp. 237-259, 1965.
- [87] L. Grosch, "Chest Injury Criteria for Combined Restraint Systems," in *SAE Government Industry Meeting and Exposition*, 1985.
- [88] A. Petitjean, P. Baudrit and X. Trosseille, "Thoracic Injury Criterion for Frontal Crash Applicable to All Restraint Systems," *Stapp Car Crash J*, 2003.
- [89] D. Adomeit, "Evaluation Methods for the biomechanical quality of restraint systems during frontal impact," *Proceedings of the 21st Stapp Car Crash Conference*, pp. 911-932, 1977.
- [90] D. Adomeit and A. Heger, "Motion sequence criteria and design proposals for restraint devices in order to avoid unfavorable biomechanic conditions and submarining," *Proceedings of the 19th Stapp Car Crash Conference*, 1975.
- [91] R. W. Kent, J. R. Crandall, J. R. Bolton and D. S. M, "Driver and right-front passenger restraint system interaction, injury potential and thoracic injury prediction," *Ann Proc Assoc Adv Automot Med* 44, pp. 261-282, 2000.
- [92] L. Kuebler, S. Gargallo and K. Elsaesser, "Characterization and evaluation of frontal crash pulses with respect to occupant safety," *Airbag 2000. 9th International Symposium and Exhibition on Sophisticated Car Occupant Safety Systems*, 2008.
- [93] M. Kleinberger, E. Sun, R. Eppinger, S. Kuppa and R. Saul, "Development of Improved Injury Criteria for the Assessment of Advanced Automotive Restraint Systems," 1998.
- [94] R. Eppinger, E. Sun, F. Bandak, M. Haffner, N. Khaewpong, M. Maltese, S. Kuppa, T. Nguyen, E. Takhounts, R. Tannous, A. Zhang and R. Saul, "Development of improved injury criteria for the assessment of advanced automotive restraint systems – II," Washington, D.C., USA, 1999.
- [95] I. V. Lau and D. C. Viano, "How and When Blunt Injury Occurs: Implications to Frontal and Side Impact Protection," *Proceedings of the 32nd Stapp Car Crash Conference*, pp. 81-100, 1988.
- [96] H. J. Mertz, „Hybrid III Sternal Deflection Associated with Thoracic Injury Severities of Occupants Restrained with Force-Limiting Shoulder Belts“ .*SAE International Congress and Exposition*.
- [97] R. Eppinger, "On the Development of a Deformation Measurement System and its Application Toward Developing Mechanically Based Injury Indices," *Proceedings of the 33rd Stapp Car Crash Conference*, pp. 21-28, 1989.
- [98] R. M. e. a. Morgan, "Thoracic Trauma Assessment Formulations for Restrained Drivers in Simulated Frontal Impacts," *Proceedings of the 38th Stapp Car Crash Conference*, 1994.
- [99] J. D. e. a. Horsch, "Thoracic Injury Assessment of Belt Restraint Systems Based on Hybrid III Chest Compression," *35th Stapp Car Crash Conference*, pp. 85-108, 1991.
- [100] V. K. Lau and D. C. Viano, "Influence of impact velocity on the severity of nonpenetrating hepatic injury," *J Trauma* 21, pp. 115-123, 1981.
- [101] L. I. Viano DC, "Thoracic impact: a viscous tolerance criterion," *Proceedings of the Tenth international technical conference on experimental safety vehicles*, pp. 104-114, 1985.
- [102] I. V. Lau and D. C. Viano, "The viscous criterion – Bases and applications of an injury severity index for soft tissues," *Proceedings of 30th Stapp CarCrash Conference*, pp. 123-142, 1986.
- [103] J. Y. Foret-Bruno, X. Trosseille, J. Y. Le Coz, F. Bendjellal and C. Steyer, "Thoracic Injury Risk in Frontal Car Crashes with Occupant Restrained with Belt Load Limiter," *Proceedings of 42nd Stapp Car Crash Conference*, 1998.
- [104] R. W. Kent, J. Patrie and N. Benson, "The hybrid III dummy as a discriminator of injurious and non-injurious restraint loading," *47th Annual Proceedings, Association for the Advancement of Automotive Medicine*, 2003.
- [105] L. Grosch, "Chest injury criteria for combined restraint systems" .*Society of Automotive Engineers*.
- [106] X. Trosseille, E. Song and A. Petitjean, "Chest injury criterion: an update of the equivalent deflection (Deq)," *Proceedings of the 23th Int. Tech. Conf. Enhanced Safety Vehicle*, 2013.
- [107] R. Kent, J. Patrie, F. Poteau, F. Matsuoka and C. Mullen, "Development of an age-dependent thoracic

- injury criterion for frontal impact restraint loading". *Proceedings of the 18th Int. Tech. Conf. Enhanced Safety Vehicle*.
- [108] J. Horsch and D. Schneider, "Biofidelity of the hybrid III thorax in high velocity frontal impact," *SAE*, 1988.
- [109] S. Kuppa and R. H. Eppinger, "Development of an improved thoracic injury criterion," *Proceedings of the 42nd Stapp Car Crash Conference*, 1998.
- [110] D. Kallieris, A. Rizzetti, R. Mattern, R. Morgan, R. Eppinger and L. Keenan, "On the synergism of the driver air bag and the 3-point belt in frontal collisions," *39th Stapp Car Crash Conference*, 1995.
- [111] R. Banglmaier, L. Wang and P. Prasad, "Various statistical methods for the analysis of experimental chest compression data," *Proceedings of the American Statistical Association, Section on Physical and Engineering Sciences*, 2002.
- [112] D. Viano, "Evaluation of biomechanical response and potential injury from thoracic impact," *Symposium on Biodynamic Models and their Applications, Aviation Space and Environmental Medicine, Vol. 49*, 1977.
- [113] J. Foret-Bruno, F. Hartemann, C. Thomas, A. Fayon, C. Tarriere, C. Got and A. Patel, "Correlation between thoracic lesions and force values measured at the shoulder of 92 belted occupants involved in real accidents". *Proceedings of the 22nd Stapp Car Crash Conference*.
- [114] R. Kent, J. Bolton, J. Crandall, P. Prasad, G. Nusholtz, H. Mertz and D. Kallieris, "Restrained hybrid III dummy-based criteria for thoracic hard tissue injury prediction," *Conference of the International Research Council on the Biomechanics of Impact (IRCOBI)*, 2001.
- [115] D. Cesari and R. Bouquet, "Comparison of Hybrid III and Human Cadaver Thorax Deformations Loaded by a Thoracic Belt," *Stapp Car Crash Conference*, 1994.
- [116] J. Davidsson, "Injury risk curve development," Bergich Gladbach, Germany, 2013.
- [117] NHTSA, "NHTSA / Biomechanics and Trauma / THOR," [Online]. Available: <https://nhtsa.gov/biomechanics-trauma/thor>.
- [118] M. Torba and S. Hijazi, "Seat belt syndrome, a new pattern of injury in developing countries. Case report and review of literature," *G Chir*, pp. 177-180, 2014.
- [119] J. P. Lechaux, J. P. Poinard, Y. Ravaud, J. Asseraf and C. Boulakia, "Abdominal traumas due to the safety belt," *Nouv Presse Med*, pp. 3385-3388, 1981.
- [120] M. Smith and V. Ball, *Cardiovascular/respiratory physiotherapy*, Mosby, 1998, p. 217.
- [121] A.-a. Khoriaty, R. Rajakulasingam and R. Shah, "Sternum fractures and their management," *J Emerg Trauma Shock*, 2013.
- [122] R. Watkins, L. W. R. Williams, S. Ahlbrand, R. Garcia, A. Karamanian, L. Sharp, V. C and T. Hedman, "Stability provided by the sternum and rib cage in the thoracic spine," *The Spine J*, pp. 1283-6, 2005 (Phila Pa 1976).
- [123] C. G. Shaw, D. P. Parent, S. Purtsezov, D. J. Lessley, J. R. Kerrigan, J. Shin, J. R. Crandell, Y. Zama, S. Ejima, K. Kamiji and T. Yasuki, "Frontal impact PMHS sled test for FE torso model development," *IRCOBI*, 2009.
- [124] E. A. Kennedy, W. J. Hurst, J. D. Stitzel, J. M. Cormier, G. A. Hansen, E. P. Smith and S. M. Duma, "Lateral and Posterior Dynamic Bending of the Mid-Shaft Femur: Fracture Risk Curves for the Adult Population," *Stapp Car Crash J, Vol. 48*, 2004.
- [125] H. Zellmer, C. Kahler and B. Eickhoff, "Optimized pretensioning of the belt system: A rating criterion and the benefit in consumer test," *Proceedings of the 19th Int. Tech. Conf. Enhanced Safety Vehicle*, 2005.
- [126] J. Forman, F. Lopez-Valdes, D. Lessley, M. Kindig, R. Kent, S. Ridella und O. Bostrom, „Rear Seat Occupant Safety: An Investigation of a Progressive Force-Limiting, Pretensioning 3-Point Belt System Using Adult PMHS in Frontal Sled Tests,“ *Stapp Car Crash J, Vol. 53*, 2009.
- [127] A. Ressler, M. Lienkamp and F. Fürst, "Method to estimate the field effectiveness of an automatic braking system in combination with an adaptive restraint system in frontal crashes," *Proceedings of the 23th Int. Tech. Conf. Enhanced Safety Vehicle*, 2011.

- [128] R. Segura, F. Fürst, A. Langner und S. Peldschus, „Real World Accident Reconstruction with the Total Human Model for Safety (THUMS) in Pam-Crash,“ *ESAR Experts Symposium on Accident Research*, 2012.
- [129] "PC-Crash," [Online]. Available: www.dsd.at/index.php?option=com_content&view=article&id=323:pc-crash-deutsch&catid=53&Itemid=174&lang=de.
- [130] A. G. Lau, M. W. Kindig and R. W. Kent, "Morphology, distribution, mineral density and volume fraction of human calcified costal cartilage," *Acta Biomaterialia* 7, 2011.
- [131] I. O. f. Standarization, ISO 13216-3:2006 Road Vehicles -- Anchorages in vehicles and attachments to anchorages for child restraint systems --Part 3: Clasification of child restraint dimensions and space vehicle, 2006.

INDEX OF FIGURES

Fig. 1.1	Bony thorax.....	12
Fig. 1.2	Cortical and trabecular bone	13
Fig. 1.3	Hierarchical structure of the bone.....	14
Fig. 1.4	Road Accident fatalities in Europe [13].....	16
Fig. 1.5	Torso injuries overview form EU data. Taken from [16]	17
Fig. 1.6	AIS3+ Injuries distribution in frontal crashes. Subsample from the NASS-CDS. Taken from [1]	17
Fig. 1.7	Distribution of crash modes in the US according to [20]	17
Fig. 1.8	Aging population projection for USA [1] and Europe [21]	18
Fig. 1.9	Distribution of car occupant fatalities in the EU per age [13]	18
Fig. 1.10	Thoracic injuries clustered by age. Based on [1]	19
Fig. 1.11	Only thoracic injuries distribution. Adapted from [16]	20
Fig. 1.12	Full Euroncap frontal test.....	24
Fig. 1.13	Frontal Euroncap ODB (Offset Deformable Barrier)	24
Fig. 1.14	Left: Spine and chest deflection transducer. Right: Torso assembly [46]	28
Fig. 1.15	Current H350 USNcap thoracic injury risk curve [48]	29
Fig. 1.16	Thums® v3 (Total Human Model for Safety). Some parts not displayed for visualization 31	
Fig. 1.17	Left: Human thorax structure [10]. Right: Thums thorax structure	33
Fig. 2.1	Diagram for the sterna extraction protocol (red represents the cutting locations) and specimen	36
Fig. 2.2	Left: GE phoenix 3D v/tome/x m. Center: Sternum mounted. Right: Voxel size.	37
Fig. 2.3	Diagram of the μ CT Machine. Credits GE Measurement & Control, Volume Graphics [53].....	38
Fig. 2.4	Example of the scanned region on the detector	38
Fig. 2.5	CAD162, example of sternum cross sections ventral to coronal from the μ CT-Scan (left to right). Step approx. 1 cm	39
Fig. 2.6	Left: Diagram and coordinates of sternum μ CT Scan. Right: Cross section as an example of a local cortical thickness.....	39
Fig. 2.7	Cortical thickness groups for the 7 th rib generated by 3-Matic Software Package. Credits: Anja Wagner LMU	40

Fig. 2.8	Four calcification levels from left to right: 0%, 15%, 60% and 100% represented by the growing of the brown region	43
Fig. 2.9	Four calcification levels in Table-Top environment. Soft tissues blended.....	43
Fig. 2.10	From Kemper [61] experiments: Coupon test dimensions or “dog bone”	45
Fig. 2.11	From Kemper experiments [61]: Grey curves represent the experimental data. In black the average and $\pm\sigma$ until 13000 microstrain.	45
Fig. 2.12	Stress-Strain curve of human costal cartilage in tension as published by Yamada [62]	46
Fig. 2.13	Left: Test setup for sternum bending. Right: Test diagram taken from [64]	47
Fig. 2.14	Convexity of the sternum generate significant forces in X due to the fixation setup with pin-joints: Rotation [64]	47
Fig. 2.15	Dynamic response corridor for sternum: Right: Fx on LC1. Left: Fx on LC2. Accuracy of experimental data under question.	48
Fig. 2.16	Dynamic response corridor for sternum under bending loading [65]	49
Fig. 2.17	Test setup diagram as presented by Charpail et al. [65].....	50
Fig. 2.18	K, rupture energy and reaction forces (mean and $\pm\sigma$ per rib level) from the experiments	51
Fig. 2.19	Left: Clavicle three-point bending test from the HUMOS2 project. Right: Test corridor	52
Fig. 2.20	Left: Costal cartilage specimens [8]. Right: Loading configuration	53
Fig. 2.21	Left: FX mean $\pm\sigma$. Right: FY mean $\pm\sigma$. Unscaled data.	54
Fig. 2.22	Left: Fx mean $\pm\sigma$. Right: Fx mean $\pm\sigma$. Scaled data.	54
Fig. 2.23	Intact and eviscerated linear stiffness of the experimental data as presented by Kent et al. [69].....	55
Fig. 2.24	Table-top test set up [60] for imposed chest deflection with diagonal belt (middle) and distributed load (right)	56
Fig. 2.25	Left: Corridor for posterior force scaled to 45 YO 50 th %-ile male vs. chest deflection in belt loading [60].	57
Fig. 2.26	Blunt impact configuration with PMHS [76]. Here the skin was removed for visualization purposes.	58
Fig. 2.27	Original corridor from Kroell with muscle tensing shift and chest deflection including superficial soft tissue.....	59
Fig. 2.28	Modified corridors from [78]. The dotted line corridor includes muscle tensing shift and represents total deflection.....	60
Fig. 2.29	PMHS positioned for lateral hub impact [72]	61
Fig. 2.30	Corridors for lateral and oblique hub impact response	61
Fig. 2.31	GS1 pulse and photograms of test 1358. Taken from [81]	63
Fig. 2.32	Belt tension and multipoint chest deflection corridors wrt. T8. The simulation results are shown in 2.2.4.4.	64
Fig. 2.33	Results of the μ CT scans, each color represents a “Thickness group”	65
Fig. 2.34	Thickness groups for Thums-elderly sternum. Manual mapping to the FE model..	67
Fig. 2.35	Thickness groups for Thums-elderly (7 th rib)	67
Fig. 2.36	Cortical thickness of the “Thickness Groups” per rib implemented on the Thums-elderly	68

Fig. 2.37	Von Mises (VM) stress distribution in GPa on ribs and sternum. Note the higher VM stresses in the fully calcified model.....	69
Fig. 2.38	VM-Stress [GPa] distribution on the sternum. Left: Non-calcified model. Right: Fully calcified model.....	69
Fig. 2.39	Peak Von Mises stresses of all elements of the anterior cortical layer of the sternum on both 0% calcification (left).....	70
Fig. 2.40	Left: 0% Calcification. Right: 100% Calcification. Note the anterior-posterior shift of the stress concentration of the ribs and the higher stresses on the sternum in the 100% calcified model.....	70
Fig. 2.41	VM-Stress [GPa] shift on the 6 th rib. Top: From the 0% calcification model. Bottom: From the 100% calcification model. Note anterior-posterior shift of the stress concentration. The reference points are shown.	71
Fig. 2.42	Structural effect of cartilage calcification: Anterior-to-posterior Von Mises stress shift. Note also the stress concentration on the reference point 100	71
Fig. 2.43	Chest deflections upper left (UL), upper right (UR), center (C), lower left (LL) and lower right (LR). Note the increased lower chest deflection in the fully calcified model	72
Fig. 2.44	Left: Geometry of the coupons [61]. Right: Simulation Model and boundary condition	73
Fig. 2.45	Stress-Strain response of the dog-bone model. Left: Ribs. Right: Sternum.....	74
Fig. 2.46	Experiment stress-strain response and simulation of a single-element model with both Thums-original and Thums-elderly material.....	75
Fig. 2.47	Left: Experiment set up from Kerrigan et al. [64]. Right: Simulation model	76
Fig. 2.48	Left: Bending with the Thums-original sternum. Right: Dynamic response corridor for sternum under bending loading	77
Fig. 2.49	7 th Rib under anterior-posterior loading. Boundary conditions and prescribed velocity	78
Fig. 2.50	Bending moments per rib level using the test configuration from Charpail et al [65] with	79
Fig. 2.51	Reaction forces (Fx) under AP bending per rib	80
Fig. 2.52	Regression between 15 mm and 25 mm cap displacement for K calculation.....	81
Fig. 2.53	K, rupture energy and reaction forces (mean and $\pm\sigma$ per rib level). Simulation results with Thums-original and Thums-elderly	82
Fig. 2.54	Left: Three-point bending test simulation setup. Right: Bending response of both Thums-original and Thums-elderly.....	83
Fig. 2.55	Costal cartilage model with boundary conditions following the description of Forman et al [8]	84
Fig. 2.56	Young's modulus from Thums-original for the increase of stiffness by calcification	84
Fig. 2.57	Thums-original and Thums-elderly Fx and Fy reaction forces	85
Fig. 2.58	Intact and eviscerated linear stiffness of the experimental data and simulations with the Thums-elderly	86
Fig. 2.59	Diagonal belt and distributed load simulations. Note the "Y-notch Point" for chest deflection reference.....	87
Fig. 2.60	H350 in table-top diagonal belt loading	88

Fig. 2.61	Left: Table-Top diagonal belt test response comparison: Hybrid-III, Thums-original and Thums-elderly. Right: Distributed loading	89
Fig. 2.62	Left: Lateral, frontal and isometric views of the hub impact simulation with both Thums-original and Thums-elderly.....	90
Fig. 2.63	Frontal lateral and isometric views of the lateral hub impact simulation with both Thums-original and Thums-elderly.....	91
Fig. 2.64	Frontal lateral and isometric views of the oblique hub impact simulation with both Thums-original and Thums-elderly.....	91
Fig. 2.65	Left: Corridors for and model response for lateral hub impact. Right: Corridors for and model response for oblique hub impact	91
Fig. 2.66	Comparison of the belt routing between subject 1358 and Thums. Path taken from [81]	92
Fig. 2.67	Comparison of GS1 seating position between a PMHS [81] and Thums	92
Fig. 2.68	Thums-original / -elderly as positioned in the GS1 simulations.....	93
Fig. 2.69	Test and Thums-original forward excursion comparison	93
Fig. 2.70	Belt tension and multipoint chest deflection wrt. T8. Thums-original and Thums-elderly simulation results	94
Fig. 3.1	Typical crash vehicle velocity as a function of time. Modified example based on the example from Kent et al. (2015) [83].....	97
Fig. 3.2	Green: simple belt restraint. All: No pretensioner, no load limiters. The forward excursion is around 300mm.	98
Fig. 3.3	Purple: Effect of a pretensioner. The forward excursion is around 300mm.	99
Fig. 3.4	Cyan: Combined effect a pretensioner and load limiters. The forward excursion is again ~300mm.....	100
Fig. 3.5	Black: Standard belt with Airbag. Blue: Pretensioned, load limited belt with airbag	100
Fig. 3.6	Effect of the load limiter on the occupant acceleration [84].....	101
Fig. 3.7	Occupant Load Criterion (OLC). Diagram taken from [92] . Note the 65mm (yellow) and 235mm (green) areas.....	106
Fig. 3.8	Correlation central chest deflection vs. max. chest deflection [93]	109
Fig. 3.9	Left: Viscous criteria development diagram [102]	110
Fig. 3.10	Left: IRC AIS4+ based on VCmax. Right: Applicability range of the criterion [102]	111
Fig. 3.11	Injury risk curves force-based with age dependency proposed by Foret-Bruno [103]	112
Fig. 3.12	Block diagram for DEQ calculation with the H350 [106]	113
Fig. 3.13	Plotted age dependent injury risk curves developed by[48]. Applicable to PMHS.	115
Fig. 3.14	Gray: Undeformed ribcage and 7 th rib. Bony color: Ribcage and 7 th rib under bending due to seatbelt loading. Simplified representation of the loading configuration involved in an oblique crash.....	118
Fig. 3.15	Left: Table-top (belt loading) and GS1 as test loadcases for the injury mechanism analysis. Right: Bending moments measurement locations at the inter-costal spaces (ics) via section-force cards in VPS.....	120
Fig. 3.16	Bending moments per rib level under AP loading	122
Fig. 3.17	Location of the section forces and coordinate systems for bending output	123

Fig. 3.18	Reference risk curves for Thums-original.....	124
Fig. 3.19	Reference risk curves for Thums-elderly	124
Fig. 3.20	Injury risk curve for NFR>6 (AIS3+) from the core dataset [116].....	125
Fig. 3.21	Current H350 USNCAP thoracic injury risk curve.....	126
Fig. 3.22	Example of different triggering strategies (A vs. B) for some of the crash cases of the chapter 4.	130
Fig. 3.23	FX, FY and FZ for both Thums-original (orig) and Thums-elderly (elde) in Table-top (dotted line) and GS1 (solid line)	132
Fig. 3.24	MX, MY and MZ for both Thums-original (orig) and Thums-elderly (elde) in Table-top (dotted line) and GS1 (full line).....	133
Fig. 3.25	Absolute-loading-difference comparison for all ics_2 and ics_3 in Thums-original and Thums-elderly	134
Fig. 3.26	Ribcage's bottom view to illustrate twisting under the same loadcase but different restraint.	135
Fig. 3.27	Resultant moments at the ICS_2 for both Thums models and IRV	135
Fig. 3.28	Humat one-pager summary for one validation loadcase	136
Fig. 3.29	Positioned model in GS1. Left: H350. Right: Thums-original and Thums-elderly.....	136
Fig. 3.30	GS1: PMHS Test, H350 (second row) and both Thums (third row).....	137
Fig. 4.1	Selected accident scheme (AARU). Skoda Octavia (red), Audi A4 (blue)	142
Fig. 4.2	Collision trajectories for the selected accident. Skoda Octavia (red) vs. Audi A4 (blue) Credits: Thomas Schenk (AARU)	143
Fig. 4.3	Left: FE models. Right: Resulting trajectories from PC-Crash	143
Fig. 4.4	Structure deformation comparison. Left: Real accident. Right: Simulation. Credits: Adrian Langner (ASTech)	144
Fig. 4.5	Resultant velocity pulses (normalized) from the structural simulation	144
Fig. 4.6	Right: Interior view of the Audi A4 after the crash	145
Fig. 4.7	HBMs in driver and passenger side. Occupant-cell shown in gray. Roof, A- and B-pillars were blended for visualization	146
Fig. 4.8	Simulations with H350, Thums-original and Thums-elderly in driver and passenger positions.....	147
Fig. 4.9	Normalized trigger times and belt loading for all models in passenger position. Sternal loading reduction in terms of inter-costal-space-2 resultant moment. Note that the H350 was not designed for this type of loading assessment. The loading reduction cannot be assessed with the H350	148
Fig. 4.10	Driver and passenger positions. Overlap with Hybrid-III (red) and HBM (Bony color)	156
Fig. 4.11	Accident reconstruction, ICS resultant moments for both Thums models and four restraint variants	156
Fig. 4.12	Driver H350 thoracic injury risk for all restraint system variants.....	184
Fig. 4.13	Passenger H350 thoracic injury risk for all restraint system variants	184
Fig. 4.14	Driver Thums-original thoracic injury risk for all restraint system variants.....	185
Fig. 4.15	Passenger Thums-original thoracic injury risk for all restraint system variants	185
Fig. 4.16	Driver Thums-original ICS_2 bending for all restraint system variants	185
Fig. 4.17	Passenger Thums-original ICS_2 bending for all restraint system variants	185
Fig. 4.18	Driver Thums-elderly thoracic injury risk for all restraint system variants	186

Fig. 4.19	Passenger Thums-elderly thoracic injury risk for all restraint system variants	186
Fig. 4.20	Driver Thums-elderly ICS_2 bending for all restraint system variants	186
Fig. 4.21	Passenger Thums-elderly ICS_2 bending for all restraint system variants.....	186
Fig. 4.22	Driver HJ350 injury reduction per system	187
Fig. 4.23	Passenger H350 injury reduction per system	187
Fig. 4.24	Driver Thums-original injury reduction per system.....	187
Fig. 4.25	Passenger Thums-original injury reduction	187
Fig. 4.26	Driver Thums-elderly injury reduction per system	188
Fig. 4.27	Passenger Thums-elderly injury reduction.....	188
Fig. 4.28	Driver Thums-original ICS_2 MXYZ reduction per system	188
Fig. 4.29	Passenger Thums-original ICS_2 MXYZ reduction.....	188
Fig. 4.30	Driver Thums-elderly ICS_2 MXYZ reduction per system.....	189
Fig. 4.31	Passenger Thums-elderly ICS_2 MXYZ	189
Fig. 4.32	VX, VY and VZ pulses of all loadcases.....	190
Fig. A.1	Side barrier Euroncap (Green: starting on 2015).....	228
Fig. A.2	Side pole Euroncap	228
Fig. A.3	Whiplash (Rear crash) [41]	229
Fig. A.4	Impactors: Adult and child head, upper leg, and lower leg [37].....	230

INDEX OF TABLES

Table 1.1	Injury severities defined in the AIS code [3]	10
Table 1.2	AIS Codes for thoracic skeletal injuries.....	11
Table 1.3	Current frontal crash testing programs.....	23
Table 1.4	Highlight of frontal crash test dummies-development.....	26
Table 1.5	Current application fields for frontal crash test dummies. Partly taken from Safety Update 2012 proceedings. Child dummies not addressed here.....	26
Table 1.6	Taken External dimensions of the H350 dummy [46]	27
Table 1.7	Overview of the H350 thorax instrumentation. Full equipped.	28
Table 1.8	Injury assessment reference values for the H350. Taken from [47]	28
Table 1.9	Comparison H350 vs. HBMs	30
Table 1.10	THUMS® upgrades (*Baseline in this dissertation).....	32
Table 1.11	THUMS® v3 in VPS. Model data with rounded numbers.	32
Table 1.12	Bony Material descriptions of the Thums thorax components in VPS®	33
Table 2.1	Subjects details. All male	37
Table 2.2	μCT specifications.....	38
Table 2.3	Rib modeling characteristics (cortical layer of the Thums-original)	40
Table 2.4	Cortical thickness groups for the 7 th rib	41
Table 2.5	PMHS details, sorted by age [61].....	45
Table 2.6	Summary of the PMHSs as presented by Charpail et al. [65].....	50
Table 2.7	Summary of PMHS data as presented by Forman et al. [8].....	53
Table 2.8	Summary of the Kroell's experimental data published in 1971 and 1974.	58
Table 2.9	Data used by [78] for the scaled corridors	59
Table 2.10	GS1 characteristics	62
Table 2.11	Sterna μCT scans Cortical thickness groups generated by 3-Matic Software Package. Credits: Anja Wagner LMU.....	66
Table 2.12	Thickness groups and thickness values	67
Table 2.13	Thicknesses assigned to each group (Thums-elderly).....	68
Table 2.14	Elements thicknesses repartition	68
Table 2.15	Rib and sternum cortical bone material model properties.....	74
Table 2.16	Costal cartilage element type and E	75
Table 2.17	Material properties of cortical and trabecular layers of the sternum model.....	76

Table 2.18	Material properties of cortical and trabecular layers of the rib models.....	78
Table 2.19	Material properties of cortical and trabecular layers of the clavicle model	83
Table 2.20	Material properties of the cartilage model	84
Table 2.21	Simulation matrix for table-top test	88
Table 2.22	Chest deflection normalization factors.....	88
Table 2.23	Angle ranges for positioning as defined in [81] vs. Thums position	92
Table 3.1	Crash pulse characterization criteria	105
Table 3.2	Correlation analysis of injury-outcome with pulse criteria as presented in [92] ..	106
Table 3.3	Regression parameters for the reference curves.....	124
Table 3.4	Rated effectiveness of pretensioner configurations	127
Table 3.5	Restraint System Parameters for deployment strategy used in this study.....	129
Table 3.6	Relation restraint parameters and design guidelines	130
Table 3.7	Abbreviations	131
Table 3.8	Sternum bending in table-top belt and GS1	131
Table 3.9	Experiments, H350 and Thums models injury outcome	137
Table 3.10	Assessment of sternal loading for both Thums models.....	138
Table 4.1	Frontal crash severity scale, and equivalent cases addressing occupant injury risk evaluation	141
Table 4.2	Anthropometric characteristics, age and injury severity of the occupants in the Audi A4	142
Table 4.3	Initial kinematic conditions obtained with PC-Crash simulations	142
Table 4.4	Accident reconstruction simulation matrix	146
Table 4.5	Restraint System variants description	147
Table 4.6	Crash Case 1: Drivers AIS3+ Prediction.....	149
Table 4.7	Crash Case 1: Driver, Thums-original sternal loading.....	149
Table 4.8	Crash Case 1: Driver, Thums-elderly sternal loading	150
Table 4.9	Crash Case 1: Passengers AIS3+ Prediction	151
Table 4.10	Crash Case 1: Passenger, Thums-original sternal loading	151
Table 4.11	Crash Case 1: Passenger, Thums-elderly sternal loading.....	152
Table 4.12	Ribcage twisting for visualization under four restraint variants	155
Table 4.13	Characteristic crash cases including an accident reconstruction*. Based on [127]	158
Table 4.14	Simulation matrix	159
Table 4.15	Crash Case 2: Drivers AIS3+ Prediction.....	160
Table 4.16	Crash Case 2:Driver, Thums-original sternal loading.....	160
Table 4.17	Crash Case 2:Driver, Thums-elderly sternal loading	161
Table 4.18	Crash Case 2: Passengers AIS3+ Prediction	162
Table 4.19	Crash Case 2:Passenger, Thums-original sternal loading	162
Table 4.20	Crash Case 2:Passenger, Thums-elderly sternal loading.....	163
Table 4.21	Crash Case 3: Drivers AIS3+ Prediction.....	164
Table 4.22	Crash Case 3:Driver, Thums-original sternal loading.....	164
Table 4.23	Crash Case 3:Driver, Thums-elderly sternal loading	165
Table 4.24	Crash Case 3: Passengers AIS3+ Prediction	166
Table 4.25	Crash Case 3:Passenger, Thums-original sternal loading	166
Table 4.26	Crash Case 3:Passenger, Thums-elderly sternal loading.....	167
Table 4.27	Crash Case 4: Drivers AIS3+ Prediction.....	168

Table 4.28	Crash Case 4:Driver, Thums-original sternal loading.....	168
Table 4.29	Crash Case 4:Driver, Thums-elderly sternal loading	169
Table 4.30	Crash Case 4: Passengers AIS3+ Prediction	170
Table 4.31	Crash Case 4:Passenger, Thums-original sternal loading	170
Table 4.32	Crash Case 4:Passenger, Thums-elderly sternal loading.....	171
Table 4.33	Crash Case 5: Drivers AIS3+ Prediction.....	172
Table 4.34	Crash Case 5:Driver, Thums-original sternal loading.....	172
Table 4.35	Crash Case 5:Driver, Thums-elderly sternal loading	173
Table 4.36	Crash Case 5: Passengers AIS3+ Prediction	174
Table 4.37	Crash Case 5:Passenger, Thums-original sternal loading	174
Table 4.38	Crash Case 5:Passenger, Thums-elderly sternal loading.....	175
Table 4.39	Crash Case 6: Drivers AIS3+ Prediction.....	176
Table 4.40	Crash Case 6:Driver, Thums-original sternal loading.....	176
Table 4.41	Crash Case 6:Driver, Thums-elderly sternal loading	177
Table 4.42	Crash Case 6: Passengers AIS3+ Prediction	178
Table 4.43	Crash Case 6:Passenger, Thums-original sternal loading	178
Table 4.44	Crash Case 6:Passenger, Thums-elderly sternal loading.....	179
Table 4.45	Crash Case 7: Drivers AIS3+ Prediction.....	180
Table 4.46	Crash Case 7:Driver, Thums-original sternal loading.....	180
Table 4.47	Crash Case 7:Driver, Thums-elderly sternal loading	181
Table 4.48	Crash Case 7: Passengers AIS3+ Prediction	182
Table 4.49	Crash Case 7:Passenger, Thums-original sternal loading	182
Table 4.50	Crash Case 7: Passenger, Thums-elderly sternal loading.....	183
Table A.1	Current crash testing programs.....	227
Table B.3	Highlights of the crash test dummy-development.....	233
Table B.4	Overview of application fields for crash test dummies. Partly taken from Safety Update 2012 proceedings. Child dummies not addressed here.....	234
Table B.4	Overview of the H350 complete instrumentation. Full equipped.	235
Table B.4	Injury assessment reference values for the H350. Taken from [47]	236

A. APPENDIX: CRASH TESTS

To depict the current status of crash-testing and crash-avoidance test protocols, an overview of the current crash test protocols of Euroncap (2015) follows (mainly taken from the Euroncap website [41]).

Level	Test	Regulations	Consumer Test
Full Scale	Full Frontal	FMVSS 203, 204, 205, 208, 209, 210, 212, 301 UN R12, R14, R16, R33, R94	US NCAP 56km/h EURO NCAP 50km/h
	Offset Frontal	FMVSS 208 UN R94	IIHS 64 km/h (40% ODB) EURONCAP 64 km/h
	Small Overlap	-	IIHS 64 km/h (25%)
	Side Barrier	FMVSS 214, UN R95	US NCAP 62 km/h (27° MDB) IIHS 50 km/h (90° MDB) EURONCAP 50 km/h (90° MDB)
	Side Pole	FMVSS 214	US NCAP 32 km/h (Pole 75°) EURO NCAP 32 km/h (Pole 75°)
	Rollover	FMVSS 208, 216a, 226	US NCAP SSF(Static Stability Factor) IIHS Roof Crush
	Rear	FMVSS 202a, 301 UN R32	IIHS Whiplash Static and dynamic EURO NCAP Whiplash Static (Front, Rear) and dynamic. AEB (Autonomous Emergency Brake Systems) City
Component	Pedestrian	FMVSS 201U R (EC) 78/2009, 631/2009, UN R127, UN R21	EURO NCAP Flex PLI, Upper Legform, Headforms, AEB Interurban and VRU (Vulnerable Road Users*)

Table A.1 Current crash testing programs

Frontal

See 1.4.2.

Side Barrier

MDB (Movable Deformable Barrier) driven at 50 km/h. Full lateral collision on the driver's side. The occupants are WS50 (World Side Impact Dummy 50th Percentile) on the driver side and Q1.5 and Q3 child dummies seating in the rear positions. Test introduced due to the higher frequency of fatalities in this type of accident. Specially challenging for automakers due to the short crumple zone at disposal for energy dissipation. Current strategies of designers to minimize the risk of injury are the use of high-strength steel in the B-Pillar, curtain airbags, energy-absorption management in the door and seat components and shorter fire times for side airbags.

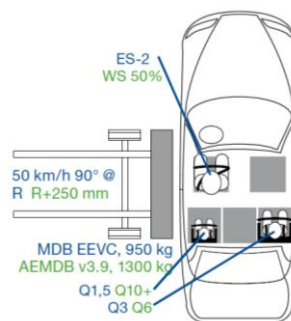


Fig. A.1 Side barrier Euroncap (Green: starting on 2015)

Side Pole

Car moved sideways at 32 km/h. Barrier: Static rigid pole. The car is moved on a platform with a impact angle against the pole of 75°. The occupant is a WS50 (World Side Impact Dummy 50th Percentile) on the driver position. Test introduced to represent accidents where the driver, after losing the control of the car, collides laterally into a rigid roadside objects (trees, poles etc). The higher structural intrusion values in this kind of test increases the injury risk especially for the head. Similar safety design strategies as for the side barrier are applied here.

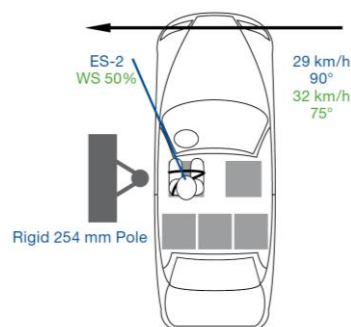


Fig. A.2 Side pole Euroncap

Whiplash (Rear crash)

Sled test with accelerated using 3 different pulses. Seat mounted on a sled. The occupant is a BioRID (Biofidelic Rear Impact Dummy). The test represents low-speed rear crashes where WAD (Whiplash Associated Disorders) are likely to occur. The motivation is to encourage principally seat designers to optimize materials, head restraint geometries and active systems helping to minimize an excessive distortion of the cervical spine in rear crash scenarios.



Fig. A.3 Whiplash (Rear crash) [41]

Child Safety

EURONCAP's approach divides the assessment in three fields:

- Child restraint system performance: In frontal and side crash test child dummies are included as occupants. The motivation is to reduce the more than 500 children fatalities in Europe per year in traffic accidents, being this number just for occupants, without including pedestrians and cyclists. The injury criterias analyzed with the child dummies cover head exposure and excursions, neck acceleration and chest acceleration.
- Child restraint system installation check: Incompatibilities between vehicle and children restraint systems could reduce dramatically the performance of such systems. Additionally, a misuse of the user could even worsen the situation. In this case the protocol verified some characteristics of the system using a selected group of child seats, among others the buckle location, seat belt length and ISOFIX mounts accessibility and stability. Automakers are encouraged to provide easy-to-install CRS (Child Restraint Systems) and are compelled to specify in the vehicle's manual the seat position where the child seat cannot be fixed.
- Check of ISOFIX provision: The most secure method for attaching a child seat to the vehicle structure is ISOFIX (see [131]). The "installation check" evaluates if the ISOFIX mounts are installed in different seat positions, "i-Size" seat use, frontal airbag disabling switch, integrated child seats etc.

Pedestrian Protection

Automakers are encouraged to develop safety systems and pedestrian-friendly front-end structures attempting to reduce the injury risk in a crash event of pedestrians, cyclist and motorcyclist. The front-end structures of the car are evaluated by impacting test. Principally the bonnet, leading edge of the bonnet, windshield and the bumper are tested. The risk of injury in a crash event of the head, pelvis, and legs (upper and lower) are evaluated as follows:

-Head impact: Impact test to represent a collision of a pedestrian head to the bonnet at 40 km/h. Head-impactors (Adult and child sizes) are used to evaluate the deceleration ranges. Front-end designers are encouraged the develop energy-dissipation structures, external airbags, advance safety systems as pop-up bonnets etc. The evaluation rates the test locations on the bonnet with a good, adequate, marginal, weak or poor safety level depending on the deceleration levels achieved by the underlying structure.

-Upper leg impact: Impact test to represents a collision of the upper leg on the leading edge of the bonnet at 40 km/h. Upper leg impactors are used to evaluate decelerations, deformations and reaction forces. This test is targeting a reduction of the pelvis and femur injuries in pedestrian accidents by optimizing a pedestrian-friendly design of the front-end shape. The evaluation ranking method is the same as for the head impact.

-Lower leg impact: Impact test to represent a collision of the lower leg on the bumper at 40 km/h. Lower leg impactors are used to evaluate bending moments and knee ligament elongations. The target of this test is to evaluate the bumper performance to mitigate non-fatal (but costly) lower leg injuries. The evaluation ranking method is the same as for the head impact.

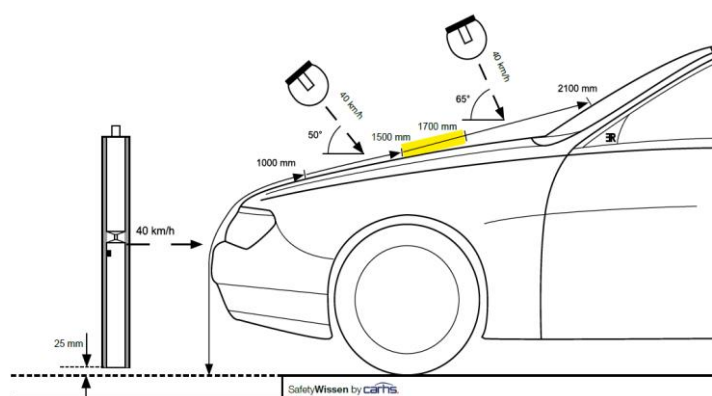


Fig. A.4 Impactors: Adult and child head, upper leg, and lower leg [37]

Safety Assist (Active Systems)

Assisted driving systems will become more and more the main topic in vehicle safety design. The effectiveness of such systems have been boosted with the rapid development and introduction of reliable sensor systems, actuators and, in the near future, interconnected communications between vehicles and infrastructure [41]. To assess the performance and functionality of these driver- assist systems the following test have been implemented:

-ESC (Electronic Stability Control) test: The vehicle is driven at 80 km/h. Steering wheel rotations up to 270°. The lateral displacement of the vehicle and stability among others are the criteria for the assessment. The ESC systems are now mandatory and this test is not performed anymore. Nevertheless it is included as clarification.

-Seatbelt reminders: Is of common knowledge that unbelted occupants will have always a higher injury risk in a car crash. A simple reminder is a cost-effective feature in order to reduce the chance that the occupants forget to wear the seatbelt or just try to avoid the “discomfort”.

-Speed Assistance Systems: Crashes very often are related with excessive speed. Exceeding the defined velocity limits in specific traffic environments will increase the risk of injury if an accident occurs. This test assesses the capabilities of the system to inform and warn the driver when the velocity threshold is reached. The test is performed under three velocity limits.

-AEB Interurban (Autonomous Emergency Braking at Interurban Speeds): This test assesses the capabilities of the system regarding warning the driver and semi- or fully automatically braking the vehicle in an imminent rear-end crash. Three test conditions are evaluated including (i) approach to a stationary target: From 30 km/h to 80 km/h in 5km/h steps, (ii) approach to a slower target: From 30 km/h to 80 km/h in 5 km/h steps (the target drives at 20 km/h) and (iii) approach to a braking target (vehicle drives at 50 km/h, with initial braking distances of 12 m and 40 m when the target drives at 50 km/h and brakes with $a=-2 \text{ m/s}^2$ and $a=-6 \text{ m/s}^2$ each).

-Lane Departure Assistance: Standard test are performed and reported by the car manufacturer based on the procedure described in the *Lane Departure Warning System Confirmation Test from the NHTSA*. Euroncap gives credit to automakers [41] that develop of warning- and active- lane departure systems. The target is to warn the driver when the lane is unintentionally leaved or when the lane-change indicator is not activated by the driver.

Other NCAPs protocols slightly differ from the Euronap test. Specific local-market-defined requirements and political decisions shape the protocols conditions. Detailed information about other NCAPs can be found in [42].

.

B.APPENDIX: DUMMIES

Historical Development of the Dummies

Year	Designation	Developer	Comment
1946	ALDERSON	ARL (Alderson Research Laboratory) & Sierra Engineering	Mechanical surrogate of Para-gliders
1949	Sierra-SAM	Sierra Engineering	Dummy for the US-Air Force
1952	GARD	Grumman-Alderson	Research-Dummy
1954	FBP	ARL	Evolution of the GARD to be applied in both US-Air Force und Automotive industry
1956	ASP	ARL	Dummy for the APOLLO Space program
1962	VIP	ARL	Dummies in seated position for automotive applications in sizes 50th, 5th, and 95th percentiles. Child dummy (3 und 6 Y.O.).
1963	Biofidelity test: Sierra-SAM vs. VIP	Holliman Air Force Base	Comparison test of SIERRA SAM- und ARL's VIP-Dummy to volunteer test. From this point the VIP proved to be more biofidelic than the Sierra-SAM.
1964-69	VIP 50 A and B Versions	ARL	Improved versions based on the VIP 50 th Percentile to test ejection seats for the US-Navy and the US-Air Force.
1950-70	ACTD	ARL & Sierra Engineering	Joint development of Crash-Test-Dummies for vehicle safety resulting in the ACTD based on GARD, VIP and SAM.
1971	Hybrid-I	ARL	Merge of the ARL- and SAM resulting in a hybrid dummy with the body of the ARL and head of the SAM.
1972	Hybrid-II	General Motors (GM)	Improvements of the Hybrid-I head, neck, shoulder, spine and knee.
1973	Part 572	NHTSA	Adoption of the Hybrid-II as standard test device for the FMVSS208 / Part 572.
1973	ATD 502	NHTSA / GM	Evolution of the Part 572 (or Hybrid-II). Improvements of the head, neck, articulations and ribs. The spine and knees were redesign. Also the posture were improved.
1976	Hybrid-III (H350)	NHTSA / GM	Evolution of the ATD 502: Redesign neck and thorax. More sensors implemented. Optional use to replace the Hybrid-II as standard for the FMVSS 208.
1979-87	US-SID	NHTSA / UMTRI	Side Impact Dummy (SID) based on the

		(Univ. of Michigan Transportation Institute)	Hybrid-II. New development of the thorax to be applied in side crash testing. Defined as standard for the FMVSS 214.
1983-89	EuroSID	EEVC-WG9 / TRL, INRETS, APR, Bast & TNO	New development of a side-crash dummy. Planed for the ECE-R 95.
1988-89	Hybrid-III (H395 and H305)	HUMANETICS & SAE	Derivatives development of the Hybrid-III: 95 th Percentile (male) and the 5 th Percentile (female)
1988-90	Bio-SID	GM, FTSS & SAE	Development of a more biofidelic side-crash Dummy based on the Hybrid-III. BioSID means Biofidelic Side Impact Device
1985-95	TAD-50M	NHTSA / GESAC (General Engineering and Systems Analysis)	Predecessor of a new generation of frontal-crash dummies: The THOR.
1995	THOR-ALPHA	NHTSA / GESAC	New development for a more biofidelic frontal-crash dummy “THOR” (Test Device for Human Occupant Restraint). Planned to replace the current Hybrid-III in regulations and consumer test.
2000	RID-II and RID-3D		Derivative based on the THOR dummy for rear crash.
200-	BioRID	Chalmers University	Rear impact dummy developed in parallel to the RID-II and RID-3D. Developed to assess WADs (Whiplash Associated Disorders)
2000	EuroSID-II		Replace the Euro-SID-I.
200-	ES-2re		Evolution of the EuroSID-II with re (rib extensions)
2000	WSID50	WorldSID Task Group / HUMANETICS / DENTON	New development for a side-crash dummy. WorldSID50 means World Side Impact Dummy 50 th Percentile.
2005	THOR-NT	NHTSA	Improved version of the THOR-ALPHA after evaluation by JARI (Japan Automobile Research Institute) and JAMA (Japan Automobile Manufacturers Association). Anthropometry, biofidelity, durability and usability were improved for this release [44]
2000-2009	THOR-FD	FID / APROSYS	Updated version of the THOR-NT carried out in the projects FID and APROSYS
2011	THOR-K (SAE)	NHTSA / SAE	Re-evaluated version of the THOR-NT by the THOR-TASK-FORCE (formed by SAE supported by NHTSA) and including recommendations based on the FID and Aprosys projects. This dummy includes an add-on modification kit that improves it's biofidelity.
2011	THOR-M (Metric)	NHTSA / HUMANETICS	Humanetics was contracted by the NHTSA to develop a metric version of the THOR-K called THOR-M (Metric)

Table B.2 Highlights of the crash test dummy-development

Application Fields of the Dummies

		ECE-R94	ECE-R95	ECE-R44	EuroNCAP	FMVSS208	FMVSS214	FMVSS213	FMVSS202a	USNCAP	IIHS	Research
Frontal	H395											X
	H350	X			X	X			X	X	X	
	H305					X				X		
	H350+THOR LX Leg											X
	THOR50 – X*									X	X	X
Side	ES-2		X		X							
	ES-2re						X			X		
	SID-IIs						X				X	
	WSID50				X		X					
	WSID05											X
	US-DOTSID											X
	SID-H3											X
Rear	BioRID				X						X	
	EVA-RID											X
	P-Serie (Part572-S)			X				X				
	Q-Serie			X	X							
Pedestrian	Upper Legform			X								X
	Flex-PLI			X								
	Headforms			X								
	Polar I and II											X

Table B.3 Overview of application fields for crash test dummies. Partly taken from Safety Update 2012 proceedings. Child dummies not addressed here.

H350 Instrumentation Overview

Region	Description	Accelerometer			Loadcell			Transducer		
Head	Head accelerometers	AX	AY	AZ						
Neck	Upper Neck Load Cell				FX	FY	FZ	MX	MY	MZ
	Lower Neck Load Cell				FX	FY	FZ	MX	MY	MZ
Clavicle	Load Cell (Left and Right)				FX	FZ				
Humerus	Load Cell (Left and Right)				FX	FY		MX	MY	
Thorax	Accelerometers in a triaxial array	AX	AY	AZ						
	Chest Displacement Transducer									DX
	Rib/Spine Load Cells				FX	FY	FZ		MY	
	Thoracic Spine Load Cell				FX	FY	FZ	MX	MY	
Lumbar Spine	Lumbar Spine Load Cell				FX	FZ			MY	
Pelvis	Accelerometers	AX	AY	AZ						
	Submarining Load bolts				FX					
Femur	Femur Load Cell				FX					
	Upper Femur Load Cell				FX	FY	FZ	MX	MY	MZ
Knee	Knee Displacement									DX
Lower Legs	Knee Clevis Load Cell						FZ			
	Upper Tibia Load Cell							MX	MY	
	Lower Tibia Load Cell					FY	FZ	MX		
	Upper Tibia Load Cell				FX	FZ		MX	MY	
	Lower Tibia Load Cell				FX	FY		MX	MY	
Ankle	Load Cell				FX	FY	FZ	MX	MY	MZ
Toe	Load Cell						FZ			

Table B.4 Overview of the H350 complete instrumentation. Full equipped.

Injury Assessment Reference Values for the H350

Region	Metric	Intercepts
Head	Peak 15ms HIC	700
	Peak COG Acceleration [G]	180
Neck	Shear Force, FX and FY (Upper / Lower) [N]	3100/3100
	Tension Force (Upper / Lower) [N]	4170/4170
	Compression Force (Upper / Lower) [N]	4000/400
	Lateral moment (Upper / Lower) [Nm]	144/287
	Flexion moment (Upper / Lower) [Nm]	190/380
	Extension moment (Upper / Lower) [Nm]	97/194
	Twist (Upper / Lower) [Nm]	97/97
		1/1
	Nij (Upper / Lower)	Force Tension (Upper / Lower) [N] 6780/6780
		Force Compression (Upper / Lower) [N] 6200/6200
		Moment flexion (Upper / Lower) [Nm] 305/610
		Moment compression (Upper / Lower) [Nm] 133/266
Humerus	Peak Resultant Moment [Nm]	214
Forearm	Peak Resultant Moment [Nm]	90
Thorax	Peak sternal deflection with shoulder belt [mm]	50
	Peak sternal deflection w/out shoulder belt [mm]	47.7
	Peak deflection rate [m/s]	8.3
	Peak T4 Acceleration [G]	60
Lower Extremities	Femur Compression [N]	0 ms to 10 ms: Linear decreasing from 9070 N to 7560 N
		>10ms: 7560 N
	Peak medial or lateral knee clevis [N]	4000
	Peak tibia compression [N]	8000
	Tibia Index	1
		Force intercept [N] 35900
		Moment intercept [Nm] 225
	Peak ankle moment [Nm]	225

Table B.5 Injury assessment reference values for the H350. Taken from [47]